

POLITECNICO DI MILANO

Scuola di Ingegneria Industriale e dell'Informazione
Corso di Laurea Magistrale in Ingegneria Energetica
Dipartimento di Energia



PERFORMANCE AND COST ASSESSMENT OF INTEGRATED SOLAR COMBINED CYCLES USING DIRECT STEAM GENERATION IN LINEAR COLLECTORS

Relatore: Prof. Andrea GIOSTRI

Co-Relatore: Prof. Marco BINOTTI

Tesi di Laurea di:

Angela D'Angelo, matricola 817329

Alessandra Ferrara, matricola 816318

Anno Accademico 2014-2015

Summary

The incoming sun radiation can be converted in electricity directly with photovoltaic technology, or transferred to a working fluid and then converted into electric energy into a power plant. Costs of solar thermal collectors employed in stand-alone power plants are noticeably higher than more mature technologies one. A suitable alternative to exploit the solar thermal energy is the integration of solar collectors in already existing fossil-fuelled power plants; in this way, the investment cost of the power block is avoided and solar thermal energy is converted at higher efficiency.

The present thesis work presents the analysis of several layouts of Integrated Solar Combined Cycle (ISCCs) in terms of nominal and annual performances and costs of the electricity.

In the first part of the work, an analysis of the existing integrated plants and the state of the art of the ISCC technology have been presented. Advantages and disadvantages of the integration of solar collectors in different kind of power plants have been pointed out and a literature review of present studies about ISCCs has been made. Several commercial solar collectors have been analysed and a thermal model has been built to estimate the heat losses of collectors receiver.

The reference Combined Cycle has been designed in Thermoflex®, using the HRSG arrangement of an existing combined cycle and thermodynamic inputs from the European Benchmarking Task Force (EBTF) document. The behaviour of this plant has been analysed in off-design conditions and its annual performances have been obtained.

The base cycle has been used as a base to build the Integrated Solar Combined Cycle layouts. Several different integrations on the bottoming cycle have been studied, including integrations with revamping of some components. In addition, fuel preheating and solar cooling hybridisations have been investigated. Nominal conditions evaluation has been performed for all ISCC layouts.

Variation of temperature, effective DNI and load have been simulated for a defined series of values, to obtain a good interpolation of parameters; this is necessary in order to evaluate the response of the power plant to meteorological conditions variation. The chosen location for the ISCC is Las Vegas, with a typical desert climate, high annual DNI and high mean temperatures. Meteorological data for Las Vegas were taken from the National Renewable

Energy Database (NREL). Effective DNI has been evaluated for each collector for every hour of the year, starting from the calculated sun position.

To analyse the power plants behaviour at varying operating conditions, both daily and annual simulations have been carried out. It must be noticed that, with the aim of avoiding the overload on the steam turbine, a control on GTs load has been activated to limit the inlet steam turbine mass flow at about 115% of its nominal value. Yearly simulations have been carried out for a power boosting scenario, assuming full load operation for 8760 h per year, and for a fuel saving scenario, where the power plants had to follow a scheduled power request.

Results of yearly simulations have been employed in the economic analysis. The cost of the electricity produced has been evaluated, using the International Energy Agency (IEA) simplified method, based on the Levelised Cost of Electricity (LCOE). A sensitivity analysis on the main economic assumption (i.e. fuel price and solar field specific cost) has also been performed.

Power boosting scenario simulations have been performed for all configurations analysed and the ISCC layout with best performances has been found. In this case, the parameter of merit selected is the solar marginal LCOE, since it is the more appropriate for comparisons among different solar configurations. Then, the best configuration has been simulated in fuel saving scenario over a year period. In this case, the LCOE is regarded as the suitable parameter of merit, since it accounts for different fuel expenditures for the analysed configuration.

In the last section of this work, considerations about obtained results are exposed. It has been found that, thermodynamically, the best layouts are the ones that includes a superheating section. The cost analysis concluded that the layout with integration of high pressure evaporation only (EVA HP layout) shows the best compromise between additional electricity production and incremental costs. However, the cost of electricity generated in this ISCC results higher than the one produced in the reference combined cycle. In the fuel saving scenario, EVA HP configuration has been compared with the reference combined cycle and it has been found that the ISCC cost of electricity results lower.

Riassunto

L'energia proveniente dal Sole può essere convertita in direttamente in energia elettrica, grazie alla tecnologia fotovoltaica, oppure trasferita come energia termica ad un fluido di lavoro. I costi della tecnologia solare termodinamica, utilizzata in impianti solari stand-alone, sono ancora particolarmente elevati, in confronto ad altre tecnologie più mature. Un'alternativa agli impianti stand-alone, per sfruttare l'energia solare termodinamica, è quella di integrare i collettori solari in impianti fossili già esistenti, risparmiando così il costo di investimento del blocco di potenza e convertendo l'energia solare con una maggiore efficienza.

In questo lavoro di tesi viene presentata l'analisi di diversi layout di cicli combinati integrati con la tecnologia solare termodinamica (Integrated Solar Combined Cycle –ISCC); ne sono state valutate le prestazioni nominali, le medie annuali e i costi dell'elettricità prodotta.

Per prima cosa, è stata fatta una revisione della letteratura e dello stato dell'arte della tecnologia, evidenziandone le debolezze e i punti di forza. Le specifiche tecniche dei diversi collettori commerciali sono state raccolte ed è stato implementato un modello termico per la stima delle perdite termiche nel ricevitore, che saranno poi utilizzate per le successive fasi dello studio.

Per l'analisi dell'integrazione è stato necessario definire il layout di un impianto a ciclo combinato, usato come base per gli impianti integrati. Dell'impianto di base sono stati valutati il comportamento nominale e in condizioni di off-design durante l'anno.

Sono state studiate diverse integrazioni nel ciclo a vapore, anche considerando alcuni casi di ridimensionamento dei componenti della caldaia a recupero. Inoltre, sono state studiate anche le integrazioni sullo scambiatore di preriscaldamento del gas naturale e in un ciclo frigorifero ad assorbimento usato per il raffreddamento dell'aria in ingresso alla turbina.

Sono state simulate le condizioni di off-design degli impianti integrati al variare di temperatura, radiazione efficace e carico delle turbine a gas. I valori ottenuti sono stati interpolati per valutare il funzionamento annuale dell'impianto. La località selezionata per la valutazione dell'impianto è Las Vegas, che è caratterizzata da un clima tipicamente desertico, elevate radiazione annuale ed alte temperature medie. I dati meteorologici per questa località sono stati presi dal "National Renewable Energy Database" (NREL) ed è stata valutata la radiazione efficace per ciascun collettore, per ogni ora dell'anno.

Sono state condotte analisi giornaliere e annuali sugli impianti integrati per valutare la risposta del ciclo integrato alle variazioni delle condizioni ambiente. Per evitare condizioni di sovraccarico sulla turbina a vapore, è stato posto, come limite massimo della portata in ingresso, il 15% in più della portata nominale. Per verificare tale limite si è tenuto un controllo sul carico delle turbine a gas.

Due possibili scenari di carico sono stati presi in considerazione: uno in cui l'impianto funziona per 8760 ore all'anno al suo carico massimo (power boosting) e uno in cui il carico è imposto dalla rete (fuel saving).

I risultati ottenuti dalle simulazioni annuali sono stati utilizzati per l'analisi economica. Il costo dell'elettricità prodotta è stato calcolato utilizzando il metodo semplificato dell'International Energy Agency, basato sul "Levelised Cost Of Electricity" (LCOE). È stata infine fatta un'analisi di sensibilità sui principali parametri di costo utilizzati (costo dei campi solari e del combustibile).

Il caso di power boosting è stato valutato per ogni configurazione presentata; per questo caso, il parametro di merito selezionato come più appropriato per il confronto tra gli impianti integrati è stato l'LCOE solare marginale. La configurazione che risulta migliore dall'analisi in condizioni di power boosting è poi stata analizzata anche in modalità fuel saving. In quest'ultimo caso, si è effettuato il confronto dell'LCOE delle diverse configurazioni, in quanto tiene conto del risparmio del combustibile che si può ottenere grazie all'integrazione solare.

Le considerazioni riguardo i risultati ottenuti sono state riportate nell'ultima sezione. Dal punto di vista termodinamico, l'integrazione più efficiente è quella che prevede l'integrazione del campo solare anche nella sezione di surriscaldamento. L'analisi dei costi ha, invece, evidenziato che la configurazione migliore è quella che integra il solare sul solo evaporatore di alta pressione (EVA HP); essa mostra il miglior compromesso tra produzione addizionale di energia e costi incrementali. In ogni caso, il costo dell'energia generata negli impianti ISCC è superiore a quello del ciclo combinato di base per quanto riguarda la modalità power boosting. Infine, nello scenario di fuel saving, dal confronto tra il ciclo combinato e il ciclo integrato si è ottenuto un costo dell'elettricità prodotta con il layout EVA HP inferiore a quello dell'impianto di riferimento.

Table of contents

Introduction	1
<i>Chapter 1: Solar hybrid power plants</i>	3
1.1 Hybridisation	4
1.1.1 Hybrid solar-steam power plants	6
1.1.1.1 Coal Rankine cycles	6
1.1.1.2 Non-coal Rankine cycles.....	9
1.1.2 Hybrid solar-gas power plants	10
1.2 Integrated Solar Combined Cycles	12
1.2.1 Solar bottoming cycle hybrid: Integration point.....	14
1.2.2 Performance parameters	15
1.2.3 Bibliographical review	16
1.3 Existing plants.....	20
<i>Chapter 2: Solar collectors</i>	21
2.1 Heat transfer fluid and Direct Steam Generation.....	22
2.2 Low temperature solar collectors.....	24
2.3 Medium temperature solar collectors.....	24
2.4 High temperature solar collectors - Point focus systems	25
2.5 High temperature solar collectors - Linear focus collectors	27
2.5.1 Parabolic Trough Collectors.....	28
2.5.1.1 Reflectors	28
2.5.1.2 Receiver.....	29
2.5.2 Linear Fresnel Collectors.....	30
2.5.2.1 Reflectors	31
2.5.2.2 Receiver.....	32
2.6 Performance parameters	32
2.6.1 Parabolic trough.....	33

2.6.2	Linear Fresnel.....	35
2.7	Commercial collectors.....	38
2.7.1	Heat loss model.....	38
2.7.2	Eurotrough ET 150.....	40
2.7.3	SkyTrough.....	44
2.7.4	Archimede HEMS08.....	45
2.7.5	Polytrough 1800.....	46
2.7.6	Nova 1 & Supernova.....	47
2.7.7	Industrial solar LF11.....	48
2.8	CSP power plant cost analysis.....	50
<i>Chapter 3: Natural Gas Combined Cycle.....</i>		<i>53</i>
3.1	Thermodynamic principles.....	53
3.2	Components.....	55
3.2.1	Gas turbine.....	55
3.2.2	Bottoming cycle.....	59
3.2.2.1	HRSG.....	59
3.2.2.2	Steam turbines.....	60
3.2.2.3	Condenser.....	61
3.3	Performance parameters.....	61
3.4	Effects of variation of operating conditions on CC performances.....	62
3.4.1	Gas cycle.....	62
3.4.1.1	Ambient pressure.....	63
3.4.1.2	Pressure drops.....	63
3.4.1.3	Ambient temperature.....	63
3.4.2	Bottoming cycle.....	64
3.5	Reference NGCC.....	64
3.5.1	EBTF Combined Cycle.....	64
3.5.2	Simeri Crichi Combined Cycle.....	73
3.5.3	Base Case.....	81
<i>Chapter 4: Solar integration.....</i>		<i>87</i>
4.1	Solar bottoming cycle hybridisation.....	89
4.1.1	Fresnel integrations.....	90

4.1.1.1	High Pressure Evaporator.....	90
4.1.1.2	High Pressure Evaporator and Superheater.....	97
4.1.1.3	High Pressure Economiser, Evaporator and Superheater.....	98
4.1.1.4	High Pressure Evaporator and Intermediate Pressure Evaporator	100
4.1.1.5	Intermediate Pressure Evaporator	101
4.1.2	Fresnel integrations performance parameters in design conditions	103
4.1.3	Parabolic troughs integrations	106
4.2	Other configurations	113
4.2.1	Solar fuel preheat hybridisation.....	113
4.2.2	Solar cooling hybridization	116
<i>Chapter 5: Yearly Simulations.....</i>		<i>119</i>
5.1	Simulation method.....	119
5.2	Power boosting	125
5.2.1	Representative days simulations.....	125
5.2.1.1	Solar Field analysis	126
5.2.1.2	Cycle analysis.....	130
5.2.2	Yearly simulations results	138
5.3	Fuel saving.....	145
5.4	Other integrations – Power boosting	149
5.4.1	Solar fuel preheat hybridisation.....	149
5.4.2	Solar cooling hybridisation.....	149
<i>Chapter 6: Economic analysis.....</i>		<i>151</i>
6.1	Method and cost assumptions	151
6.2	Cost evaluation	153
6.2.1	Bottoming cycle - Power boosting	153
6.2.1.1	Sensitivity analysis.....	160
6.2.2	Bottoming cycle – Fuel saving	162
6.2.3	Other configurations – Power boosting.....	163
Conclusions		165
APPENDIX A: Sun position		171
Bibliography		173

List of Figures

Figure 1: CO ₂ emission reduction strategy effects , according to the IEA [8].	2
Figure 2: Solar-coal integration - Preheating process arrangement	7
Figure 3: Solar-coal integration - Boiling process arrangement	8
Figure 4: Solar-coal integration – superheating process arrangement	8
Figure 5: Process diagram of a geothermal plant with CSP steam superheating [19].	9
Figure 6: Possible solar-gas hybridisation layouts – Adapted from [28].	10
Figure 7: Solar air preheat hybrid –SOLGATE project [30].	11
Figure 8: Solar cooling hybrid [29].	12
Figure 9: Possible solar integration points in a combined cycle – Adapted from [40]	15
Figure 10: Classification of solar collectors based on typology of tracking and focusing [48].	22
Figure 11: Example of flat plate collector [51].	24
Figure 12: Schematic design of a CPC collector [51].	25
Figure 13: Solar field dispositions: surrounded field in Germasolar thermosolar plant (left figure [55]) and north field in Abengoa Solar power plant (right figure [56]), Spain.	26
Figure 14: Monthly energy production in Almeria (36° 50' 0" N, 2° 27' 0" W) with different parabolic trough orientation [52].	27
Figure 15: Schematic representation of parabolic trough reflector [57].	28
Figure 16: Heat collection element of parabolic trough collectors – adapted from [10].	30
Figure 17: Linear Fresnel concentrator concept [65].	32
Figure 18: Heat collection elements adopted for LFC [11].	32
Figure 19: Schematic representation of receiver end losses [52].	35
Figure 20: Schematic representation of LFC losses [66].	36
Figure 21: Angles definition of a concentrating reflector with horizontal N-S orientation [64].	37
Figure 22: Longitudinal and transversal IAM as a function of incidence angle [67]	38
Figure 23: a) One-dimensional steady-state energy balance and b) thermal resistance model for a cross-section of the receiver [68].	39
Figure 24: Schott PTR70 receiver tube [63].	41
Figure 25: $K\theta i$ and $\cos\theta$ as functions of incidence angle for Polytrough 1800 collector. $K\theta i$ already includes cosine effect.	47
Figure 26: Schematic representation of Industrial solar LF11. (1)supporting structure, (2) primary reflectors, (3) receiver, consisting of secondary reflectors and absorber tubes [75].	48

Figure 27: heat loss curves as a function of the fluid mean temperature between tube inlet and outlet.....	50
Figure 28: Total installed costs (left) and LCOE (right) breakdown for a parabolic trough plant in South Africa [76].....	51
Figure 29: Specific cost and LCOE for LFR solar thermal power plant with 6 hours storage in a medium irradiance region (DNI 2000 kWh/m ² /year) [77].	51
Figure 30: Schematic representation of a NGCC equipped with two GTs, two HRSGs and a shared steam power block [80].....	55
Figure 31: GE 9F.03 gas turbine [82]	55
Figure 32: Variation of GT parameters as a function of GT load. The variation is defined as the ratio of the parameter with respect to its nominal value.	58
Figure 33: GT efficiency as a function of GT load.	58
Figure 34: Different possible layouts of HRSGs - Adapted from [31].	59
Figure 35: TQ diagrams for a single pressure level HRSG and a three pressure levels HRSG – Adapted from [31].	60
Figure 36: Thermflex® layout of the reference EBTF combined cycle plant.	66
Figure 37: GTs net efficiency as a function of total GTs load.....	72
Figure 38: Variation of TIT and TOT as a function of total GTs load, where Δ indicates the ratio of the parameter with respect to its nominal value.	73
Figure 39: HRSG layout of the Simeri Crichi combined cycle.....	74
Figure 40: comparison of the χ of the two analyzed plants as a function of the total load of gas turbines for the fixed ambient temperature of 15°C	77
Figure 41: comparison of the $\eta_{steam\ cycle}$ of the two analyzed plants as a function of the total load of gas turbines for the fixed ambient temperature of 15°C	78
Figure 42: comparison of the η_{HRSG} of the two analyzed plants as a function of the total load of gas turbines for the fixed ambient temperature of 15°C.	79
Figure 43: comparison of the η_{CC} of the two analysed plants as a function of the total load of gas turbines for the fixed ambient temperature of 15°C	80
Figure 44: Trend of exhaust losses of the LP stage of the steam turbine of the reference plant at 30°C of ambient temperature and 100% of GTs load.	83
Figure 45: Combined cycle efficiency as a function of ambient temperature and GTs load.	84
Figure 46: Recovery factor as a function of ambient temperature and GTs load.	85
Figure 47: Steam cycle efficiency as a function of ambient temperature and GTs load.....	86
Figure 48: HRSG efficiency as a function of ambient temperature and GTs load.	86
Figure 49: T-Q diagram for one HRSG of the reference combined cycle with the heat from gases for every section.	88
Figure 50: Layout of the integration of the solar field in the high-pressure evaporation section. Reported numbers are referred to the SM1 case.	90
Figure 51: T-Q diagram for one HRSG for the high pressure evaporator integration with the heat from gases for every section.	93

Figure 52: T-Q diagram for one HRSG for the high pressure evaporator integration with adjusted steam turbine and SH3. Heat from gases reported for every section. 96

Figure 53: T-Q diagram for one HRSG for the high pressure evaporator integration with adjusted steam turbine and high pressure SHs. Heat from gases reported for every section. 96

Figure 54: layout of the integration of the solar field in the high-pressure evaporation and superheating section of the combined cycle. 97

Figure 55: layout of the integration of the solar field in the high-pressure economiser, evaporation and superheating section of the combined cycle. 99

Figure 56: layout of the integration of the solar field in the high and intermediate pressures evaporators of the combined cycle. 100

Figure 57: Layout of the integration of the solar field in the intermediate pressure evaporator of the combined cycle..... 102

Figure 58: Layout of the integration of the solar field in the fuel preheating section of the combined cycle. Flows 58 and 128 are, respectively, the withdrawal and the reinjection in the HRSG..... 114

Figure 59: T-Q diagram of the fuel preheater exchanger for the CC (continue lines) and for the ISCC (dotted lines) 115

Figure 60: Layout of the solar cooling integration for the combined cycle. 117

Figure 61: Solar irradiance world map, where the Sun Belt is highlighted [96]. 120

Figure 62: Hourly DNI distribution for each day of the year in Las Vegas (NV)..... 121

Figure 63: Inverse cumulative function of the direct normal irradiation and ambient temperature in Las Vegas. 122

Figure 64: Inverse cumulative function of the effective DNI in Las Vegas for PTC (ET II) and LFC (Supernova EVA HP). 122

Figure 65: Daily trends of DNI..... 126

Figure 66: Daily trends of effective DNI for LFC..... 126

Figure 67: Daily trends of effective DNI for PTC..... 127

Figure 68: Trend of ambient temperature during representative days..... 127

Figure 69: Trends of DNI and net heat absorbed by fluid in the solar field in the reference summer day for PTC and LFC. 128

Figure 70: Trends of DNI and net heat absorbed by fluid in the solar field in the reference autumn day for PTC and LFC. 129

Figure 71: Trends of DNI and net heat absorbed by fluid in the solar field in the reference winter day for PT and LFC..... 129

Figure 72: Daily trends of incremental solar-to-electricity efficiency for EVA HP SM1 configuration..... 130

Figure 73: Daily summer trends of net power produced by reference CC with GTs at 100% load and ISCC SM1. 131

Figure 74: Daily summer trends of net power produced by reference CC with GTs at 100% load and ISCC SM1,5..... 132

Figure 75: Daily summer trends of net power produced by reference CC with GTs at 100% load and ISCC SM2..... 132

Figure 76: Trends of fuel consumption of reference CC with GTs at 100% GT load and SM1, SM 1.5 and SM2 ISCCs during the reference summer day. 133

Figure 77: Fuel consumption as a function of the ratio between the produced power and the nominal power for the SM2 EVA HP integration at $T_{amb} 30^{\circ}C$, DNI 800 W/m². 135

Figure 78: Trends of net power produced by reference CC with GTs at 100% GT load and ISCC SM2 with new ST and SHs during summer and winter days..... 135

Figure 79: Trends of HP turbine inlet temperature for EVA HP SM1 configuration during representative days. 136

Figure 80: Trends of HP turbine inlet temperature for three different configurations during summer representative day..... 136

Figure 81: Trends of HP turbine inlet pressure for EVA HP SM1 configuration during representative days. 137

Figure 82: Annual electricity production for the reference CC and ISCC different layouts with LFC and different solar multiples. 138

Figure 83: GTs load regulation as a function of the effective DNI and ambient temperature for EVA HP layout..... 139

Figure 84: GTs load regulation as a function of the effective DNI and ambient temperature for EVA HP+IP layout. 139

Figure 85: Annual electricity production attributed to the solar resource for different layouts with LFC and different solar multiple..... 140

Figure 86: Annual electricity production with and without defocusing for the EVA HP layout with LFC and different solar multiples. 141

Figure 87: Annual solar electricity production with and without defocusing for the EVA HP layout with LFC and different solar multiples. 141

Figure 88: Annual electricity production for the reference CC and EVA HP LFC with and without revamping..... 142

Figure 89: Annual solar production for the EVA HP LFC layout with and without revamping. 142

Figure 90: Annual electricity production for different layouts with SM1 and different solar technologies..... 143

Figure 91: Annual solar electricity production for different layouts with SM1 and different solar technologies..... 144

Figure 92: $\eta_{incr, sol - el, annual}$ for different layouts, SM1 and different solar technologies..... 145

Figure 93: Scheduled load profile for the fuel saving scenario..... 146

Figure 94: Fuel consumption over 48 hours (August 16th and 17th) for the reference combined cycle and EVA HP SM2 in the scheduled load scenario. 147

Figure 95: Fuel consumption over 48 hours (August 16th and 17th) for the reference combined cycle and EVA HP SM2 in the modified scheduled load scenario..... 148

Figure 96: LCOE for the reference CC and ISCC layouts with LFC and different solar multiple..... 154

Figure 97: Solar marginal LCOE for the reference CC and layouts with LFC and different solar multiple. 155

Figure 98: LCOE for EVA HP configuration with and without defocusing 156

Figure 99: Solar marginal LCOE for EVA HP configuration with and without defocusing. 156

Figure 100: LCOE for EVA HP SM2 configurations with the replacement of the ST..... 157

Figure 101: Solar marginal LCOE for EVA HP SM2 configurations with the replacement of the ST..... 157

Figure 102: LCOE for different ISCC layouts with solar multiple equal to 1. 158

Figure 103: Solar marginal LCOE for different ISCC layouts with solar multiple equal to 1. 159

Figure 104: Reference combined cycle LCOE as a function of the fuel price..... 160

Figure 105: LCOE for the reference combined cycle and for ISCC as a function of the solar collectors cost specific to the aperture area. 161

Figure 106: Δ LCOE, defined as the difference of the reference CC LCOE with the ISCC LCOE, as a function of the fuel price. 161

Figure 107: LCOE for the reference CC and EVA HP configuration with two different solar multiple in fuel saving scenario..... 162

List of tables

Table 1: CSP Capacity in operation, under construction and under development in 2012 [18].	4
Table 2: Summary of published studies on ISCCs.....	18
Table 3: operative solar integrated cycles worldwide.	20
Table 4: Thermal model heat flux definitions [68].....	40
Table 5: SchottPTR70 - ET150 collector datasheet [63].....	42
Table 6: ET150 - Uvac collector datasheet [70], [71]	43
Table 7: SkyTrough collector datasheet [72].	44
Table 8: Archimede HEMS08 collector datasheet [61].....	45
Table 9: Polytrough 1800 collector datasheet [73].....	46
Table 10: Nova1 and Supernova collectors datasheet [74].	48
Table 11: Industrial Solar LF11 collector data sheet [75].....	49
Table 12: Gas/air/fuel stream table of the reference EBTF combined cycle plant. h is the fluid enthalpy referenced zero at 25°C and H ₂ O as vapor.	67
Table 13: water/steam stream table of the reference EBTF combined cycle plant. h is the enthalpy referenced to zero at 0°C and H ₂ O as vapor.	68
Table 14: Comparison between three different GT models and the percentage errors of their parameters with respect for GS results.	70
Table 15: Main results for NO TG configuration and for GE 9F.03 configuration.	71
Table 16: GTs regulation strategies analysed.....	72
Table 17: Water/steam stream table of the reference EBTF combined cycle plant at 30°C ambient temperature. h is the enthalpy referenced to zero at 0°C and H ₂ O as vapor. Fluxes are reported for only one HRSG.....	75
Table 18: Gas/air/fuel stream table of the Simeri Crichi power plant at 30°C ambient temperature. h is the fluid enthalpy referenced zero at 25°C and H ₂ O as vapor. Fluxes are reported for only one HRSG.....	76
Table 19: Combined cycle efficiencies for different evaporative pressure combinations [bar], where red cells contain lower values and green higher ones.....	81
Table 20: Combined cycle specific costs [€/kWe] for different evaporative pressure [bar] combinations, where green cells contain lower values and red higher ones.	81
Table 21: Main results for the new plant at ambient temperatures of 15°C and 30°C.....	82
Table 22: reference CC steam mass flow rates and pressures for HP, IP, LP stages of a single HRSG and steam turbine inlet conditions.	87
Table 23: Overview of solar integrations performed in this work.	89

Table 24: Supernova collector optical and geometrical parameters.	91
Table 25: Steam mass flow rates and pressures for HP, IP, LP stages of a single HRSG and steam turbine inlet conditions for the high pressure evaporator integration.	92
Table 26: Steam mass flow rates and pressures for HP, IP, LP stages of a single HRSG and steam turbine inlet conditions for the integration with a new turbine, solar multiples 1 and 2.	94
Table 27: Steam mass flow rates and pressures for HP, IP, LP stages of a single HRSG and steam turbine inlet conditions for the integration with new steam turbine and HP SH3 and the integration with new ST and all HP SHs.	95
Table 28: Steam mass flow rates and pressures for HP, IP, LP stages of a single HRSG and steam turbine inlet conditions for the EVA+SH integration.	98
Table 29: Steam mass flow rates and pressures for HP, IP, LP stages of a single HRSG and steam turbine inlet conditions for the ECO+EVA+SH1 integration.	99
Table 30: Steam mass flow rates and pressures for HP, IP, LP stages of a single HRSG and steam turbine inlet conditions for the EVA HP+IP integration.	100
Table 31: Noval collector optical and geometrical parameters.	101
Table 32: Steam mass flow rates and pressures for HP, IP, LP stages of a single HRSG and steam turbine inlet conditions for the EVA IP integration.	102
Table 33: Results for Fresnel integration configurations.	104
Table 34: Eurotrough 150+ Schott PTR70-DSG collector optical and geometrical parameters.	107
Table 35: Polytrough 1800 collector optical and geometrical parameters.	108
Table 36: Steam mass flow rates and pressures for HP, IP, LP stages of a single HRSG and steam turbine inlet conditions for the integration Parabolic trough collectors with Aperture area equal to the corresponding Fresnel case.	109
Table 37: Steam mass flow rates and pressures for HP, IP, LP stages of a single HRSG and steam turbine inlet conditions for the integration Parabolic trough collectors with Land area equal to the corresponding Fresnel case.	110
Table 38: Results for Parabolic integration configurations.	112
Table 39: Main nominal results for the solar fuel preheat integration.	116
Table 40: Main nominal results for the solar cooling hybrid integration.	117
Table 41: η_{CC} analysis for solar cooling integration.	118
Table 42: Las Vegas geographical coordinates and weather data.	120
Table 43: electricity production, solar share and CO ₂ emissions for SM1 and SM2 EVA HP with three different load regulations.	148
Table 44: Annual simulation results for solar fuel preheat hybridization.	149
Table 45: Annual simulation results for solar cooling hybridization.	150
Table 46: Economic assumptions for FCR evaluation [34].	152
Table 47: Costs assumptions for ISCC and CC power plants.	153

Acronyms

3LR	Three pressure level+ RH HRSG configuration
CC	Combined Cycle
CCS	Carbon Capture & Storage
CO₂	Carbon Dioxide
COE	Cost Of Electricity
CPC	Compound Parabolic Collector
CR	Concentration Ratio
CSP	Concentrated Solar Power
DNI	Direct Normal Irradiance
DSG	Direct Steam Generation
EBTF	European Benchmarking TaskForce
ECO	Economiser
ECO3 + EVA + SH1	ISCC with SSG in parallel to third high pressure economiser, high pressure evaporator and first high pressure superheater
ECO3 + EVA + SH2	ISCC with SSG in parallel to third high pressure economiser, high pressure evaporator and first and second high pressure superheaters
ETC	Evacuated Tube Collector
EVA	Evaporator
EVA + SH1	ISCC with SSG in parallel to high pressure evaporator and to the first high pressure superheater
EVA + SH2	ISCC with SSG in parallel to high pressure evaporator and to first and second high pressure superheaters
EVA HP	ISCC with SSG in parallel to high pressure evaporator

EVA HP+IP	ISCC with SSG in parallel to the high and medium pressure evaporators
E-W	East-West
FPC	Flat Plate Collector
GT	Gas Turbine
HP	High pressure
HRSC	Heat Recovery Steam Cycle
HRSG	Heat Recovery Steam Generator
HTF	Heat transfer Fluid
IAM	Incidence Angle Modifier
IP	Intermediate Pressure
ISCC	Integrated Solar Combined Cycle
LFC	Linear Fresnel Collector
LHV	Lower Heating Value
LP	Low Pressure
New ST and SH3	ISCC with SSG in parallel to high pressure evaporator, with new ST and new SH3
New ST and SHs	ISCC with SSG in parallel to high pressure evaporator, with new ST and new HP SH
NGCC	Natural Gas Combined Cycle
NO_x	Nitrogen Oxide
NREL	US National Renewable Energy Laboratory
N-S	North-South
PSA	Plataforma Solar de Almeria
PTC	Parabolic Trough Collector
R&D	Research and Development
RH	Reheater
SEGS	Solar Electricity Generating Systems
SH	Superheater
SM	Solar Multiple

SSG	Solar Steam Generator
ST	Steam Turbine
STPP	Solar Thermal Power Plant
TIT	Turbine Inlet Temperature
TMY	Typical Meteorological Year
TOT	Turbine Outlet Temperature
VIGV	Variable Inlet Guide Vanes
DNI_{eff}	Effective DNI
LCOE	Levelised cost of electricity
$LCOE_{sm}$	Solar marginal levelised cost of electricity
IEA	International Energy Agency
FCR	Fixed Charge Rate
C_{inv}	Total investment cost
$C_{O\&M}$	Yearly operation and maintenance costs
C_{fuel}	Annual fuel cost
COP	Coefficient of Performance

Symbols

η	Overall efficiency
θ	Incidence Angle
$\Delta\dot{W}_{ST}$	Power output increase of the steam bottoming cycle
\dot{Q}_{sol}	Absorbed solar thermal power
\dot{W}_{tot}	Total electric power (fossil+solar)
\dot{Q}_{tot}	Total absorbed thermal power
η_{sf}	Solar field thermal efficiency
$\eta_{incr\ sol-el}$	Incremental solar-to-electrical efficiency
$\eta_{incr\ th-el}$	Incremental thermal-to-electrical efficiency
F_{sf}	Solar Fraction
x_{sf}	Solar Share
W	Single Mirror Aperture
D_{abs}	Absorber Diameter
$\eta_{o\ peak,PTC}$	PTC peak optical efficiency
$\eta_{o,PTC}$	Overall PTC optical efficiency
$\eta_{shading}$	Shading coefficient
$\eta_{end\ losses}$	End losses coefficient
$\eta_{o\ peak,LFC}$	LFC peak optical efficiency
$\eta_{o,LFC}$	Overall LFC optical efficiency
θ_{\parallel}	Incident angle projection on longitudinal plane
θ_{\perp}	Incident angle projection on transversal plane
θ_i	Angle between beam vector and its projection on transversal plane
χ	Recovering Factor

$\dot{Q}_{in,steam\ cycle}$	Thermal power transferred to water in HRSG
$\dot{Q}_{flue\ gases,av}$	Thermal power available in the exhaust gas (cooled to ambient temperature)
\dot{W}_{ST}	Electrical power produced by Steam turbine
η_{CC}, η_{NGCC}	NGCC overall efficiency
η_{TG}	Gas Turbine efficiency
$\eta_{steam\ cycle}, \eta_{SC}$	Steam cycle efficiency
η_{HRSG}	Bottoming cycle efficiency
β	Gas turbine compression ratio
Δp	pressure drop
\dot{Q}_{sf}	Heat absorbed by the solar field
ΔT	Temperature difference
$\phi_{LONG,STZ}$	Standard time one meridian longitude
STZ	Standard Time Zone
δ	Solar Declination
n	Day of the year
E_n	Equation of time
t	Local Time
t_s	Solar time
ω	Solar Angle
θ_z	Zenith Angle
α_s	Solar altitude
γ_A	Azimuth Angle
θ_i	Incidence Angle
L_{abs}	Absorber Length
D_{pm}	Mean distance between primary mirrors and receiver
$k(\theta_i)$	DNI eff correction factor (PTC)
$L_{spacing}$	Spacing length between rows

E_{sol}	Annual electricity production from solar resource
$E_{ISCC,annual}$	Annual electricity production of the ISCC
$E_{CC\ eq,annual}$	Annual electricity production of the equivalent CC
$Q_{sf,annual}$	Annual heat collected by the solar field
$m_{fuel,annual}$	Annual fuel consumption
$\eta_{CC,annual}$	Annual CC efficiency
$\eta_{incr\ sol-el,annual}$	Annual incremental solar-to-electricity conversion efficiency
$\eta_{incr\ sol-th,annual}$	Annual incremental solar-to-thermal conversion efficiency
$\eta_{SF,annual}$	Annual solar field efficiency
$x_{sf,annual}$	Annual solar share
k_D	Real debt interest
$P1$	Annual insurance rate
l	Power plant life expectancy
ΔC	Additional expenditure for the integration
$\Delta[\%]$	Percent variation

Introduction

Global energy consumption in the last half century has increased very rapidly and it is expected to grow over next years. The energy demand has mainly been satisfied by fossil fuels during the last century. In 2012, world's primary energy supply based on fossil sources was above the 80% of the total and the 68% of the electricity was generated through fossil fuels [1]. However, the excessive exploitation of fossil resources puts the scientific world to face two upcoming problems: the easy-access reservoir depletion and climate changes.

The Fifth Assessment Report from the Intergovernmental Panel on Climate Change (Working Group I Contribution to the IPCC, 2013) states that the human influence on the climate system is clear: among the anthropogenic sources of greenhouse gases, the use of energy represents, by far, the largest source of emissions. To be more precise, the 69% of the total production, and the 42% is produced because of the electricity and heat generation [2].

There are several ways to overcome these problems: carbon capture & storage (CCS) [3], subsidies for energy-saving policies [4], diversification of supplies [5] and progressive substitution of fossil-fuels based technologies for electricity generation with carbon-free ones, such as renewables [6] or nuclear [7]. CCS implies the removal of a CO₂ flux by adding new treatment units to the base plant without changing the fuel employed but this leads to higher costs and additional efficiency losses due to not-ideal removal processes. Finally, increasing conversion efficiencies is a suitable option, but alone, it is not enough to achieve the total goal of CO₂'s emissions reduction. The scenario presented by the International Energy Agency (IEA) for the reduction of 48Gt of carbon dioxide emissions provides the combined use of all the previously cited strategies (see Figure 1).

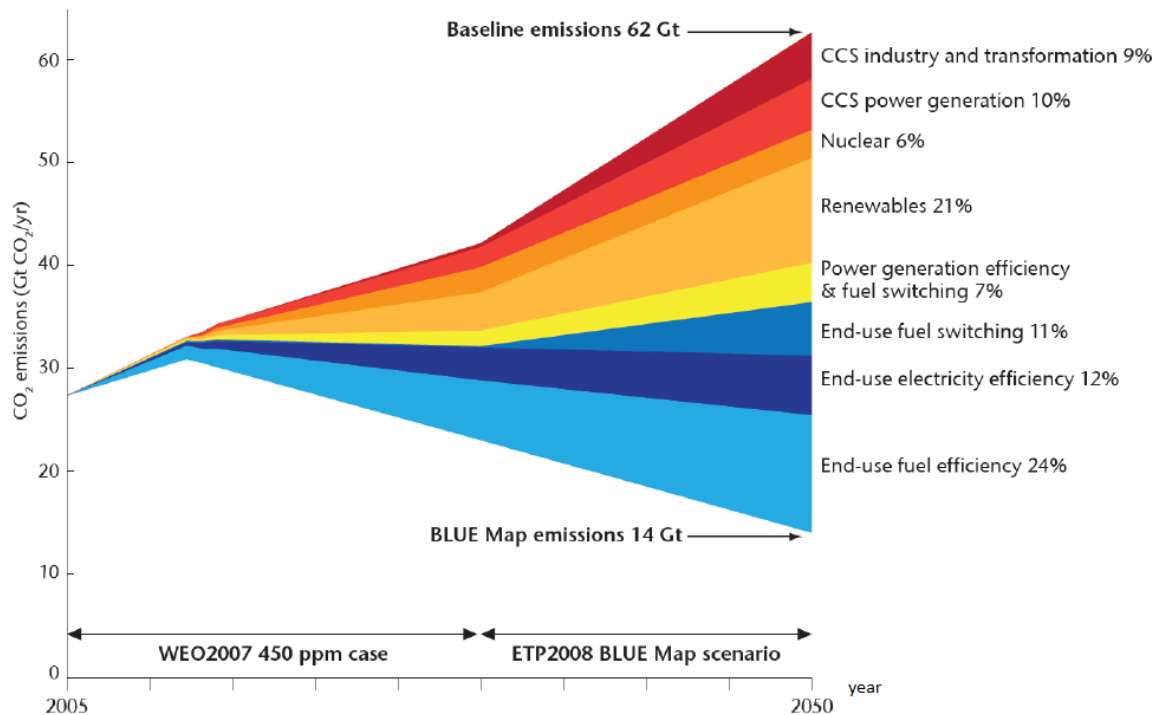


Figure 1: CO₂ emission reduction strategy effects , according to the IEA [8].

Renewable energies could be the most effective option in the energy production sector: in fact, they are generally well distributed worldwide in contrast to other energy sources, their carbon dioxide emissions are theoretically¹ null and represent an alternative to the conventional technologies.

Of all the available renewable sources, solar energy is the most abundant one and it is available almost everywhere. In the last years R&D focused on the photovoltaic systems because of subsidy policies, especially in Europe. Nevertheless, the efficiency of solar panels is still low, with nominal values around the 20% (higher or lower with respect to the employed technology)[9]; therefore thermodynamic conversion may be an effective alternative, most of all because it allows thermal energy storage (TES) and integration with conventional plants. Thermodynamic solar technologies are still characterised by high costs and low efficiencies but their implementation into conventional plants may be more attractive; in this way the renewable resource can be exploited with the higher efficiency of a more mature technology, thus reducing the cost of the solar electricity produced.

This work aims to point out the advantages of integrating the solar thermal technology with the existing fossil power plants: the hybridisation may lead to synergies and to an efficient use of both the resources, in order to make the solar energy dispatchable and more affordable and to reduce the fossil fuel consumption.

¹ CO₂ emissions from a renewable source power plant are not equal to zero because it requires energy, during the construction, the operative life and the decommissioning, likely produced by fossil source.

Chapter 1

Solar hybrid power plants

There are two ways of producing electricity from solar radiation: photovoltaics and thermodynamic systems. Photovoltaic solar systems produce energy by direct conversion of the solar radiation thanks to the photovoltaic effect [10]; solar thermal systems instead convert radiation into thermal energy to be used in conventional thermal plants.

Photovoltaic has already a large employment in the electrical production in distributed generation (1-100kW) [11], while thermodynamic applications are suited for large scale power plants (above 10MW [11]) thanks to scale economies and to the possibility of exploiting thermal storage which can improve the dispatchability of the electrical energy produced.

The working principle of solar thermal power plants (STPPs) has ancient historic origins; according to the legend it comes from the burning glasses used by Archimede, during the siege of Syracuse, to burn the Roman ships [12]. The device was composed of 24 plane glasses, arranged on a hexagonal rotating structure, where the central glass was used to direct the solar rays reflected by the lateral ones. Since then, many progresses were made until professor Mouchout and his assistant Abel Pifre showed at the universal exposition in Paris in 1878 a solar engine able to produce steam at the pressure of 7 bar which could activate an ice-making machine. The device included a parabolic mirror with a diameter of 4 m and a boiler of 70 litres capacity. The American engineer Frank Shuman made one of the most important implementations of concentrated solar power (CSP) in 1913. Thanks to a subsidy, he built in Maadi (Egypt) the biggest CSP plant existing: the solar field, made of 5 parabolic trough collectors for a total area of 1200 m² [13], powered an engine which pumped 450 l/s of water used for irrigation and it could work even during nights thanks to a thermal storage with hot water. In 1964, Professor Giovanni Francia designed and built the first plant in the world based on linear Fresnel reflector, the S. Ilario sun station located in Genova [14]. In conjunction with the petroleum crisis, in the seventies, more attention was given to possible alternatives to fossil-based technologies. By the end of the 70s Sandia National Laboratories started collaborating with SERI (Solar Energy Research Institute, now NREL, National Renewable Energy Laboratory) in order to develop the CSP technology. In 1984, the first commercial power plant with parabolic collectors, the SEGS (Solar Energy Generating System) I, came into operation in the Mojave Desert, California, a region characterised by a

high solar irradiance. During the 80s, the research towards alternative CSP technologies, such as solar tower, dish Stirling and linear Fresnel collectors continued. In 1990, after a period of stasis in the research, 8 SEGS power stations were realised in the same location of the first one; for a total installed power of 354 MW. In 1980s and 1990s, Solar 1 and Solar 2 power plant based on solar tower technology came into operation in California [15]. Solar 2 guaranteed operations during nights thanks to a thermal storage with molten salts as heat transfer fluid. Molten salts are a mixture that is liquid at plant operative conditions and it can reach temperatures above 500°C. Between 2006 and 2010, many solar power plants were realised: in 2007 PS10 in Spain and NEVADASOLAR 1 in the USA, in 2008 Andasol-1 in Spain and Kimberlina in the USA, in 2009 PS20, Sierra Sun Tower and PE1 and in 2010 Andasol 2 and Maricopa. The launch of the largest solar thermal power plant, “Ivanpah Solar Power Facility” in 2014 in the Mojave Desert of California was an important step in the development of the solar thermodynamic technology. Anyway, costs of these kind of plants are still very high to be economically competitive with more mature technologies [16].

Today, the total nominal power installed of STPPs is evaluated to be of about 4,5 GW and it is expected to grow up to 12,4 GW within 2018 [17]. The majority of the CSP market share is covered by parabolic trough technology while solar tower and linear Fresnel technologies have a limited share, as shown in Table 1. Solar technologies will be further discussed in Chapter 2.

	Parabolic trough [MW]		Solar tower [MW]		Linear Fresnel [MW]	
Operating	1824	0,943	67,9	0,035	40	0,021
Under construction	2433	0,767	567,7	0,179	172	0,054
Under development	1280	0,500	800	0,313	367	0,143

Table 1: CSP Capacity in operation, under construction and under development in 2012 [18].

1.1 Hybridisation

Solar thermal plants are based on the conventional Rankine cycle and so they take advantage of well-known technologies. However, costs of solar equipment are very high, especially because technologies applied are not enough mature to compete with conventional ones. Moreover, capacity factors of this kind of plants are low due to the intermittent nature of the solar energy. Thermal storage can release energy production from solar hours but investment costs increase with increasing size of the storage. Cost analysis leads to the identification of an economic optimum, which is a storage that allows the plant to work in the full load condition for 7-8 hours [11].

In order to reduce costs and maximise the energy production, it is possible to hybridize solar production with other plants of different kind. The integration can follow two different ways: the first one is to consider the solar source as the main plant input while the fossil is used to keep continuous operation in the plant, the other is to assume the fossil system as the dominant one. In this work, the second approach has been chose as a promising way to exploit the solar technology since it can be exploited in systems with higher efficiency than stand alone solar plants. As a consequence, following considerations are referred to the second approach. Hybridisation is achievable with different types of plant and it can be categorized in several ways, first of all depending on the degree of integration [19]:

- *Light hybrid synergies*: there is a reduced interaction between the two plants, they only share minimal plant infrastructures. This hybridisation results in a minimum cost saving but it can be useful to enhance the dispatchability of the host plant. An example could be a system made by a Concentrating Solar Power (CSP) plant and a wind farm, which share the switchyard and substation. The thermal storage of the solar plant can be connected to the wind farm through electrical heaters; in this way, it is possible to store electricity generated in the wind farm during low price periods. This is particularly helpful during winters when solar radiance is low and it is difficult to “fill” the thermal storage with the solar plant only.
- *Medium hybrid synergies*: plants are physically connected and they share major equipment. Normally, in this kind of integration, the solar plant needs the components of the host plant to operate while the last one can operate independently: nowadays this is the most common type of integration. Costs reduction is noticeable but the solar share (defined as the ratio between the thermal power of the solar field and the total thermal power of the plant) is low, generally below 10% of the installed plant capacity.
- *Strong hybrid synergies*: plants are physically connected, they share major equipment and the cost reduction is significant. The solar share is normally higher than 30% of the installed plant capacity, which means systems where the solar and the other energy sources provide for similar amount of steam to the shared turbine. Termosolar Borges, a 22,5 MW_e facility near Les Borges Blanques in Spain, is an example of this kind of plant: the facility combines a solar field of 24 MW_{th} with two biomass burners of 22 MW_{th} each.
The use of CSP systems for enhancing thermodynamic conditions of the steam produced from low temperatures renewable sources is also included in the strong hybrid category.

The integration of solar technology into conventional plants can be performed in two ways: fuel saving and power boosting. Fuel saving aims to reduce fossil fuel consumption and greenhouse gases emissions. Power boosting on the other hand consists in exploiting solar field to increase the power plant output.

Different plant types can be used as base plant for the hybridisation with solar technologies: Rankine cycles fed with coal, biomasses, waste material or geothermal steam or gas cycles (either simple or combined cycle). In the following section, different hybridisation strategies will be discussed.

1.1.1 Hybrid solar-steam power plants

The solar-coal hybridization leads to several advantages: the plant can work at nominal conditions during nights and periods of low solar irradiation, avoiding the installation of a thermal storage. Moreover, the steam is converted with a higher efficiency into a relatively larger capacity units and the plant can be built using an existing power plant, allowing low implementation costs [20].

1.1.1.1 Coal Rankine cycles

The most common type of solar-steam integration is with coal Rankine cycles. This kind of hybridisation can be implemented in countries like China or Australia, where a great part of the energy generation is based on coal power plants [21], contributing to the reduction of greenhouse gases and increasing the efficiency of conventional power stations. This solution can be particularly attractive for the repowering of small old coal power stations [22].

The integration is applicable and effective in both the power boosting and the fuel saving modes. In power boosting, modern cycles are able to accept an increment of about 10 ÷ 15% of the steam mass flow over the design turbine capacity; this solution is suited to cover the peak load due to air conditioning that coincides with peaks of solar irradiation. On the other side, the fuel saving mode, where the production of the steam boiler is reduced, allows the reduction of consumption and emissions, in addition to an increased thermal efficiency of the steam boiler itself [23].

Solar hybridisation with coal plants can be achieved in 3 main ways [22], [24]:

- *Preheating process arrangement*: the solar field is employed in parallel to the plant main boiler to implement the feed-water preheating (Figure 2). This layout avoids regenerative extractions from the steam turbine thus enhancing the power output thanks to a greater mass flow expanded in the turbine.
- *Boiling process arrangement*: as shown in Figure 3, the solar field receives preheated water and generates saturated steam. This steam is then sent to the superheating section of the main boiler. There is no variation in steam flows withdrawal from the turbines to preheat the water.
- *Superheating process arrangement*: in this type of integration (Figure 4), solar power is used to produce part of the superheated steam injected in the turbine, starting from pre-heated water.

It is also possible to combine these layouts directly superheating the water from the condenser.

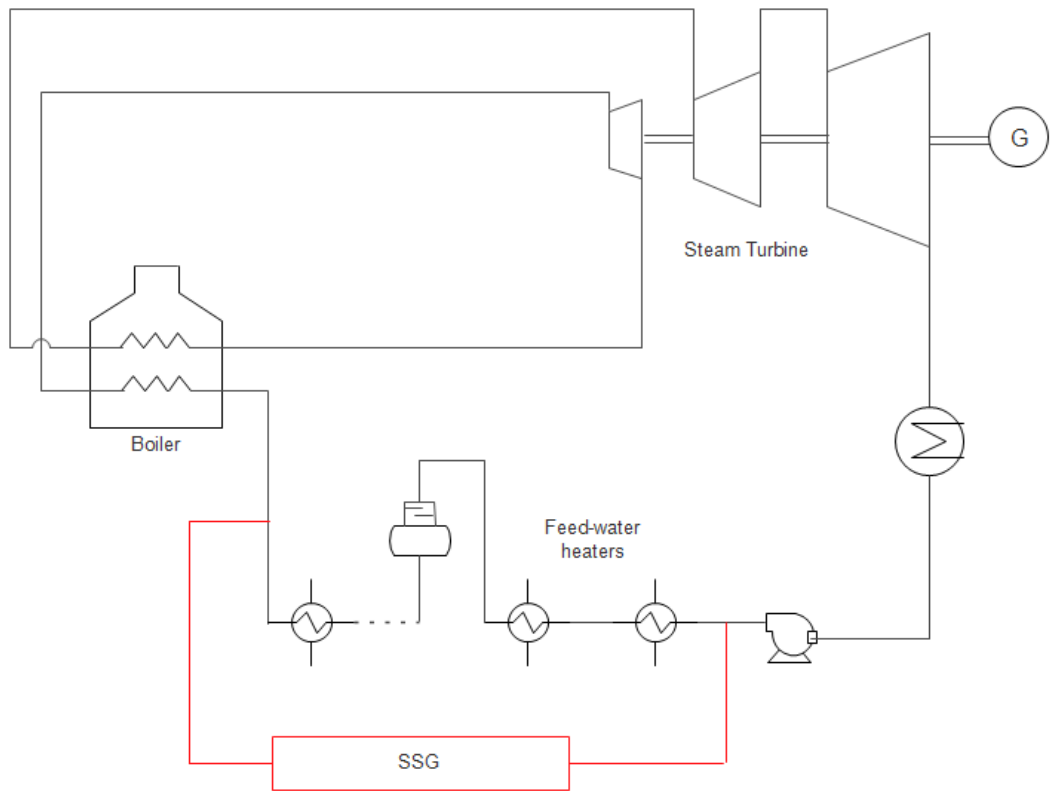


Figure 2: Solar-coal integration - Preheating process arrangement

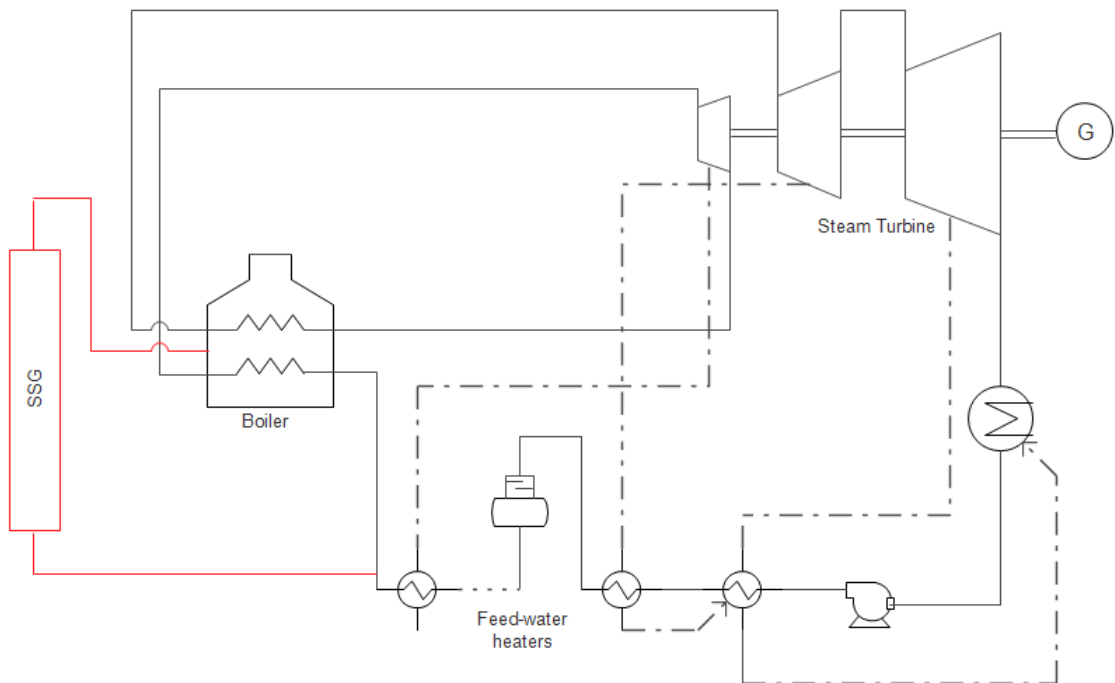
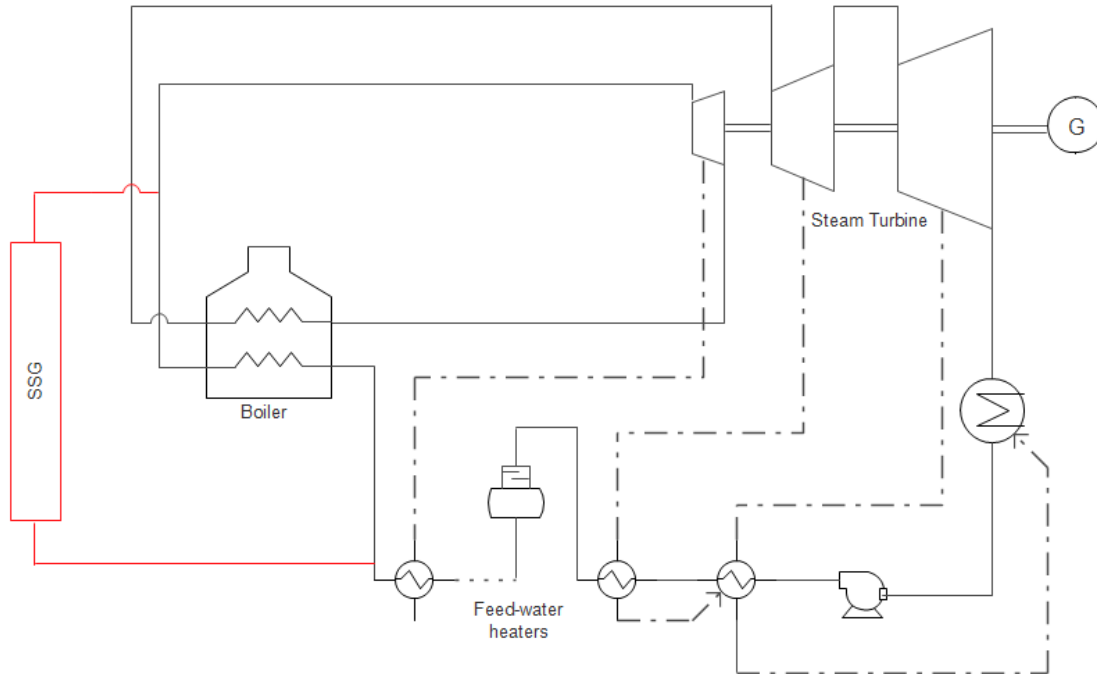


Figure 3: Solar-coal integration - Boiling process arrangement**Figure 4:** Solar-coal integration – superheating process arrangement

It is possible to analyse the energy benefits from the different configurations in order to understand which one gives the best advantages. General Electric Company carried out some studies at this purpose, finding out that the best method for hybridisation is to combine evaporation and superheating [25] because of the higher exergetic level of the steam produced. This kind of integration needs high-temperature solar collectors (above 250°C), whose costs are still high. The Kogan Creek solar boost project (Queensland, Australia) with 44 MW_e of solar electrical power at peak conditions, still under construction, is one of the coal plants with the biggest solar field integrated in an existing fossil-fuelled plant. It employs Linear Fresnel collectors in parallel to the boiler; the solar steam generated is injected in the cold reheat line. Also feed-water preheating in a regenerative Rankine power cycle is a convenient integration method, in fact it allows avoiding steam extraction from the turbine enhancing the overall efficiency of the cycle; it appears to be the most practical application for medium-temperature integration because it avoids complex issues of direct steam generation and integration with the boiler [26]. It is also possible to use low temperature solar collectors, which have poorer performance but are less expensive than high temperature collectors. Finally, the solar field can also be used to improve the combustion process by preheating of the combustion air.

1.1.1.2 Non-coal Rankine cycles

Solar-steam hybridisation can be performed even in Rankine cycles not feed with coal, such as those fuelled with biomass, waste materials and geothermal. In particular, in these plants, the steam reaches lower temperatures and it is thus possible to employ lower temperature solar collectors, with a noticeable reduction of costs.

The integration between solar technologies and biomass plants aims to decrease investment and levelised costs of electricity and to increase power dispatchability. Early studies of this kind of hybridisation took place in the 80s but, due to technical and financial issues, they remained purely theoretical [27]. The basic principles of this integration are similar to those of the solar-coal one: the solar field can be used to produce live steam or to preheat feed water or combustion air. However, if temperatures are generally lower than 430°C , the conversion efficiency is limited [19]. The development of this technology is held back because of the necessity to find suitable locations for plants, in terms of land and resources availability. Several CSP-biomass concepts have been investigated in the past but only the previously cited Termosolar Borges was built [27].

Solar and geothermal stand-alone plants are very expensive, because of components such as solar field and production wells. Thus, the integration can be useful to reach lower investment costs than the ones for single plants, allowing plants equipment to be shared. The integration can be achieved in several ways, as, for example, feed-water heating or steam superheating. As geothermal steam is generally at low temperatures (typically $150\div 200^{\circ}\text{C}$, $6\div 10$ bar), it is also possible to use the solar system to further superheat the flow, maximising the cycle efficiency [19] as in Figure 5.

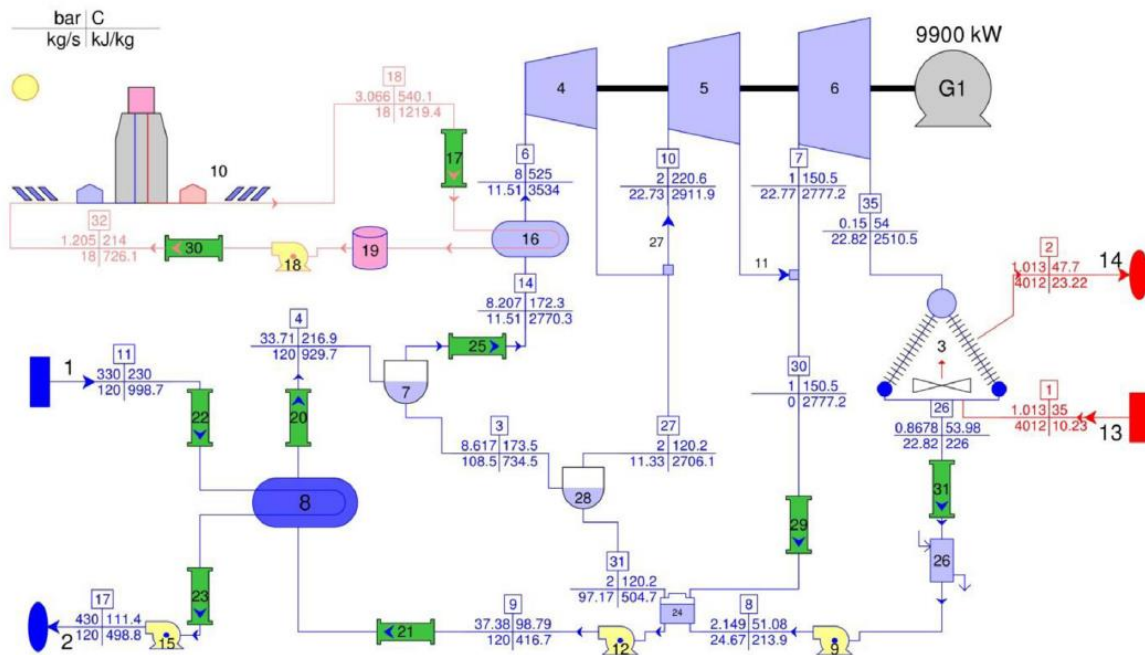


Figure 5: Process diagram of a geothermal plant with CSP steam superheating [19]

1.1.2 Hybrid solar-gas power plants

The integration between solar systems and gas power plants can be performed both in a Brayton cycle and in a Combined Cycle (CC); Figure 6 summarises different available strategies.

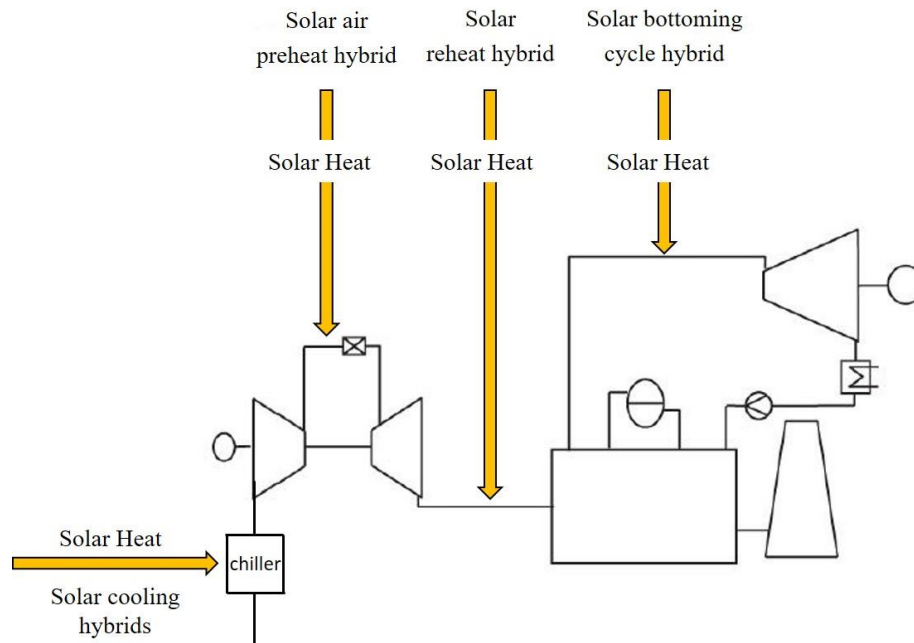


Figure 6: Possible solar-gas hybridisation layouts – Adapted from [28].

Configurations here represented can be classified in: [28], [29]

- *Solar air preheat hybrids:* the heat from the solar field is used to preheat the compressed air before the combustion chamber. The air inlet temperature in the combustor is determined by the solar technology used for the integration. A solar technology with high concentration factors is normally required, such as solar towers; they are capable to preheat the air from 400°C (compressor outlet temperature) to 800°C and above. There are several difficulties in the implementation of this innovative design; for example, in the combustor there is a significant variation of the air inlet temperature, which modifies combustion parameters. The solar field presents some problems too; special kinds of receivers are needed in this application, heat losses must be minimised since temperatures are very high, so evacuated solar receiver tubes must be used. Nowadays, the development of this technology is still at experimental state. In Figure 7, the “Solgate” project is shown, it employs a volumetric receiver to preheat air up to about 1000°C [30].

- *Solar cooling hybrids*: the Natural Gas Combined Cycle (NGCC) or the gas turbine is equipped with an absorption chiller for gas turbine inlet air cooling and subsequent power augmentation during hot days (Figure 8). In this integration there is no the need to reach high temperatures in solar collectors, so the low/medium temperature collectors ($100 \div 200$ °C) are particularly suited as solar technology. Additionally, this kind of system can be easily implemented to all kind of existing NGCC because of its simple design.
- *Solar preheat hybrids*: the solar reheating substitutes the duct burner for the post-firing. This operation requires the solar receiver to be capable of increasing the air temperature from about 500°C up to 1000°C. Even in this case, the most suitable technology is the solar tower.
- *Solar bottoming cycle hybrids*: this category includes all the solutions in which the solar collector is employed to enhance the steam production of the heat recovery steam generator. Depending on the solar collector used and on the characteristics of the fossil plant, the integration point can vary slightly: the solar heat can be used to replace or boost the steam produced in the evaporator, to preheat the feed-water in the economisers or to produce superheated steam.

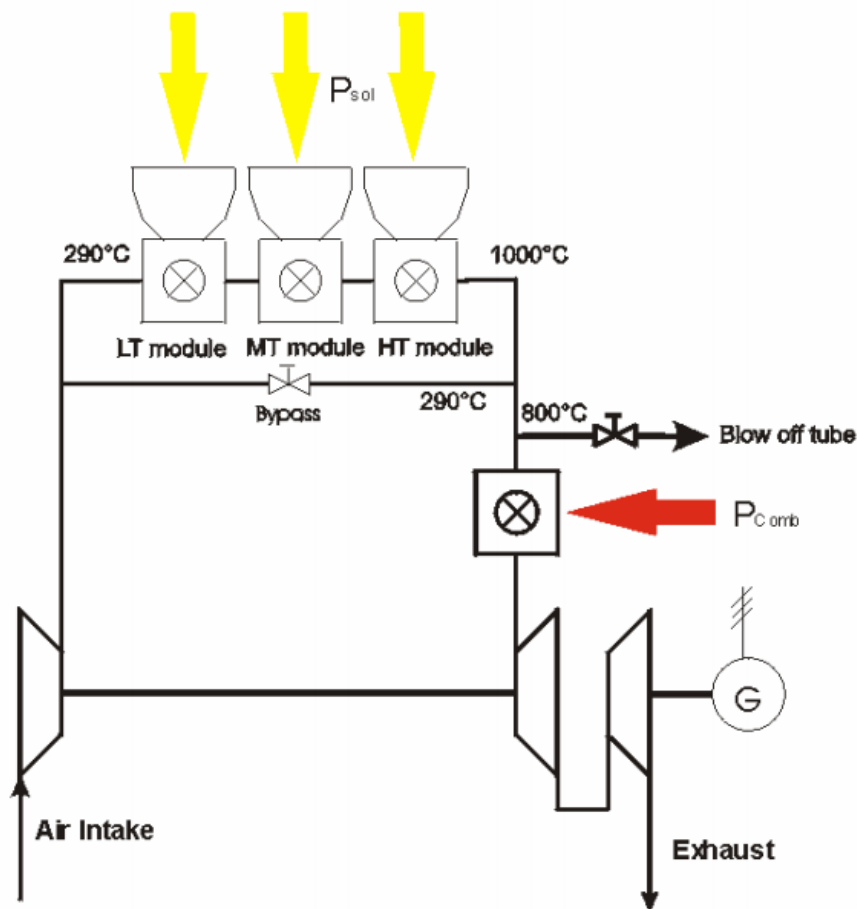


Figure 7: Solar air preheat hybrid –SOLGATE project [30].

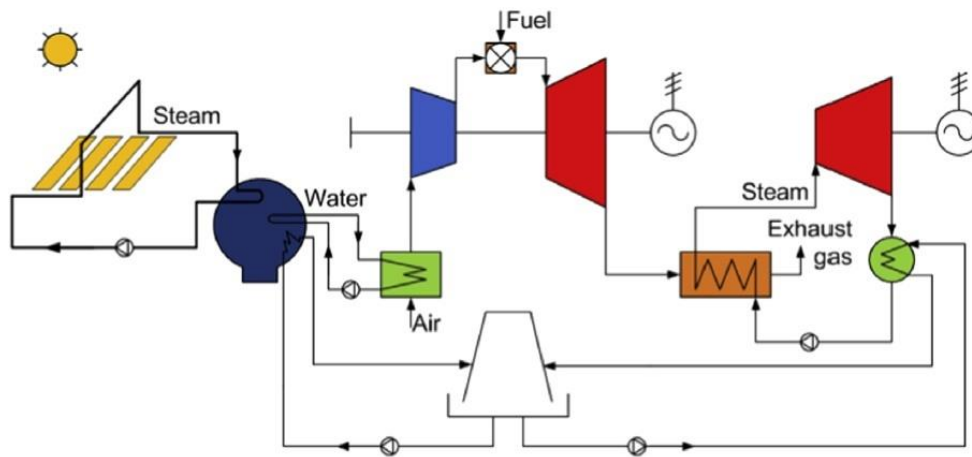


Figure 8: Solar cooling hybrid [29].

Solar air preheat and solar cooling hybrids can be implemented both in the Brayton cycle and in the CC while reheat and steam cycle hybrids are related to CC only. Among the possible solutions, the integration of solar steam into combined cycles seems to be one of the most promising ways to perform the integration between fossil plants and thermal solar technology. In fact, combined cycle have both the advantages of having high plant efficiency and of using a clean fuel. The solar bottoming cycle hybridisation will be further discussed in next paragraphs.

1.2 Integrated Solar Combined Cycles

The growing energy demand of the last years required the installation of many new power plants, which had to be characterised by high efficiencies and reduced installation times. The high efficiency, together with low investment costs and restrained emissions, made possible the spread of Combined Cycle power plants starting from the late 1980s [31]. Combined Cycles technology will be examined in Chapter 3.

The Integrated Solar Combined Cycle (ISCC) hybridises a conventional combined cycle with the solar thermal technology. The plant, basically, consists in a gas turbine, the Heat Recovery Steam Generator (HRSG) with its own steam turbine and generator and a solar field. It can be realised as a boost of an already existing power plant, with low solar share, bounded to technical limits of CC components, or as a greenfield power plant, which could handle higher solar share.

Several advantages promote ISCCs over solar only power plants; for example, ISCC plants have a higher solar to energy conversion compared to a solar only system, since the solar steam is converted in a more efficient steam turbine. If the increase of the steam flow in the turbine exceeds the maximum allowable limit, the steam turbine must be modified or substituted. In this case, for an ISCC the additional cost of a higher size steam turbine section

is lower than the overall cost of a dedicated steam power plant in a solar only system [32]–[34]. The hybridisation allows an improvement in solar energy dispatchability, especially if 24-hour operation is required, since the host plant can sustain the minimum load even when the solar system is not running. This configuration does not need a storage system, reducing the investment costs. In a solar only power plant without storage, as solar radiation varies, the turbine is subjected to sudden load variations, which can cause operational problems; on the contrary, the hybrid plant steam turbine does not suffer from the daily start up and shut down. One of the parameters that most affect the efficiency of a combined cycle is the ambient temperature, especially if the plant is equipped with an air condenser which is a common solution for arid areas where the DNI is high and so the integration with solar collectors can be most effective. When the ambient temperature increases, the mass flow aspired by the compressor reduces, implying a reduction of its power output and efficiency. Moreover, air condenser performances decreases because of the higher condensation temperature. The addition of solar energy can balance the gas turbine efficiency drop in off design conditions and the improvement is more evident in very hot atmospheric conditions [35]. In fact, as the DNI increases along with the ambient temperature, the solar hybridisation could smooth the total power plant output during the day or during the whole year [36]. In addition, the integration allows a gradual but greater diffusion of the solar thermal plants towards a maturation of the technology at lower cost rather than in the solar-only plants.

The main limit of the hybridisation is the maximum allowable solar contribution to the total generated electricity (from the gas turbine and the steam turbine), generally it could reach the value of 6% for the integration in an already existing Combined Cycle [37], [38]. A feasibility study is needed, not only to evaluate the thermodynamic impact of solar integration, but also to point out the physical and operational constraints of the existing plant configuration [36]. First of all, physical limitations can be on the maximum land area available for the solar field, depending on the CC location. Moreover, heat exchangers are designed to accommodate only the steam flow rate generated with fossil fuel: during daytime operations, exchange areas are not sufficient to guarantee the nominal temperature because of the augmentation of the total steam due to the production of the SSG. Instead, if the areas were designed to provide the desired temperatures using the combined fossil and solar flow rates, a higher efficiency could be reached, but attemperation during nights or period of low irradiation would become necessary to avoid excessive thermal stresses on components materials. The solar field is often used to replace the latent heat of evaporation, with the purpose of reducing the average temperature differences in the HRSG.

Another issue of the integration is that the steam turbine should have an higher size than the one of a conventional plant in order to accept the steam flow from the solar field and, when the solar steam generated is low or absent, the turbine will run at partial load conditions, with low steam pressure and lower conversion efficiency. The higher the solar contribution is, the greater the decaying of performance under part load condition will be [38]. An alternative is to maintain the steam turbine unchanged to assure the lowest possible retrofit

costs. In this case the maximum amount of solar integration is defined by the swallowing capacity of the steam turbine and by the maximum pressure in the evaporating drums [39].

Since ISCCs have several promising features, the purpose of this thesis work is to consider the hybridisation of a base combined cycle with different solar technologies and with different integration points, in order to study how the integration affects the plant behaviour and which configuration may be the most effective.

1.2.1 Solar bottoming cycle hybrid: integration point

Solar bottoming integration seems to be the most promising configuration between the ones explained in paragraph 1.1.2.

In a conventional heat recovery steam cycle (HRSC), several possible points of integration can be found, as illustrated in Figure 9, overlooking the solar technology employed [40]:

- EVA: the solar steam generator (SSG) is fed with hot water from the economizer and it generates saturated steam, which is returned to the HRSG for the superheating. The water from the economiser is split into two streams; a fraction is evaporated in the solar field, while the remaining flow is evaporated in the HRSG. The streams of saturated steam are then mixed and sent to the superheater (SH).
- ECO-EVA: SSG is directly fed from the deaerator; it firstly preheats and then evaporates the water, which is introduced at the outlet of the evaporation drum. The purpose of this configuration is to minimise thermal losses in the solar field, thanks to the lower fluid average working temperature in the solar collector.
- EVA-SH: SSG takes water from the exit of the economiser. Water is firstly evaporated and then superheated in the solar field; this steam is further superheated in the HRSG. Therefore, the HRSG superheater is divided into two stages: the low temperature one heats up only the steam produced in the HRSG drum, while the high temperature one heats up the solar and the fossil streams. This configuration aims to achieve the higher exergy input from the solar collectors.
- ECO-EVA-SH: SSG receives water from the deaerator, which is preheated, evaporated and superheated in the solar field. The generated steam is directed to the high temperature superheater of the HRSG as in the previous configuration. This implementation has the benefit of creating an independent pressure line in the SSG, avoiding the reinjection of steam in the HRSG.

These four configurations can be implemented at any pressure level; in a conventional three pressure levels HRSG, the most efficiency way to integrate solar thermal energy is producing high pressure steam because it allows the higher exergy level integration [38], [39].

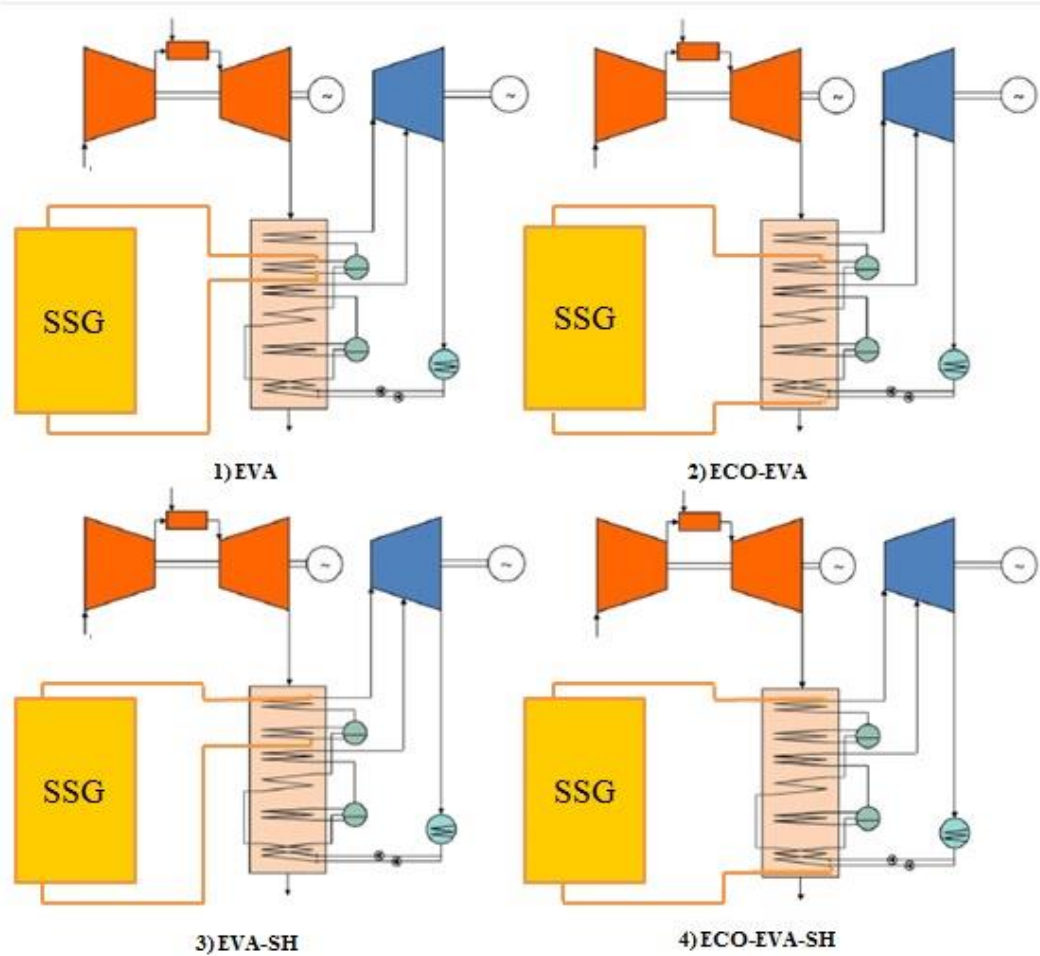


Figure 9: Possible solar integration points in a combined cycle – Adapted from [40]

1.2.2 Performance parameters

In this work, some figures of merit will be used to evaluate the performance of the analysed layouts.

Incremental solar efficiency accounts for how the additional heat given by the solar field is converted in the cycle. It can be specified as solar-to-electrical or thermal-to-electrical whether the efficiency of the solar field is considered or not[33], [37].

Incremental solar-to-electrical efficiency:

$$\eta_{incr\ sol-el} = \frac{\Delta \dot{W}_{ST}}{A_A DNI} \quad (1)$$

Incremental solar thermal-to-electrical efficiency:

$$\eta_{incr,th-el} = \frac{\Delta\dot{W}_{ST}}{\dot{Q}_{sf}} \quad (2)$$

Solar field thermal efficiency, which accounts for the absorbed solar heat over the incident solar radiation:

$$\eta_{sf} = \frac{\dot{Q}_{sf}}{A_A DNI} \quad (3)$$

Where:

$\Delta\dot{W}_{ST}$: power output increase of the steam bottoming cycle in the ISCC plant compared to the NGCC plant;

A_A : collectors aperture area;

DNI : Direct Normal Irradiance;

\dot{Q}_{sf} : Net heat absorbed by fluid in the solar field.

Solar Fraction is defined as the ratio of electricity generation boosted by solar heat compared to the overall electricity generation [36]:

$$F_{sf} = \frac{\Delta\dot{W}_{ST}}{\dot{W}_{tot}} \quad (4)$$

\dot{W}_{tot} : total power (fossil + solar).

Solar share accounts for the contribution of solar heat in the total heating load:

$$x_{sf} = \frac{\dot{Q}_{sf}}{\dot{m}_f LHV + \dot{Q}_{sf}} \quad (5)$$

1.2.3 Bibliographical review

ISCC technology is an interesting hybridisation system and thus some studies have been done and are available in literature. However, these studies are generally little exhaustive about the considered integrations and, in most cases, they do not specify under which assumptions the integration is performed (e.g. whether the cycle is projected from greenfield or as integration of a reference CC). Moreover, in most cases, studies consider the revamping of steam turbine and condenser because of the higher steam mass flow while it could be interesting to study integration conditions whether the CC components remain unchanged. Finally, there is not a univocal definition of solar share, solar fraction and solar incremental

efficiencies, so reported values are different to compare among different articles. In this paragraph, a review of available studies on ISCCs is presented.

The integration point is often on the maximum pressure line, since previous studies concluded that a higher pressure and temperature solar injection point leads to higher solar conversion efficiencies [36]. Kelly et al. [38] found out that the best integration point is the EVA in the high pressure line of a three pressure HRSG, achieving an higher solar thermal-to-electrical efficiency, about 40% against the 32% of the solar only power plant. Zhu et al. [36] used the same configuration in their study and they obtained high incremental solar thermal-to-electrical efficiency (about 44%) for solar fraction up to 10%; for higher solar fractions the efficiency decreases slightly, since the penalty for partial load operations during night and periods of low solar irradiation increases with the increasing of solar heat contribution. Dersch et al. [33] studied the EVA-SH configuration on the high pressure line, obtaining an incremental solar thermal-to-electrical efficiency of 37,5% with a solar share of 10%.

A. Rovira et al. [40] compared all the four different ISCC configurations using a base NGCC with a dual pressure level HRSG. They found that the best kind of integration is the EVA one, in parallel with the high pressure drum, because it is the best compromise between power, irreversibilities and $\eta_{incr\ sol-th}$, which reaches the value of about 43%. The EVA-SH configuration shows similar performances but the EVA one results in a simpler installation. The layouts with the feed-water preheating have lower efficiencies as there is already abundance of low temperature heat from the exhaust gases, which otherwise would not be exploited and the $\eta_{incr\ sol,th}$ registers values in the range of 32÷38%.

Manente et al. [37] analysed several configurations: also in this study the high pressure evaporator only seems to be the best integration mode, since it reaches the highest incremental solar efficiencies ($\eta_{incr\ sol-rad}=29,7\%$ $\eta_{incr\ sol-th}=48,73\%$ net), the lowest irreversibilities and the lowest collectors area required. The ISCC assets that include the preheating of the feed-water register lower solar thermal-to-electrical efficiencies (45,6 ÷ 46,3% net). The analysis of the T-Q diagram shows an improvement in the matching between exhaust gases and water/steam, due to the reduction of the heat load associated to the evaporation at constant temperature. In addition, the usage of the solar source to generate superheated steam worsens the thermal matching, since the exhaust gases are not completely exploited.

Cau et al. [41] analysed two different ISCC configurations, both based on the same triple pressure HRSG: in the first one the SSG produces steam in parallel to the high and medium pressure drums, in the second one the solar heat feeds a complete pressure line (ECO-EVA-SH) in parallel to the high pressure one. The EVA solution allows reaching better conversion efficiencies, but the maximum F_{solar} is about 10%. ECO-EVA-SH configuration allows reaching a greater power output.

An alternative two-stage ISCC was proposed by Li et al. [42]: a double pressure level NGCC is integrated with the EVA configuration in both the drums of the HRSG. The optimum working parameters of the HRSG, in order to enhance the system performances, are pointed out. $\eta_{incr\ sol,rad}$ achieves the value of 29,8% (that is $\eta_{incr\ sol,th} = 45,85\%$ considering the nominal efficiency of the solar collector) for the optimised system. This solution is compared to an ISCC with the integration in a single pressure drum (single-stage integration); the two-stage cycle shows better results than the single stage one. Moreover the two-stage integration allows reaching lower stack temperatures, resulting in better thermal matching in the HRSG, and achieving higher solar share (of 27,8% versus 23,1% of the single stage). Petela et al. [43] studied a plant that uses the solar heat input to produce steam in parallel to each drum of the three pressure levels of the bottoming cycle. The solar thermal input to each drum is accounted through a dynamic allocation control law, which minimises the irreversibilities of the solar collectors, giving the priority to the medium pressure level collector that showed the best thermal efficiency.

Montes et al. [35] analysed the same ISCC configuration in two different geographical location, Almería (Spain) and Las Vegas (USA). The solar field is coupled to the high-pressure level in the HRSG following the ECO-EVA configuration. The highest annual $\eta_{incr\ sol,th}$ is registered for the site of Las Vegas: its low value of 27,3%, even considering that the results are referred to an annual simulation, confirms that the use of solar heat input for the feed-water preheating involves a penalty on the $\eta_{incr\ sol,th}$.

The following table (

Table 2) summarises previous studies about the integration of the solar field into NGCCs.

Table 2: Summary of published studies on ISCCs.

<i>Authors</i>	<i>Year</i>	<i>HRSG pressure levels</i>	<i>Solar integration point</i>	<i>Heat Transfer Fluid</i>	<i>CSP technology</i>
G. Cau et al. [41]	2012	3	HP ECO-EVA-SH	CO2	PT
		3	HP EVA + IP EVA	CO2	PT
A. Perdichizzi et al. [44]	2015	2	HP ECO 2 - HP EVA - HP SH (mix prima dell'SH)	Therminol VP-1	PT
M.J. Montes et al. [35]	2010	2	HP ECO - HP EVA	DSG	PT
J. Dersch et al. [33]	2004	1	HP EVA - SH (lieve)	HTF	PT
G. Barigozzi [45]	2013	2	HP ECO 2 - HP EVA - HP SH (mix prima dell'SH)	Therminol VP-1	PT
		2	Combustor	Air	Central receiver

Table 2.1: Summary of published studies on ISCCs (continued).

<i>Authors</i>	<i>Year</i>	<i>HRS G pressure levels</i>	<i>Solar integration point</i>	<i>Heat Transfer Fluid</i>	<i>CSP technology</i>
H. Nezammahalleh et al. [46]	2010	1	EVA-SH	DSG	PT
		1	EVA-SH	HTF	PT
G. Zhu et al. [36]	2014	3	HP EVA	DSG	PT
G. Manente et al. [37]	2015	3	HP EVA	Therminol-VP1	PT
		3	HP EVA - SH1	Molten Salts	PT
		3	HP ECO3 - EVA - SH1	Molten Salts	PT
		3	HP EVA-SH1-SH2	Molten Salts	Central receiver
		3	HP ECO3 - EVA	DSG	Linear Fresnel
		3	HP ECO3 - EVA - SH1	DSG	Linear Fresnel
A. Rovira et al. [40]	2012	2	HP EVA	Therminol-VP1	PT
		2	HP ECO-EVA		PT
		2	HP EVA-SH		PT
		2	HP ECO-EVA-SH		PT
		2	HP EVA	DSG	PT
		2	HP ECO-EVA		PT
		2	HP EVA-SH		PT
		2	HP ECO-EVA-SH		PT
K. Petela et al. [43]	2015	3	HP EVA + IP EVA + LP EVA	SYLTHERM 800	PT
M. Horn et al. [32]	2004	1	EVA	HTF	PT
Y. Li et al. [42]	2014	2	HP EVA + LP EVA	DSG	PT
B. Kelly et al. [38]	2001	3	HP EVA	HTF	PT
C. Ojo et al. [39]	2012	3	HP ECO-EVA-SH	/	Central receiver

1.3 Existing plants

Currently, a small number of plants already exploit the integration with solar thermal technology, the following table (Table 3) reports a summary of the operative integrated plants. As it can be seen, integrated solar combined cycle is nowadays the most frequently performed solution for the solar integration, although the number of existing plants is very small.

Table 3: operative solar integrated cycles worldwide.

<i>Plant</i>	<i>Location</i>	<i>Overall power</i>	<i>Type of plant</i>	<i>CSP technology</i>	<i>Heat Transfer Fluid</i>	<i>HRSB pressure levels</i>	<i>Solar integration point</i>
Hassi R'Mel	Algeria	150 MW	ISCC	PT	Therminol VP1	1	EVA
Ain Beni Mathar	Morocco	470 MW	ISCC	PT	Therminol VP2	3	/
Kuraymat	Egypt	140 MW	ISCC	PT	Thermal VP1	1	EVA-SH
Yazd	Iran	467 MW	ISCC	PT	/	2	HP EVA
Archimede	Italy	760 MW	ISCC	PT	Molten Salts	3	HP ECO-EVA-SH
Martin Next Generation	Florida	3750 MW	ISCC	PT	Diathermic oil	/	/
Termosolar Borges	Spain	22,5 MW	biomass	PT	HTF	/	/
Kogan Creek	Australia	750 MW	coal	Fresnel	DSG	/	/
Liddell thermal station	Australia	50 MW	coal	Fresnel	DSG	/	/

Chapter 2

Solar collectors

The integrated solar combined cycle, as described in the previous chapter, integrates the steam produced in a thermodynamic solar collector into a standard combined cycle. In this chapter solar collector technology is presented while the next chapter will discuss the combined cycle technology.

A solar collector is a high-absorptance and transmittance, low-reflectance, radiative/convective heat exchanger that emulates as closely as possible the performances of a radiative black body in the visible light spectrum [10]. Solar collectors technologies can be classified in [47]:

- *Low temperatures solar technologies*: used for the production of household hot water, for pool heating and industrial processes; they can reach temperatures up to 120 °C.
- *Medium temperature solar technologies*: employed in solar cooling, process heat generation up to 250°C.
- *High temperature solar technologies*: used in power generation sector, with temperatures above 250°C.

Solar collectors can be divided in concentrating and non-concentrating/plane. For plane collectors, the area which absorbs the solar radiation is the same that intercepts the solar beams, while concentrating solar power (CSP) collectors have several reflectors that focus the solar beams onto a receiver with a smaller area.

CSP collectors are characterised by the use of mirrors or lens in order to redirect the incident solar radiation, received on the collector surface, to the smaller surface of the receiver. These systems have several advantages, first of all the possibility to reach higher temperatures, collecting “higher-quality” energy, and to reduce thermal losses in comparison to non-concentrating collectors, thanks to the smaller area of the receiver. The temperature increase leads to higher surface temperatures and consequently to higher radiative losses, that can be reduced, for linear collectors, with the use of selective surfaces and vacuum receivers. They

can also exploit the solar direct irradiance² in a better way but they're not able to collect the diffusive radiation. For this reason CSP collectors need a tracking system and without it solar radiation would be collected on the receiver only for few minutes per day.

CSP technologies can be grouped following two different criteria: the typology of focusing and the receiver mobility. The receiver can be fixed, if it remains stationary independently from the concentrating system, or aligned, when it moves together with the concentrating system. Fixed collectors derive from the projection and the segmentation of parabolas of tracking systems on a plane. Collectors can also be distinguished in linear focus collector, characterised by a single-axis tracking system, and point focus systems, that have two-axis tracking and can reach higher concentration ratio (CR) values. CR is defined as the ratio between the receiving surface and the collector surface. Figure 10 summarizes different typologies of solar collectors.

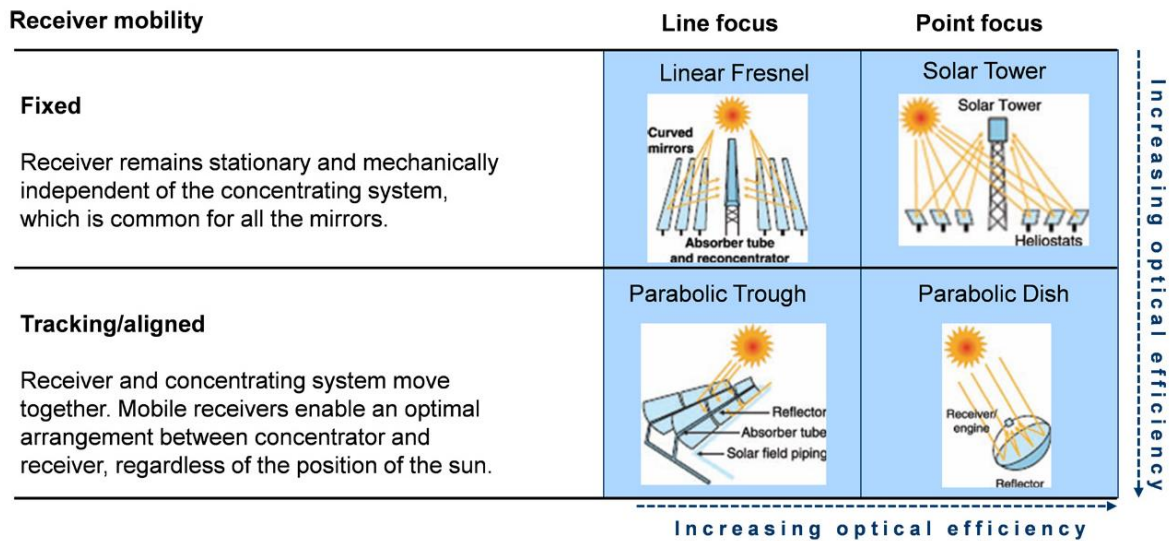


Figure 10: Classification of solar collectors based on typology of tracking and focusing [48].

2.1 Heat Transfer Fluid and Direct Steam Generation

The heat transfer fluid (HTF) is the medium that is heated up in the absorber. Several kinds of fluids can be employed in solar fields. The most common HTF is a synthetic oil, such as Therminol VP1, used in the majority of commercial systems. The use of synthetic oil has several advantages, such as its high vapour pressure, the reduction of freezing risk (freezing temperatures of about 12÷20°C), a high thermal stability in the operating range, low viscosity, with reduction of problems in start-up and pumping, and low fluid corrosiveness. There is also the possibility of implementing a thermal storage system, but it usually requires an additional heat exchanger since molten salts are preferred as storage mean. On the other side, there are also disadvantages; first of all the maximum reachable temperature, which is

² Due to the scattering effect the global solar radiation can be divided in a diffusive component and a direct component, which can be used by the CSP systems.

set to about 400°C in order to avoid problems of chemical decomposition of the oil. In addition, it is necessary to take precautions to prevent thermal oil leakages because it is toxic and can cause fires. To prevent evaporation at the operating temperatures, the HTF works under pressure of about 25÷35 bar. Oil is also very expensive, with a cost of about 4 €/kg. These disadvantages push the researchers to find search for alternatives to the synthetic oil [49].

Molten salts are a possible alternative to synthetic oil. They are a mixture of salts, solid at ambient pressure and temperature and liquid at operating temperatures of solar collectors. For example, the mixture used in Archimede power plant (Priolo Gargallo, Sicily) is made by sodium nitrate ($\text{NaNO}_3 \sim 60\%$ w/w) and potassium nitrate ($\text{KNO}_3 \sim 40\%$ w/w). Their main advantage over the synthetic oil is the possibility of reaching higher temperatures, up to 550°C. They are also cheaper, with costs around $\sim 0,5\div 2$ €/kg, without toxicity and flammability problems and they can be used with lower working pressure ($\sim 1\div 10$ bar). Moreover, the storage system heat exchanger (if present) can be eliminated, since the solar field and the thermal storage use the same fluid, and the size of the storage can be reduced. Their principal disadvantage is the high freezing temperature, with difficulties in managing at night and the necessity of precautions to avoid the solidification, such as electric heating tubes or circulation of hot fluid [50].

Another possibility is the production of saturated or superheated steam directly into the receiver tubes: this technology is called Direct Steam Generation (DSG). In this way the maximum temperature limit and the cost of the oil-steam/water heat exchanger can be avoided. This is an attractive concept: the average operating temperature in the collector would be higher and the use of a phase changing fluid reduces the required water flow, the size of the solar field and its investment costs too. Water employment can also avoid risks related to the use of oil, such as fires and dangerous leakages, but also O&M costs for the oil (i.e. oil reintegration for leaks, antifreeze protection for temperatures below the freezing one). If direct steam generation is employed, it is preferable not to reach the saturated steam conditions in solar field piping in order to maintain good exchange performances and to avoid excessive thermal stress on the receiver tube. Normally, the steam produced has a quality minor than 1; steam and water fractions are then separated and saturated steam is sent to the cycle or to the superheater (depending on the plant configuration). The liquid fraction is recirculated to the evaporative section inlet. DSG technology introduces new challenges for the solar collector technology, such as problems of process stability, stress in receiver pipes because of high steam pressures (~ 100 bar), difficulties to control the temperatures along the absorber tubes and high steam losses. For these reasons, the DSG technology is more suitable for LFC, since it has a fixed receiver and the sealing problems on joints of the receiver are avoided [10].

Some experimental facilities and studies are made on the use of CO_2 or other pressurized gases as heat transfer fluid with the aim of avoiding the problems of freezing, sealing and chemical stability to increase the maximum temperature limit. [41]

2.2 Low temperature solar collectors

The most common technologies in the field in the range of low temperatures are the Flat Plate Collector (FPC) and the Evacuated Tube Collector (ETC).

The FPC is a low-cost technology made by an absorbent dark plate that can be selectively coated, a piping system, an insulation layer and a covering glass as shown in Figure 11. The working principle of this system is based on the ability of the glass to be transparent to the solar radiation but opaque to the infra-red radiation and on the high absorptivity of the dark plate. The radiation collected is used to heat up the fluid in the piping tubes, usually water or glycol, up to 60°C.

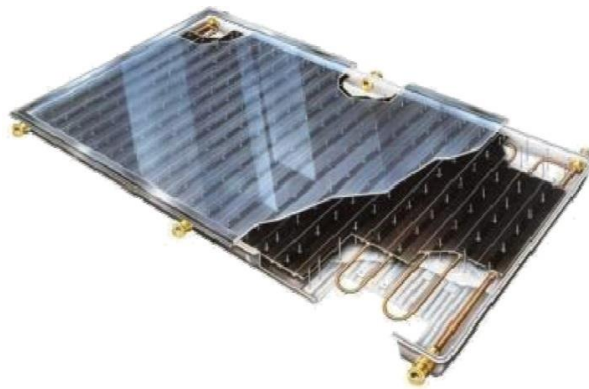


Figure 11: Example of flat plate collector [51].

A possibility to reduce the investment cost is to use collectors without the covering glass, but this implies thermal convective losses too high in winter and for this reason they are mainly used for pools or residential applications.

The ETC is an attempt to improve the plane collectors' concept and to reach temperatures above 100°C. They are made of series of evacuated glass tubes with the aim to reduce thermal losses and improve the conversion efficiency, about 15% higher than the FPC. The heat can be collected in two different ways: the first possibility is the use of “U” piping, in which the fluid is heated up and then give its thermal power to the user, and the other one is an heat pipe in which a phase change fluid circulates [47], [51].

2.3 Medium temperature solar collectors

Compound Parabolic Concentrators (CPCs) are one of the most common technology in the medium temperature range. They are included in the non-imaging collectors category, so called because they do not attempt to form an image of the source, but optimise the optical system to maximise the radiative transfer from the source. The two sides of a CPC are designed using two different parabolas with the focus on their front side (Figure 12). They can receive the solar radiation with a wide incidence angle and all the radiation that enters

in the aperture within the acceptance angle is conveyed on the absorber. They can be cylindrical or plane and they are usually covered with a protective glass.

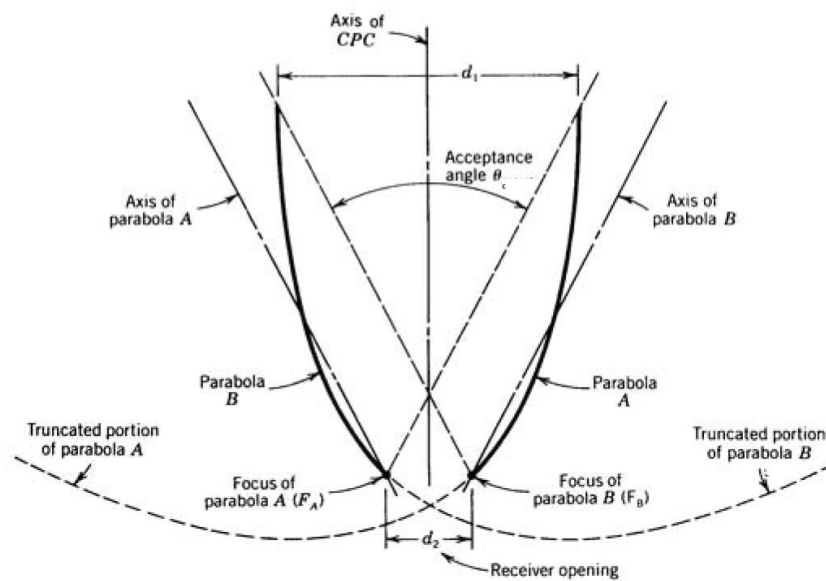


Figure 12: Schematic design of a CPC collector [51].

PT and LF systems for high temperature can also be easily adapted to medium temperature applications. Often, the structure remains unchanged and only the CR is reduced. The receiver can be evacuated, to reduce thermal losses, similar to the PTC for high temperatures, or without vacuum, to reduce investment costs. For lower temperatures the external glass can be also removed and substituted with a plane covering glass: in this way the receiver is displaced into a close chamber to avoid excessive convective losses.

2.4 High temperature solar collectors - Point focus systems

Point focus systems concentrate theoretically the radiation in a single point. They are characterised by two-axis tracking systems; this allows reaching higher CR (up to 40000 [52]) and so higher temperatures (up to 1200°C theoretically, the effective operational temperature is then defined also by the heat fluid employed). These systems are parabolic dishes and solar towers.

Dish systems are made of a paraboloid-shaped mirror which concentrates sunrays in a central point. Usually, in the focus point a Stirling engine is placed but also applications with steam engines exist [53]. Dish Stirling systems can reach the highest sun to electricity conversion (up to 32%) [54], but they don't exploit some of the advantages of CSP systems, such as dispatchability, since they can't have a storage system.

Solar tower systems are made of large mirrors collector, named heliostats, which reflect and concentrate solar radiation onto the receiver, placed on the top of the tower. They are generally flat or with a small curvature.

There are two principal layouts of the solar field: surround field and north field (south fields in the southern hemisphere). In the first one heliostats surround the receiver, while in the second one they are just on the north side of the tower. The second disposition underlines higher efficiencies for high latitude or high incidence angle while the first is better suited for location close to the equator [11]. There is also the possibility to build the solar field with a configuration in between the previous ones. The solar field layout also depends on the power plant size: as the size of the solar field increases, external mirrors become farther from the central receiver and the optical losses become more important. For this reason, even for high latitudes, the first layout can be more attractive for big power plants, since the reflectors are closer to the central receiver.



Figure 13: Solar field dispositions: surrounded field in Gemasolar thermosolar plant (left figure [55]) and north field in Abengoa Solar power plant (right figure [56]), Spain.

The concentration ratio in this case is definable as:

$$CR = \frac{\text{total mirror aperture area}}{\text{receiver area}} = \frac{n \cdot A_A}{A_R} \quad (6)$$

Where n is the total number of the heliostats and A_A the area of the single heliostat.

There are different types of central receivers: tubular and volumetric. The choice depends on the particular application and on the heat transfer fluid employed. Tubular design is normally used for water boilers and molten salts receivers because they have high heat transfer coefficient and so tube temperature can be controlled. Volumetric receivers have a porous structure which increases the heat transfer surface and allows the highest temperatures reachable with solar tower systems; they can be a suitable choice in particular for gaseous fluids.

Generally, increasing the height of the tower helps reaching higher efficiency because higher CR values can be reached and shading and blocking among heliostats are minimised, as well as cosine effect.

2.5 High temperature solar collectors - Linear focus collectors

Linear focus concentrators are bi-dimensional systems which concentrate solar radiation onto a focal line in which the receiver is placed. Concentrators can be made up of a parabolic curved mirror (Parabolic Trough systems) or of segmented mirrors with different curvatures (Linear Fresnel systems).

Solar incidence angle affects system performances, so concentrators are usually dynamic devices that follow the apparent daily movement of the sun minimising incidence angle. Solar collectors orientation may be imposed by the shape and orientation of the site where they are installed [10] so it can be in a general direction; normally, however, East-West (E-W) or North-South (N-S) ones are preferred. In particular, N-S orientation allows collectors to follow the sun in its azimuthal motion with a single axis tracking. This guarantees higher yearly energy outputs even with a noticeable seasonal variation. In fact, the impact of solar altitude is not balanced by the tracking system and the influence of the solar incident angle, at moderate latitudes, is more significant in winter. E-W orientation, instead, follows the solar altitude so performances are governed by solar azimuth; in this way annual electricity output is more uniform during the year (see Figure 14). At different latitudes the results are slightly different in quantitative terms, the trend is the same but the differences increase at lower latitudes and decreases at higher latitudes [11].

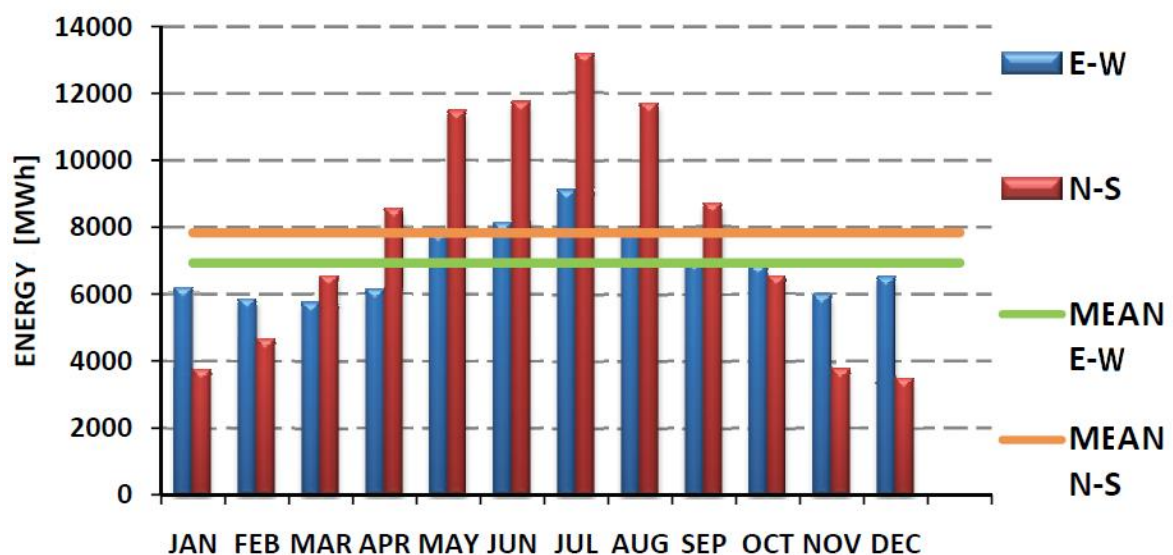


Figure 14: Monthly energy production in Almeria (36° 50' 0" N, 2° 27' 0" W) with different parabolic trough orientation [52].

For linear focus concentrators, the concentration ratio is defined as:

$$CR = \frac{\text{aperture width}}{\text{absorber diameter}} \quad (7)$$

Eventually, the circumference of the absorber can be used instead of the diameter in the definition of the concentration ratio.

2.5.1 Parabolic Trough Collectors

A PTC (Parabolic Trough Collector) is made up of a parabolic trough-shaped mirror that reflects and concentrates solar radiation onto the absorber tube, which is located in the focal axis of the parabola. Figure 15 shows a schematic representation of a parabolic collector. Concentration of the direct solar radiation reduces the absorber surface area needed with respect to the collector aperture, reducing overall thermal losses [10].

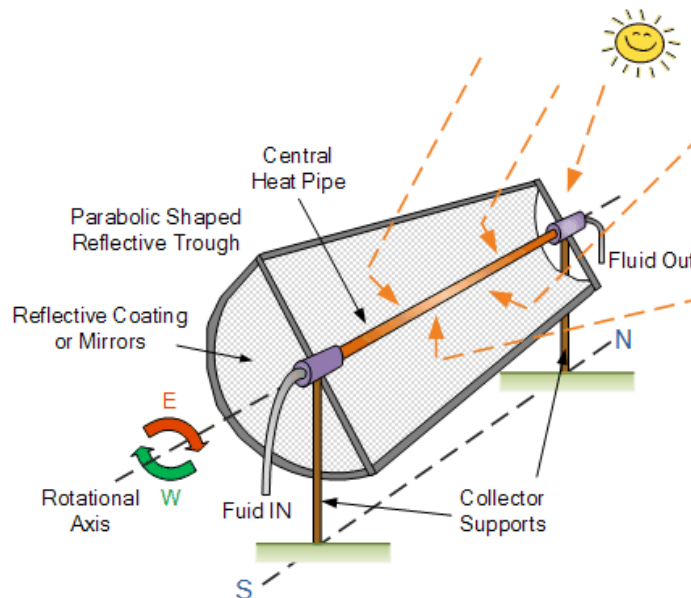


Figure 15: Schematic representation of parabolic trough reflector [57].

2.5.1.1 Reflectors

Reflectors must guarantee endurance and good performances even in adverse conditions. In fact, they can be installed in desert locations, where there are the highest solar radiation values and the greatest land availability, but also a great sand transportation which can consume mirrors and reduce their reflectivity. However, reflectors must maintain a high reflectivity over the years so they are normally covered with a layer of protective coating which increases reflectivity and reduces wear effects. They are also periodically cleaned, implying a certain water consumption.

Mirrors reflectivity (ρ) is normally defined as a nominal value at an incident angle equal to 0° where it assumes the highest value. However, it varies with the incidence angle, modifying the optical performances of the system.

There are several kinds of trough-shaped mirrors; they can be made by a glass layer and a reflective silvered film (like Flabeg technology) or by multiple layers of polymer film with a pure silver one (Skytrough) [58], [59]. An alternative is provided by polished aluminium which has better characteristics in terms of weight and resistance even though it has lower reflectivity and durability than silver [11].

Mirrors are placed onto the parabolic structure which has normally a one-axis tracking system; this means that the parabola can rotate in order to follow the apparent motion of the sun. Collectors distance should be optimised in a way to minimise shadowing of one collector on the other, to avoid additional efficiency losses.

2.5.1.2 Receiver

The solar energy that hits the reflector surface is reflected on the receiver, increasing its temperature and heating the fluid that circulates in the receiver. The receiver temperature is higher than the ambient temperature and it causes the presence of thermal losses towards the ambient. The balance equation for a receiver can be written as:

$$\dot{Q}_{receiver} = \dot{Q}_{absorbed} - \dot{Q}_{loss} = \alpha \cdot CR \cdot DNI - \sigma \varepsilon (T_{rec}^4 - T_{amb}^4) \quad (8)$$

Where α is the receiver absorptivity, σ is the Stefan-Boltzmann constant ($5,67 \cdot 10^{-8} \frac{W}{m^2 K^4}$), ε is the thermal emissivity of the receiver, T_{rec} is the receiver temperature and T_{amb} the ambient temperature.

The higher the absorptivity and the CR are and the lower the emissivity can be kept, the higher the useful heat gained by the receiver is. Therefore, the receiver is made of a steel tube with a selective coating layer, which improves absorption properties within the solar spectrum, maintaining low emissivity in the thermal emission spectrum and reducing radiative thermal losses. According to Kirchoff's law [60], for each wavelength, the absorptivity and the emissivity are equal; so a material with high emissivity for short wavelengths and low for long wavelengths is needed. Selective coatings are generally made by aluminium and titanium oxides (CERMET) and they are applied by the chemical vapour deposition technique. Recent coatings can withstand tube temperatures of about 550°C with significant thermodynamic advantages [61], [62].

The receiver is surrounded by a glass tube (normally made by Pyrex®) in which vacuum conditions are made (typically $\leq 10^{-3}$ mbar [63]); in this way the absorber coating is protected from oxidation and convective thermal losses, significant at high temperatures, are reduced. However, receivers with operative temperatures up to 250°C generally do not require vacuum conditions as thermal losses are less important [10]. Glass tubes are also coated with

an antireflective layer which maximises solar transmittance, limiting reflective losses. In order to maintain correct pressure conditions inside the vacuum annulus and to protect tube coating, several chemical getters are placed in the cavity. They adsorb hydrogen or other gases which can gather inside the gap because of cracking reactions at high temperatures (if the thermal fluid is synthetic oil) and mass diffusion through the tube.

Steel and glass tubes have different thermal expansions which must be compensated in order to guarantee adequate work conditions, so they are connected by means of flexible expansion bellows. Glass-metal welding is a weak point of the structure and it is usually covered with an aluminium shield in order to protect it from concentrated solar radiation which may cause thermal and mechanical stresses.

In Figure 16, principal components of a typical receiver are shown.

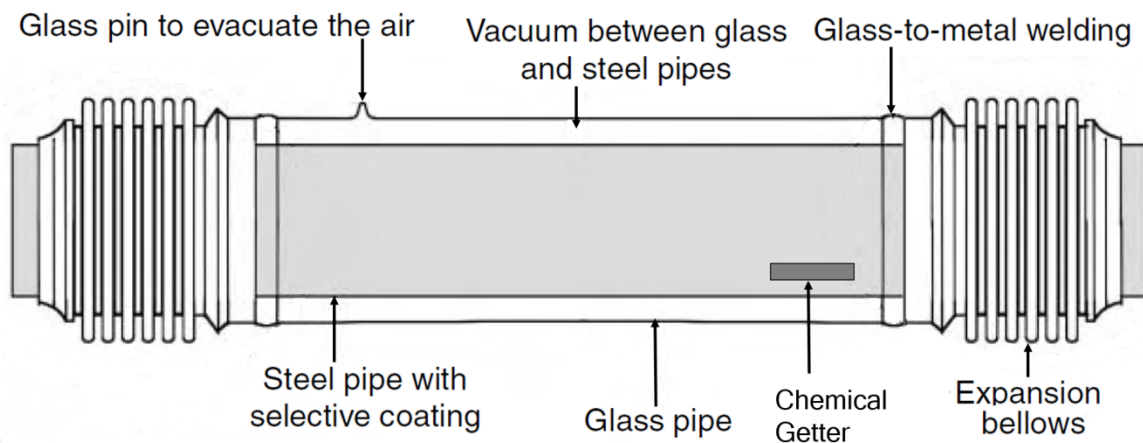


Figure 16: Heat collection element of parabolic trough collectors – adapted from [10].

Manufacturing constraints limit the length of the single receiver that must be shorter than 4m [64], so the complete receiver is made up of several welded receivers making a module; the total length of a module is normally about 100÷150 m in order to reduce movement system costs and collectors end losses (see paragraph 2.6) [52]. Receiver tubes of adjacent parabolic modules must be connected by flexible joints, in order to allow independent rotation during the day; two types of joints are available, ball joints and flexible hoses. Ball joints allow higher freedom of movement and can bear higher temperatures (over 300°C).

2.5.2 Linear Fresnel Collectors

A LFC (Linear Fresnel Collector) is based on the similar concept of a Parabolic trough but, instead of a single mirror in the shape of a parabola, the reflector is made of several plane mirrors which are placed on the ground and can be moved independently one to another. The receiver is still in the focus line of the collector but it is fixed. Compared to parabolic troughs, this is a newer technology but it shows potential economic advantages [11]:

- Lighter structures thanks to ground-based mirrors and reduced wind drag effects;
- Easier cleaning of the mirrors with reduced water consumption;
- Reduced shadowing between collectors rows which minimises land areas required;
- Fixed absorber which does not require expensive rotating joints as the PTCs;
- Reduced tracking energy consumption;
- Higher concentration ratio than parabolic system because it is not limited by parabola aperture width.

Their principal disadvantages are the lower nominal optical efficiency and the strong off-design performances penalty. In addition, there is the blocking effect between mirrors that further reduces the optical efficiency of LFC, as explained in paragraph 2.6.2.

Equation (7) can be written, specifically for Fresnel, as:

$$CR = \frac{n \cdot W}{D_{abs}} \quad (9)$$

Where W is the aperture of each mirror, D_{abs} is the absorber diameter and n is the number of mirrors.

2.5.2.1 Reflectors

The type of mirrors employed is very similar to the one of PTCs, though their layout is quite different. Primary reflectors are placed 1-2 m above the ground, they are flat or with a small curvature and they have different inclinations in order to concentrate solar radiation into a focal line, as shown in Figure 17. A secondary mirror with the shape of a CPC (see paragraph 2.3), can be placed above the absorber to reflect solar radiation coming from primary mirrors, increasing the concentration ratio of the single absorber tube and the intercept factor (which takes into account that not all the rays reflected by the mirrors hit the receiver surface). Moreover, the secondary reflector can insulate the absorber from the ambient, thus reducing radiative thermal losses; in fact the receiver sees the reflector temperature instead of the sky temperature, which is lower.

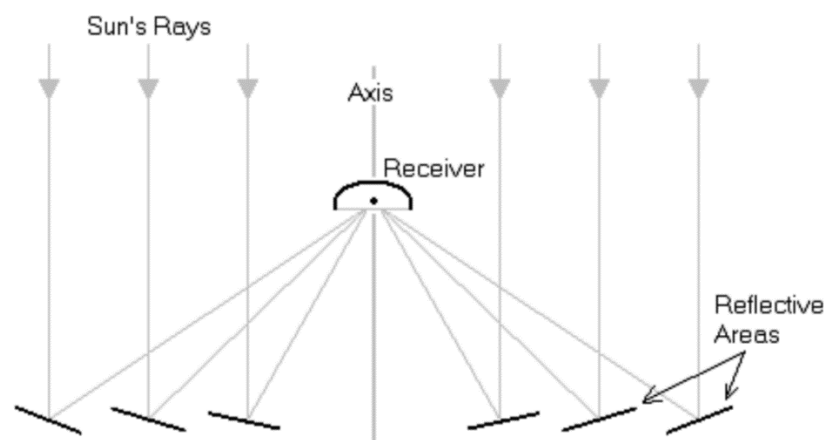
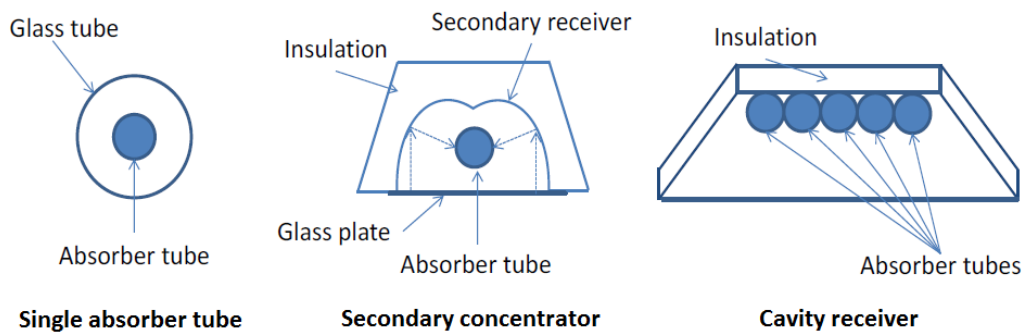


Figure 17: Linear Fresnel concentrator concept [65].**2.5.2.2 Receiver**

The absorber tube for Fresnel systems has the same physical properties as PTCs one. The layout is simpler, since it is fixed, and so connections are much easier. Three heat collector concepts are available, as in Figure 18:

- Single absorber tube;
- Secondary reflector;
- Cavity receiver.

**Figure 18:** Heat collection elements adopted for LFC [11].

The single absorber tube is similar to that of parabolic trough, the steel tube is surrounded by a glass one in order to limit convective thermal losses. The secondary concentrator layout uses the secondary mirror and a glass plate can be put under the receiver in order to limit convective losses. A different design is based on multiple absorbers placed in a cavity which provides thermal insulation. The last two configurations allow the increase of the intercept factor, but they are more expensive and complicated than the first and they add optical losses because insulation and secondary reflector shadow part of the primary reflector.

2.6 Performance parameters

The radiation available from the sun can't be completely transferred to the heating fluid, since there are several losses before the heat reaches the receiver. The optical efficiency is defined as the ratio between the heat absorbed by the receiver and the incident solar radiation upon reflectors:

$$\eta_o = \frac{\dot{Q}_{receiver}}{A_A DNI} \quad (10)$$

The collector heat losses are defined as:

$$\dot{Q}_{loss} = U(T_R - T_{amb})A_R \quad (11)$$

The thermal efficiency is defined as the ratio between the useful heat gained by the fluid (\dot{Q}_{fluid}) and the heat absorbed by the receiver:

$$\eta_{th} = \frac{\dot{Q}_{fluid}}{\dot{Q}_{receiver}} = 1 - \frac{\dot{Q}_{loss}}{A_A DNI \eta_o} \quad (12)$$

Finally, the overall solar field efficiency is defined as follows:

$$\eta_{overall} = \eta_o \eta_{th} \quad (13)$$

Where:

η_o : collector optical efficiency [-]

A_A : total mirror aperture area [m^2]

U : heat transfer global coefficient [$\frac{W}{m^2K}$]

T_R : receiver temperature [K]

T_{amb} : external ambient temperature [K]

A_R : receiver area [m^2]

DNI : Direct Normal Irradiance³ [$\frac{W}{m^2}$]

U includes convective and radiative coefficients and it is a function of the receiver temperature T_R . θ is the angle between an incident ray on the collector aperture area and the normal to the surface at the point of incidence.

Thermal losses are approximately constant as the DNI varies; for this reason, thermal efficiency increases with the DNI . In the following paragraphs the efficiencies for each solar system are described.

2.6.1 Parabolic Troughs

The peak optical efficiency, defined for solar incidence angle equal to 0° , for a PT is:

³ Direct Normal Irradiance – DNI [W/m^2]: amount of solar radiation received in a collimated beam on a surface normal to the sun at its current position in the sky

$$\eta_{o\ peak,PTC} = \frac{\text{energy impinging on the absorber}}{\text{energy impinging on mirrors}} = \tau_g \alpha_R \rho_M \gamma \quad (14)$$

Where:

τ_g : covering glass transmissivity [-]

α_R : receiver absorbance [-]

γ : intercept factor [-]

ρ_M : mirror reflectivity [-]

α_R , τ_g , ρ_M and γ must be as high as possible in order to maximise the heat gain. γ takes into account that not all the rays reflected by the mirrors hit the receiver surface; it depends mainly on receiver and parabola geometries, tracking errors, direction of solar beams (parallax angle) and the parabola deformation caused by external loads (i.e. wind and other atmospheric events).

Solar field efficiency strongly depends on operating conditions, such as ambient temperature, wind speed, sun position and solar radiation. The overall optical efficiency is influenced by several factors:

$$\eta_{o,PTC} = \eta_{o\ peak,PTC} K(\theta) \eta_{shading} \eta_{end\ losses} \quad (15)$$

Where $\eta_{shading}$ is a coefficient which includes losses caused by the mutual mirrors shading in some hours of the day (first hours in the morning and last hours in the evening). It is evaluated as:

$$\eta_{shading} = \min \left[\max \left(0; \frac{L_{spacing}}{A_A} \cdot \frac{\cos(\theta_z)}{\cos(\theta)} \right); 1 \right] \quad (16)$$

Where $L_{spacing}$ is the spacing length between rows and θ_z is the zenith angle⁴

$\eta_{end\ losses}$ takes into account the penalisation caused by the lack of irradiation on the tail end of the receiver, as shown in Figure 19, and by the spillage of rays over the end of the receiver.

⁴ Angle between the central ray of the sun and the line perpendicular to the horizontal plane.

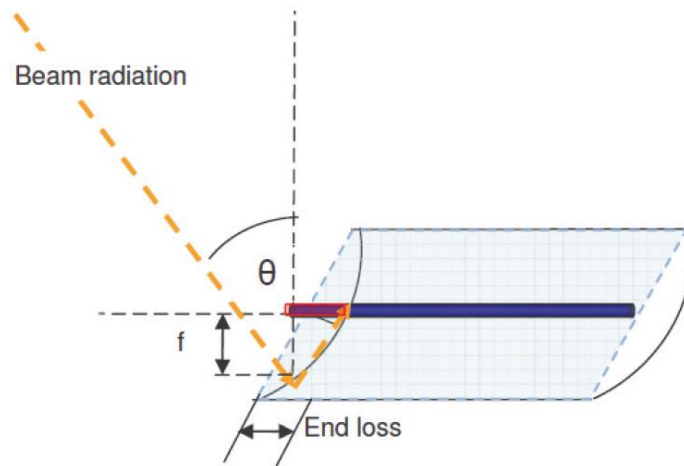


Figure 19: Schematic representation of receiver end losses [52].

$\eta_{end\ losses}$ can be evaluated as:

$$\eta_{end\ losses} = 1 - \tan(\theta_i) \frac{D_{pm}}{L_{abs}} \quad (17)$$

Where D_{pm} is the mean distance between primary mirrors and receiver while L_{abs} is the length of the receiver tube.

$K(\theta)$ is a correction factor that accounts for the differences from the nominal efficiency due to the incidence angle and it is defined as:

$$K(\theta) = IAM \cdot \cos(\theta) \quad (18)$$

Where IAM is the Incidence Angle Modifier which accounts for variations in material properties like τ and α and for the effect of shadow projection of the support. The factor $\cos(\theta)$ is usually named “cosine effect”, it is lower than 1 and it consists in a reduction of solar radiation on the mirror surface due to the variation of solar incidence angle. Tracking systems aim to reduce the incidence angle on the solar reflector in order to reduce its impact on overall efficiency.

2.6.2 Linear Fresnels

The nominal optical efficiency in linear Fresnel takes is defined as:

$$\eta_{o\ peak,LFC} = \frac{\text{energy impinging on the receiver}}{\text{energy impinging on mirrors}} \quad (19)$$

The LFC optical efficiency takes into account the following effects, some of them reported in Figure 20:

- Reflectivity of primary and secondary mirrors;
- τ_G of the covering or envelope glass;
- α_R ;
- $\cos(\theta)$ (a);
- Shading effect (b);
- Blocking effect (c).

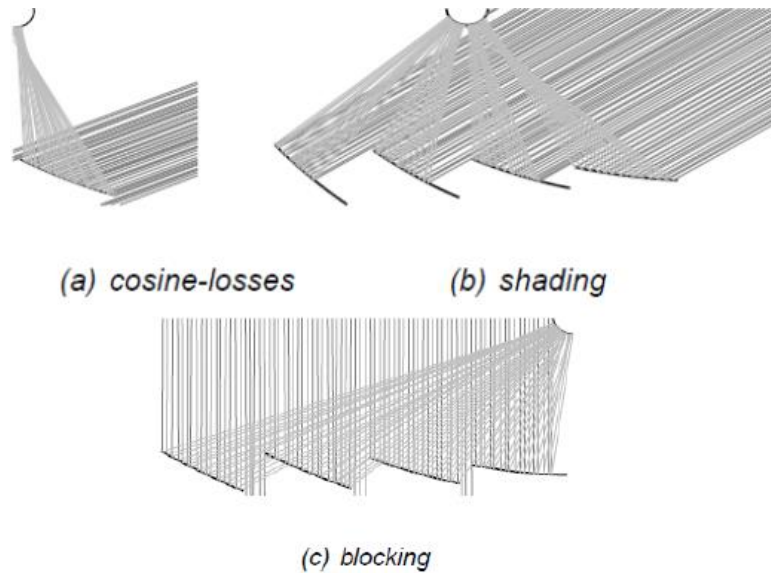


Figure 20: Schematic representation of LFC losses [66].

The blocking effect considers losses due to the arrest of the beam reflected by the mirror caused by the next solar collector.

In analogy with PTCs, also for LFCs an off-design overall efficiency can be defined. It can be written as:

$$\eta_{o,LFC} = \eta_{o\ peak,LFC} \cdot IAM \cdot \eta_{end\ losses} \quad (20)$$

IAM takes into account penalties on $\eta_{o\ peak,LFC}$ due to the incidence angle of solar radiation. Linear Fresnel have lower design efficiency than parabolic trough because, even with a solar incidence angle of 0° , mirrors can't be oriented perpendicularly to solar beams, in order to reflect the radiation onto the absorber tube. In this way the cosine term can never be equal to 1. $\eta_{end\ losses}$ is defined in the same way as for PTCs.

The description of LFs requires the definition of two projections of the incidence angle; one on the longitudinal plane (θ_{\parallel}) and one on the transversal plane (θ_{\perp}). θ_{\parallel} is defined as the angle between the vertical axis and the beam vector projection on the longitudinal plane while θ_{\perp} is defined as the angle between the vertical axis and the beam vector projection on

the transversal plane. Finally, θ_i is the angle between the beam vector and its projection on transversal plane. The characteristic angles on the planes are illustrated in Figure 21.

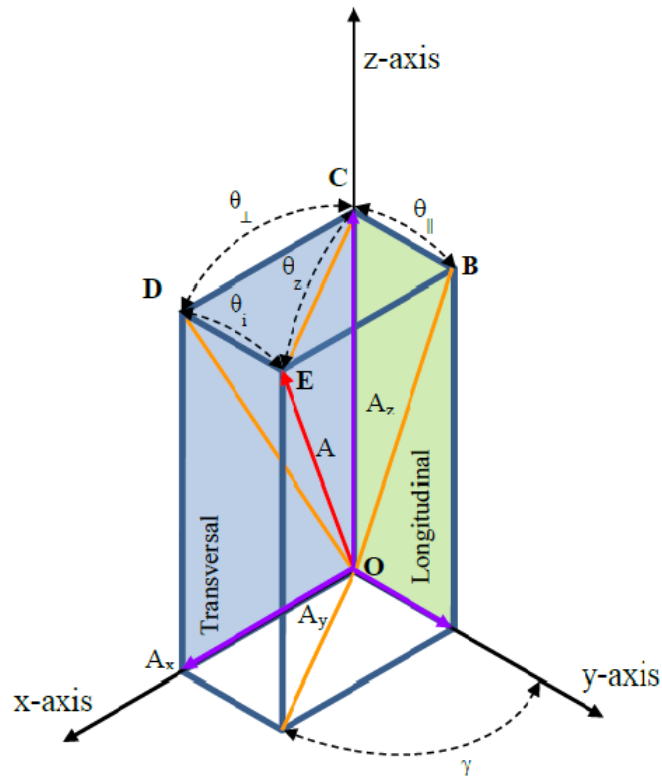


Figure 21: Angles definition of a concentrating reflector with horizontal N-S orientation [64].

The overall IAM for a LFR collector is defined as the product of two different factors, each one related to the above defined angles:

$$IAM \cong IAM(\theta_i) IAM(\theta_{\perp}) \quad (21)$$

Figure 22 shows $IAM(\theta_i)$ and $IAM(\theta_{\perp})$ variations as a function of the incidence angle (from Thermoflex® database). $IAM(\theta_{\perp})$ shows irregularities for angles between 0° and 45° because of the shading effect of the secondary reflectors over the primary ones.

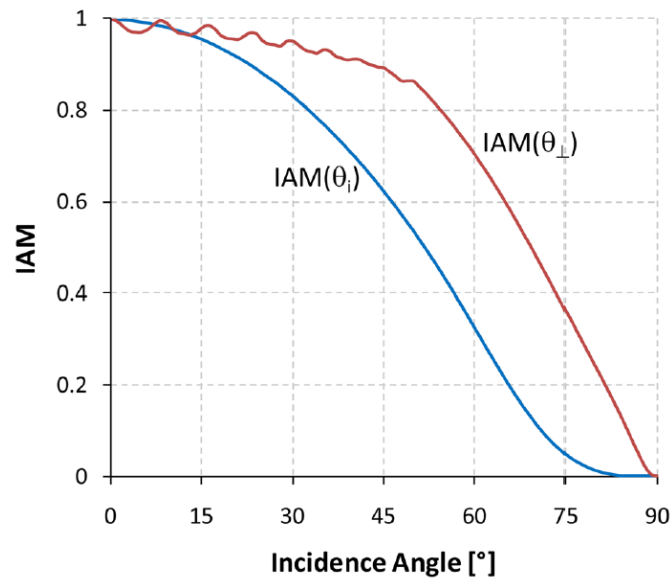


Figure 22: Longitudinal and transversal IAM as a function of incidence angle [67] .

LFCs have a lower nominal and yearly optical efficiency compared to PTCs, since the last are only affected by θ_i while θ_{\perp} can be nullified thanks to the tracking system. The off-design penalty with respect to PTC is very strong.

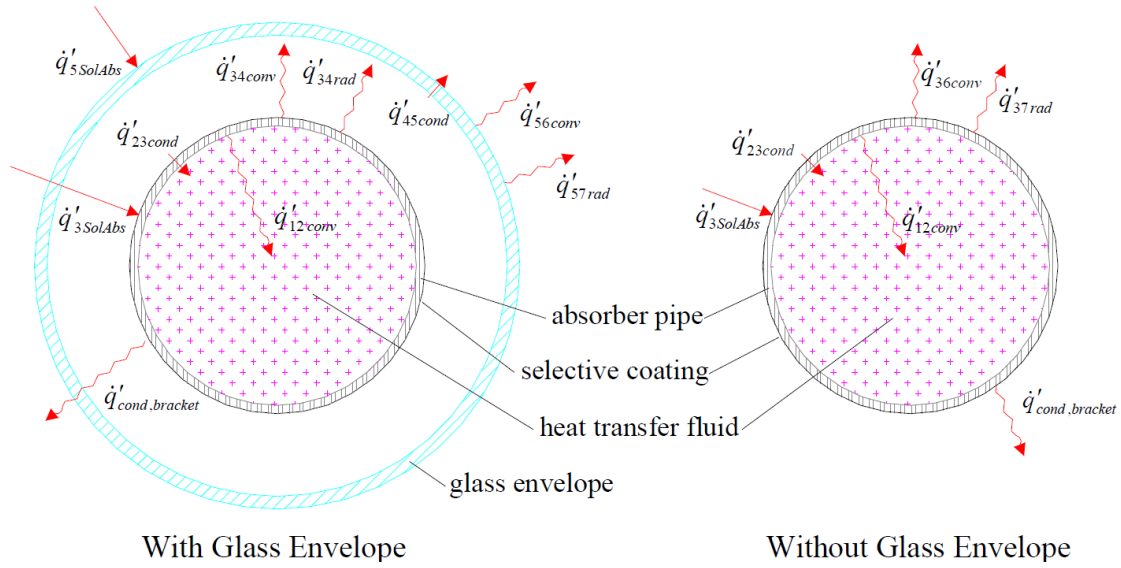
2.7 Commercial collectors

A review of different typologies of solar collectors available on markets is now proposed. The review focuses on linear solar collectors, since they are regarded as the best choice for the investigated ISCC. In fact, they operate in the temperature range needed for the integration. Moreover, they are less expensive and have a higher commercial maturity with respect to point focus systems. For each one the heat loss equation is reported, directly founded on the technical brochure or derived by interpolation of available data.

2.7.1 Heat loss model

When heat loss data were not available, a simplified thermal model of the solar collector has been implemented to estimate heat losses and the useful power transferred to fluid. This model is based on a previous study founded in bibliography [68]; the receiver is split up in a finite number of control volumes and the one-dimensional steady state heat balance between the HTF and the atmosphere is solved for each one of them. Energy balance equations are determined by conserving energy at each surface of the receiver cross-section, as shown in Figure 23 together with the thermal resistance model. It must be noticed that optical losses are already deducted from the incoming solar energy.

a) One-dimensional energy balance



b) Thermal resistance model

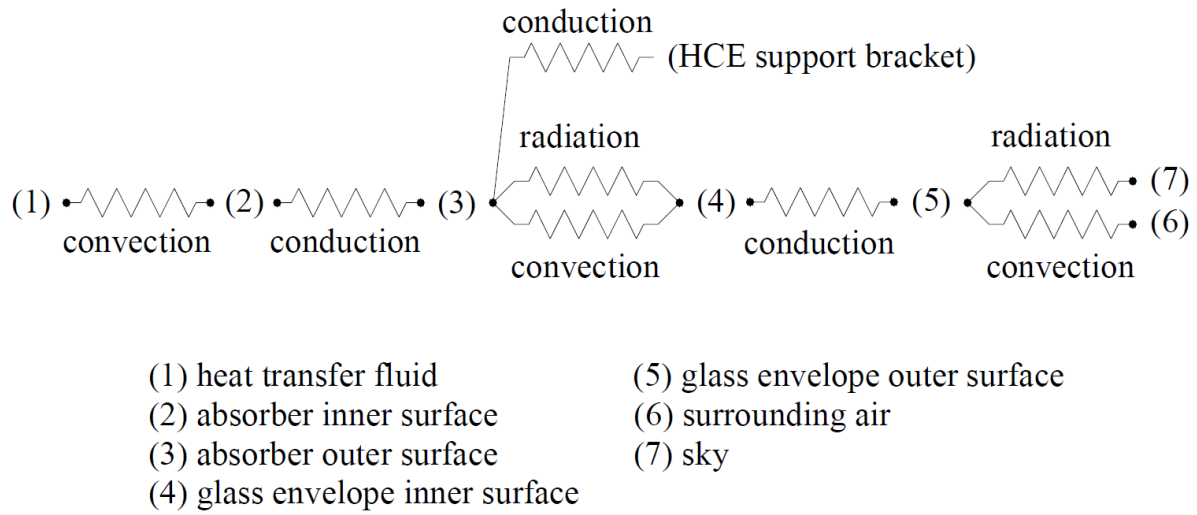


Figure 23: a) One-dimensional steady-state energy balance and b) thermal resistance model for a cross-section of the receiver [68].

The heat balance for a receiver with an intact glass envelope can be expressed with the following equations system:

$$\begin{cases} \dot{q}'_{12,conv} = \dot{q}'_{23,cond} \\ \dot{q}'_{3,sol\ abs} = \dot{q}'_{34,conv} + \dot{q}'_{34,rad} + \dot{q}'_{23,cond} + \dot{q}'_{cond,bracket} \\ \dot{q}'_{34,conv} + \dot{q}'_{34,rad} = \dot{q}'_{45,cond} \\ \dot{q}'_{45,cond} + \dot{q}'_{5,sol\ abs} = \dot{q}'_{56,conv} + \dot{q}'_{57,rad} \\ \dot{q}'_{heat\ loss} = \dot{q}'_{56,conv} + \dot{q}'_{57,rad} + \dot{q}'_{cond,bracket} \end{cases} \quad (22)$$

Where \dot{q}' indicates the thermal power exchanged per unit length of the receiver. The heat fluxes definitions are summarised in Table 4:

Table 4: Thermal model heat flux definitions [68].

Heat Flux (W/m)*	Heat Transfer Mode	Heat Transfer Path	
		From	To
\dot{q}'_{12conv}	convection	inner absorber pipe surface	heat transfer fluid
\dot{q}'_{23cond}	conduction	outer absorber pipe surface	inner absorber pipe surface
$\dot{q}'_{3SolAbs}$	solar irradiation absorption	incident solar irradiation	outer absorber pipe surface
\dot{q}'_{34conv}	convection	outer absorber pipe surface	inner glass envelope surface
\dot{q}'_{34rad}	radiation	outer absorber pipe surface	inner glass envelope surface
\dot{q}'_{45cond}	conduction	inner glass envelope surface	outer glass envelope surface
$\dot{q}'_{5SolAbs}$	solar irradiation absorption	incident solar irradiation	outer glass envelope surface
\dot{q}'_{56conv}	convection	outer glass envelope surface	ambient
\dot{q}'_{57rad}	radiation	outer glass envelope surface	sky
$\dot{q}'_{cond,bracket}$	conduction	outer absorber pipe surface	HCE support bracket
$\dot{q}'_{HeatLoss}$	convection and radiation	heat collecting element	ambient and sky

* Per unit aperture length.

Some simplifications are applied to the model; the support bracket thermal resistance is neglected since the heat fraction lost through the brackets is smaller than the fraction lost for convection and radiation. When vacuum conditions are made in the space between the glass and the steel tube, the convective resistance between points 3 and 4 is neglected as well, since the majority of heat is transferred through radiation.

The receiver has been split in 30 segment obtaining 31 sections, where the heat balance has been applied. Collectors characteristics, needed to solve the system (diameters, glass properties etc.), have been extracted from collectors brochures. For each collector, a temperature range comprised between minimum and maximum operative temperatures of the fluid in the receiver is considered. The intermediate temperatures (points 2,3,4,5) can be found solving the implicit system reported above. Once all the temperatures are known, the heat loss for each temperature of the fluid can be found.

2.7.2 Eurotrough ET 150

“Eurotrough” defines a parabolic trough model developed starting from Luz’s collector, with the help of the finite element analysis and detailed wind tunnel tests. It identifies the structure

characteristics while the receiver tube may change; it now represents the standard for PT technology. Two models of Eurotrough are available: the ET100, with 8 modules and a length of 100 m, and the ET150, with 12 modules and 150 m long. In this performance analysis, two receivers are considered: Schott PTR70 and UVAC. [69]

Schott PTR70

Schott solar CSP manufactures and sells only the receiver tube, which can be used for both PT and LF collectors. Three different diameters are available: 70mm, 80mm and 90mm. Schott PTR70 model (Figure 24) has a diameter of 70mm. It is available in its standard version and in the premium one, which employs a noble gas capsule installed to maintain better thermal properties over the full operational period. Data available online on Schott's website (Table 5) are referred to the standard Schott PTR70. Heat loss measurements were carried out in a round robin test performed by the company in cooperation with NREL (US National Renewable Energy Laboratory). They confirmed a heat loss of less than 250 W/m at working temperatures (about 400 °C) [63]. The Schott PTR70 is coupled, in this case, with an ET150 PT.

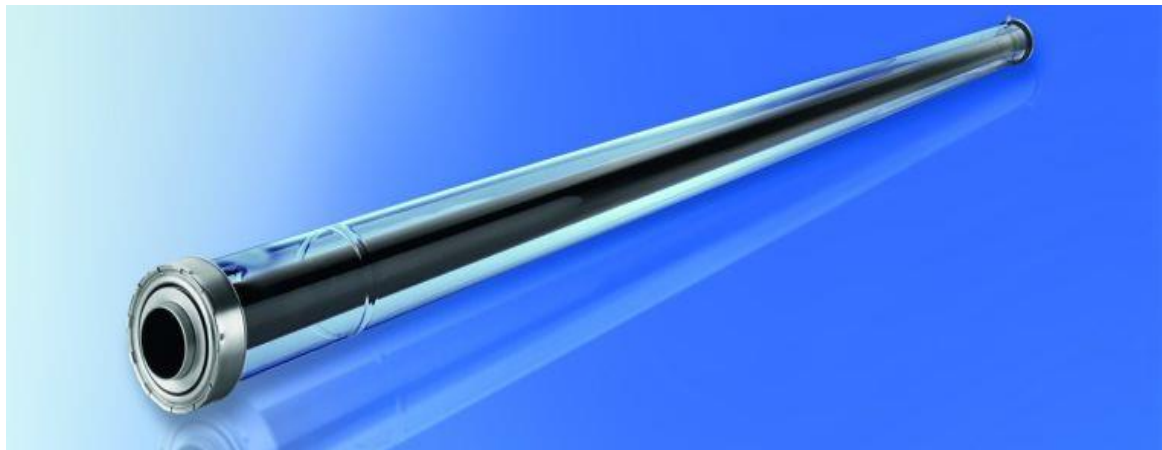


Figure 24: Schott PTR70 receiver tube [63].

Table 5: SchottPTR70 - ET150 collector datasheet [63].

SCHOTT PTR70 - ET150	
ρ_{mirror}	0,94
Length	148,5 m
Aperture width	5,77 m
Focal Length	1,71 m
Aperture area	817,5 m ²
Number of modules per drive	12
Optical efficiency	0,75
$K(\theta)$	$\cos(\theta) - 5,251 \cdot 10^{-4}\theta - 2,8596 \cdot 10^{-5}\theta^2$
q loss oil [W/m]	$0,0045 T_{abs}^2 - 1,735 T_{abs} + 223,25$
q loss DSG [W/m]	$8 \cdot 10^{-6} T_{abs}^3 - 0,0034 T_{abs}^2 + 0,7157 T_{abs} - 27,329$
T max	400 °C
SCHOTT PTR70 Receiver	
Material	DIN 1,4541 Steel
Coating	Antireflective
Outer Diameter	70 mm
Thickness	2 mm
Length	4,06 m
α ISO	$\geq 0,955$
ϵ abs	$\leq 0,095$
HTF	Thermal oil / Steam
Operating pressure	≤ 41 bar (absolute)
Glass envelope	
Glass type	Borosilicate glass
Outer Diameter	0,125 m
Thickness	2,5 mm
Coating	Antireflective
Vacuum Pressure	$\leq 10^{-3}$ mbar

UVAC

For the UVAC analysis, data from the prototype installed in the Plataforma Solar de Almeria (PSA), in Spain, are considered (Table 6): it is equipped with a ET150 collector and an UVAC absorber[70], [71].

Table 6: ET150 - Uvac collector datasheet [70], [71] .

UVAC – ET150	
ρ_{mirror}	0,94
Length	148,5 m
Aperture width	5,77 m
Focal Length	1,71 m
Aperture area	817,5 m ²
Number of modules per drive	12
Optical efficiency	0,7408
q loss [W/m]	$0,0027 T_{htf}^2 + 0,0978 T_{htf} - 4,1559$
T max	400 °C
UVAC Receiver	
Material	Stainless steel
Coating	sputtered, selective
Outer diameter	88,9 mm
Thickness	2,5 mm
α ASTM	$\geq 0,962$
ε abs	$\leq 0,095 @ 400^\circ\text{C}$
Operating pressure	≤ 40 bar
Glass envelope	
Glass type	Borosilicate glass
Outer diameter	135 mm
τ ASTM	$\geq 0,964$
Vacuum pressure	$\leq 10^{-4}$ mbar

2.7.3 SkyTrough

SkyTrough is SkyFuel's high performance parabolic trough for the utilisation in thermal power plants or industrial heat generation. The design of the latest model aims to reduce masses and costs, keeping intact the stability of the structure. It is available in two version, one provided with Schott PTR80 and the other with the 90mm Schott receiver tube, as shown in Table 7.

Table 7: SkyTrough collector datasheet [72].

SkyTrough	
ρ_{mirror}	> 0,94
Length (assembly)	115 m
Aperture width	6 m
Number of modules per assembly	8
Material	Aluminium
Typical land use	2 ha/MW _e
Optical efficiency	> 0,77
Thermal Efficiency	0,73 @ DNI=1000 W/m ² and 350°C
q loss [W/m] (80mm)	$10^{-5} T_{htf}^3 - 0,0037 T_{htf}^2 + 0,7618 T_{htf} - 28,119$
q loss [W/m] (90mm)	$1,3965 + 0,28843 T_{abs} + 6 \cdot 10^{-5} T_{abs}^2 - 9 \cdot 10^{-8} T_{abs}^3 + 10^{-8} T_{abs}^4$
T max	500 °C
Receiver	
Model	Schott PTR 80/90
Length	4,06 m
Outer Diameter	80 or 90 mm
Steel type	DIN 1,4541
α ISO	$\geq 0,955$
ϵ abs	$\leq 0,095$
HTF	Molten Salts or Thermal oil
Operating pressure	≤ 41 bar (absolute)
Glass envelope	
Glass type	Borosilicate glass
Coating	Antireflective
Vacuum pressure	$\leq 10^{-3}$ mbar

2.7.4 Archimede HEMS08

Archimede produces its own receiver tubes. HEMS08 model uses molten salts as heat transfer fluid. The coating is made of a thin multilayer film: a top layer of ceramic material with a high anti-reflective power, an intermediate layer of CERMET, a nano-composite material with a high absorption coefficient for solar radiation, and a lower layer of metallic material that reflects the infrared radiation. The HEMS08 absorber is coupled with Ronda High Tech mirrors, which have already been used together in Archimede project at power plant in Priolo Gargallo. Data are reported in Table 8.

Table 8: Archimede HEMS08 collector datasheet [61].

HEMS08 - Ronda	
ρ_{mirror}	> 0,94
Length (panel)	1,604 m
Aperture width	5,9 m
Focal length	1,81 m
q loss [W/m]	$2 \cdot 10^{-5} T_{abs}^3 - 0,0111 T_{abs}^2 + 3,4219 T_{abs} - 345,41$
HEMS08 Receiver	
Material	Stainless steel
Coating	CERMET
Outer Diameter	70 mm
Thickness	3 mm
Length	4,06 m
α ISO	$\geq 0,95$
ϵ abs	$\leq 0,1$ @ 400°C
	$\leq 0,14$ @ 580°C
HTF	Molten salts
Operating pressure	≤ 30 bar (relative)
Glass envelope	
Glass type	Borosilicate glass
Outer Diameter	0,125 m
Thickness	3 mm
Coating	AR CIEMAT
τ ASTM	$\geq 0,966$

2.7.5 Polytrough 1800

NepSolar's Polytrough 1800 is a medium temperature collector, whose main advantages are low installation and maintenance costs. Its small dimensions and its ease of installation make it suitable also for roof installation. It is particularly suited for generating heat for industrial processes, solar cooling systems, ORC for power generation and desalination. In Table 9 technical data of the collector are summarised and Figure 25 reports $K(\theta)$ as a function of the incidence angle.

Table 9: Polytrough 1800 collector datasheet [73].

Polytrough 1800	
Length	20,9 m
Height	1,75 m
Focal length	0,65 m
Aperture area	36,9 m ²
Weight (referred to aperture area)	30 kg/m ²
Rim angle	71°
Geometric CR	54
Optical Efficiency	0,6865
Efficiency@ 200°C	0,6
q loss [W/m]	$0,0019T_m^2 + 0,41653T_m - 11,963$
T max	250 °C
Mirror	
ρ_{mirror}	>0,93
Length	1,25 m
Width	1,845 m
Depth	16 mm
Receiver	
Material	1.4307 Stainless Steel tubing
Coating	Black chrome
Outer Diameter	34 mm
Wall Thickness	1,5 mm
Glass envelope	
Material	Borosilicate glass
Outside diameter	56 mm
Wall thickness	2,5 mm

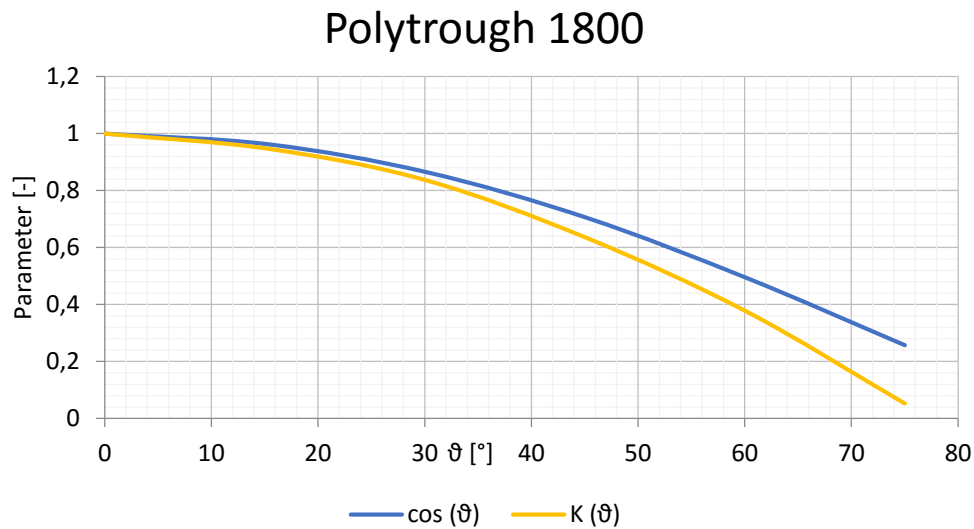


Figure 25: $K(\theta_i)$ and $\cos(\theta)$ as functions of incidence angle for Polytrough 1800 collector. $K(\theta_i)$ already includes cosine effect.

2.7.6 Nova 1 & Supernova

Nova 1 is Novatec's linear Fresnel model, suited for low and medium temperatures, since the absorber (a SchottPTR70) is not equipped with vacuum insulation; a glass plate to reduce convective thermal losses is located under the secondary receiver. Its typical applications are solar enhanced oil recovery and medium temperature heat generation. It uses water in DSG applications, generating saturated steam. Novatec also produces a linear Fresnel able to produce superheated steam through DSG and to reach higher temperatures thanks to a vacuum absorber tube; the Supernova collector. It is particularly suited for electricity generation, augmentation and ISCC applications. The newest Novatec's model is the Nova-DMS, which uses molten salts as heat transfer fluid. The following data refers to the Nova 1 model (Table 10). These collectors are equipped with a secondary receiver. The IAM for the Nova1 collector is the one reported in Figure 22; qualitative trend is similar for the Supernova collector even though absolute values differ because of collectors differences.

Table 10: Nova1 and Supernova collectors datasheet [74].

Nova 1 & Supernova	
Control unit width	16,56 m
Control unit length	44,8 m
Receiver height above primary reflector	7,4 m
Reflector height above the ground	0,75-1,05 m
Aperture area of primary reflectors	513,6 m ²
HTF	Saturated/superheated steam
q loss Nova 1 [W/m]	$0,929 T_m - 23,345$
q loss Supernova [W/m]	$8 \cdot 10^{-6} T_{abs}^3 - 0,0035 T_{abs}^2 + 0,6779 T_{abs} - 26,431$
Receiver	Schott PTR70
T max	250°C Nova1/550°C Supernova

2.7.7 Industrial solar LF11

The Industrial Solar linear Fresnel collector LF-11 (**Figure 26**) is a linear high temperature collector for generating process heat at pressure up to 120 bar and temperatures up to 400°C. Different heat transfer fluids can be used, like water, thermal oil or steam with DSG methodology. Its modularity and light weight make it appropriate for rooftop installations. The basic module consists of 11 primary reflectors with one Schott PTR receiver (**Table 11**).

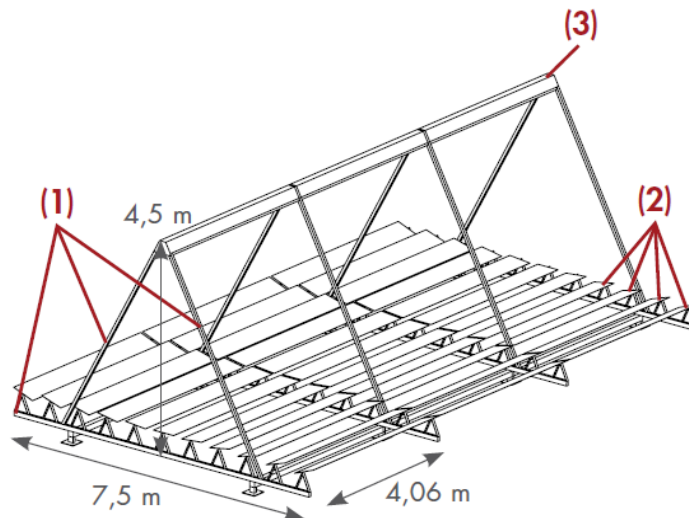


Figure 26: Schematic representation of Industrial solar LF11. (1) supporting structure, (2) primary reflectors, (3) receiver, consisting of secondary reflectors and absorber tubes [75].

Table 11: Industrial Solar LF11 collector data sheet [75].

Industrial solar LF11	
Width	7,5 m
Length	4,06 m
Area	22 m ²
Receiver height above primary reflector	4 m
Reflector height above the ground	0,5 m
Specific weight (per installation surface area)	27 kg/m ²
T max	400 °C
Life expectancy	20 years
Standard row length	65 m
Optical efficiency	0,635
Receiver type	Schott PTR70
ρ_{mirror}	0,95
q loss [W/m]	$0,0035 T_{abs}^2 - 0,3085 T_{abs} + 7,8941$

In Figure 27, heat loss curves are represented; as expected, the heat loss increases with the tube diameter.

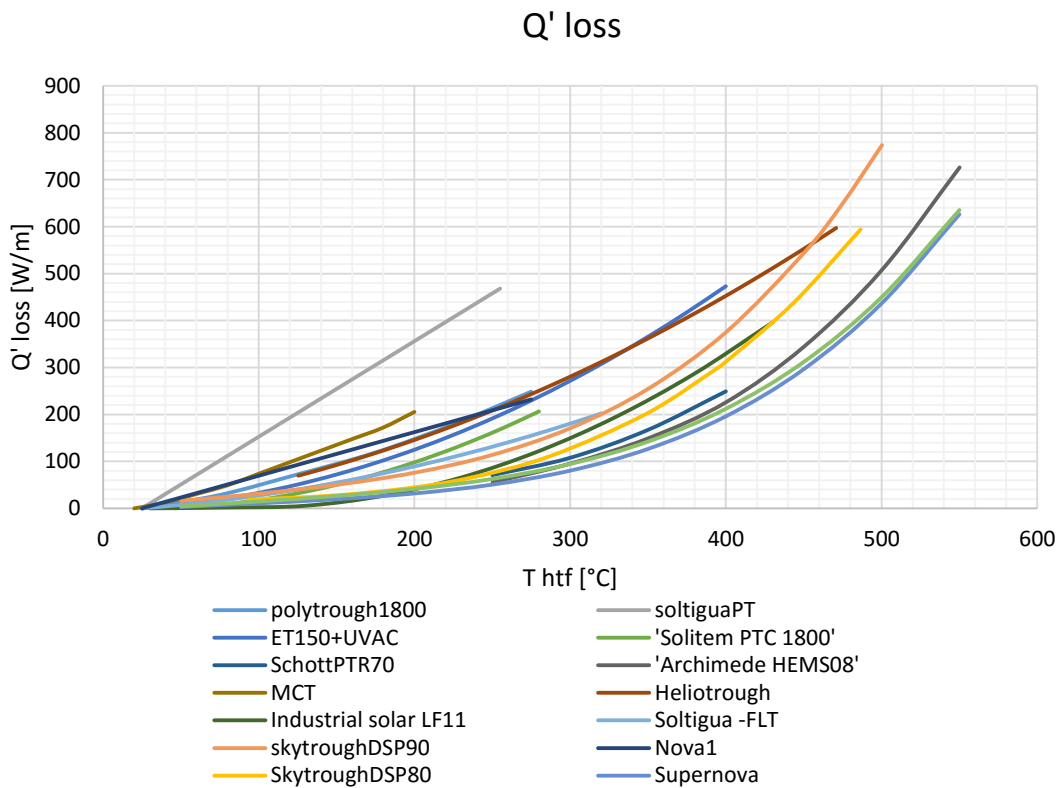


Figure 27: heat loss curves as a function of the fluid mean temperature between tube inlet and outlet.

2.8 CSP power plant cost analysis

Solar collectors are normally employed for the steam production into solar only power plants. These can be a good reference to be compared with the integrated solar combined cycles: in terms of efficiencies and electricity production costs.

Overall efficiency of solar only power plants, defined as the ratio between net power and solar energy impinging on the collector (in terms of $A_A \cdot DNI$) is generally not very high, it arrives at about 20% at nominal conditions (slightly higher for indirect PTCs and lower for DSG LFCs) [67], most of all because of the efficiency of the power block which is low.

The Levelised Cost of Electricity (LCOE) of this type of plant can be compared with the ISCC solar marginal LCOE, defined as the ratio of the additional costs due to solar integration with respect to the electricity production from solar resource.

The highest fraction of the total LCOE of CSP plants is attributed to the initial investment expenditure, contrary to fossil fuel power plant where the mature technology guarantees

lower investment costs but higher ones are due to the fuel purchase. Investment costs increase if a thermal storage is implemented in the solar power plant, even if it increases the plant capacity factor and, consequently, the electricity generated. Investment cost for PTCs power plants are generally between 4500 \$/kWe and 10000\$/kWe. In Figure 28, the LCOE breakdown of an illustrative 100 MW PTC plant installed in South Africa is shown. LCOE for PTC power plants is between 200\$/MWh and 330\$/MWh [76].

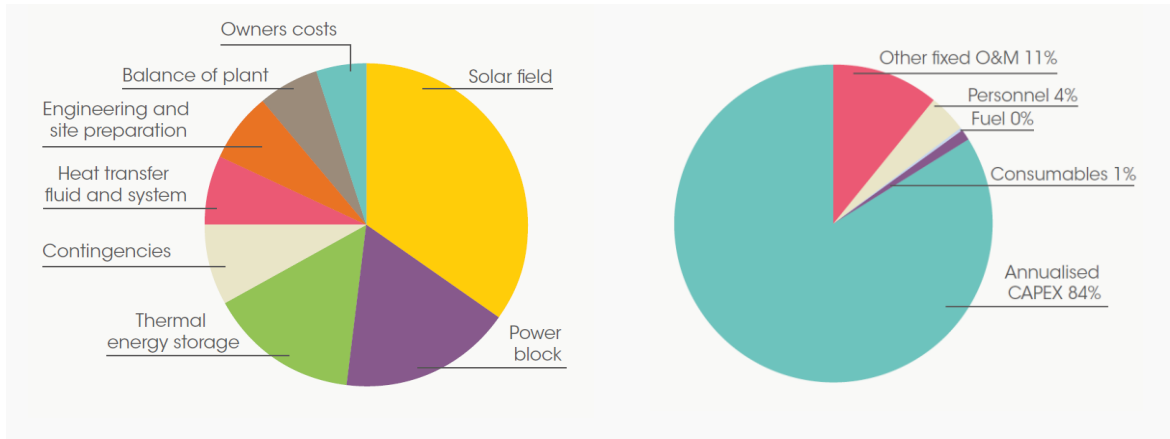


Figure 28: Total installed costs (left) and LCOE (right) breakdown for a parabolic trough plant in South Africa [76].

Investment cost of LFCs plants are generally lower because mirrors, tracking systems are simpler, and, since LFCs are in early stages of development, the cost reduction potential is quite high, as shown in Figure 29.

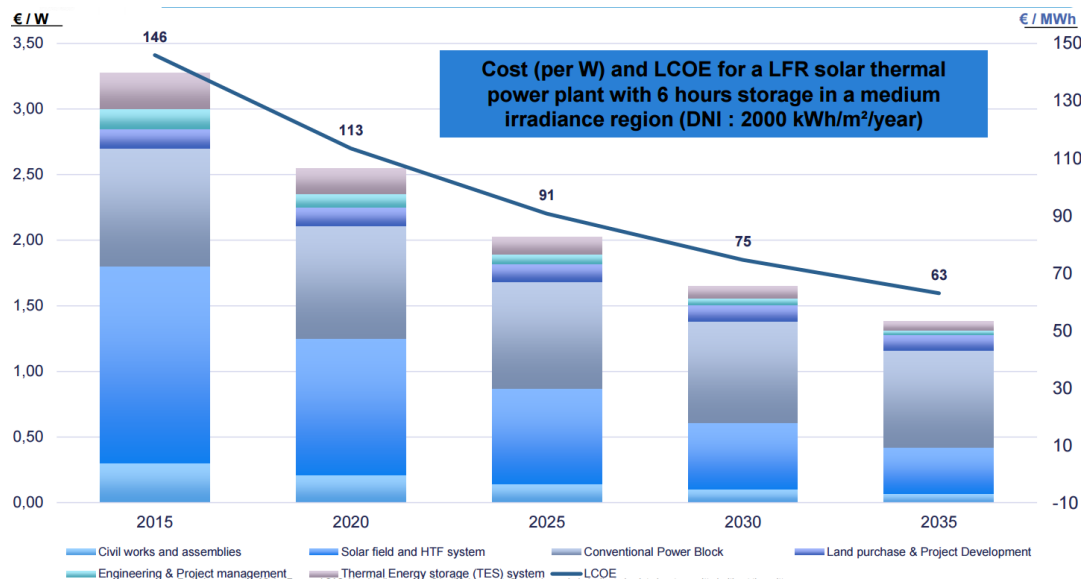


Figure 29: Specific cost and LCOE for LFR solar thermal power plant with 6 hours storage in a medium irradiance region (DNI 2000 kWh/m²/year) [77].

O&M costs are low compared to the fossil-fuel power plant and include, for example, the replacement of receivers and mirrors because of glass damages and mirror washing. The major fraction of O&M costs is fixed and is estimated to be about the 92% in the above-mentioned PTC plant [76].

Chapter 3

Natural Gas Combined Cycle

A combined cycle is a power generation technology which combines the power production of a gas turbine and of a steam turbine to improve the fuel conversion efficiency. The most common kind of CC in stationary generation is the Natural Gas Combined Cycle (NGCC), made up of a gas turbine that burns natural or synthesis gas whose flue gases feeds a bottoming steam cycle. In this chapter the NGCC technology is analysed and a base model, made with the software Thermoflex® v.25 [78], is provided; this will be further implemented in the ISCC modelling. Thermoflex® is a commercial software that allows design and off-design simulations of thermal systems. It also provides the engineering and cost estimation of several components (PEACE components) depending on the hardware specifications. Thermodynamic and engineering modes allow the design simulation, where the program computes the heat and mass balance of the system based on user's input data and it initialises the hardware components description. Some differences between thermodynamic and engineering model may arise because, while the thermodynamic calculation only implies heat and mass balances, the engineering mode considers technical restraints due to real components sizing. In off-design mode the performances of the system, under varying conditions (i.e. ambient temperature, solar radiation), are evaluated using the previous defined hardware data.

3.1 Thermodynamic principles

The fundamental of a CC stands in the high residual energy still available in flue gases at the outlet of the gas turbine, which are at temperatures above 500°C [31]. In a simple cycle gas turbine, this remaining heat is discharged in ambient and wasted, while in a CC it can be exploited in a Heat Recovery Steam Generator (HRSG) where it can be used to produce saturated or superheated steam that can be converted in electricity in a steam turbine (ST).

The NGCC technology has several advantages:

- *High efficiency* compared to other generation technologies. In fact NGCC efficiencies are generally above 50% against 30÷45% of simple cycle gas turbine and the 46÷48% of Ultra-Super-Critical steam power plants [31].

- *Limited environmental impact* thanks to the employment of high efficiency power technologies and of natural gas, which guarantees low emissions concentrations in flue gases. For example, with respect to coal plants, CO₂ emissions are reduced.
- *Good flexibility*, that is highly required nowadays in electricity markets and makes NGCCs suitable for both baseload and mid-range duty with daily startup [79].
- *Compactness, competitive investment costs and installation timings*, compared to other generation technologies. For example, the overnight capital cost of a CC is of about 1000 \$/kW against 3000\$/kW required for an advanced pulverized coal power plant [80]. Moreover installation timings are estimated to be about 1 year for a simple cycle gas turbine, 1,5 ÷ 2 years for a NGCC and 4 ÷ 6 years for a conventional steam cycle [31].
- *High annual availability*: thanks to the high reliability of gas turbines, CC can theoretically achieve a high number of working hours.
- *High commercial maturity* since they had a great commercial success that led to the installation of a high number of NGCC facilities. From 1949, when the first example of CC entered service, many power plants were built and many progresses were made, in particular in the GT technology [32]. In 2007 the global NGCC installed capacity was 610 GW with respect to a worldwide 4810 GW power generation capacity [81].

Figure 30 shows a schematic representation of the combined cycle; exhaust gasses from the gas turbine outlet, enter the heat recovery steam generator. They are cooled to the stack temperature, generating superheated steam that is expanded in a three stages steam turbine. Steam leaving the low pressure stage of the steam turbine is then condensed in an air condenser.

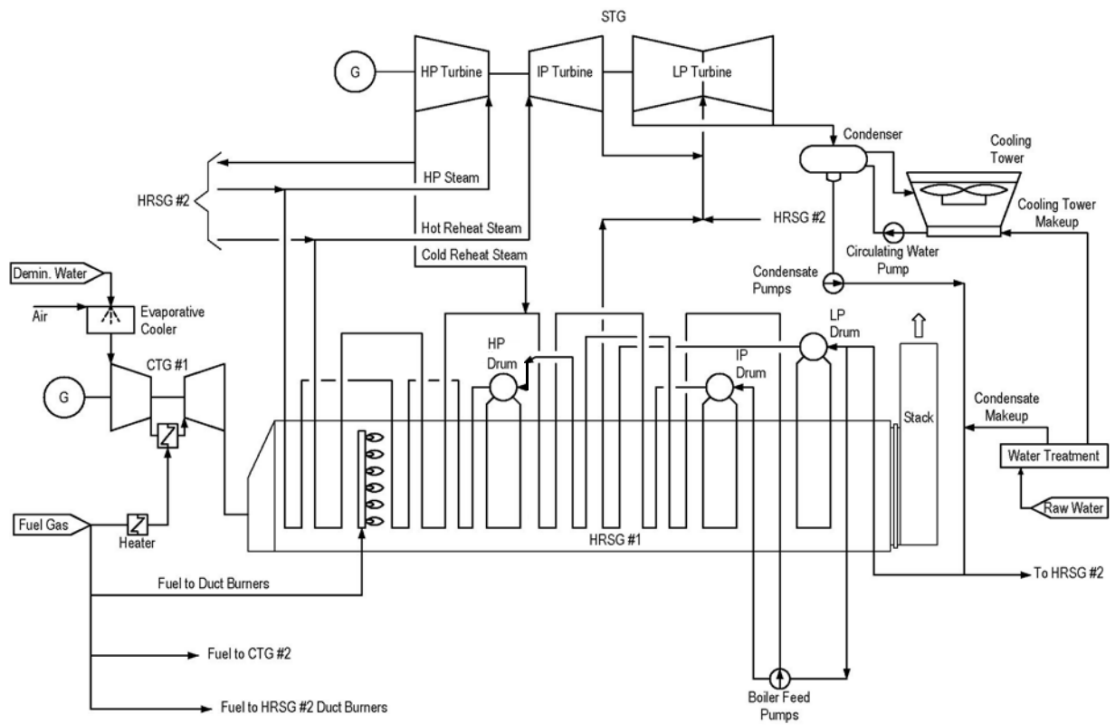


Figure 30: Schematic representation of a NGCC equipped with two GTs, two HRSGs and a shared steam power block [80].

3.2 Components

3.2.1 Gas Turbine



Figure 31: GE 9F.03 gas turbine [82]

Gas turbines (GTs) in open cycles are made up of three principal machines: compressor, combustor and expander (Figure 31). These machines were born in the aeronautic sector for military use in the 40s and later they have been adapted to stationary energy generation sector, with particular attention to emissions control. The compressor is usually an axial machine with a high number of stages, which can guarantee higher isentropic efficiencies; there are only few exceptions, generally limited to low size turbines.

Some parameters are used in gas turbine sector to compare different models:

- $\eta_{GT} = \frac{\dot{W}_{GT}}{\dot{m}_{fuel}LHV}$, the GT efficiency;
- *TIT*, Turbine Inlet Temperature, it is the temperature at the first rotor inlet temperature and represents the start point of the cycle work extraction;
- *TOT*, Turbine Outlet Temperature, it is the expander exit temperature (in a combined cycle it is also the HRSG inlet temperature);
- $\beta = \frac{p_{out,compr}}{p_{in,compr}}$, the compression ratio;
- Air and fuel mass flows.

Gas turbines can be classified in two great families [31]:

- *Heavy-duty*: developed expressly for industrial and electricity generation application. They are big size machines, particularly suited for continuous and stationary working conditions. The stages are arranged on a single shaft, whose rotation speed allows the direct matching with the grid. These turbines reach power values of 250÷300 MW with β of 15÷20. The use of a β value lower than the optimal one (i.e. maximum efficiency) guarantees a high specific works and allows the use of simpler turbomachines with a lower number of stages. Consequently to the beta reduction, the heat rejected by the GT increases but it can be well exploited in stationary applications (i.e. with an HRSG).
- *Aero-derivative*: adapted, with fewer modifications as possible, from machines designed for aeronautical propulsion, they are more adaptable to dynamic load conditions. Aero-derivative gas turbines can reach high η_{GT} (of about 40%) at the price of higher investment costs. In order to reach high efficiencies they generate less power (30÷110 MW) with higher β (20÷43) than heavy-duty turbines [83].

Gas turbines are internal combustions engines and because of that they can only accept fuels whose flue gases aren't chemical or physical aggressive towards combustor and expander surfaces and whose composition respect the emissions restrictions. The combustor must be designed with the respect of the NO_x emissions limits: usually there are multiple combustion stages, a design that allows the limiting of emissions and guarantee flame stability and the complete conversion of fuel.

The expansion, in particular for high power gas turbine, is cooled to keep TIT as high as possible while keeping the internal wall temperature of the expander under the maximum steel tolerable temperature. Increasing the TIT results in an improvement of gas turbine cycle performances. Since increasing TIT means increasing TOT , CCs also take advantage from a higher TIT because it improves thermal recovery.

The optimal regulation of a gas turbine is the one that avoids the compressor stall and keeps the thermodynamic efficiency as high as possible. The possible ways of varying the power output of the GT are:

- *Variation of fuel mass flow*: the inlet air mass flow is kept constant and only the fuel mass flow is varied. This solution leads to a TIT decreasing and so η_{GT} decreases as well.
- *Variable Inlet Guide Vanes (VIGV)*: with axial compressors there is the possibility of varying the guide vane angle of statoric blades. In this way, as the air mass flow decreases, the compressor inlet section is smaller, keeping the air velocity and the velocity triangles the same as in nominal case. This kind of regulation is widely applied for a decrease of air mass flow up to 50÷70%.
- *Lamination valve*: with a pressure drop at the compressor inlet, it is possible to keep the same volumetric airflow with a reduced air mass flow. This solution is highly dissipative and it is difficult to apply with high air mass flow; for these reasons this solution is scarcely diffused.
- *Variation of revolution per minute*: where applicable (e.g. twin-shaft GT) is the favourite solution, since it is flexible and not dissipative.

The typical regulation for a GT from the 100% to the 50% of nominal load is made with the VIGV; this can allow the TIT to remain equal to the one of the nominal case. However, the regulation is made keeping the TOT unvaried to avoid excessive thermal stresses on metal surfaces. In this range η_{GT} decreases slowly. For loads from 50% to 0% the inlet area section is kept at the minimum allowable by the VIGV and TIT decreases as the fuel mass flow is decreased; in this range the η_{GT} reduction is more evident. In Figure 32, the typical GT regulation is described (GT load equal to 0 is the “full speed-no load condition”):

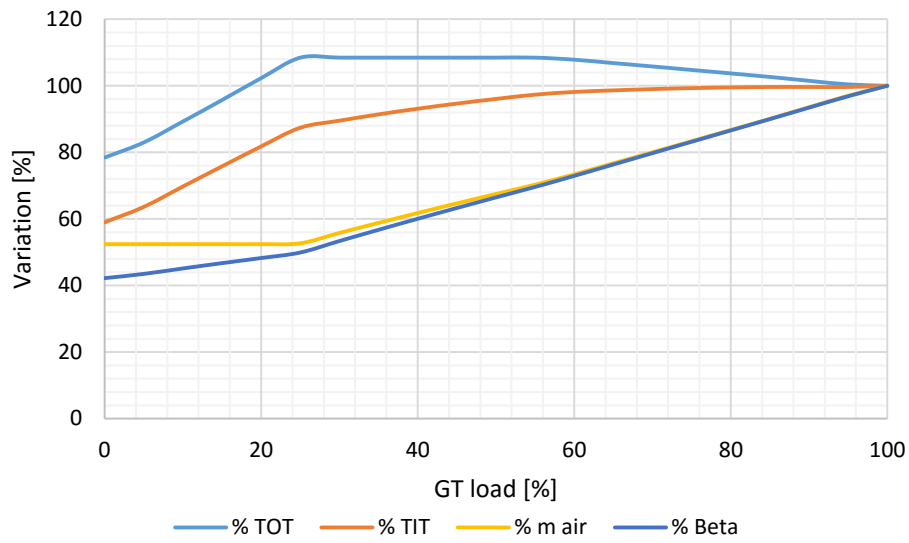


Figure 32: Variation of GT parameters as a function of GT load. The variation is defined as the ratio of the parameter with respect to its nominal value.

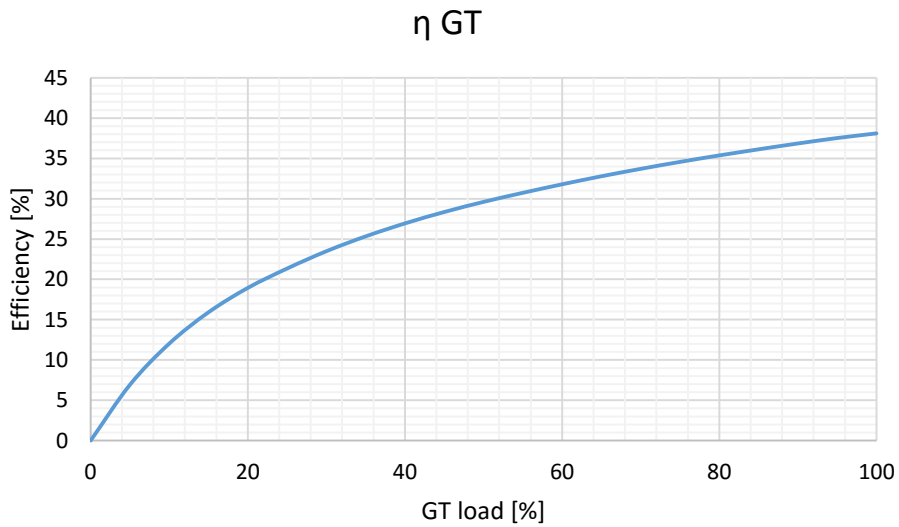


Figure 33: GT efficiency as a function of GT load.

The GT model employed in the combined cycle and in the ISCC studied in this thesis, is a GE's class F gas turbine (GE 9F.03 shown in Figure 31); the F class actually is the most qualified and diffused technology for stationary application within heavy duty GTs.

3.2.2 Bottoming cycle

3.2.2.1 HRSG

Flue gases can be sent to HRSG at the turbine outlet conditions or a post-firing section can be added. In this case a certain amount of fuel is injected in a duct burner to increase gases temperature. The HRSG (Figure 34) is the bottoming part of the combined cycle, it is similar to a Rankine, though it presents some differences, starting from the heating process.

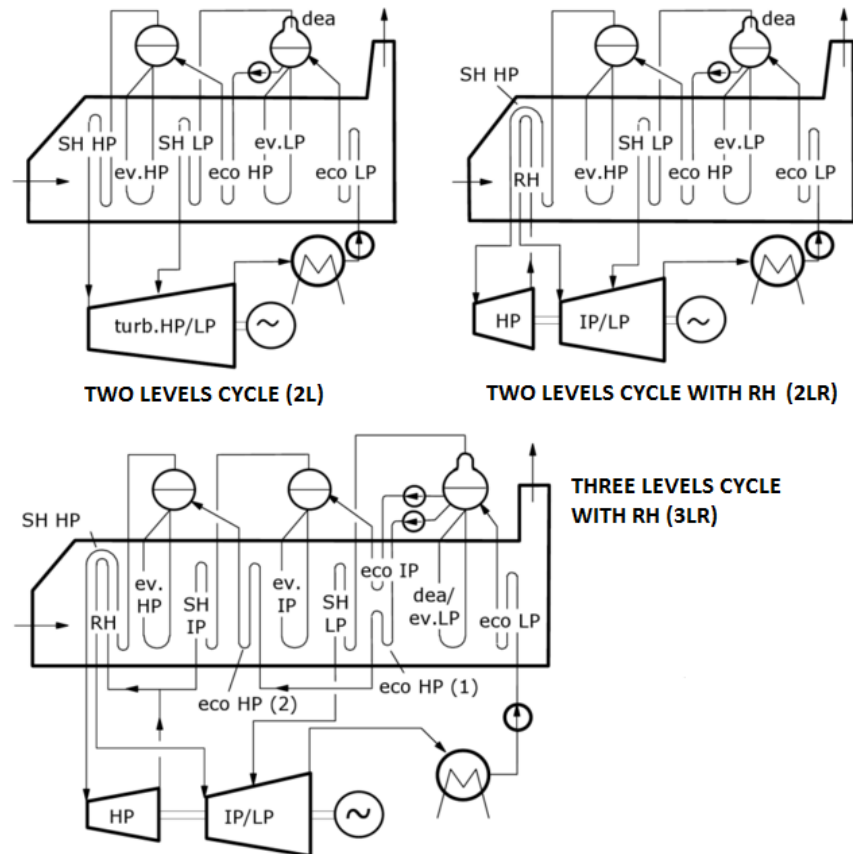


Figure 34: Different possible layouts of HRSGs - Adapted from [31].

In the HRSG, there is not a combustion process but the heat is recovered by cooling the flue gases. The heat exchangers are counter-current, even the superheater which, in conventional Rankine cycles, is con-current and separated from the high temperatures zones to avoid excessive thermal stresses. Flue gases are indeed cooler than combustion products, so heat exchangers can be counter-current since they are not affected by very high temperature fluxes. Regenerative bleeds from the ST are avoided in CCs, since these would reduce the energy production from the ST and the recovery factor without a reduction of the fuel consumption.

Several HRSG configurations can be defined and classified on the basis of:

- Boilers arrangement (vertical or horizontal);
- Type of circulation within evaporators (once-through, natural or forced circulation);
- Deaerator disposition;
- Number of pressure levels in the bottoming cycle.

In order to reduce exergetic losses of the heat transfer process, the bottoming cycle can be realised with several evaporation levels of pressure: nowadays the most common solutions are based on configurations with two or three pressure levels. In fact, the increase in number of pressure levels allows the reduction of irreversibilities through lower ΔT between fluids in the heat exchangers.

As it can be seen in Figure 35, the introduction of other pressure lines can help to follow better the gas cooling line, allowing a better thermal recovery.

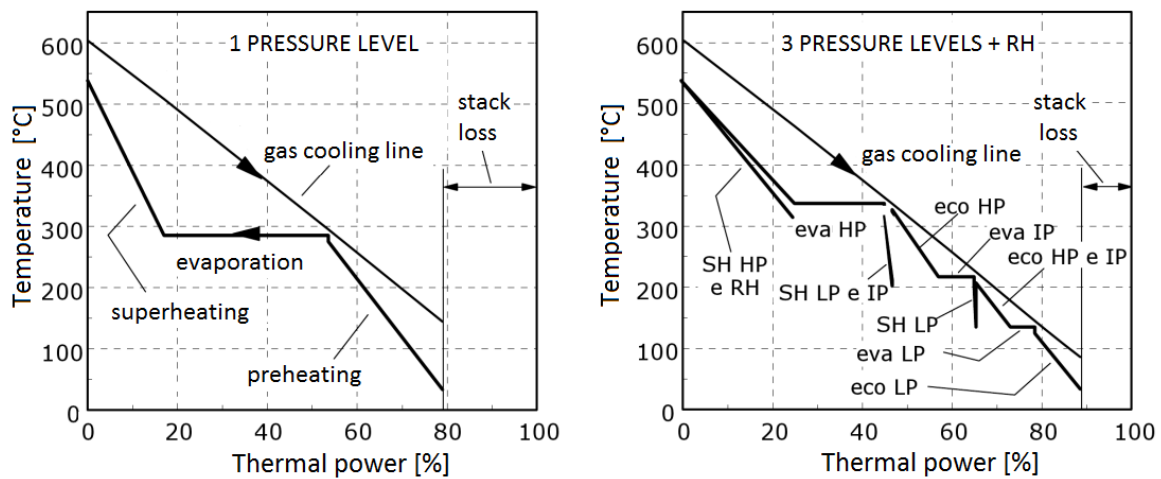


Figure 35: TQ diagrams for a single pressure level HRSG and a three pressure levels HRSG – Adapted from [31].

The introduction of a reheater (RH) can further improve the plant's performances: it reduces the presence of liquid droplets in the turbine, maintaining high expansion efficiencies, and increases the medium temperature level of heat's introduction in the cycle. Even if the introduction of the RH involves additional complexity and costs, the solution with three pressure levels plus RH (3LR) is the most efficient and widely used in big power plants.

3.2.2.2 Steam turbines

Steam turbines for CCs usually are not so different from the ones employed for conventional Rankine cycles. However, there are some differences, such as the maximum inlet pressure that is generally lower in CCs since an optimum evaporation pressure can be defined. In a conventional steam cycle, on the contrary, an increase of the maximum pressure means an improvement in cycle performances. Maximum steam pressures in combined cycles are frequently between 60 and 140 bar while for conventional steam cycles 300÷320 bar can be

reached. The advantage, for combined cycles, is a simplification of the high pressure stage. Steam mass flow distribution in the expansion differs a lot from the one of conventional plants. In CCs the steam mass flow increases during the expansion (at the outlet of low pressure turbine the mass flow is about 25÷35% higher than at the high pressure inlet), while in conventional plants it is reduced because of the presence of regenerative bleeds (the steam sent to condenser is the 55÷60% of the total). Even if the power produced from CCs steam turbines is considerably lower, they require a detailed design because of the high volumetric flow in low pressure sections. They can reach isentropic efficiencies up to 95% for medium pressure stages [31].

3.2.2.3 Condenser

There are three principal kind of condenser that can be employed in a CC:

- *Open circuit condenser*
- *Evaporative tower condenser*
- *Air condenser*

In the first solution, cool water is withdrawn, used for condensation in the heat exchanger and then reintroduced slightly hotter in its natural basin (such as rivers or lakes). The open circuit is the simplest and most economical solution, but it requires availability of massive amount of water (not always available for environmental and ethical concerns) and often there are restrictions on the maximum ΔT of the cooling water to avoid overheating of the water resource.

In the solution with evaporative tower, liquid water is used in a semi-closed circuit and its heat is removed by the evaporative tower, mostly thanks to evaporation of a fraction of the water mass flow in contact with ambient air. This solution leads to a significant reduction of water consumption, but it is still present since the tower requires the introduction of a make-up flow to replace the evaporated water mass flow. Furthermore, water is required to fill up the blowdown flow, necessary to maintain the correct salt concentration in the water. The air mass flow is rather small, so fans power is reduced.

In the air condenser solution, the condenser is cooled with a “dry” convective process directly with ambient air. This solution requires no water consumption, but a significant increase in the air used in the refrigeration process with respect to the evaporative tower and, consequently, an increase in the auxiliary power consumption. This solution is particularly useful in ambient with scarcity of water resources, typical condition of the locations where CSP plants are installed. This is the reason why air condensers are becoming the favourite choice for CSP plants under construction, as for the Ivanpah facility, in California [84].

3.3 Performance parameters

The “recovery factor” (χ) accounts for the amount of heat from exhaust gases recovered by the HRSG. It can be expressed as follows:

$$\chi = \frac{\dot{Q}_{in,steam\ cycle}}{\dot{Q}_{flue\ gases,av}} \quad (23)$$

The steam cycle efficiency is defined on the heat provided to the water as:

$$\eta_{steam\ cycle} = \frac{\dot{W}_{ST}}{\dot{Q}_{in,steam\ cycle}} \quad (24)$$

The HRSG efficiency accounts for the overall bottoming cycle, it can be written as:

$$\eta_{HRSG} = \frac{\dot{W}_{ST}}{\dot{Q}_{flue\ gases,av}} = \chi \eta_{steam\ cycle} \quad (25)$$

Where \dot{W}_{ST} is the electrical power produced from the steam turbine, $\dot{Q}_{flue\ gases,av}$ is the heat available from turbine exhaust gases if cooled to the ambient temperature and $\dot{Q}_{in,steam\ cycle}$ is the heat given to water in the HRSG.

The overall NGCC efficiency can be written as:

$$\eta_{CC} = \frac{\dot{W}_{GT} + \dot{W}_{ST}}{\dot{m}_{fuel} LHV} = \eta_{GT} + (1 - \eta_{GT})\varphi\chi \eta_{steam\ cycle} \quad (26)$$

Where \dot{W}_{GT} is the electrical power generated by the gas turbine, $\dot{m}_{fuel} LHV$ is the total power input as fuel heat value and η_{GT} is the net efficiency of the gas turbine. φ is defined as:

$$\varphi = \frac{\dot{Q}_{flue\ gases,av}}{\dot{m}_{fuel} LHV - \dot{W}_{GT}} \quad (27)$$

3.4 Effects of variation of operating conditions on CC performances

3.4.1 Gas cycle

GT performances described on producers' brochures are referred to "ISO conditions", defined below:

- Ambient temperature: 15°C;

- Ambient pressure: 101325 Pa;
- Relative humidity: 60%;
- Pressure drops absent at compressor inlet and expander outlet;
- Natural gas available at sufficient pressure;
- New and clean machines.

As ambient operating conditions vary, the GT performances can differ slightly from the nominal ones. As ISCC power plants are installed in hot and arid climatic zone, their operating conditions will deviate often from the ISO conditions. In addition, the presence of the HRSG introduces a permanent pressure drop at the outlet of the expander.

3.4.1.1 Ambient pressure

The ambient pressure can change because of climatic conditions or site altitude. As the temperature increases, since the volumetric air flow remains unchanged, the air mass flow decreases, with a consequent decrease of the cycle power output. There are no significant effects on η_{GT} , since the “shape” of the cycle doesn’t change; all the cycle pressure are lower. In this thesis, pressure variations will not be considered in the off-design plant simulations.

3.4.1.2 Pressure drops

Pressure drops can be present at compressor inlet (e.g. for the presence of a filter) and at expander outlet (e.g. for the presence of components such as an HRSG).

The *intake pressure drop* reduces the air mass flow aspired by the compressor with a consequent reduction of cycle power output. In addition, pressure at expander inlet is reduced, with a decreased expansion work, while compressor β remains unchanged. For these reason, the pressure drop affects not only the cycle power output, but also its overall efficiency.

The *discharge pressure drop* doesn’t affect the compressor and the air mass flow remains unchanged. The expander outlet pressure is reduced by the Δp imposed and consequently its expansion work and cycle efficiency are reduced as well.

The solar integration on the bottoming cycle does not affect pressure drops on the gas turbine.

3.4.1.3 Ambient temperature

Ambient temperature is the parameter that most considerably affects the performances of a GT and it can vary a lot during the day and seasonally (e.g. a range from 0°C to 45°C during the year in a desert climate). The air mass flow decreases as the specific volume increases with ambient temperature with a consequent decrease of the cycle power output. β and the cycle maximum pressure decrease and results in an increase of the TOT , being constant the TIT . This leads to a reduction of cycle efficiency, more intense than the reduction caused by pressure drops. Different cooling solutions can be employed in order to keep the air inlet temperature within certain limits, such as evaporative humidification and compression or

adsorption cooler. These solutions, like the solar cooling hybridisation studied in this work, introduce an additional intake pressure drop.

3.4.2 *Bottoming cycle*

The decrease of *ambient pressure* comes along with a decrease of flue gases mass flow. In this way, the thermal power available at HRSG inlet is reduced and so the steam produced and the ST power output also decreases.

The *ambient temperature* increase has similar effect on the steam produced because of reduced flue gases mass flow. In fact, the bottoming cycle naturally reacts to this effect by reducing the steam mass flow produced, with a consequent reduction of evaporative pressures if the steam turbine works in sliding pressure; this leads to a reduction of stack temperature and an increase of χ . In addition, it makes the condensation process more difficult with a consequent increase of the condensing pressure (except for the open circuit condenser). In this way there is a reduction of the expansion ratio and consequently of ST expansion work and net power output.

Relative humidity variations are not considered since their impact on the gas turbine is negligible while they have no effects on the air condenser.

3.5 Reference NGCC

It is necessary to build a reference combined cycle as a starting point for the solar integration and to compare annual performances. As a first step, the model developed European Benchmarking Task Force (EBTF) [85] was reproduced in Thermoflex®, then some adjustments were made in order to solve some problems related to heat exchanger sizing. This first step allows the comparison of GS code [86], developed by the Department of Energy of Politecnico di Milano [87] output of with Thermoflex® ones and it help to understand the program responses to input variations.

3.5.1 *EBTF Combined Cycle*

The NGCC model built in Thermoflex® is based on the European best practice guidelines made by the EBTF, where a compilation of projects, including one NGCC, is presented. The chosen cycle is a large-scale, base-load plant, representative of the current state of the art. Data are based on calculations carried out by the GS code.

The power plant is made of two GTs, which feed with their exhaust gases one HRSG connected to a single ST, as shown in Figure 36. The gas section is composed by two identical “F class” GTs, following the values of parameters of the generic models specified in the EBTF Common Framework Definition Document. The GT used in the EBTF model is a “reference, average” F-class large-scale gas turbine, whose parameters derives from three GT models (i.e. Alstom GT-26, GE 9371F and Siemens STG5-4000F) [85]. The HRSG is a three pressure levels plus reheat kind (3LR). The natural gas is preheated up 160°C in a

heat exchanger using saturated liquid extracted from IP drum. Cycle parameters will be reported in the following paragraphs, when confronted with Therrmoflex® output.

Figure 36 shows the EBTF plant layout and Table 12 and Table 13 show thermodynamic points of the cycle, divided by fluid type.

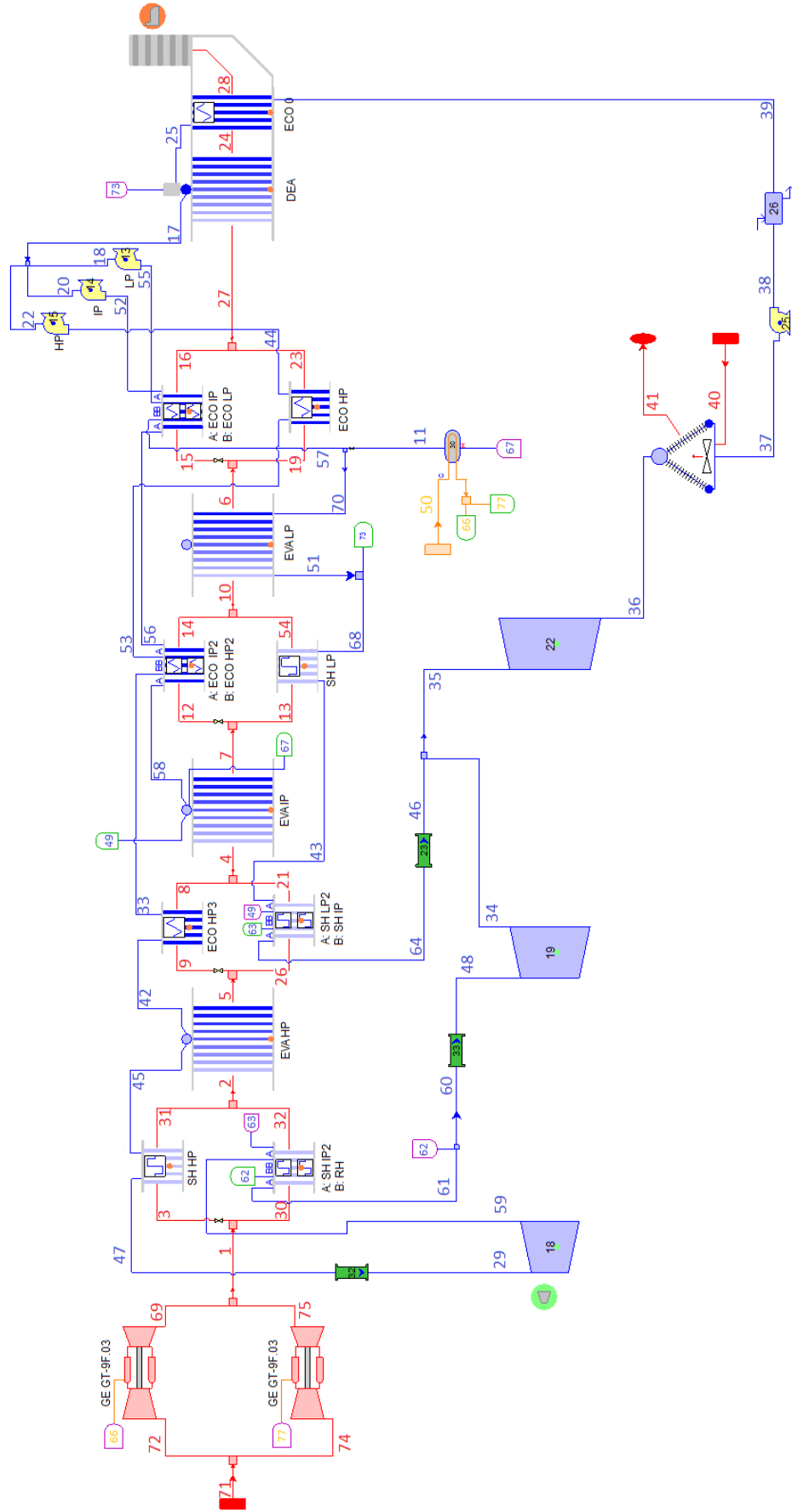


Figure 36: Thermflex® layout of the reference EBTF combined cycle plant.

Table 12: Gas/air/fuel stream table of the reference EBTF combined cycle plant. h is the fluid enthalpy referenced zero at 25°C and H₂O as vapor.

	p	T	\dot{m}	h	Type of fluid
	[bar]	[°C]	[kg/s]	[kJ/kg]	[-]
1	1,053	604,6	1327	642,4	Gas
2	1,045	458,1	1327	472	Gas
3	1,053	604,6	753,7	642,4	Gas
4	1,032	277,7	1327	270,1	Gas
5	1,038	341,7	1327	340,7	Gas
6	1,018	156,7	1327	139,4	Gas
7	1,028	232,3	1327	220,7	Gas
8	1,032	277,7	1158,2	270,1	Gas
9	1,037	341,7	1158,2	340,7	Gas
10	1,02	186,1	1327	170,8	Gas
12	1,024	232,3	1272,9	220,7	Gas
13	1,028	232,3	54,09	220,7	Gas
14	1,02	186,1	1272,9	170,8	Gas
15	1,018	156,7	354,6	139,4	Gas
16	1,015	135,2	354,6	116,4	Gas
19	1,018	156,7	972,4	139,4	Gas
21	1,032	278	168,9	270,4	Gas
23	1,015	135	972,4	116,3	Gas
24	1,015	129	1327	109,8	Gas
26	1,038	341,7	168,9	340,7	Gas
27	1,015	135,1	1327	116,3	Gas
28	1,013	88,34	1327	66,74	Gas
30	1,053	604,6	573,3	642,4	Gas
31	1,045	458,1	753,7	471,9	Gas
32	1,045	458,1	573,3	472	Gas
40	1,013	15	38392	-10,13	Air
41	1,013	26,7	38392	1,725	Air
54	1,02	186,1	54,09	170,8	Gas
69	1,053	604,6	663,5	642,4	Gas
71	1,013	15	1296,9	-10,13	Air
72	1,013	15	648,5	-10,13	Air
74	1,013	15	648,5	-10,13	Air
75	1,053	604,6	663,5	642,4	Gas
50	70	10	30,1	46478	Fuel
66	69,67	110	15,05	46695	Fuel
77	69,67	110	15,05	46695	Fuel

Table 13: water/steam stream table of the reference EBTF combined cycle plant. h is the enthalpy referenced to zero at 0°C and H₂O as vapor.

	p	T	\dot{m}	h
	[bar]	[°C]	[kg/s]	[kJ/kg]
11	23,99	50	9,04	211,4
17	1,399	109,3	202,3	458,2
18	1,399	109,3	8,689	458,2
20	1,399	109,3	43,84	458,2
22	1,399	109,3	149,8	458,2
25	1,399	99,25	202,3	415,9
29	120,9	560,7	149,8	3508
33	132,1	222,3	149,8	957,6
34	3,52	297,1	183,7	3062
35	3,52	297,1	201,4	3062
36	0,0477	32,06	202,2	2386,3
37	0,7656	32,06	202,2	134,3
38	1,873	32,07	202,2	134,5
39	1,873	32,06	202,3	134,4
42	131,4	326,7	149,8	1501,7
43	3,73	215	17,73	2893,6
44	133,7	111,3	149,8	476,7
45	131,4	331,7	149,8	2659,5
46	3,52	297,9	17,73	3064
47	127	565	149,8	3513
48	22,96	562,9	181,2	3605
49	24,26	222,4	34,8	2801,7
51	4,357	146,7	17,73	2741,9
52	25,12	109,6	43,84	461,5
53	133	146,7	149,8	626,2
55	4,401	109,3	8,689	458,6
56	24,86	146,7	43,84	619,4
57	4,357	141,7	8,689	596,6
58	24,26	217,3	43,84	931,5
59	24,3	327,6	146,4	3077
60	23,28	565	181,2	3609
61	23,28	565	146,4	3609
62	23,28	565	34,8	3609
63	23,74	316,7	34,8	3053
64	3,7	299,6	17,73	3067
67	24,26	222,4	9,04	954,5
68	4,357	146,7	17,73	2741,9
70	4,357	95,45	17,73	400,2

First of all, a model of the HRSG with the ST has been made in Thermoflex® in order to match the results of the new model with the ones from GS.

Heat exchangers thermal efficiency (set to 99,6%) and disposition inside the HRSG derive from available data output of the GS software.

Pressure levels, pressure and thermal losses, pump efficiencies and characteristic ΔT have been imposed in thermodynamic mode. In this first step the inlet of the HRSG on exhaust gases side has been modelled as a gas source with fixed temperature and gas composition (“no TG” model); in this way it is easier to verify the correspondence between Thermoflex® model and EBTF data.

The ST is subdivided in three stages: high pressure (HP), intermediate pressure (IP) and low pressure (LP). The modelling has been made through the use of the “steam turbine assembly” tool available in Thermoflex®; it evaluates ST stages efficiencies and leakages. The part-load regulation is made by sliding pressure.

An air condenser has been employed, in prevision of the application of this model to ambient with scarcity of water resources. Variable RPM pumps have been employed in order to avoid efficiency losses at part loads for throttling across a valve. SH and RH temperature control has been imposed by desuperheating at the end of heat exchangers.

Thermoflex® provides a single component for two parallel boilers; however, in the GS model there are three parallel components. In this case, to find the correct gas mass fraction for every component, control loops⁵ have been enabled. The control variables were exit gas temperatures from the three boilers, which had to be equal. Once the mass fractions were founded, control loops had been disabled to perform off-design simulations.

Performing the engineering analysis of the plant, some issues have been highlighted; first of all, the first LP economiser had a reduced mass flow and the software was not able to size the component. The reason had to be found in the preheating of the fuel. To preheat the fuel up to 160°C a shell and tube exchanger was provided; it was fed with saturated water from the IP drum and the water was then sent to the inlet of LP drum. In this way, since Thermoflex® estimates the total flow at the evaporator, the mass flow resulting in the economiser was too low.

In order to avoid this problem, the fuel temperature at the inlet of the gas turbine has been set to 156°C; this value has been chosen as it resulted as the value, which guaranteed a right sizing of the economiser. The 4°C decrease of the inlet fuel temperature, however, does not affect significantly the gas turbine efficiency.

The TOT is really high compared to the exit temperature of the HP superheated steam (604°C vs. 565°C), indeed, at partial loads, the maximum value of pressure set by material resistance

⁵ Control loops are a particular Thermoflex® feature that allows reaching a desired value of Set Point Variable by adjusting certain Control Variables. It is also possible to use a Parameter Matching Control to cause a pair of variables to attain equality one to another. [65]

was exceeded. In order to avoid structural problems, the tube wall thickness of the HP superheater has been increased from 3,404mm to 3,491mm.

In the second step, the fixed gas source has been substituted with the two GTs. The aim was to find, in the available turbine models, a GT whose TIT , TOT , air and fuel mass flows were as similar as possible to the GS ones. The GE GT-9F.03 [88] has been chosen as it highlighted minor percentage error with GS data, as shown in Table 14.

Table 14: Comparison between three different GT models and the percentage errors of their parameters with respect for GS results.

	GS	Alstom GT26	GE 9F03	GE 9F 3series	e%		
					Alstom GT26 vs.GS	GE 9F03 vs.GS	GE 9F 3series vs.GS
$\eta_{CC,net}$ [%]	58,57	56,89	57,32	56,83	-2,87	-2,14	-2,97
$\dot{W}_{NGCC,net}$ [MW]	833,22	896,38	800,24	784,73	7,58	-3,96	-5,82
\dot{W}_{GT} [MW]	544,22	607,16	525,07	508,21	11,57	-3,52	-6,62
$\eta_{GT,gross}$ [%]	38,26	38,54	37,61	36,81	0,72	-1,70	-3,80
\dot{m}_{fuel} [kg/s]	30,61	33,88	30,02	29,69	10,68	-1,92	-3,01
$\dot{m}_{flue\ gases}$ [kg/s]	1330,60	1372,36	1326,93	1324,38	3,14	-0,28	-0,47
TOT [°C]	607,96	609,94	604,42	606,29	0,33	-0,58	-0,28

In **Table 15** main results for both the configurations analysed and their percentage errors are shown. The results These errors are in absolute value below 5% and so the results can be considered quite accurate. Greater errors are registered on the water mass flow and pressures values of the IP and LP heat exchanger. These differences are due to the passage from thermodynamic mode to engineering mode, in particular to the sizing of heat exchangers tubes and of piping at the end of SH and RH sections. The greatest error in “no TG” model and GS data comparison is the one on the ST power output. This error is attributed to the ST assembly tools, since it employs a method for automatically estimate the efficiency of the various ST groups, as well as methods of automatically treating the various steam turbine leakage flows. In this way these values are slightly different from the ones used in GS, while in the GE9F.03 case the error is reduced because of the presence of negative errors which compensate for the positive ones. For the reason the fuel is assumed to be clean, the corrosion issue is not considered and it is possible to keep the low stack temperatures, shown in Table 15.

Table 15: Main results for NO TG configuration and for GE 9F.03 configuration.

	GS	no TG	GE 9F03	e%	
				no TG vs. GS	GE 9F03 vs. GS
$\eta_{CC,net}$ [%]	58,57	/	57,35	/	-2,084
$\dot{W}_{NGCC,net}$ [MW]	833,22	/	800,97	/	-3,870
$\eta_{GT,gross}$ [%]	38,26	/	37,55	/	-1,844
\dot{W}_{GT} [MW]	544,22	/	524,51	/	-3,622
\dot{m}_{fuel} [kg/s]	30,61	30,61	30,03	0,000	-1,89
TOT [°C]	607,96	608,00	605,08	/	-0,474
TIT [°C]	1359,95	/	1342,57	/	-1,278
χ [%]	88,16	87,91	87,78	-0,284	-0,438
T_{stack} [°C]	86,76	88,19	88,66	1,639	2,183
$\dot{Q}_{flue\ gases,av}$ [MW]	873,95	874,79	866,995	0,097	-0,796
$\dot{Q}_{in,steam\ cycle}$ [MW]	770,49	769,05	761,01	-0,187	-1,230
\dot{Q}_{loss} [MW]	3,09	3,09	3,06	-0,188	-1,230
\dot{W}_{ST} [MW]	292,41	298,36	294,967	2,037	0,876
$\eta_{steam\ cycle}$ [%]	37,95	38,80	38,76	2,23	2,13

Once the design model matched the GS model with minimum possible errors, the off-design study has been performed by changing ambient temperature and GTs load. It first showed that, as the load was decreasing, the system was not able to maintain the fuel temperature constant. That resulted in an error occurring on the LP economiser, which was characterised by a zero mass flow. To avoid this problem two solutions were possible: changing the water mass flux in the heat exchanger consistently with the load reduction or fixing a lower fuel temperature. The second solution was applied and the temperature was set at 110°C.

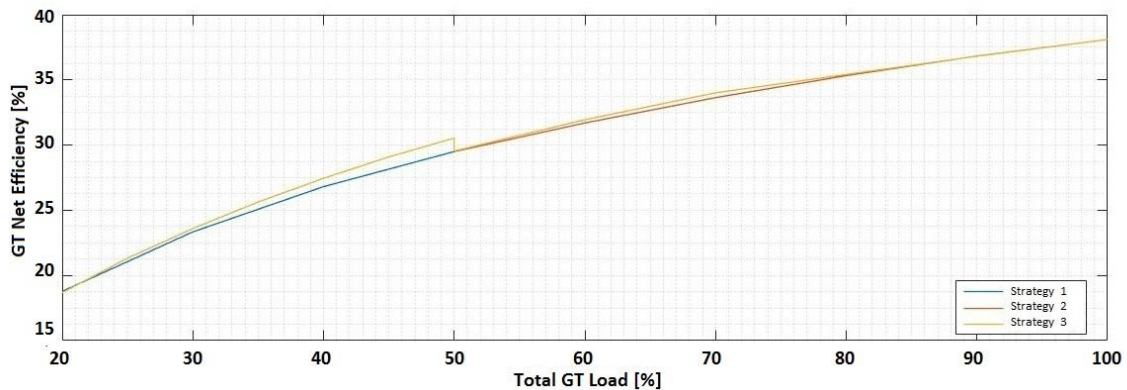
As the plant presents two turbines, an analysis of the best control strategy has also been performed.

The analysed regulations are shown in the following table (Table 16):

Table 16: GTs regulation strategies analysed.

	Total GT Load [%]	100	90	80	70	60	50	40	30	20
Strategy 1	TG1 [%]	100	90	80	70	60	50	40	30	20
	TG2 [%]	100	90	80	70	60	50	40	30	20
Strategy 2	TG1 [%]	100	90	80	70	60	100	80	60	40
	TG2 [%]	100	90	80	70	60	0	0	0	0
Strategy 3	TG1 [%]	100	100	100	100	80	100	80	60	40
	TG2 [%]	100	80	60	40	40	0	0	0	0

The effect of different regulations on the gas turbines net efficiency has been analysed through off-design simulations of the turbines in a simple cycle. As it can be seen in Figure 37, strategy 3 assures the best GT efficiency; however, since the efficiency drop between strategies 2 and 3 is small ($< 1,1\%$), strategy 2 has been chosen because it is simpler to handle and it is in accordance with the normal practice in NGCC plants.

**Figure 37:** GTs net efficiency as a function of total GTs load.

In Thermoflex®, two methods to control the turbine at partial loads can be chosen. The one employed in this model, controls the TIT in order to follow a “target” exhaust temperature, as can be seen in Figure 38, that is typically a function of the pressure ratio (in this case the target temperature is of about 649°C). The same target temperature is reached, where possible, independently from ambient temperature. The other method applies a direct firing temperature control model; with this regulation, at part load condition the TIT is kept constant.

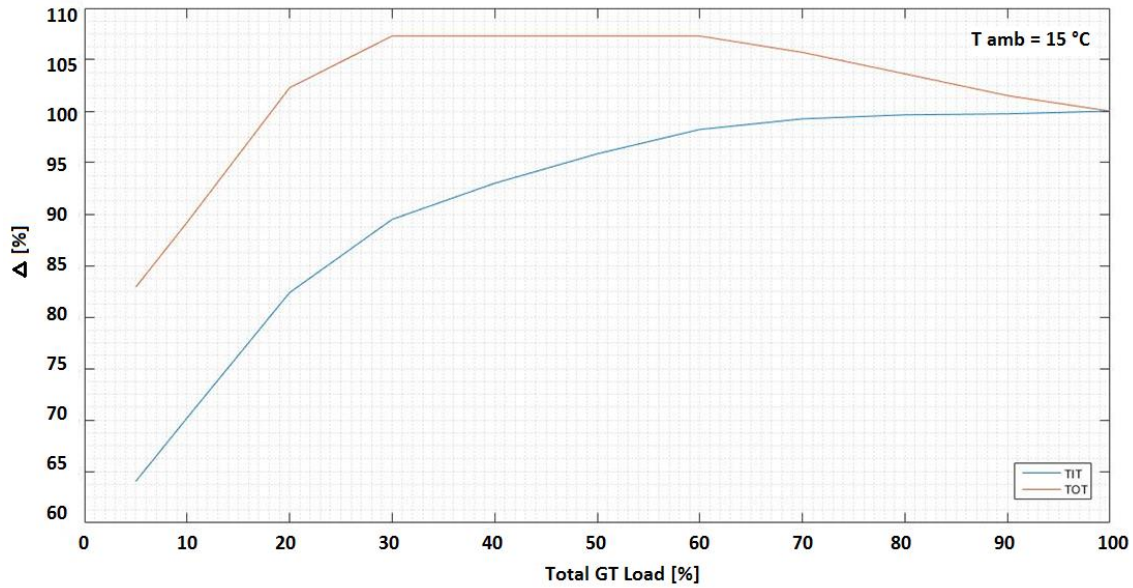


Figure 38: Variation of TIT and TOT as a function of total GTs load, where Δ indicates the ratio of the parameter with respect to its nominal value.

3.5.2 Simeri Cricchi Combined Cycle

The plant as it has been presented had a set of problems, especially for particularly stressing conditions (i.e. high temperatures and low GT loads), such as the impossibility to reach a total GT load below 25% of the nominal one. Moreover, the presence of water withdrawal from IP drums and its reintroduction before the LP drum increased the sub-cooling at LP drum inlet and caused difficulties in the sizing of LP economiser and in the management of the downline of the HRSG. For these reasons and with the purpose of simulate a realistic and manageable power plant, a new HRSG layout has been employed. The new plant is based on the layout the Simeri Cricchi power plant [89], in Calabria. In this new plant there are two HRSGs, one for each gas turbine; in Figure 39 the layout of one HRSG and the steam turbine is presented, the second HRSG is totally equal to the one reported while the steam turbine is shared. Table 17 and Table 18 show plant streams.

Table 17: Water/steam stream table of the reference EBTF combined cycle plant at 30°C ambient temperature. h is the enthalpy referenced to zero at 0°C and H₂O as vapor. Fluxes are reported for only one HRSG.

	p	T	\dot{m}	h
	[bar]	[°C]	[kg/s]	[kJ/kg]
4	0,1226	49,85	196,3	2478,5
5	4,98	49,88	196,3	209,2
6	0,8404	49,85	196,3	208,7
24	28,21	344,5	148,6	3107
44	27,17	565	174,5	3606
45	126,2	565	152,2	3514
53	3,96	294,6	195,3	3056
54	3,96	293,1	177,1	3053
62	126,2	565	76,11	3514
63	126,2	565	76,11	3514
64	28,21	344,5	74,28	3107
65	28,21	344,5	74,28	3107
66	4,98	49,87	196,3	209,2
83	27,17	565	87,27	3606
84	127,9	519,9	76,11	3394
85	129,1	440	76,11	3164
86	130,4	331,1	76,11	2661,9
87	4,147	144,9	76,11	610,4
88	4,147	144,9	17,1	610,4
89	28,33	230,7	13	2803,1
90	131,2	230,7	76,11	995,7
91	28,98	145,4	17,1	613,9
92	132,1	147,4	76,11	628,9
93	132,1	147,4	76,11	628,9
94	28,21	339,8	87,27	3096
95	28,21	313,5	13	3033
96	28,04	479,8	87,27	3414
97	3,96	294,6	97,64	3056
98	3,96	293,1	88,57	3053
99	130,7	300	76,11	1339,8
100	130,4	326,1	76,11	1498
103	28,33	225,7	13	970,2
104	28,33	225,7	17,1	970,2
105	28,98	145,4	17,1	613,9
106	4,147	144,9	93,21	610,4
107	4,147	144,9	104	610,4
108	4,147	144,9	9,067	2739,7
109	4,147	139,9	98,17	588,8
110	4,147	136,4	102,3	573,7
111	27,17	565	87,27	3606
112	3,96	309,2	9,067	3086
113	3,96	293,1	88,57	3053
114	4,147	144,9	10,83	2739,7
115	3,96	294,6	97,64	3056
116	4,98	49,87	98,17	209,2
119	28,11	50	4,104	211,7
121	28,33	225,7	4,104	970,2
122	4,147	144,9	1,763	2739,7
123	4,98	49,87	98,17	209,2

Table 18: Gas/air/fuel stream table of the Simeri Crichi power plant at 30°C ambient temperature. h is the fluid enthalpy referenced zero at 25°C and H₂O as vapor. Fluxes are reported for only one HRSG.

	p	T	\dot{m}	h	Fluid type
	[bar]	[°C]	[kg/s]	[kJ/kg]	[-]
1	1,013	30	601,8	5,108	Air
2	1,013	30	31069	5,108	Air
3	1,013	44,03	31069	19,45	Air
8	1,014	98,19	615,8	77,74	Gas
9	1,017	154,9	615,8	138,5	Gas
10	1,02	189,8	615,8	176,1	Gas
11	1,025	240,7	615,8	231,6	Gas
12	1,028	276	615,8	270,4	Gas
13	1,031	314,6	615,8	313,1	Gas
14	1,031	319,2	615,8	318,2	Gas
15	1,032	323,6	615,8	323,1	Gas
16	1,035	341,1	615,8	342,7	Gas
17	1,042	468	615,8	487,2	Gas
18	1,045	521,6	615,8	549,4	Gas
19	1,047	560,1	615,8	594,7	Gas
20	1,048	584,2	615,8	623,3	Gas
21	1,05	607,2	615,8	650,5	Gas
23	1,051	619,6	615,8	665,4	Gas
48	70	10	13,95	46478	Fuel
49	69,67	110	13,95	46695	Fuel

Heat exchangers are disposed in series, except for the LP and IP economisers that are in parallel and there is one HRSG for each GT instead of a single HRSG. The plant is provided with a deaerator integral to the HRSG that utilizes low-pressure evaporator energy to perform the feed-water deaeration, instead of the deaerator with its own evaporating drum. The GT used is the same GE GT 9F.03 employed in the EBFT power plant. Pressure levels in evaporators, pumps efficiencies and ΔT in heat exchangers have been kept equal to the ones of the EBTF NGCC. The fuel temperature at the outlet of the heat exchanger for the fuel preheating is kept at 110°C, while the water employed for the preheating process is withdrawn from the outlet of IP economiser and reintegrated at the inlet of the deaerator. Piping at steam turbine levels inlet provided a constant heat loss specific to the mass flow circulating ([kJ/kg]), however the thermal power loss is normally proportional to ΔT .

The plant presents three stages of high pressure superheating and two of reheating; this allows a better exploitation of exhaust gases heat and an intermediate desuperheating, which can control the wall temperature of the SH/RH better than the previous control of temperature at the outlet of the exchangers. It has been necessary to define intermediate outlet temperatures of the steam; these have been calculated starting from the available data of areas of the heat exchangers of the plant of Simeri Crichi, maintaining the same fraction of the exchanged heat.

Simulations of both the presented plants, at varying load conditions and constant temperature (15°C), have been made and the results were compared. In particular, 4 parameters have been analysed: χ , $\eta_{steam\ cycle}$, η_{HRSG} and $\eta_{CC,net}$.

Figure 40 shows trends for χ as a function of the total GT load. At 50% of the total load, trends show a step due to the GT turning off. In the new power plant the step reduces χ . In fact, since there is one HRSG for each GT, the one that is still running results closer to its nominal condition because exhaust gas mass flow and TOTs return to their nominal values. χ value is still higher than the nominal one because of the pressure reduction in the evaporators deriving from the sliding pressure regulation of the steam turbine. In the EBTF power plant, the step is smaller and moves towards an increase of the recovery factor. In this case, there is only one HRSG and the exchange areas result oversized with respect to the circulating mass flow; that leads to an augmentation of the heat recovered. At 15% of total GT load of the New power plant χ begins decreasing because the TOT starts decreasing as well. The same trend cannot be enlightened in EBTF power plant because it cannot reach such low loads.

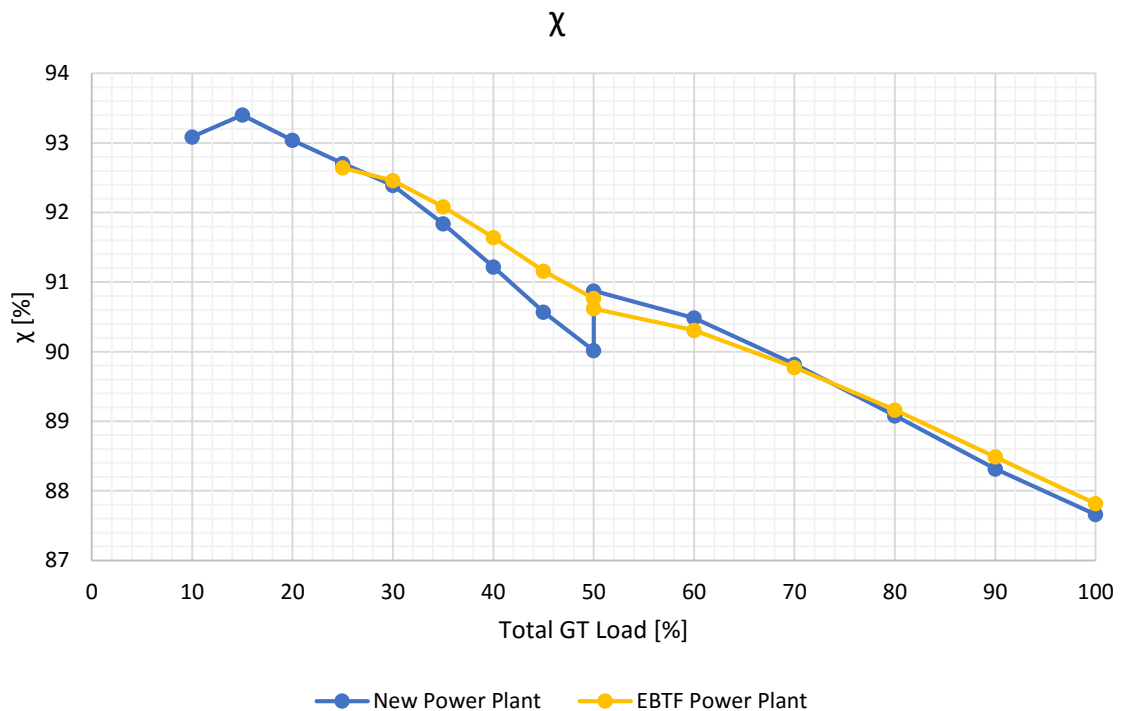


Figure 40: comparison of the χ of the two analyzed plants as a function of the total load of gas turbines for the fixed ambient temperature of 15°C

In Figure 41, the steam cycle efficiency is shown. Normally, the steam cycle efficiency decreases with the GT load because the exhaust mass flow reduces and so does the heat recovered by the HRSG. The steam turbine operates in sliding pressure so the steam mass flow and the evaporation pressure decrease, with a consequent reduction of the steam turbine power.

The blue line (New Power Plant) replicates this trend while for the EBTF Power Plant the steam cycle efficiency increases up to the 60% of the load since piping heat losses decrease with the mass flow reduction. Nominal values are also quite different because of the piping presence. The step for 50% of the GTs load is smaller for the new power plant because the operative HRSG returns to its nominal operative conditions.

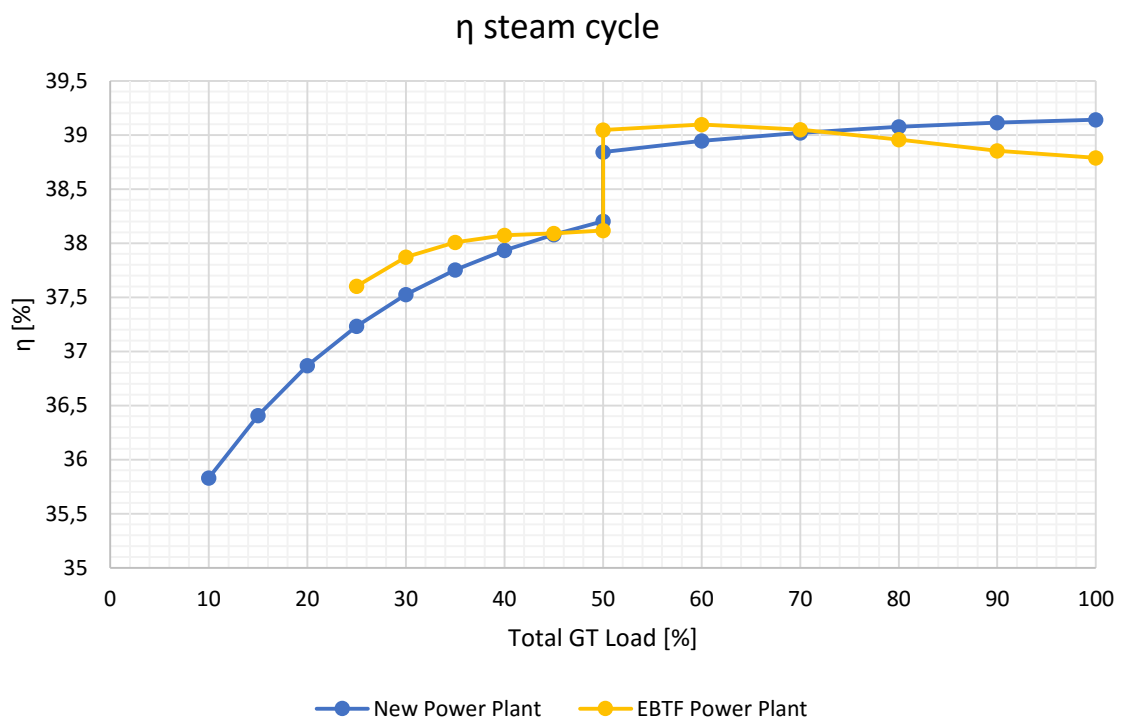


Figure 41: comparison of the $\eta_{steam\ cycle}$ of the two analyzed plants as a function of the total load of gas turbines for the fixed ambient temperature of 15°C

Figure 42 shows the efficiency of the bottoming cycle; its trend is defined by χ and $\eta_{steam\ cycle}$. Trends for total GTs load below 50% are due to TOT variations: it returns to its nominal value when one GT is turned off and then it increases as the GT load decreases until it reaches its “target” value at about 35% of total GT load. The yellow line trend is always defined by piping heat losses, so the nominal value is lower than the one of the new plant. The step at half the load is smaller for the EBTF plant because the higher recovery factor balances the $\eta_{steam\ cycle}$ drop.

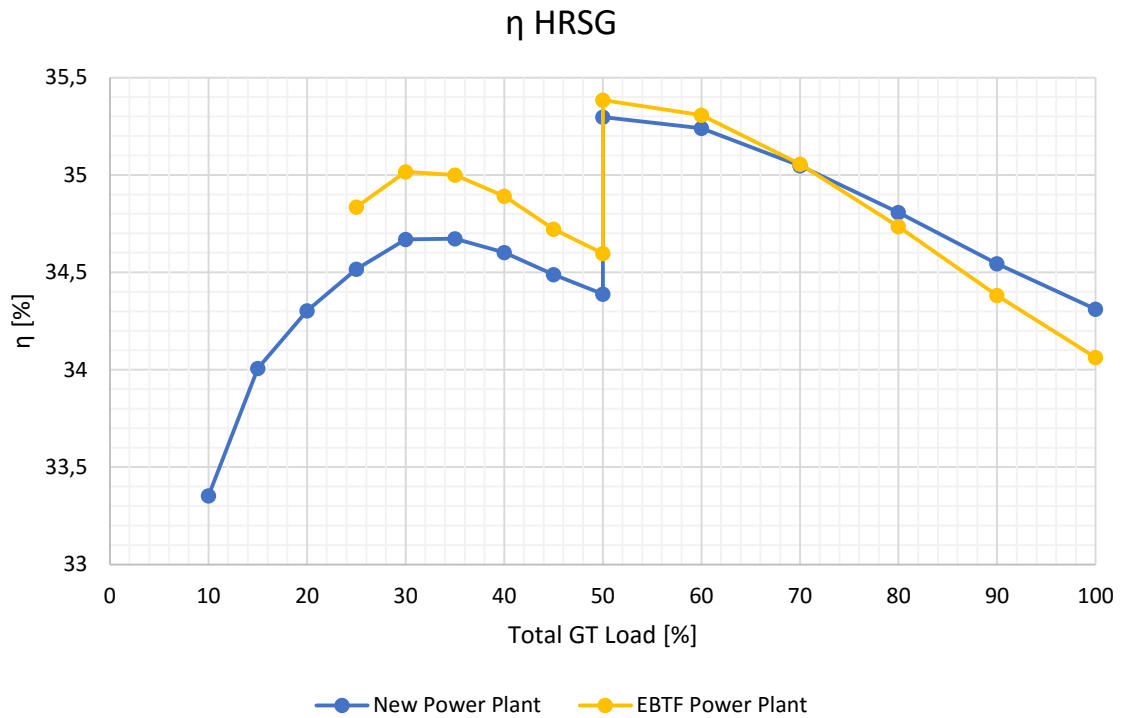


Figure 42: comparison of the η_{HRSG} of the two analyzed plants as a function of the total load of gas turbines for the fixed ambient temperature of 15°C.

Figure 43 shows the trend of the net efficiency of the two proposed cycles; as the gas turbines and the main inputs of the cycle are the same, there is not a noticeable difference between the two. When one GT is shut down, the working one returns to its nominal efficiency, so the CC efficiency increases. The efficiency of the EBTF plant is slightly higher for low loads because its recovery factor is higher having the plants a single HRSG.

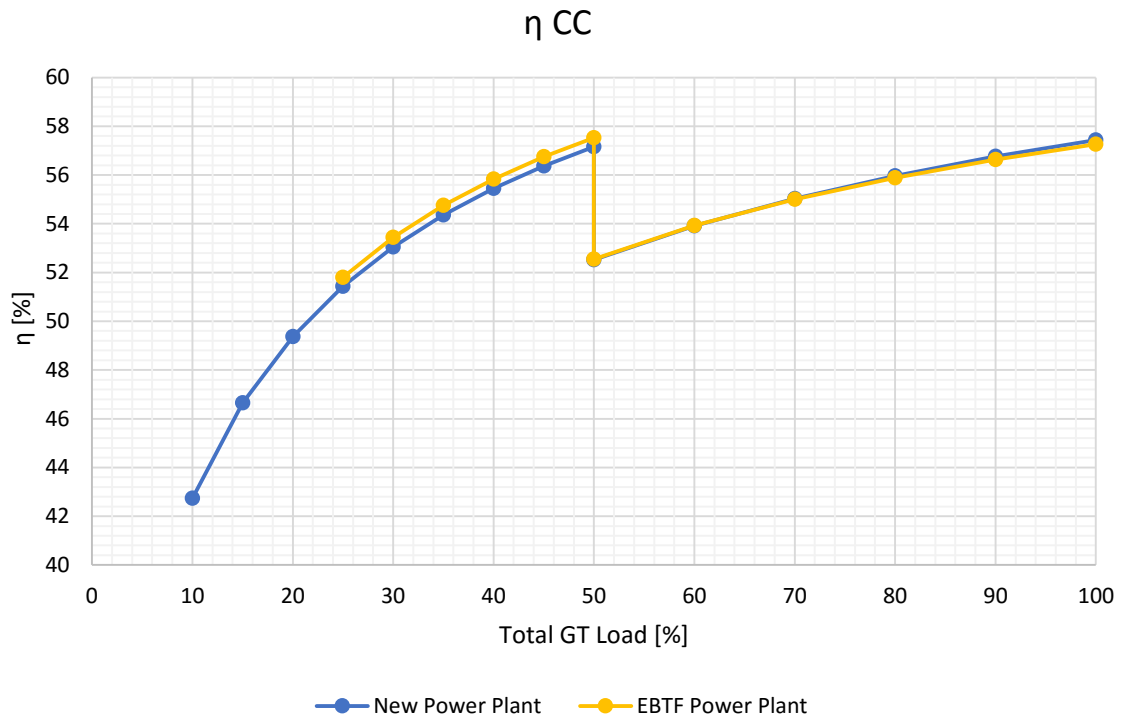


Figure 43: comparison of the η_{CC} of the two analysed plants as a function of the total load of gas turbines for the fixed ambient temperature of 15°C

In order to optimise the new cycle, an analysis of the evaporative pressures and of the intermediate temperatures in RH/SH heat exchangers has been carried out. Two parameters were observed to decide whether to change the settings or not: specific costs [\$/kW] and combined cycle efficiency. In Table 19 and Table 20 results of combined cycle efficiency and specific costs for different combinations of high and medium evaporative pressure are reported.

Table 19: Combined cycle efficiencies for different evaporative pressure combinations [bar], where red cells contain lower values and green higher ones.

MP \ HP	111	116	121	126,25	131	136	141
12	57,14368	57,14793	57,15176	57,15277	57,14889	57,14397	57,13643
17	57,26149	57,27552	57,28876	57,30427	57,31233	57,31707	57,32381
22	57,32349	57,34483	57,36619	57,37812	57,38976	57,40292	57,41053
27,18	57,31422	57,34455	57,38131	57,40046	57,41633	57,43712	57,45327
32	57,27078	57,31046	57,33573	57,36594	57,38874	57,42093	57,44134
37	57,21752	57,25172	57,28736	57,31845	57,35059	57,37437	57,39505
42	57,06553	57,11404	57,18499	57,22216	57,2562	57,28409	57,30807

Table 20: Combined cycle specific costs [€/kWe] for different evaporative pressure [bar] combinations, where green cells contain lower values and red higher ones.

MP \ HP	111	116	121	126,25	131	136	141
12	408,7983	409,1327	409,9645	411,2034	411,4244	412,1186	412,5494
17	407,0882	407,8489	408,6083	409,3409	409,9612	410,2631	411,4921
22	406,9868	407,6543	408,3324	408,2264	408,9406	409,8377	410,1085
27,18	408,009	408,6784	408,8414	408,6602	409,3187	409,9534	410,382
32	408,5202	408,5892	408,6169	409,4845	409,8023	410,4281	410,8127
37	411,3734	410,285	409,8629	409,4675	409,9974	410,7022	410,7323
42	410,6952	411,5058	410,1686	410,2183	410,5697	410,0694	410,1928

The analysis showed that, as expected, increasing pressures on the evaporators increases performances of the cycle. However, it has been decided to keep EBTF values in view of the solar integration; in fact solar collectors performances and endurance may be compromised at too high pressure levels. Besides, benefits gained by changing temperatures are not so important to justify higher costs; so pressure and temperature values were not changed, since the original values coincide with the best compromise between costs, performance and plant endurance.

3.5.3 Base Case

In order to have a realistic base plant to integrate with the solar field, it has been decided to take a nominal ambient temperature of 30°C; so the final sizing of the plant has been made for this condition. The condenser pressure has been increased according to the typical values for dry condensers (i.e. 0,1 ÷ 0,13 bar) [31]. In Table 21, the main results for the new power plant at the two different ambient temperatures are shown:

Table 21: Main results for the new plant at ambient temperatures of 15°C and 30°C.

	$T_{amb} = 15^{\circ}\text{C}$	$T_{amb} = 30^{\circ}\text{C}$
$\eta_{CC,net}$ [%]	57,434	55,985
$\dot{W}_{NGCC,net}$ [MW]	0,152	726,266
$\eta_{GT,gross}$ [%]	37,538	36,625
\dot{W}_{GT} [MW]	525,363	475,117
\dot{m}_{fuel} [kg/s]	30,092	27,892
TOT [°C]	604,165	604,165
TIT [°C]	1342,6	1341,7
χ [%]	37,538	88,659
T_{stack} [°C]	89,296	98,250
$\dot{Q}_{flue\ gases,av}$ [MW]	865,679	813,091
$\dot{Q}_{in,steam\ cycle}$ [MW]	758,790	720,875
\dot{Q}_{loss} [MW]	6,095	5,790
\dot{W}_{ST} [MW]	296,958	268,022
p_{cond} [bar]	0,048	0,1235
$\eta_{steam\ cycle}$ [%]	39,136	37,180

Since this is the reference case for the analysis of the impact of the solar integration into the CC, plant performances have been evaluated by performing simulations, modifying different parameters (ambient temperature and load). In particular, it has been highlighted that, as the nominal ambient temperature is quite high, it is necessary to regulate condenser fans at low temperature conditions to avoid reaching choking conditions at the outlet of the low pressure steam turbine. In this case, Δp from choke to condenser pressure cannot be exploited by the turbine because the volume flow cannot increase further.

The steam turbine cannot completely utilise the energy content of the steam; effects of losses due to steam velocity not converted to work, pressure drops through the exhaust hood and inefficiencies related to LP stage performance with low velocities are included in the exhaust losses [90]. These can be represented as a function of the volumetric flow at the outlet of the turbine, as shown in Figure 44. As the condenser pressure decreases, the specific volume of the expanded steam increases and so the exhaust losses increase, up to the choke conditions. Reducing the number of condenser active fans increases the condenser pressure; this slightly lowers η_{CC} but it can avoid choking and it reduces fan power consumption.

ST Group [8] - Exhaust Loss

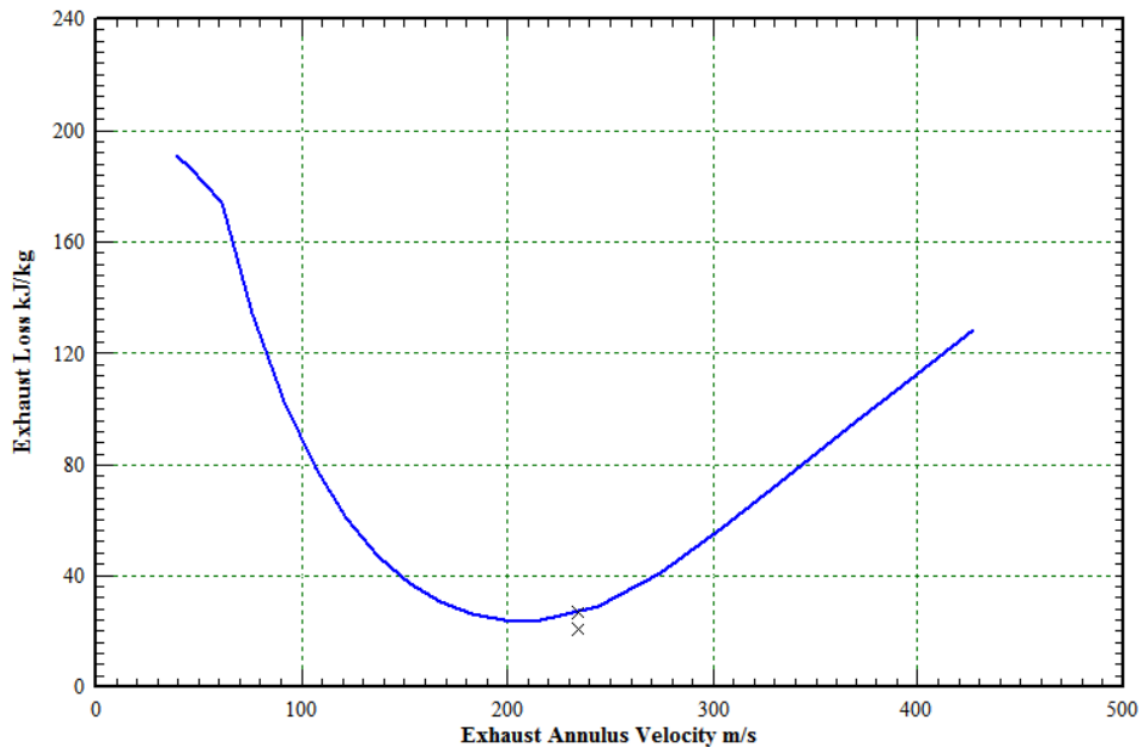


Figure 44: Trend of exhaust losses of the LP stage of the steam turbine of the reference plant at 30°C of ambient temperature and 100% of GTs load.

The ideal condition is the one that maximise the power from the ST; the optimum number of fan that maximises the ST power output is generally higher than the one that minimises exhaust losses. In this way is possible to avoid the steeper section of the curve (left side of Figure 44). The optimal fan number has been found for a discrete number of ambient temperature values; these values have been interpolated to find the optimal operating fan number for other air ambient temperatures.

To compare the reference plant with the ISCCs configurations it is necessary to estimate the performances at every condition of temperature and load.

Figure 45 shows combined cycle efficiency variations with the ambient temperature and the gas turbines load. At high temperatures, η_{CC} is lower than at nominal temperature and it decreases with the load; gas turbines exhaust flow reduces and the HRSG produces less steam, in this way both gas and steam turbines power reduces. Moreover, at partial loads, gas turbines are less efficient, affecting fuel consumption. At low temperatures, both steam and gas turbines power increases, however, the higher fuel consumptions prevails and η_{CC} slightly decreases.

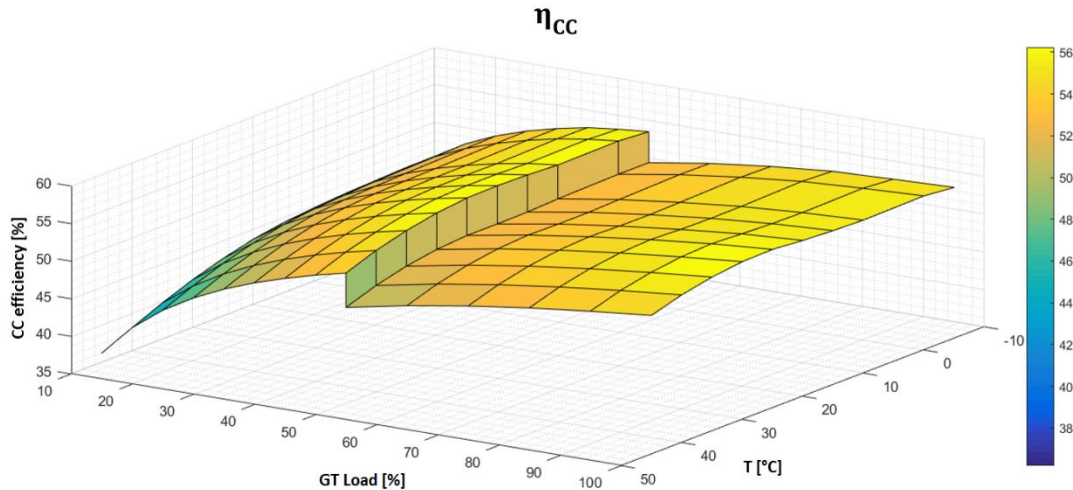


Figure 45: Combined cycle efficiency as a function of ambient temperature and GTs load.

Figure 46 shows the trend of the recovery factor as a function of load and ambient temperature. It is affected by two main parameters: TOT and steam mass flow (and, as a consequence, by pressure levels).

As the ambient temperature increases, the gas turbines exhaust flow is hotter and as the load decreases, the TOT raises up to the target value of 649°C because of the software regulation. In this way, Δ TOT between partial load and 100% load conditions is smaller for high temperatures.

Steam mass flows reduce with increasing ambient temperature and decreasing load because the exhaust gas mass flow is lower, with a consequent reduction of evaporation pressures in the HRSG drums. This results in a better recovery for increasing temperatures and decreasing loads.

At 50% load, one gas turbine and one HRSG are shut down so the others return to their 100% load conditions. However, there is one common steam turbine so the evaporation pressures keep decreasing. For low ambient temperatures, Δ TOT is higher and it prevails on the reduction of pressures with a total decrease of χ while, for high temperatures, Δ p effect prevails and the recovery factor step is towards an higher value.

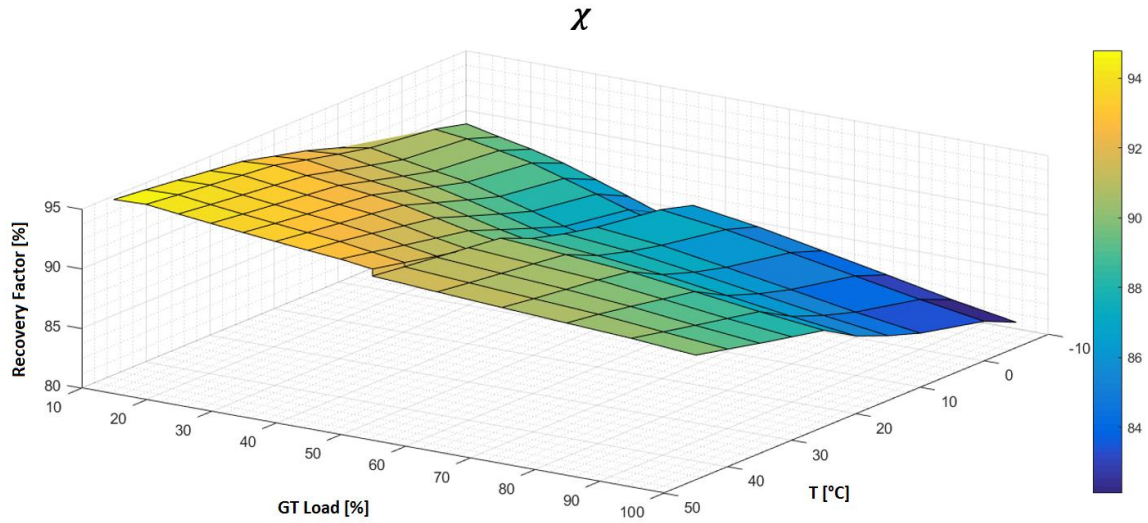


Figure 46: Recovery factor as a function of ambient temperature and GTs load.

In Figure 47, the efficiency of the steam cycle is reported, as a function of ambient temperature and load.

For high temperatures, the gas turbine is characterised by a reduced exhaust flow, so the steam production in the HRSG is limited and $\eta_{steam\ cycle}$ lowers. This effect is more evident at low loads, where the exhaust flow is even smaller.

For low temperatures, the steam turbine power is also affected by the number of operating fans in the condenser and the small variations are due to the fans adjustment.

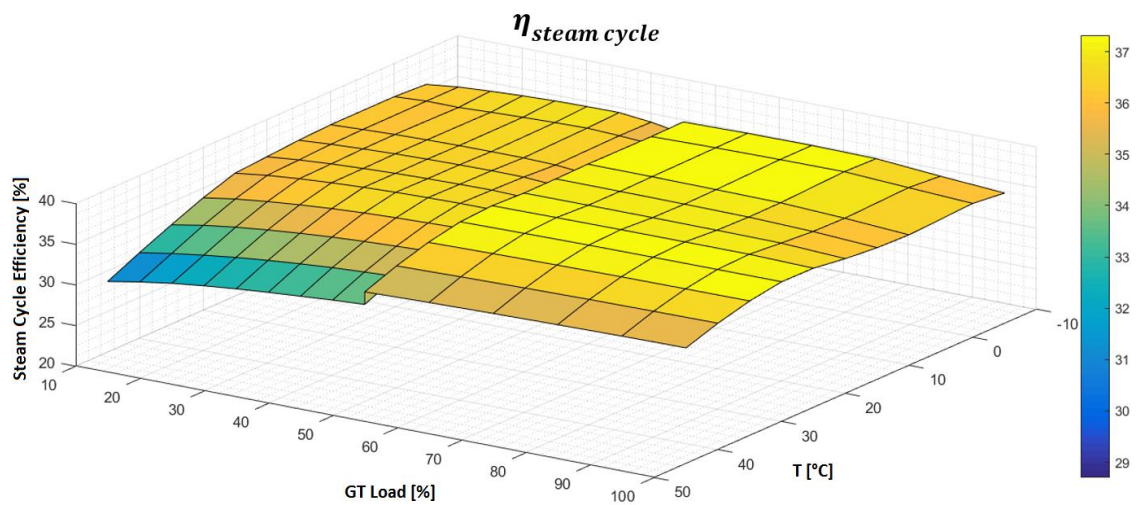


Figure 47: Steam cycle efficiency as a function of ambient temperature and GTs load.

Figure 48 represents how the HRSG efficiency varies at different load and ambient conditions. Its trend is bounded to the ones of χ and $\eta_{steam\ cycle}$, in fact lower, values are shown for high temperature and low loads and for low temperatures and high loads.

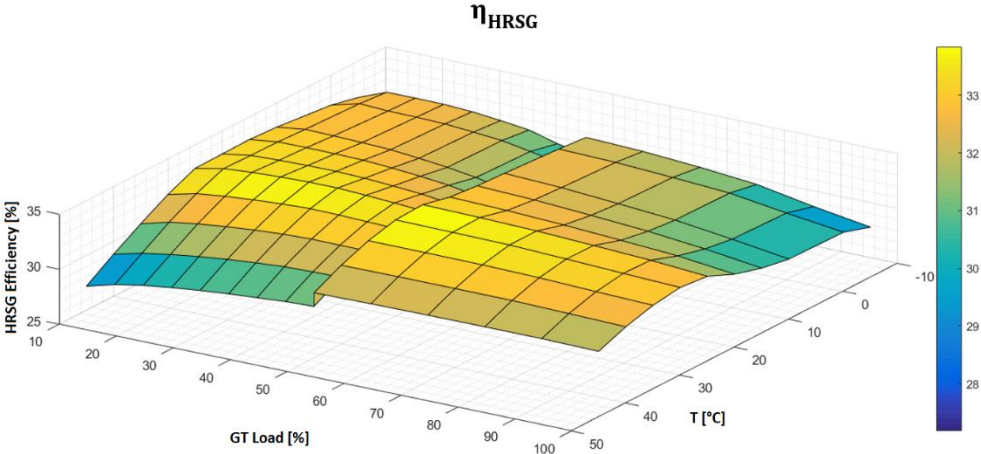


Figure 48: HRSG efficiency as a function of ambient temperature and GTs load.

Chapter 4

Solar integration

In the present work, several ISCC layouts with different solar collectors have been studied and compared in order to analyse solar integration effects on the combined cycle, in terms of nominal conditions and annual performances over a representative year. In particular, integrations on the HRSG have been evaluated as well as the use of solar steam to preheat the natural gas or to feed an absorption chiller to refrigerate the air at the gas turbine inlet. Fuel preheating and air cooling are alternative solutions which do not require high-temperature solar collector and which, with a reduced cost addition may be useful to enhance combined cycle performances.

For every case, nominal ambient conditions are the ones used for the base plant ($T_{amb}=30^{\circ}\text{C}$, $p=1,013$ bar, $\varphi=60\%$), while solar fields have been sized for a nominal DNI⁶ of 800 W/m^2 . For representative cases, the TQ diagram is reported, in order to show how, in nominal conditions, the integration affects the heat exchanged in the HRSG.

In Table 22, steam mass flow rates and pressures of the reference combined cycle are reported: they can be useful to be compared with the values after the solar integration in order to understand in which way it affects the thermodynamic behaviour of the cycle. Low pressure level is connected to the deaerator operation so, even with solar integration, it varies only slightly.

Table 22: reference CC steam mass flow rates and pressures for HP, IP, LP stages of a single HRSG and steam turbine inlet conditions.

$\dot{m}_{eva\ HP}$ [kg/s]	$\dot{m}_{eva\ IP}$ [kg/s]	$\dot{m}_{eva\ LP}$ [kg/s]	$\dot{m}_{in\ ST}$ [kg/s]	$p_{eva\ HP}$ [bar]	$p_{eva\ IP}$ [bar]	$p_{eva\ LP}$ [bar]	$p_{in\ ST}$ [bar]	$T_{in\ ST}$ [°C]
76,11	13	10,8	152,2	130,4	28,33	4,147	126,2	565

Temperature levels of high, intermediate and low pressure are, respectively, $331,1^{\circ}\text{C}$, $225,7^{\circ}\text{C}$ and $144,9^{\circ}\text{C}$. Collector choice, for every case, has been made with reference to the

⁶ Nominal DNI is considered with azimuth and zenith angles equal to 0°

thermal level of the point of integration, to select a receiver tube with appropriate thermal losses.

Figure 49 shows the T-Q diagram for a single HRSG of the reference CC, it displays the heat transfer from gases to water. The gas stack outlet temperature is equal to 98,25°C.

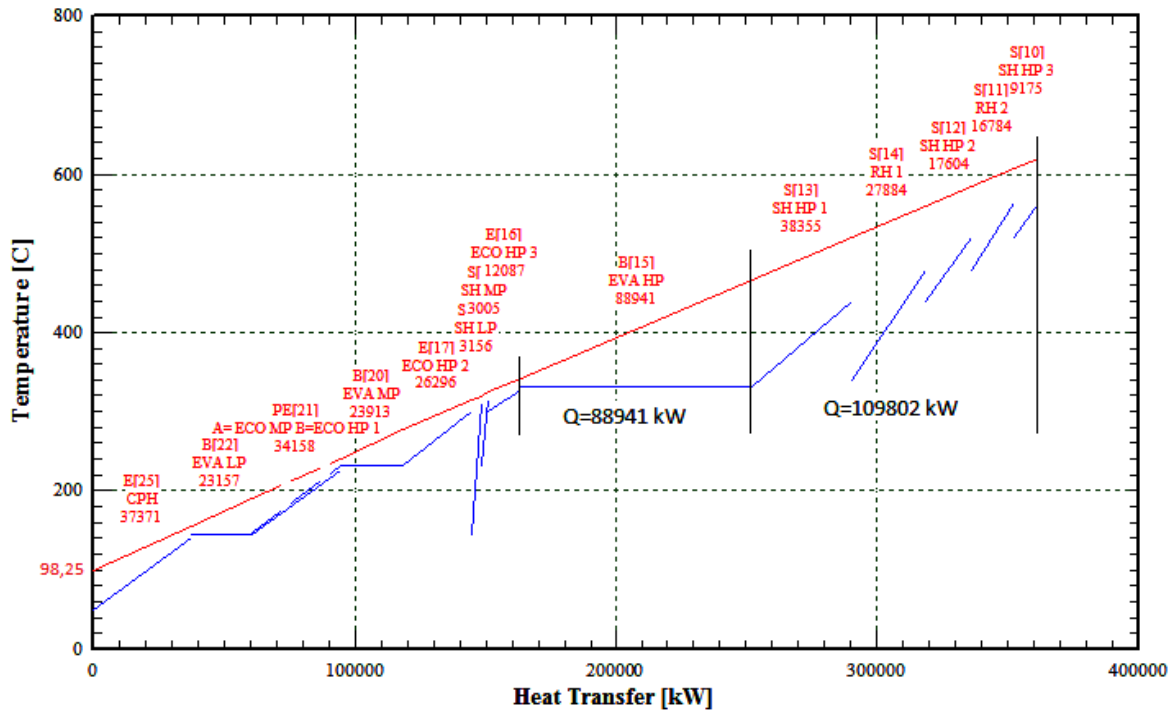


Figure 49: T-Q diagram for one HRSG of the reference combined cycle with the heat from gases for every section.

In following paragraphs, studied layouts will be discussed; Table 23 offers a review of considered integrations and collectors.

Table 23: Overview of solar integrations performed in this work.

Technology Integration	LFC	PTC	PTC + LFC
EVA HP	<i>Supernova</i> (base case) SM 1-1,5-2	<i>Eurotrough 150</i> equivalent Aperture area & land area SM1	-
EVA HP + EVA IP	<i>Supernova</i> <i>+Nova1</i> SM 1-1,5-2	<i>Eurotrough 150</i> equivalent Aperture area & land area SM1	<i>Supernova (HP) + Eurotrough 150 (IP)</i> equivalent Aperture area SM1
EVA HP +SH1	<i>Supernova</i> SM 1-1,5-2	<i>Eurotrough 150</i> equivalent Aperture area & land area SM1	-
ECO + EVA+ SH1	<i>Supernova</i> SM 1-1,5-2	<i>Eurotrough150</i> equivalent Aperture area & land area SM1	-
EVA + SH2	<i>Supernova</i> SM 1	<i>Eurotrough150I</i> equivalent Aperture area & land area SM1	-
ECO + EVA + SH2	<i>Supernova</i> SM 1	<i>Eurotrough 150</i> equivalent Aperture area & land area SM1	-
EVA IP	<i>Nova1</i> SM1	<i>Polytrough 1800</i> SM1	-
EVA HP new ST, old SHs	<i>Supernova</i> SM 1-2	-	-
EVA HP new ST, new SH3 HP	<i>Supernova</i> SM 2	-	-
EVA HP new ST, new SHs	<i>Supernova</i> SM2	-	-
Air cooling	<i>Nova1</i> SM 1	-	-
Fuel preheating	-	<i>Polytrough 1800</i> SM1	-

4.1 Solar bottoming cycle hybridisation

For the integration in the heat recovery steam generator, Fresnel and parabolic trough technologies have been compared. Direct steam generation is studied in this work because of its promising features, as discussed in paragraph 2.1, and it is employed in every configuration.

4.1.1 Fresnel integrations

At first, Fresnel integration has been studied, mainly on the high pressure level of the combined cycle. Layouts have been compared on equal solar field aperture area basis. In the next paragraphs, the different configurations will be discussed.

4.1.1.1 High Pressure Evaporator

For the first configuration, the integration of a Fresnel solar field on the high-pressure evaporator has been chosen. This choice was guided by the fact that previous studies (paragraph 1.2.3) concluded that the best way to integrate the solar fraction is the generation of high exergy steam. Figure 50 shows the disposition of plant components for this layout: the steam is withdrawn from the outlet of the last high pressure economisers (ECO HP3) of both the HRSGs and it is sent to the single solar field.

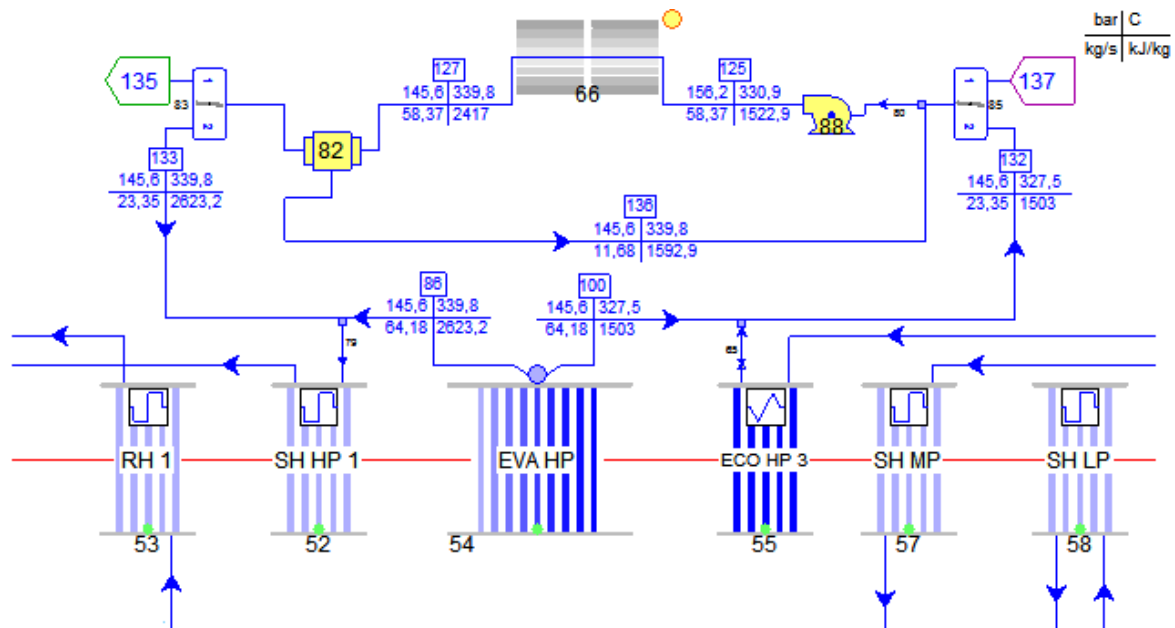


Figure 50: Layout of the integration of the solar field in the high-pressure evaporation section. Reported numbers are referred to the SM1 case.

The hot water passes through the solar field piping and it is directly heated, without the use of an intermediate heat exchanger. In order to avoid thermal stresses due to the complete evaporation, a liquid-steam mixture, with a quality of about 0.8, is produced in the solar field: this value guarantees good wettability of the solar collector, avoiding the formation of hot spots and it minimises the recirculating rate [67]. It is thus necessary to introduce a moisture separator (component 82 in Figure 50) and a recirculation of the separated saturated water.

In the reference CC, the high-pressure evaporation stage is at 130,4 bar and 331°C; such high temperature requires the implementation of evacuated solar receivers to limit the heat

loss though, normally, non-evacuated collectors can be employed for the evaporation. For this reason, Novatec's "Supernova" was selected for the solar field (paragraph 2.7.6). Table 24 shows main parameters of the collector. The operative pressure is higher than the values normally employed for this kind of collectors; this problem can be overcome by increasing the receiver tube thickness for every configuration, to withstand the particular operating conditions. This solution, at least from a theoretical point of view, does not seem to rise particular problems, since the main problem concerning the high pressure (i.e. the receiver tube resistance) is solved.

The equation employed for the heat loss estimation is [65]:

$$q'_{loss} = A1 \cdot \Delta T + A2 \cdot \Delta T^4 \left[\frac{W}{m} \right] \quad (28)$$

Where ΔT is the difference between the local receiver tube outer temperature and the ambient temperature. Coefficients A1 and A2 have been obtained by heat losses curves reported in **paragraph 2.7**.

Table 24: Supernova collector optical and geometrical parameters.

Supernova collector parameters	
Optical efficiency [%]	64,7
Receiver tube outside diameter [mm]	70
Reflector focal length [m]	7,4
Reflector aperture width [m]	12
Row pitch ⁷ [m]	20,5
Coefficient A1 in heat loss per unit length equation [W/m/K]	0,15
Coefficient A2 in heat loss per unit length equation [W/m/K ⁴]	7,5E-09

For header heat losses, a linear trend, proportional to the difference between water/steam and ambient temperatures ($T_{fluid} - T_{amb}$) was assumed as in equation (29):

$$\frac{\dot{m} \cdot q_{header}}{T_{fluid} - T_{amb}} = cost \quad (29)$$

Where q_{header} is the header (inlet or exit) heat loss in kJ/kg and \dot{m} is the mass flow throughout the header at design conditions.

Thermoflex®, starting from the thermodynamic heat balance, initialises a value of desired mass flux in receiver tubes with which it determines the number of flow paths needed and calculates the pressure drop. It has been found that a correction on this initial value was needed to obtain a reasonable pressure drop. Hence, for the evaporator, the desired mass flux

⁷ Distance between two modules centerlines.

has been set to 960 kg/s/m^2 ; this value has been calculated starting from available data of Puerto Errado II Thermosolar Power Plant, in Spain [91].

It has been chosen not to change any component of the existent plant, to avoid additional costs different from the solar field ones. To prevent steam-turbine damages due to overloading during high radiation hours, a limit on the inlet steam mass flow for the high pressure stage of the steam turbine has been set and the solar field has been sized to reach that limit in ISCC nominal conditions. The overload limit for the steam turbine has been set to the 108% of the power output of the nominal condition in the reference CC [67]; this results in an increase of the steam turbine inlet flow of the 15%. Whenever this limit would be exceeded, it is necessary to reduce the gas turbines load to reduce the steam produced.

Figure 51 shows the T-Q diagram for this plant configuration; most significant changes, with respect to the base case, are on the high pressure line but, naturally, all the cycle is affected by the integration. It can be noticed that the heat load on the high pressure evaporator decreases (of about the 19%), while the heat load on high pressure economisers and superheaters increases because of the higher mass flow. Heat loads on intermediate and low pressure evaporators and mass flows also decrease. The heat transferred inside the HRSG is slightly increased, thus the recovery factor increases (88,87% vs. 88,66% of the reference plant) and the stack temperature decreases to $96,88 \text{ }^\circ\text{C}$. As the amount of steam increases, it is not possible to reach the nominal steam turbine inlet temperature: it reduces to $539,3^\circ\text{C}$; Table 25 summarises the main thermodynamic parameters of the cycle and the percent variation from the reference CC. In the T-Q diagram, it can be enlightened that the slope of the steam curve is lower for the superheater. In addition, the introduction of the solar field causes the rise of cycle pressures.

Table 25: Steam mass flow rates and pressures for HP, IP, LP stages of a single HRSG and steam turbine inlet conditions for the high pressure evaporator integration.

	$\dot{m}_{steam SF}$ [kg/s]	$\dot{m}_{eva HP}$ [kg/s]	$\dot{m}_{eva IP}$ [kg/s]	$\dot{m}_{eva LP}$ [kg/s]	$\dot{m}_{in ST}$ [kg/s]	$p_{in SF}$ [bar]	$p_{eva HP}$ [bar]	$p_{eva IP}$ [bar]	$p_{in ST}$ [bar]	$T_{in,ST}$ [°C]
EVA HP	58,37	64,18	11,25	10,23	175	156,2	145,6	30,93	141,40	539,3
Δ [%]	-	-15,7	-13,46	-5,28	14,98	-	11,66	9,18	12,04	-4,55

Δ [%] is the parameter percent variation with respect to the reference combined cycle.

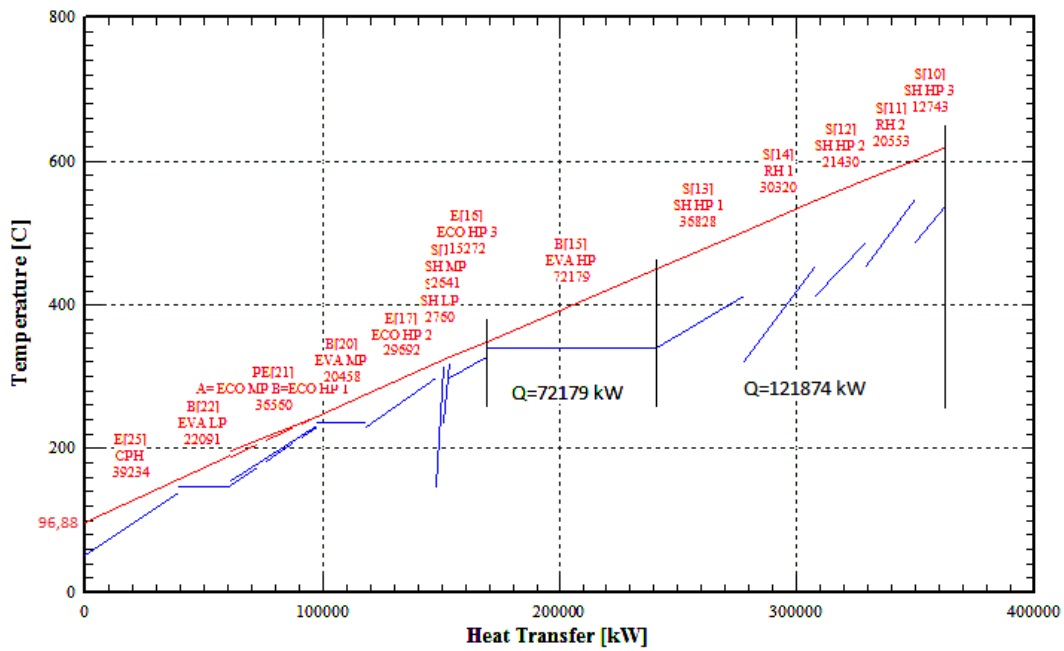


Figure 51: T-Q diagram for one HRSG for the high pressure evaporator integration with the heat from gases for every section.

For this configuration, the solar field has been also sized with different solar multiples, in particular 1,5 and 2, in order to study whether a bigger sizing of the solar field can result in better performances of the ISCC and if it can be economically convenient. Normally, for a stand-alone solar plant, the solar multiple is defined with reference to the power block as the ratio between the solar field thermal power and the power block thermal power. In this case, the definition of solar multiple is different from the one for a solar stand-alone plant: it is not defined with reference to the power block but to the aperture area (A_A) of the SM1 solar field.

$$SM = \frac{A_A}{A_{A,SM1}} \quad (30)$$

Since the SM1 solar field was sized to reach the overload limit of the steam turbine, the increased solar thermal power causes an excessive steam production, so even the nominal irradiance requires the reduction of the GTs load; for SM 1,5 GTs load is set to 81% while for SM 2 to 66%.

As a general guideline, in this work, the CC has been left unchanged to add a new analysis to the ones presented in literature (paragraph 1.2.3), where the combined cycle is generally adapted for the integration. Moreover, unchanged CC components reduce investment costs for the solar integration. However, it may be interesting to underline main changes on the cycle nominal conditions and annual performances whether some elements were redesigned. At this purpose, for the EVA HP integration, some configuration with components revamping have been studied too. In particular, steam turbine and superheaters have been

redesign, in order to admit the higher solar steam produced without reaching the overloading limit on the steam turbine and thus without the necessity of GTs load reduction. The sizing has been made keeping a mass flow produced in the solar field equal to the one of the EVA HP integration with the same solar multiple.

Steam Turbine Revamping

The steam turbine has been resized to accommodate the higher flow produced by solar integration at the same nominal pressure of the reference CC. In this way, it will not be necessary to regulate GTs load maintaining the best efficiency of the gas cycle. The steam turbine and the solar field have been sized together, maintaining the same solar steam produced in the EVA HP SM1; that means that the solar field has been sized to produce 58,37 kg/s of steam at its nominal conditions. To reduce the steam turbine inlet pressure, nozzle areas have been enlarged from 0.0109 m² to 0.014 m² and therefore steam turbine cost has increased of about 2,46 M\$. As a result, cycle pressures are lower than the ones in the previous integration while the solar field aperture area is slightly increased⁸. This resizing has been made for solar fields with solar multiple 1 and 2. Nominal values of steam mass flow, pressures and temperatures in the HRSG are displayed in Table 26 together with the percent variation of the parameter with respect to the reference combined cycle.

Table 26: Steam mass flow rates and pressures for HP, IP, LP stages of a single HRSG and steam turbine inlet conditions for the integration with a new turbine, solar multiples 1 and 2.

	$\dot{m}_{steam\ SF}$ [kg/s]	$\dot{m}_{eva\ HP}$ [kg/s]	$\dot{m}_{eva\ IP}$ [kg/s]	$\dot{m}_{eva\ LP}$ [kg/s]	$\dot{m}_{in\ ST}$ [kg/s]	$p_{in\ SF}$ [bar]	$p_{eva\ HP}$ [bar]	$p_{eva\ IP}$ [bar]	$p_{in\ ST}$ [bar]	$T_{in,ST}$ [°C]
SM 1	58,37	65,28	10,81	10,02	177,2	142,3	131,5	28,49	126,3	543
Δ [%]	-	-14,2	-16,85	-7,22	16,43	-	0,84	0,56	0,08	-3,84
SM 2	113,7	55,86	8,7	9,39	202,7	140	132,6	28,66	126,3	521
Δ [%]	-	-26,6	-33,08	-13,09	33,18	-	1,69	1,16	0,08	-7,82

Δ [%] is the parameter percent variation with respect to the reference combined cycle.

Pressures in the HRSG are similar to the ones of the base case thanks to the higher size of the steam turbine. Steam mass flows in the HRSG are lower than the nominal case, particularly for the SM2 case, because of the higher solar steam.

Steam turbine and superheaters revamping

The steam turbine revamping only does not allow reaching the nominal temperature at the inlet of the steam turbine, so two different arrangements have been tried too, the first one consists in the resizing of both the turbine and the third high pressure superheater (SH HP3) while in the second one all the heat pressure superheaters (SHs) have been. For the resized

⁸ With the pressure reduction, the latent heat needed for the evaporation of the same mass flow minimally increases, requiring a slightly bigger solar field

SHs case, nozzle areas of the steam turbine have been enlarged from 0,0109 m² to 0,0143 m² and cost has increased of about 3,11 M\$. Exchange areas of the three superheaters have also been increased to improve the superheating process, with a total enlargement of 7966 m² for each HRSG, and a cost increase of about 1,57 M\$ for the configuration with all HP SHs changed. When only the third superheater (SH3) is changed, heat exchange area increases of 3562 m² for each HRSG and the total additional cost is of 0,49 M\$. For both cases, only solar multiple 2 has been investigated because it presents the worst situation for the load reduction of gas turbines load whether the size of the turbine is not increased. Table 27 summarises main mass flows and pressure of the integrated cycle and the variation from the reference CC.

Table 27: Steam mass flow rates and pressures for HP, IP, LP stages of a single HRSG and steam turbine inlet conditions for the integration with new steam turbine and HP SH3 and the integration with new ST and all HP SHs.

	$\dot{m}_{steam SF}$ [kg/s]	$\dot{m}_{eva HP}$ [kg/s]	$\dot{m}_{eva IP}$ [kg/s]	$\dot{m}_{eva LP}$ [kg/s]	$\dot{m}_{in ST}$ [kg/s]	$p_{in SF}$ [bar]	$p_{eva HP}$ [bar]	$p_{eva IP}$ [bar]	$p_{in ST}$ [bar]	$T_{in,ST}$ [°C]
ST & SH3	113,2	55,46	8,68	9,42	201,5	138,2	130,8	28,66	126,3	565
Δ [%]	-	-27,1	-33,26	-12,81	32,39	-	0,31	1,16	0,08	0
ST & SHs	112,3	54,42	8,66	9,48	198,7	134,9	127,4	28,66	126,2	565
Δ [%]	-	-28,5	-33,36	-12,23	30,55	-	-2,30	1,16	0	0

Δ [%] is the parameter percent variation with respect to the reference combined cycle.

Figure 52 and Figure 53 show the T-Q diagrams for both the configurations. With both the modifications, the nominal temperature of the steam turbine is reached; mass flows and pressure levels are quite similar to the previous ones (i.e. new steam turbine integration). T-Q diagrams underline a better matching between water and gas lines for the second configuration (i.e. adjusted steam turbine and all HP superheaters); in fact, higher heat exchange areas allow reaching higher steam temperatures at the outlet of each exchanger, thus reducing temperature differences between the steam and flue gases streams and so irreversibilities. With the resizing of the third superheater only, instead, SH1 and SH2 areas still result undersized with respect to the higher steam mass flow with a consequent reduction of the outlet temperature with respect to the reference CC.

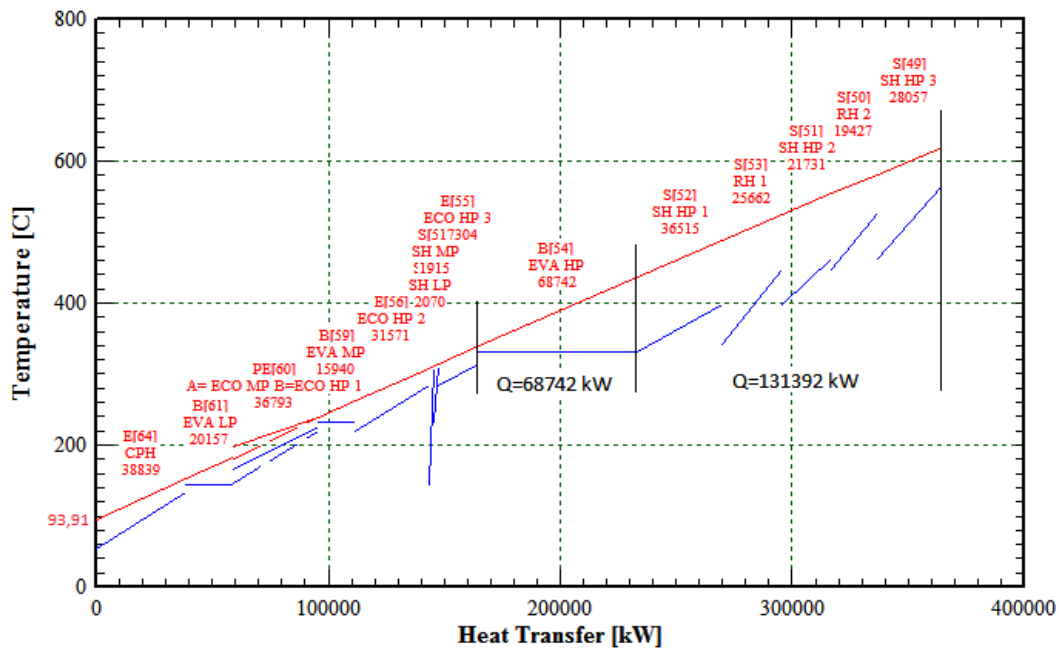


Figure 52: T-Q diagram for one HRSG for the high pressure evaporator integration with adjusted steam turbine and SH3. Heat from gases reported for every section.

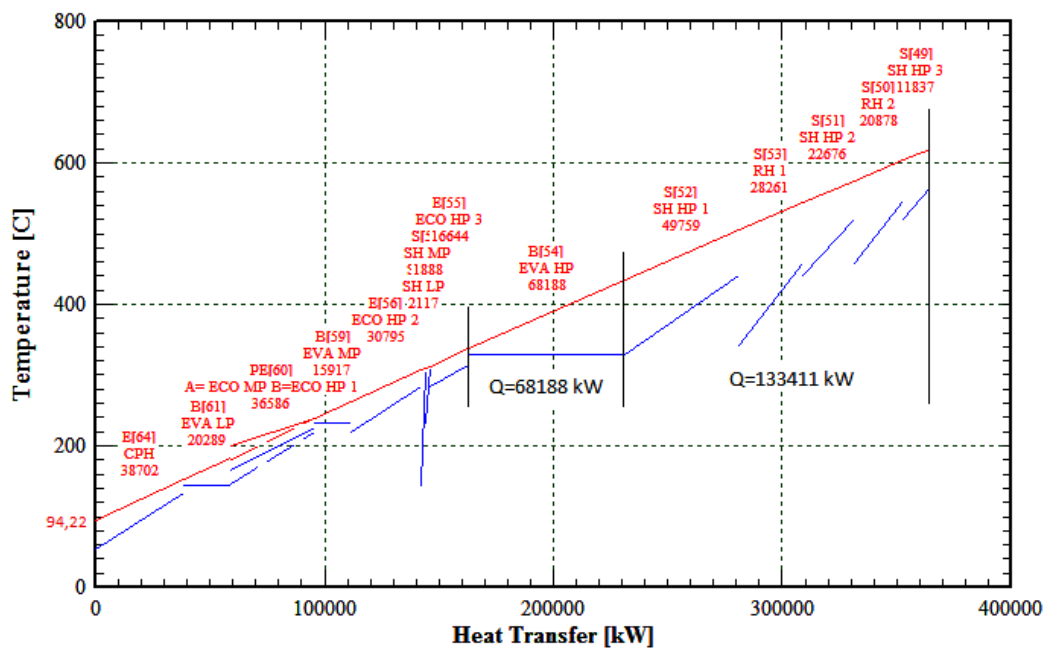


Figure 53: T-Q diagram for one HRSG for the high pressure evaporator integration with adjusted steam turbine and high pressure SHs. Heat from gases reported for every section.

After the EVA HP, other integrations on the high pressure line have been studied; these configurations (presented in following paragraphs) have been made keeping a constant aperture area (equal to the one of the high-pressure evaporator case), in order to fix a variable for the results comparison.

4.1.1.2 High Pressure Evaporator and Superheater

In this case, two LFCs solar fields are integrated in the reference combined cycle; part of the steam is evaporated and then superheated outside the HRSG, as shown in Figure 54.

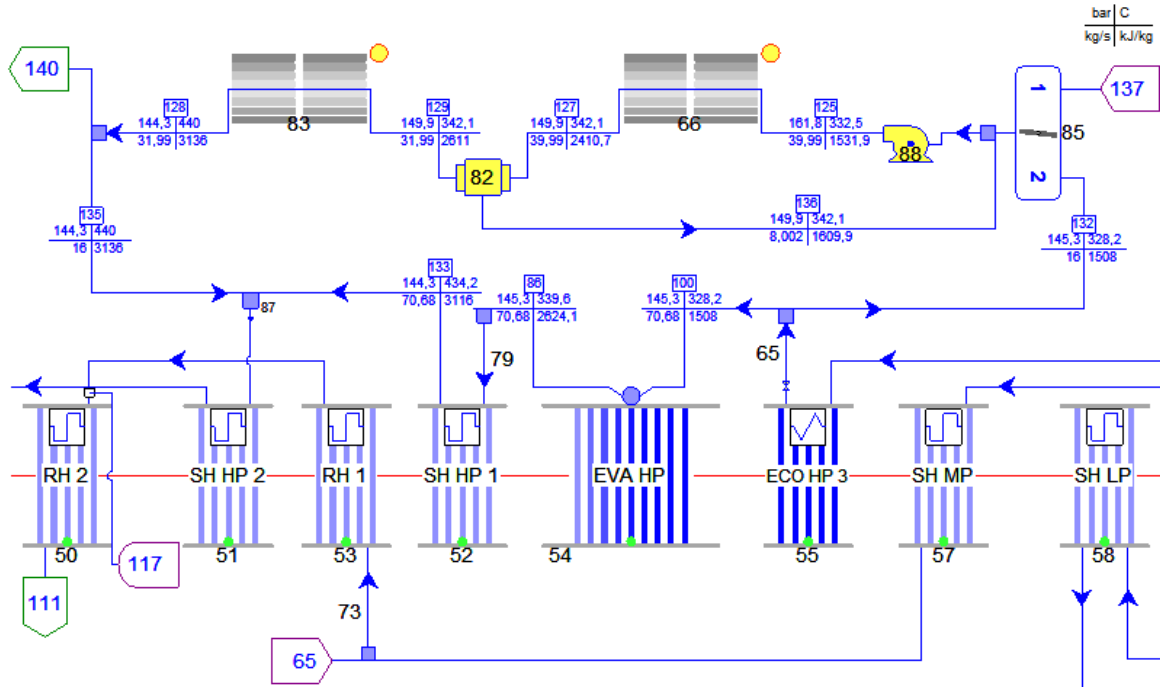


Figure 54: layout of the integration of the solar field in the high-pressure evaporation and superheating section of the combined cycle.

Even in this case, the water is taken from the third high pressure economiser (ECO HP3 in Figure 54) and it is evaporated in the solar field up to a quality of 0,8. The saturated steam ($x=1$) produced in the evaporator, once the liquid is separated, is sent to the second solar field. Only the first stage of superheating (SH HP1) is done in the solar field; the steam is sent back to the HRSG for further superheating. Because of the pressure levels in both the solar fields, Novatec's Supernova collectors are employed.

The outlet temperature of the superheater solar field is equal to 440°C: however, since the employed receiver tube is able to bare higher temperatures, up to 550°C (paragraph 2.7.6), the configuration with two stages of superheating (EVA+SH2) has been evaluated too. In that case, the solar steam is mixed with the HRSG steam before entering into the third superheating (SH3). The entire solar field has the same aperture area of the previous cases so, as it is divided differently to assure the higher superheating of the solar steam, the produced solar steam is lower (34,92 kg/s). There is a single field for the two superheating stages.

In Table 28, mass flows and pressures are shown.

Table 28: Steam mass flow rates and pressures for HP, IP, LP stages of a single HRSG and steam turbine inlet conditions for the EVA+SH integration.

	$\dot{m}_{SF,EVA}$ [kg/s]	$\dot{m}_{eva HP}$ [kg/s]	$\dot{m}_{eva IP}$ [kg/s]	$\dot{m}_{eva LP}$ [kg/s]	$\dot{m}_{in ST}$ [kg/s]	$p_{in SF}$ [bar]	$p_{eva HP}$ [bar]	$p_{eva IP}$ [bar]	$p_{in ST}$ [bar]	$T_{in,ST}$ [°C]
EVA+SH1	39,99	70,68	11,48	10,4	173,4	EVA 161,8 SH 149,9	145,3	30,85	141,2	548,7
Δ [%]	-	-7,13	-11,69	-3,70	13,93	-	11,43	8,90	11,89	-2,88
EVA+SH2	34,92	72,23	11,58	10,42	172,4	EVA 162,9 SH 150,4	145	30,79	141,2	557,3
Δ [%]	-	-5,10	-10,92	-3,52	13,27	-	11,20	8,68	11,89	-1,36

Δ [%] is the parameter percent variation with respect to the reference combined cycle.

As the total aperture area is divided, in this case, between the two solar fields, the total steam produced is smaller with respect to the EVA HP case; in fact, part of the solar heat is used to superheat the steam and so the heat available for the evaporation is reduced. It is to be noticed that the value reported in the previous table is the evaporated flow, the solar steam that is actually sent to the HRSG to finish the superheating is $\dot{m}_{steam SF,SH} = 31,99 \text{ kg/s}$. The presence of two solar fields, moreover, causes an increase of the solar evaporator inlet pressure. In the HRSG, evaporators present higher mass flows and so heat exchanged increases ($Q_{eva HP,one HRSG} = 79,2 \text{ MW}$) with respect to the EVA HP integration. Heat load on the first high pressure superheater reduces because of the smaller steam mass flow and so the outlet temperature increases.

Configurations with different solar multiples have been evaluated for the EVA+SH1: the plant produces more steam from the solar field, SM 1,5 and 2 require the reduction GT's load; respectively 85% and 70%.

4.1.1.3 High Pressure Economiser, Evaporator and Superheater

For this configuration, two solar fields have been used again (Figure 55); in the first one, water from the second high-pressure economiser (ECO HP2) is heated up to the saturation temperature and evaporated to the quality of 0,8. After the liquid removal, the first stage of superheating takes place in the second solar field. The integration with two high pressure superheating stages (ECO+EVA+SH2) has been evaluated too.

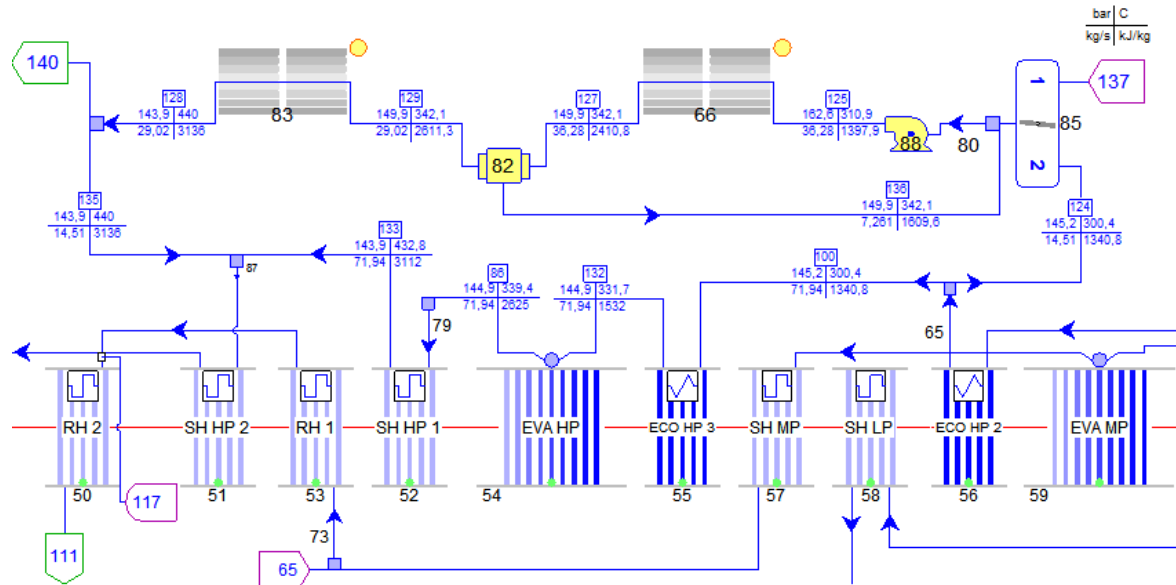


Figure 55: layout of the integration of the solar field in the high-pressure economiser, evaporation and superheating section of the combined cycle.

Table 29 shows steam mass flows and pressures, the trend is the same as the EVA+SH integration, the solar steam produced is further reduced with respect to the EVA HP configuration because of the economisation process at the inlet of the first solar field. Thus, heat loads on evaporators increase from previous integrations (remaining smaller than the ones of the reference case). The parameters percent variation with reference to the reference CC is also reported.

Table 29: Steam mass flow rates and pressures for HP, IP, LP stages of a single HRSG and steam turbine inlet conditions for the ECO+EVA+SH1 integration.

	$\dot{m}_{SF,EVA}$ [kg/s]	$\dot{m}_{eva HP}$ [kg/s]	$\dot{m}_{eva IP}$ [kg/s]	$\dot{m}_{eva LP}$ [kg/s]	$\dot{m}_{in ST}$ [kg/s]	$p_{in SF}$ [bar]	$p_{eva HP}$ [bar]	$p_{eva IP}$ [bar]	$p_{in ST}$ [bar]	$T_{in,ST}$ [°C]
ECO+EVA+SH1	36,28	71,94	11,75	10,4	172,9	ECO 162,6 SH1 149,9	144,9	30,87	140,8	550,3
Δ [%]	-	-5,48	-9,615	-3,70	13,60	-	11,12	8,97	11,57	-2,60
ECO+EVA+SH2	26,92	73,67	12	10,48	168,9	ECO 162 SH1 147,6	142,4	30,42	138,5	557,9
Δ [%]	-	-3,21	-7,692	-2,96	10,97	-	9,20	7,38	9,75	-1,26

Δ [%] is the parameter percent variation with respect to the reference combined cycle.

In this case, steam produced in the HP solar field is lower than in the previous cases, as the aperture area is divided between medium and high pressures. With respect to the other integrations, pressures in the cycle are higher but intermediate temperature (about 230°C) value allows using Novatec's Nova1 solar collector, which can bear temperatures up to 250°C (see paragraph 2.7.6). With this collector, nominal conditions do not vary a lot from Supernova ones, the main differences are related to higher heat loss since this collector is not equipped with the vacuum cavity. Table 31 summarises main collector parameters. Annual performances may be slightly different from the Supernova collector because of the different IAM coefficient⁹.

Table 31: Nova1 collector optical and geometrical parameters.

Nova1 collector parameters	
Optical efficiency [%]	64,7
Receiver tube outside diameter [mm]	70
Reflector focal length [m]	7,4
Reflector aperture width [m]	12
Row pitch [m]	20,5
Coefficient A1 in heat loss per unit length equation [W/m/K]	1,06
Coefficient A2 in heat loss per unit length equation [W/m/K ⁴]	1,2E-08

4.1.1.5 Intermediate Pressure Evaporator

The last Fresnel integration in the bottoming cycle in this work is the integration on the intermediate pressure evaporator; Nova1 collector is still employed for the same reasons explained in paragraph 4.1.1.4. Figure 57 sketches the layout of the integration, where the solar field has the same aperture area of the EVA HP case.

⁹ Nova1, since the receiver tube has no vacuum gap, is equipped with a glass plate under the secondary receiver, in order to reduce convective thermal losses. Therefore, collector performances are different from the ones of Supernova collector.

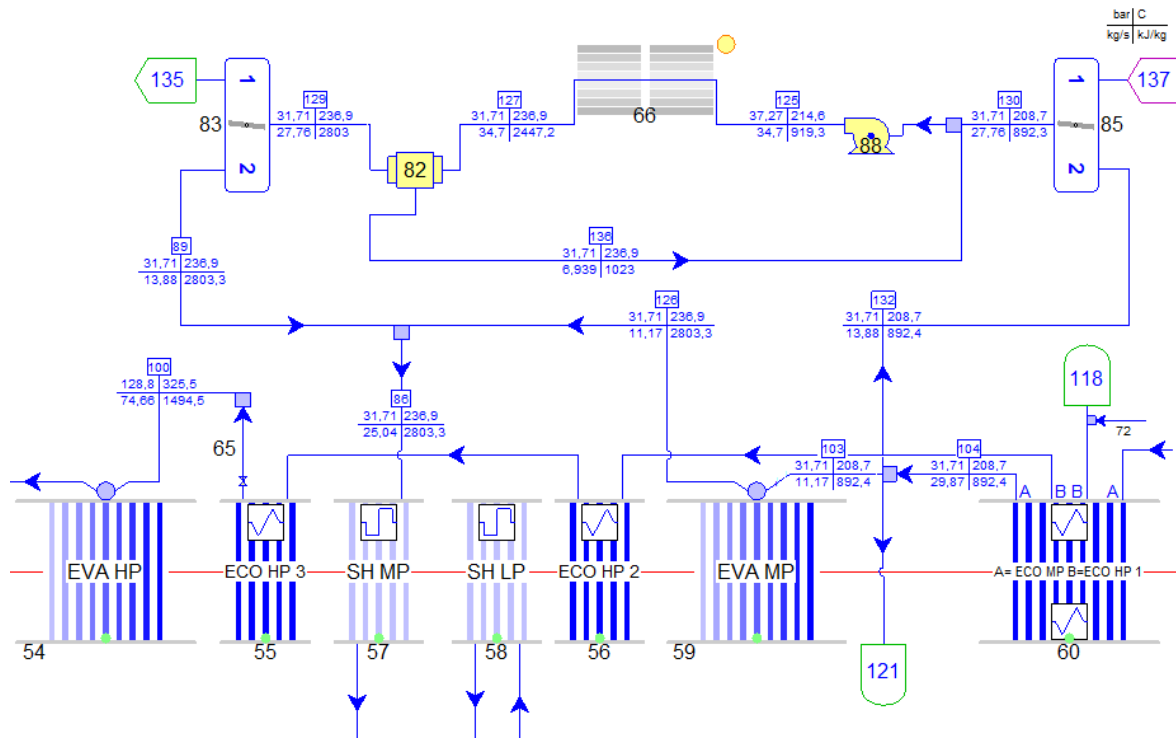


Figure 57: Layout of the integration of the solar field in the intermediate pressure evaporator of the combined cycle.

In Table 32, thermodynamic results of the integration are reported. The solar steam produced is lower, with respect to the EVA HP integration, because the evaporation heat is higher. Besides, heat losses are higher because of the lack of the vacuum gap around the receiver tube.

Table 32: Steam mass flow rates and pressures for HP, IP, LP stages of a single HRSG and steam turbine inlet conditions for the EVA IP integration.

	\dot{m}_{SF} [kg/s]	$\dot{m}_{eva\ HP}$ [kg/s]	$\dot{m}_{eva\ IP}$ [kg/s]	$\dot{m}_{eva\ LP}$ [kg/s]	$\dot{m}_{in\ ST}$ [kg/s]	$p_{in\ SF}$ [bar]	$p_{eva\ HP}$ [bar]	$p_{eva\ IP}$ [bar]	$p_{in\ ST}$ [bar]	$T_{in,ST}$ [°C]
EVA IP	34,58	74,67	11,17	10,67	HP 149,3 MP 195,6	34,58	74,67	31,7	HP 124,8 IP 30,21	565
$\Delta[\%]$	-	-1,89	-14,08	-1,20	HP -1,91 IP 12,09	-	-42,74	11,90	HP -1,11 IP 11,19	0

$\Delta[\%]$ is the parameter percent variation with respect to the reference combined cycle.

4.1.2 Fresnel integrations performance parameters in design conditions

In Table 33, main results for the Fresnel integration configurations are shown. Some parameters have been evaluated, in order to compare the different solutions, in particular:

- $Solar\ Power = Net\ Power_{ISCC} - Net\ Power_{CC}$
- $\eta_{sc} = \frac{ST\ Power}{\dot{Q}_{HRSG} + \dot{Q}_{sf, TOT}}$, steam cycle efficiency;
- $\eta_{incr, th-el} = \frac{Solar\ Power}{\dot{Q}_{sf, tot}}$, net incremental thermal to electricity efficiency;
- $\eta_{incr, sol-el} = \frac{Solar\ Power}{A_{ADNI}}$, net incremental solar to electricity efficiency;
- $x_{sf} = \frac{\dot{Q}_{sf}}{\dot{Q}_{sf} + \dot{m}LHV}$, solar share;
- $F_{sf} = \frac{Solar\ Power}{Net\ Power}$, solar fraction.

Incremental efficiencies are useful to evaluate which is the direct consequence of the integration of the solar field in the combined cycle.

Table 33: Results for Fresnel integration configurations.

	CC base	EVA HP	EVA+SH1	EVA+SH2	ECO+EVA+SH1	ECO+EVA+SH2	EVA HP+IP	EVA IP	new ST SM1	new ST SM2	new ST+SH3 SM2	new ST+Sh all SM2
Net Power [MW]	726,27	746,91	747,85	748,36	747,68	744,73	745,67	741,33	747,27	766,60	769,82	771,30
ST Power [MW]	268,02	289,84	290,82	291,32	290,61	287,46	288,38	283,37	289,89	309,90	313,46	315,22
Solar Power [MW]	-	20,64	21,58	22,10	21,41	18,46	19,41	15,07	21,00	40,33	43,56	45,03
\dot{Q}_{sf} EVA HP [MW]	-	52,19	35,15	30,60	-	-	38,17	-	55,68	111,45	111,68	111,98
\dot{Q}_{sf} EVA IP [MW]	-	-	-	-	-	-	14,11	53,02	-	-	-	-
\dot{Q}_{sf} SH HP [MW]	-	-	16,78	21,02	15,24	16,11	-	-	-	-	-	-
\dot{Q}_{sf} EVA+ECO HP [MW]	-	-	-	-	36,75	27,38	-	-	-	-	-	-
\dot{Q}_{sf} TOT [MW]	-	52,19	51,93	51,62	51,99	43,49	52,28	53,02	55,68	111,45	111,68	111,98
Aperture area tot [m^2]	-	109224	109256	109242	109231	109157	109247	109176	116328	232655	233086	233627
\dot{Q}_{HRSG} [MW]	720,87	722,62	722,45	722,35	722,50	722,15	722,64	722,38	724,08	726,58	726,53	726,16
χ [%]	88,66	88,87	88,85	88,84	88,86	88,82	88,88	88,84	89,05	89,36	89,35	89,31
η_{sc} [%]	37,18	37,41	37,55	37,64	37,52	37,55	37,21	36,55	37,18	36,98	37,40	37,61
T stack [°C]	98,25	96,89	97,03	97,10	97,03	97,26	96,88	97,08	95,77	93,85	93,91	94,22
$\eta_{incr,th-el}$ [%]	-	39,55	41,56	42,81	41,18	42,46	37,12	28,42	37,72	36,19	39,00	40,22
$\eta_{incr,sol-el}$ [%]	-	23,62	24,69	25,29	24,50	21,14	22,20	17,25	22,57	21,67	23,36	24,09
α_{sf} [%]	-	3,87	3,85	3,83	3,85	3,24	3,87	3,93	4,11	7,91	7,92	7,94
F_{sf} [%]	-	2,76	2,89	2,95	2,86	2,48	2,60	2,03	2,81	5,26	5,66	5,84

The solar integration increases the net power output of the combined cycle without the necessity to increase fuel consumption. The total increased power is of about 20 MW for the SM1 configurations. In accordance with the definition of solar multiple employed, solar integration with SM2 has about twice the solar thermal power and, consequently, about twice the power increase. However, the benefit from the SM2 integration is valuable only for the cases with revamped steam turbine and heat exchangers, otherwise the power reduction of the gas turbine would prevail on the integration benefit.

$\eta_{incr,sol-el}$ is not particularly significant to be compare between the different integrations, because integrated solar fields have the same aperture area. However, they can be compared with the overall efficiency of stand-alone solar power plants; for Fresnel DSG collector producing saturated steam in a solar only plant is about the 19% [67] while, for the ISCC with saturated solar steam (EVA HP), the resulted $\eta_{incr,sol-el}$ is about the 23,6% and it reaches the 24,5% for EVA+SH1. Thus, the integration of the solar production into the combined cycle increases the conversion efficiency of the solar thermal power.

The steam cycle efficiency (η_{sc}) results slightly higher for integrated cycles; the variation from the reference case is not very high because of the reduced solar fraction integrated. In particular, η_{sc} is higher for the integrations with evaporator and superheaters (EVA+SH1 and EVA+SH2) integrations, which also have the best $\eta_{incr,th-el}$. This is because, as the average temperature at which the heat is introduced in the cycle increases, the integration results as more efficient. The solar power is evaluated as the difference between the net cycle power and the net power of the reference CC; in this way, it accounts not only for the additional heat introduced in the cycle by the solar field but also for the fossil fraction converted with a higher efficiency. For the integrations without changings of the existing combined cycle, the solar integrated fraction results quite small; this fact is related to the maximum mass flow limit on the steam turbine. With the same mass flow, the steam turbine resizing causes a higher sizing of the solar field, with a consequent increase of the solar share; in this way, the highest HRSG efficiency value and the consequent lowest stack temperature of the SM1 configurations are achieved.

Between the three integrations with the resized steam turbine at SM2, the most efficient one is the one with the resizing of all the high pressure super heaters. This is because, when the plant operates at its nominal conditions, the temperature matching in the gas turbine exhaust heat recovery process in the HRSG is improved.

Net electric combined cycle efficiency is not reported in the following table since, for a ISCC, the definition of this parameter is not univocal, it can be defined either as:

$$\eta_{ISCC} = \frac{Net\ Power_{ISCC}}{\dot{Q}_{sf} + \dot{m} \cdot LHV} \quad (31)$$

Or as:

$$\eta_{ISCC} = \frac{Net\ Power_{ISCC}}{\dot{m} \cdot LHV} \quad (32)$$

In the first case (Equation (31)), which is the one considered in the large part of the ISCC bibliography, \dot{Q}_{sf} is compared to the fuel heat input, even if they are energetically different. Q_{sf} is the net heat absorbed by field while the fuel heat input is nearly equal to the fuel exergy.

In the second definition (Equation (32)), coherent values are compared but, with every integration, η_{CC} is higher because the fuel flow is the same and net power increases. So it is not significant to compare net electric efficiency of ISCCs with the one of the CC and, for ISCCs only, the trend is the same as the one of incremental efficiencies: integrations with the highest average temperature at which the heat is introduced in the cycle have the higher net efficiency.

4.1.3 Parabolic troughs integrations

In order to compare the Fresnel integration with an equivalent one, the Parabolic trough technology has been used to perform the same integrations previously explained. Temperature levels in the HRSG allow using both Fresnel and Parabolic technologies; CSP industry is not yet came to the definition of which technology has best performances with DSG, especially because DSG is a less mature technology than indirect generation. Despite higher investment costs for the solar field, the higher efficiency of parabolic trough may result in a more efficient integration. In fact, not only the optical efficiency at peak condition is higher for parabolic collectors, but in off-design conditions, the difference is further remarked because of the incidence of the transversal angle (θ_{\perp}) on Fresnel systems (paragraph 2.6.2). However, off-design performances will be better discussed in Chapter 5.

For each plant layout, the equivalent Parabolic trough one has been evaluated; in particular, as several comparisons can be make, it has been chosen to perform the integration with equal aperture area, land area and produced steam mass flow with respect to the same layout in the Fresnel.

With the same aperture area, parabolic troughs have a higher reflective area, allowing a higher solar steam production. With equivalent land area, steam production is lower than in Frenels cases because parabolic collectors require a larger area and they need more space between two mirrors. So, when the land area is fixed, total aperture area is lower for parabolic troughs than for Fresnel collectors. Equivalent land area cases can be useful for the comparison with the Fresnel cases whenever the available land for the solar field would be fixed and it would imply lower investment costs for the solar field. For each case, whether necessary, the GT

The reference plant has pressure levels that can result too high for a real integration with a DSG Parabolic trough, because of problems related to the mobility of the receiver tube (see Chapter 2). However, the integration has been performed to have comparable results with the Fresnel integration, in terms of performances and costs.

As Fresnel collectors can better withstand high-pressure conditions, it has also been decided to implement the EVA HP+IP integration with the Fresnel collector on the high pressure solar field and the parabolic trough collector on the intermediate pressure solar field. As the intermediate pressure solar field is small, the integration has been performed with the parabolic field at the same aperture area of the Fresnel medium pressure field without the necessity to reduce the GTs load. In this case, inlet conditions of both the high pressure and intermedium pressure stage of the steam turbine have been controlled to avoid overloading.

The collector chosen for the PT integration is the Eurotrough 150 with the Schott PTR70-DSG receiver tube [92], Table 34 summarises main collector parameters. The mass flux needs to be lower than the one of the Fresnel, in order to maintain a reasonable value of the overall distributed pressure drop. In this case, the initialised value is equal to 592 kg/s/m² [93]; in fact, since the concentration ratio is lower for PTCs than for LFC (see paragraph 2.5), longer collector rows are need for the parabolic field. Reducing the mass flux increases the number of rows per field and reduces the flow velocity and thus the distributed pressure drop along the receiver. According to the smaller mass flux per row path, distributed pressure drops in the solar field are lower for parabolic troughs than for Fresnel. However, concentrated pressure drops are higher because of the mobile structure of the receiver and the presence of expansion joints. Concentrated pressure drops are evaluated, as [94]:

$$\Delta p = 26,07\rho \frac{v^2}{2} \quad (33)$$

Table 34: Eurotrough 150+ Schott PTR70-DSG collector optical and geometrical parameters.

Eurotrough 150 collector parameters	
Optical efficiency [%]	75
Receiver tube outside diameter [mm]	70
Aperture width [m]	5,77
Collector focal length [m]	1,71
Row Pitch [m]	14,43
Coefficient A1 in heat loss per unit length equation [W/m/K]	0,2082
Coefficient A2 in heat loss per unit length equation [W/m/K ⁴]	7,21E-09

For the EVA IP integration, it has been chosen to use another collector, in particular Nep Solar's Polytrough 1800 (see paragraph 2.7.5), whose principal features are reported in Table 35. This collector is less expensive than the Eurotrough II since the receiver tube has no

vacuum conditions and the structure is smaller and lighter but it has poorer performances in terms of thermal losses and optical efficiency.

Table 35: Polytrough 1800 collector optical and geometrical parameters.

Polytrough 1800 collector parameters	
Optical efficiency [%]	68,65
Receiver tube outside diameter [mm]	34
Aperture width [m]	1,8
Collector focal length [m]	0,65
Coefficient A1 in heat loss per unit length equation [W/m/K]	0,673
Coefficient A2 in heat loss per unit length equation [W/m/K ⁴]	2,77E-8

Table 36 and Table 37 display steam mass flows and pressure for one HRSG (the other HRSG is characterised by the same pressure levels and flows) on the integrated cycle for each parabolic trough configuration, except the one with both Fresnel and PT. In the table, where Δ [%] is the percent variation with respect to the reference combined cycle.

Table 36: Steam mass flow rates and pressures for HP, IP, LP stages of a single HRSG and steam turbine inlet conditions for the integration Parabolic trough collectors with Aperture area equal to the corresponding Fresnel case.

	$\dot{m}_{SF,EVA}$ [kg/s]	$\dot{m}_{eva HP}$ [kg/s]	$\dot{m}_{eva IP}$ [kg/s]	$\dot{m}_{eva LP}$ [kg/s]	$\dot{m}_{in ST}$ [kg/s]	$p_{in SF}$ [bar]	$p_{eva HP}$ [bar]	$p_{eva IP}$ [bar]	$p_{in ST}$ [bar]	$T_{in,ST}$ [°C]
EVA HP	65,87	61,33	10,64	10	175,3	156,4	145,6	30,76	141,2	537,8
Δ [%]	-	-19,42	-18,15	-7,41	15,18	-	11,66	8,58	11,89	-4,81
EVA+SH1	45,36	69,3	11,28	10,33	174,9	EVA 163,4 SH 151,3	146	30,96	142	547,5
Δ [%]	-	-8,95	-13,23	-4,35	14,91	-	11,96	9,28	12,52	-3,10
EVA+SH2	39,7	71,64	11,38	10,37	175	EVA 165,9 SH 153,2	146,8	31,11	143	555,7
Δ [%]	-	-5,87	-12,46	-3,98	14,98	-	12,58	9,81	13,31	-1,65
ECO+EVA+SH1	41,17	70,72	11,6	10,33	174,4	ECO 163,9 SH 150,9	145,7	30,98	141,6	547,2
Δ [%]	-	-7,08	-10,77	-4,35	14,59	-	11,73	9,35	12,20	-3,15
ECO+EVA+SH2	36,42	72,78	11,65	10,38	174,7	ECO 167,7 SH 152,9	146,5	31,13	142,7	555
Δ [%]	-	-4,38	-10,38	-3,89	14,78	-	12,35	9,88	13,07	-1,77
EVA HP+IP	HP 48,08 IP 11,15	65,9	10,99	10,22	HP 170,3 IP 197	HP 155,7 IP 37,35	142,7	31,56	HP 138,3 IP 30,29	544,2
Δ [%]	-	-13,41	-15,46	-5,37	HP 11,89 IP 12,89	-	9,43	11,40	HP 9,98 IP 11,48	-3,68
EVA IP	32,62	74,75	11,26	10,66	HP 149,5 IP 194,4	37,48	129	31,50	HP 124,9 IP 30,03	565
Δ [%]	-	-1,79	-13,38	-1,30	HP -2,7 IP 11,4	-	-1,07	11,19	HP -1,03 IP 10,53	0
EVA HP LFC+EVA IP PTC	HP 42,23 IP 11,13	67,08	11,16	10,28	HP 167,9 IP 195,1	HP 153,6 IP 37,1	141,2	31,3	HP 136,8 IP 30,03	546,9
Δ [%]	-	-11,86	-14,15	-5,08	HP 10,31 IP 11,81	-	8,28	10,48	HP 8,4 IP 10,53	-3,2

Table 37: Steam mass flow rates and pressures for HP, IP, LP stages of a single HRSG and steam turbine inlet conditions for the integration Parabolic trough collectors with Land area equal to the corresponding Fresnel case.

	$\dot{m}_{SF,EVA}$ [kg/s]	$\dot{m}_{eva HP}$ [kg/s]	$\dot{m}_{eva IP}$ [kg/s]	$\dot{m}_{eva LP}$ [kg/s]	$\dot{m}_{in ST}$ [kg/s]	$p_{in SF}$ [bar]	$p_{eva HP}$ [bar]	$p_{eva IP}$ [bar]	$p_{in ST}$ [bar]	$T_{in,ST}$ [°C]
EVA HP	46,21	66,64	11,63	10,45	170,2	155,3	142,6	30,39	138,2	545
Δ [%]	-	-12,44	-10,54	-3,24	11,83	-	9,36	7,27	9,51	-3,54
EVA+SH1	32,14	71,72	11,78	10,48	169,1	EVA 161,6 SH 147,4	142,3	30,35	138,2	553,2
Δ [%]	-	-5,77	-9,38	-2,96	11,10	-	9,13	7,13	9,51	-2,09
EVA+SH2	28,01	72,96	11,86	10,49	168,3	EVA 162,8 SH 148,2	142	30,3	138,1	558,3
Δ [%]	-	-4,14	-8,77	-2,87	10,58	-	8,90	6,95	9,43	-1,19
ECO+EVA+SH1	29,16	72,72	12	4,325	168,8	ECO 162 SH 147,1	142,1	30,36	137,9	553,1
Δ [%]	-	-4,45	-7,69	-59,95	10,91	-	8,97	7,17	9,27	-2,11
ECO+EVA+SH2	25,68	73,75	12,05	10,5	168	ECO 164,1 SH 147,9	141,8	30,31	137,9	557,8
Δ [%]	-	-3,10	-7,31	-2,78	10,38	-	8,74	6,99	9,27	-1,27
EVA HP+IP	HP 33,61 IP 8,347	68,92	11,56	10,39	HP 164,7 IP 190,6	HP 153,3 IP 36,33	139,1	30,65	HP 134,7 IP 29,41	550,8
Δ [%]	-	-9,45	-11,08	-3,80	HP 8,21 IP 9,23	-	6,67	8,19	HP 6,74 IP 8,24	-2,51

Δ [%] is the parameter percent variation with respect to the reference combined cycle.

With the same aperture area of the Fresnel cases, as the reflective area of the PT collector area is higher, the solar steam produced increases, it is thus necessary to reduce gas turbines load even with SM1 nominal conditions to respect the steam turbine inlet restraint. In particular, for the EVA HP integration, GT load in nominal conditions is equal to 96% while for EVA+SH and ECO+EVA+SH it is 99%. The two integration with SH2 do not require GTs load reduction at nominal conditions because the solar steam mass flow produced is lower.

With a land area equal to the Fresnel case, naturally, the PT solar field produces less steam because of the highest size of the collectors. It is not necessary to reduce gas turbine load and pressure levels in the HRSG are lower than the previous case.

The total mass flow circulating in the superheating section is higher for the parabolic trough integration and, therefore, the steam turbine inlet temperature results reduced.

Results for the integration with the same solar steam produced as in the equivalent Fresnel layout are not reported since they are totally equal to Fresnel ones, with the exception of solar field inlet pressures.

Table 38 displays main cycle results for the parabolic configurations with equivalent Aperture and Land areas.

Table 38: Results for Parabolic integration configurations.

	Equivalent Land area										Equivalent Aperture Area (*)					
	CC base	EVA HP	EVA+SH1	EVA+SH2	ECO+EVA+SH1	ECO+EVA+SH2	EVA HP+IP	EVA HP	EVA+SH1	EVA+SH2	ECO+EVA+SH1	ECO+EVA+SH2	EVA HP+IP	EVA IP	EVA HP LFC+ EVA IP PTC	
Net Power [MW]	726,27	742,84	743,67	743,88	743,49	743,77	742,14	727,26	743,71	751,03	743,35	750,85	748,30	740,42	746,32	
ST Power [MW]	268,02	285,55	286,38	286,62	286,20	286,43	284,39	288,35	291,29	294,19	291,09	293,98	291,12	282,44	289,02	
Solar Power [MW]	-	16,57	17,40	17,62	17,23	17,51	15,87	23,72	24,24	31,57	23,89	24,58	22,03	14,15	20,06	
\dot{Q}_{sf} EVA HP [MW]	-	41,59	28,45	24,71	-	-	30,52	59,21	39,77	34,51	-	-	43,29	-	38,17	
\dot{Q}_{sf} EVA IP [MW]	-	-	-	-	-	-	12,26	-	-	-	-	-	16,37	49,74	16,37	
\dot{Q}_{sf} SH HP [MW]	-	-	13,26	16,49	12,03	15,12	-	-	18,94	23,59	17,17	21,65	-	-	-	
\dot{Q}_{sf} EVA+ECO HP [MW]	-	-	-	-	29,69	26,09	-	-	-	-	41,64	36,59	-	-	-	
\dot{Q}_{sf} TOT [MW]	-	41,59	41,71	41,19	41,72	41,21	42,78	59,21	58,71	58,10	58,81	58,24	59,66	49,74	54,54	
Aperture area tot [m^2]	-	76740	77598	77428	77487	77271	76800	109240	109253	109230	109237	109232	109241	109131	109247	
\dot{Q}_{HRSG} [MW]	720,874	722,30	722,17	361,04	722,17	722,09	722,32	709,878	717,418	722,50	717,420	722,51	722,854	722,310	722,70	
χ [%]	88,66	88,83	88,82	44,40	88,818	88,81	88,84	89,07	88,84	88,86	88,84	88,86	88,90	88,84	88,88	
η_{sc} [%]	37,18	37,38	37,49	71,26	37,47	37,52	37,17	37,49	37,53	37,69	37,50	37,65	37,20	36,58	37,19	
T stack [°C]	98,25	97,14	97,24	97,30	97,24	97,30	97,12	95,83	96,81	96,99	96,80	96,98	96,71	96,99	96,83	
$\eta_{incr,th-et}$ [%]	-	39,84	41,72	42,77	41,28	42,49	37,09	40,06	41,29	54,34	40,62	42,21	36,93	28,45	36,78	
$\eta_{incr,sol-et}$ [%]	-	26,99	28,03	28,44	27,79	28,32	25,83	27,15	27,74	36,13	27,33	28,13	25,21	16,21	22,95	
x_{sf} [%]	-	3,11	3,11	3,08	3,12	3,08	3,19	4,48	4,36	4,29	4,37	4,30	4,40	3,69	4,034	
F_{sf} [%]	-	2,23	2,34	2,37	2,32	2,35	2,14	3,26	3,26	4,20	3,21	3,27	2,94	1,91	2,69	

(*) solar power and incremental efficiencies are evaluated with regards to the reference combined cycle at the same gas turbines load.

For the equivalent aperture area layouts, only the layout that doesn't need the GTs load reduction (EVA HP+MP) has a higher net power than its equivalent Fresnel; the other are affected by the partial load functioning, which is not balanced by the higher steam turbine power. Even if the gas part of the cycle is worsened by the high solar production, heat recovery is maximised. Incremental efficiencies follow the same trend of the Fresnel cases, highlighting higher results for the EVA+SH integration. Incremental solar to electricity efficiency is higher for parabolic integrations because of the higher collector efficiency. Incremental thermal to electricity efficiency shows a particular trend: it is higher for the EVA HP configuration with parabolic troughs while, when part of the solar field is dedicated to economiser or/and superheating $\eta_{incr,th-el}$ decreases with respect to Fresnel cases.

With equivalent land area collectors, generated power is low and the solar integration (in terms of solar share and solar fraction) is the smallest among the studied integrations on the bottoming cycle. $\eta_{incr,th-el}$ values are the highest between the integrations (a part from the EVA HP case); this is caused by a higher ΔT in the superheating, to reach the same outlet temperature, since the evaporation takes place at lower pressures. In this way, the average temperature in the solar field is higher with a consequent efficiencies increase.

4.2 Other configurations

Besides the integration in the bottoming steam cycle, it has been chosen to evaluate the potential benefits of different kinds of integrations. Two cases are analysed: solar fuel preheating and solar cooling. For both the configurations, cheap collectors can be employed since temperature requirements are low and receiver tubes without vacuum conditions would not cause excessive thermal losses.

4.2.1 Solar fuel preheat hybridisation

If the generation of solar steam is used for fuel preheating, it is possible to avoid the water extraction from the HRSG. This solution is simpler than the others presented since there is no interaction between the solar field and the bottoming cycle. The solar field produces subcooled water at temperatures of about 230°C, for this temperature level, there is no need to employ high-temperature and high-efficiency solar collectors. In this way the layout allows a cheaper integration than previous ones. Moreover, it has been decided, in order to avoid additional costs, not to change the existing heat exchanger. The main benefit on the CC is the possibility of increase the flow expanded in the steam turbine; however, this is a small flow and so the power gain is very small. If the fuel flow inlet temperature considerable increases, the GTs efficiency may be positively affected by the integration. Figure 58 represents the layout of this integration.

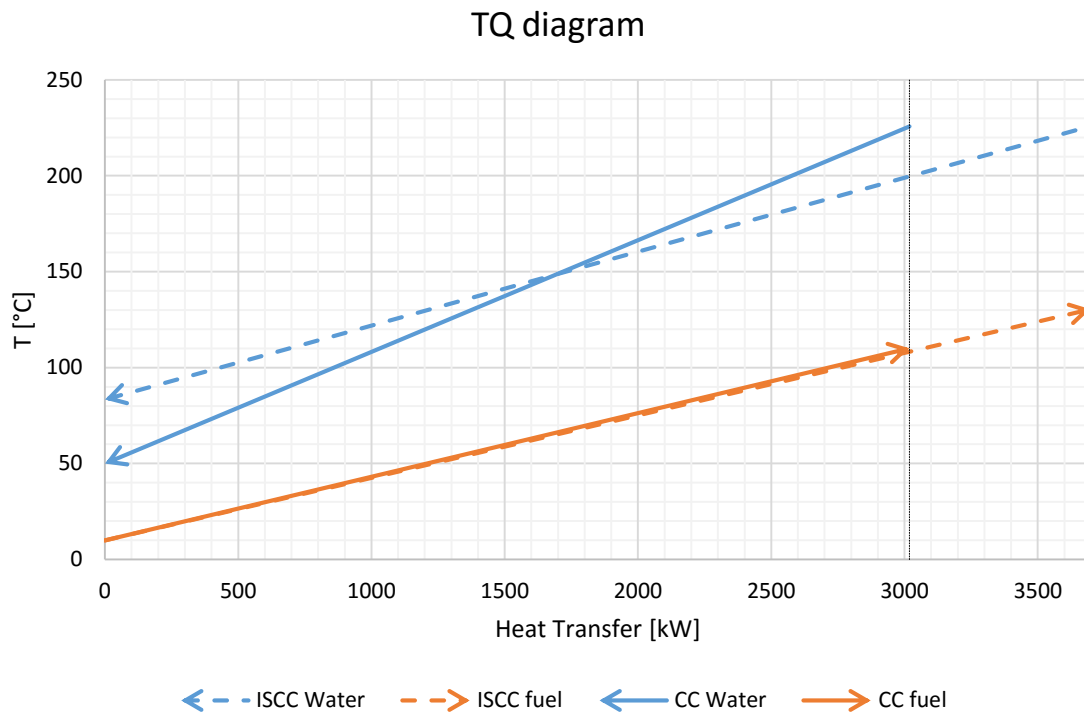


Figure 59: T-Q diagram of the fuel preheater exchanger for the CC (continue lines) and for the ISCC (dotted lines)

The nominal fuel inlet temperature in the reference CC is equal to 110°C; when the solar heat is enough to achieve a temperature higher or equal to 110°C, there is no water extraction from the HRSG. Otherwise, flows from the solar field and the HRSG are mixed together to guarantee the nominal temperature. In Table 39 main results of the integration are reported and percent variations referred to the base combined cycle show that the effects of the integration are very small; the most evident one is the 1MW increase of steam turbine power output. A higher increment of gas turbine performances may be reached with a higher fuel inlet temperature: that would require a new heat exchanger and would increase solar share and fraction of the integrated cycle.

Table 39: Main nominal results for the solar fuel preheat integration.

	Ref CC	ISCC-fuel preheating	Δ [%]
Net Power	726,27	727,35	0,15
ST power [MW]	268,02	269,11	0,41
GT power [MW]	475,12	475,10	0,00
GT fuel flow [kg/s]	27,90	27,86	-0,14
\dot{Q}_{sf} [MW] (*)	-	3,810	-
Aperture area [m²] (*)	-	8255	-
$\dot{Q}_{preheating}$ [MW]	3,019	3,698	22,49
η_{CC} [%]	55,97	56,13	0,29
η_{GT} [%]	36,62	36,67	0,14
$\eta_{incr,sol-el}$ [%]	-	8,21	-
$\eta_{incr,th-el}$ [%]	-	14,23	-
x_{sf} [%]	-	0,584	-
F_{sf} [%]	-	0,15	-

(*) values reported are referred to a single solar field.

Δ [%] is the parameter percent variation with respect to the reference combined cycle.

4.2.2 Solar cooling hybridization

The last integration performed in this work integrates the solar field in the combined cycle by introducing an absorption chiller to cool the gas turbines inlet air. In this way, gas turbines will not suffer performances reduction due to the ambient air warming. When the ambient temperature increases, the air-cooling prevents the reduction of the air flow at the compressor inlet. In this way, the Brayton cycle has increased performances, however the negative effect of the ambient temperature increase on the steam cycle air cooled condenser is not improved by this solution (i.e. condenser pressure increases with ambient temperature when an air condenser is employed, like in this case).

A double effect absorption chiller is used in this case, and the nominal COP (Coefficient of Performance) is fixed at 1,2. This system requires saturated steam at a pressure of about 9 bar [26]. The corresponding saturation temperature (about 175°C) does not require high-efficiency collectors and non-evacuated receiver tubes can be used. Both medium temperature parabolic troughs or linear Fresnel can be suitable choices; in agreement with previous studies [29], the Nova1 (see Table 31) collector has been chosen.

Figure 60 shows the chiller arrangement; ambient air passes through a coil where it is cooled to the desired temperature and then it is sent to the gas turbines.

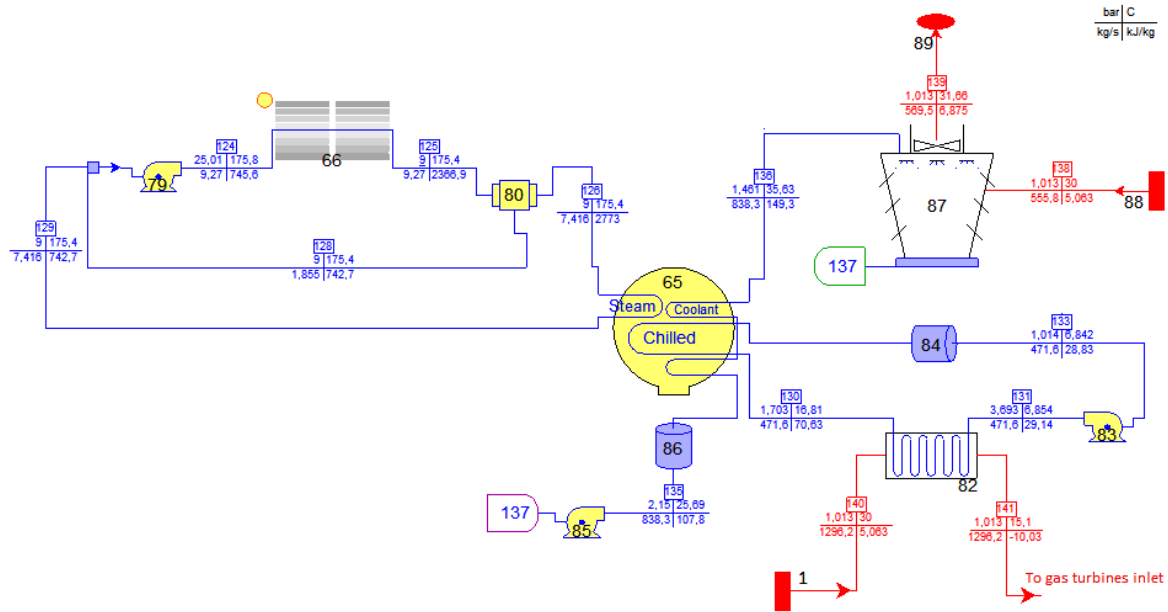


Figure 60: Layout of the solar cooling integration for the combined cycle.

The chiller has been sized to cool the air temperature from 30°C to 15°C in nominal conditions; in off-design conditions, the temperature and flow rate of the chilled water reaching the coil will determine the temperature of the air leaving the coil. To avoid water freezing, a minimum limit of temperature of 9°C has been kept [95].

Nominal performances of the ISCC are reported in Table 40, together with the reference CC ones.

Table 40: Main nominal results for the solar cooling hybrid integration.

	Ref CC	ISCC-chiller	Δ [%]
Net Power	726,27	776,59	6,93
ST power [MW]	268,02	272,03	1,50
GT power [MW]	475,12	522,70	10,01
GT fuel flow [kg/s]	27,90	30,02	7,60
$T_{in\ compressor}$ [°C]	30	15	-50
\dot{Q}_{sf} [MW]	-	15,03	-
Aperture area [m ²]	-	30934	-
η_{CC} [%]	55,97	55,62	-0,63
η_{GT} [%]	36,62	37,44	2,24

Δ [%] is the parameter percent variation with respect to the reference combined cycle.

Since the main effect of the air cooling is that the gas turbine uses a higher fuel flow, it is not possible to distinguish the solar production coherently with what has been done for others integration. Thus, in this case it is not possible to evaluate incremental solar efficiencies.

Reported data underline that the ambient air cooling is an effective way to increase the power production of the combined cycle, the variation is mainly on the gas turbines part of the cycle. This integration, in fact, is useful for the power boosting because it allows gas turbines to consume a higher fuel flow (which, at the ambient temperature, would not be possible) and to convert it into power with a higher efficiency.

On the other hand, the overall plant efficiency is decreased by the solar cooling integration. In fact, even if the GTs efficiency increases thanks to the air cooling, the steam cycle still works at the ambient temperature. The condenser works at ambient temperature but with a higher steam flow because of the reduced GT inlet temperature (the exhaust flow is higher and so the steam produced is higher), so the condenser pressure rises. In addition, the GTs TOT is lower, and it reduces the thermal recovery (χ).

The combined cycle efficiency can be expressed, as in paragraph 3.3, as:

$$\eta_{cc} = \eta_{TG} + (1 - \eta_{TG}) \cdot \eta_{SC} \cdot \chi \cdot \varphi \quad (34)$$

As said before, η_{TG} increases with the air cooling. Pressure in the HRSG slightly increase so χ decreases. Steam cycle efficiency (η_{SC}) decreases too because the steam power is limited by the condenser pressure. φ accounts for the fuel heat input that is wasted on the gas turbine (i.e. the LVH heat input that is not converted neither in GT power nor in heat available in exhaust gases); since the fuel flow is higher for the reduced air inlet temperature, this parameter decreases too. Values for these parameters are reported in **Table 41**.

Table 41: η_{CC} analysis for solar cooling integration.

	Ref CC	ISCC-chiller	$\Delta\%$
χ [%]	88,66	87,90	-0,86
η_{SC} [%]	37,16	36,67	-1,32
φ [-]	0,99	0,97	-2,02

Δ [%] is the parameter percent variation with respect to the reference combined cycle.

Chapter 5

Yearly simulations

In this chapter, main results for previously analysed configuration are presented. Off-design simulations have been carried out in order to analyse the qualitative plant behaviour during a whole representative year and to evaluate performance parameters employed for the following economic evaluation. Simulations are performed using the off-design mode in Thermoflex® to consider the effect of ambient temperature, DNI and load variations on ISCCs layouts. First, configurations results are shown for three representative days with good availability of sun radiation (one in summer, one in winter and one in autumn/spring) as representative of the seasonal variation of plant performances. Then, annual behaviour, evaluated on an hourly basis, is reported for each configuration, to compare the different solutions proposed. Plant analysis has been carried out, for the solar bottoming hybridisation, considering the plant as functioning for 8760 hours per year (i.e. in power boosting mode). Then, for one integration, a scheduled load scenario has been studied to evaluate fuel saving mode. In the end, for the other integrations studied in the previous chapter, only power boosting analysis has been performed.

5.1 Simulation method

The Sun Belt region (between 40 degrees north and south of the equator) is particularly suited for the placement of the ISCC, since the CSP technology requires high solar irradiance to work [16]. This region includes the Middle East, North Africa, South Africa, India, the Southwest of the United States, Mexico, Peru, Chile, Western China, Australia, southern Europe and Turkey, as shown in Figure 61.

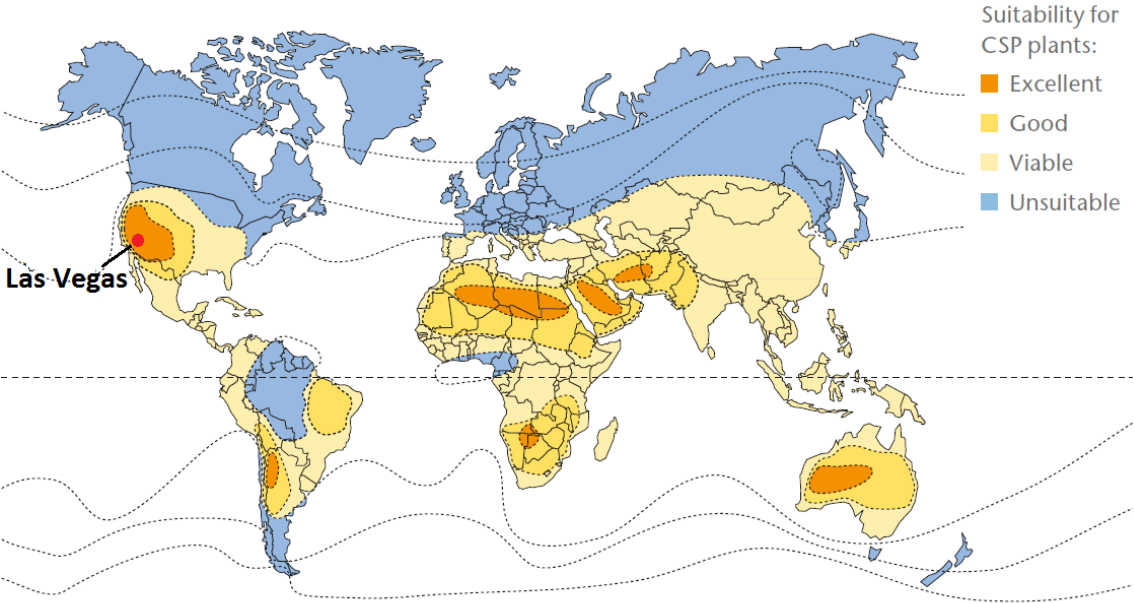


Figure 61: Solar irradiance world map, where the Sun Belt is highlighted [96].

In this work, the selected location is Las Vegas (Table 42, Figure 62 and Figure 63), an area in which there is a high solar irradiation and average ambient temperatures are quite high. Moreover, some combined cycle are already present. Therefore, it seem a potential good location for the location of an ISCC.

Table 42: Las Vegas geographical coordinates and weather data.

Site data	
Site name	Las Vegas, NV, USA
Latitude	36° 10' 30" N
Longitude	115° 08' 11" W
Annual DNI	2592 kWh/m ² /year

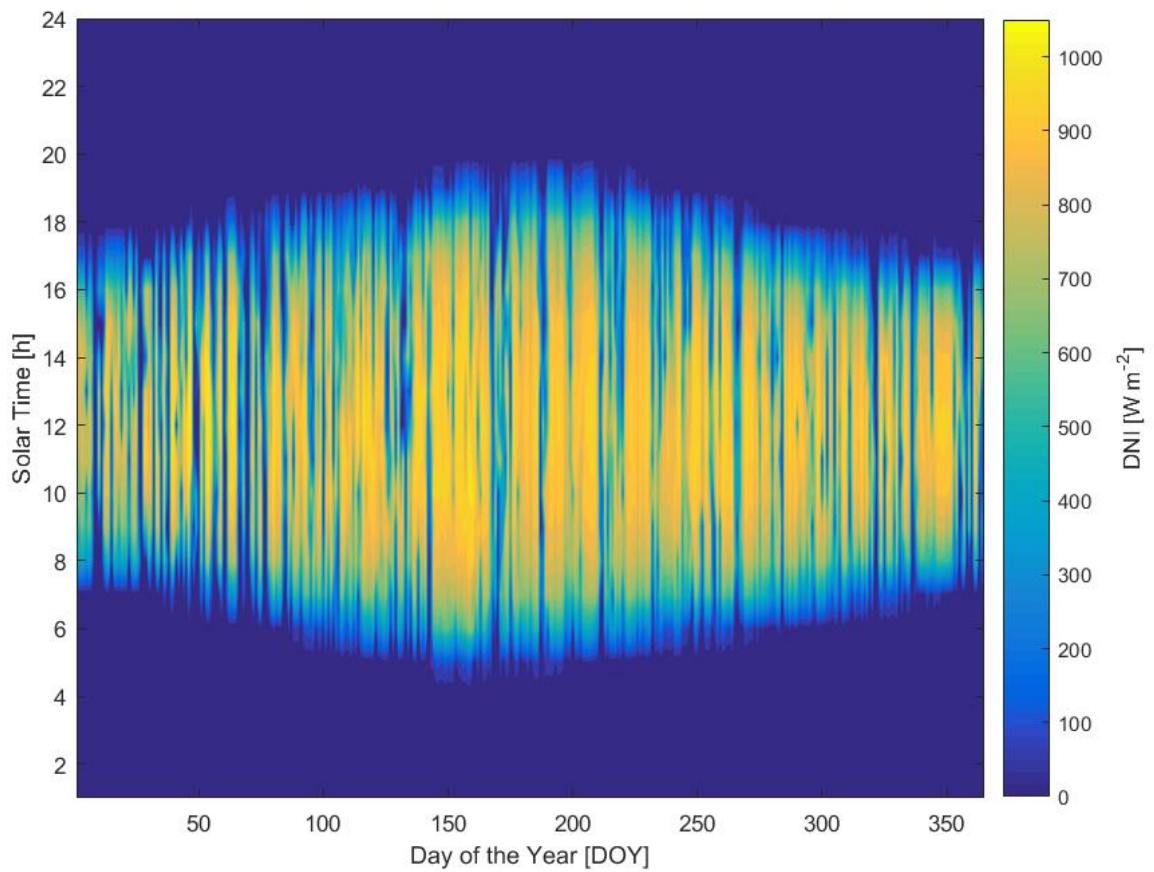


Figure 62: Hourly DNI distribution for each day of the year in Las Vegas (NV)

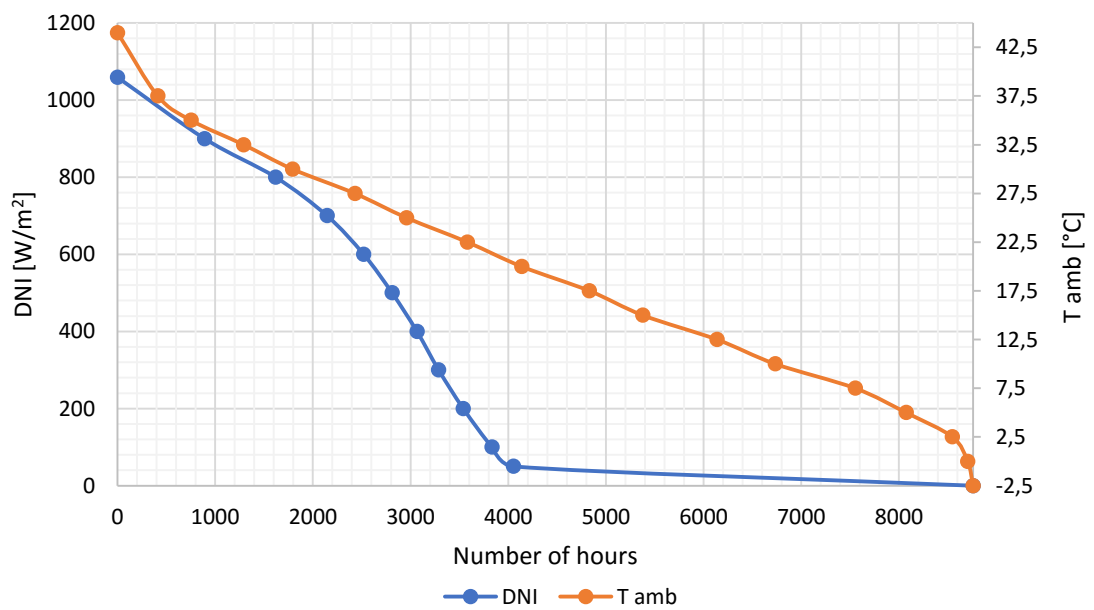


Figure 63: Inverse cumulative function of the direct normal irradiation and ambient temperature in Las Vegas.

Yearly simulations are performed using weather data available in different database; in particular, data are taken from NREL's National Solar Radiation Database [97] and have TMY3 format. The TMY3s are data sets of hourly values of solar radiation and meteorological data for a typical 1-year period.

With the purpose to avoid excessive computational costs and timings of simulations, for each operative hour of integrated plants, an interpolation method has been employed to obtain plants performances for every day of the year. For this reason, the DNI was given as a direct input to Thermoflex® setting zenith and azimuth angles equal to zero; in this way the input DNI is equal to the effective DNI¹⁰. The effective DNI is the solar irradiance that is actually absorbed by the solar field and contributes to electricity generation; it depends on the employed collector. In fact, it is affected by the collector Incidence Angle Modifier (IAM), which accounts for variation in material properties, and of the incidence angle, that reduces the irradiance available on the aperture area of the collector (see paragraph 2.6) Figure 64 shows the effective DNI cumulative function along the whole year for the Eurotrough II parabolic collector and the Supernova Fresnel collector for Las Vegas.

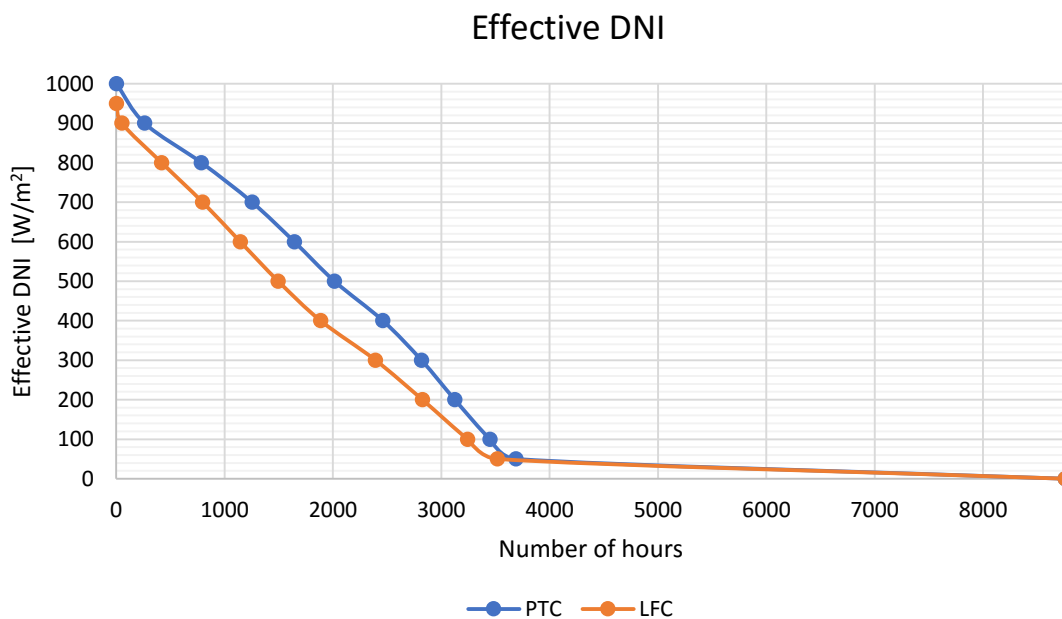


Figure 64: Inverse cumulative function of the effective DNI in Las Vegas for PTC (ET II) and LFC (Supernova EVA HP).

¹⁰ With azimuth and zenith set to 0, collector efficiency corrective values are equal to 1.

The effective DNI has been calculated for each hour of the year using relationships reported in APPENDIX A: for the calculation of the sun position [98]. Once Azimuth and Zenith angles values are known, the effective DNI can be evaluated, for Parabolic trough and Fresnel collectors can be calculated with the reported formulas.

The incidence angle [$^{\circ}$] for a parabolic trough whose axis is oriented in north-south direction can be expressed as:

$$\theta_i = \cos^{-1} \sqrt{1 - \cos^2 \alpha \cdot \cos^2 \gamma} \quad (35)$$

For Fresnel collectors, the incidence angle can be split into two components: θ_i and θ_{\perp} , as described in paragraph 2.6 θ_i is the same of The transversal angle [$^{\circ}$] can be evaluated through the following expression:

$$\theta_{\perp} = \tan^{-1} \left(\frac{\sin \gamma}{\tan \alpha} \right) \quad (36)$$

The incidence angle modifier, which is a known function of the incidence and/or transversal angles, can be calculated for both PT and LFR collectors.

The effective DNI for linear Fresnel can defined as:

$$DNI_{eff,LFR} = DNI \cdot IAM(\theta_i) \cdot IAM(\theta_{\perp}) \cdot \eta_{end\ loss} \quad (37)$$

Where $\eta_{end\ loss}$ is defined, as in paragraph 2.6:

$$\eta_{end\ losses} = 1 - \tan(\theta_i) \frac{D_{pm}}{L_{abs}} \quad (38)$$

IAM functions for Novatec's Nova-1 and Supernova collectors are taken directly from Thermoflex® database; they are reported in paragraph 2.7.6.:

The effective DNI for a generic PT collector, is expressed as follows:

$$DNI_{eff,PT} = DNI \cdot K(\theta_i) \cdot \eta_{end\ loss} \cdot \eta_{shading} \quad (39)$$

Where $\eta_{shading}$ is defined, as in

$$\eta_{shading} = \min \left[\max \left(0; \frac{L_{spacing}}{A_A} \cdot \frac{\cos(\theta_z)}{\cos(\theta)} \right); 1 \right] \quad (40)$$

$K(\theta_i)$ for Eurotrough II collector has the following expression [99]:

$$K(\theta_i)_{ET} = \cos(\theta) - 5,251 \cdot 10^{-4} \theta - 2,8596 \cdot 10^{-5} \theta^2 \quad (41)$$

In this case, $K(\theta_i)$ also accounts for end collector losses.

$K(\theta_i)$ for Polytrough 1800 has been taken from NepSolar's brochure [73] and its trend is reported in paragraph 2.7.5.

The power produced in each hour of the year has been evaluated to obtain the annual electricity production ($E_{ISCC,annual}$). In addition, since some integrations require the GTs load reduction to avoid the steam turbine overloading, the equivalent CC annual electricity production ($E_{CC eq,annual}$) has been calculated. It is the electricity that would have been produced by the reference combined cycle at the same GT load of each ISCC layout analysed. The electricity production of the equivalent CC has been used to evaluate the solar electricity production, as shown in Equation (42):

$$E_{sol} = E_{ISCC,annual} - E_{CC eq,annual} \quad (42)$$

In addition, the annual heat absorbed by the solar field ($Q_{sf,annual}$) and the annual fuel consumption ($m_{fuel,annual}$) have been calculated by interpolation. It is thus possible to determinate values of annual performance parameters, useful to evaluate and compare the different configurations.

The yearly overall efficiency:

$$\eta_{CC,annual} = \frac{E_{ISCC,annual}}{m_{fuel,annual} \cdot LHV} \quad (43)$$

The annual incremental solar-to-electricity conversion efficiency, defined as:

$$\eta_{incr sol-el,annual} = \frac{E_{sol}}{A_A DNI} \quad (44)$$

The annual incremental solar-to-thermal conversion efficiency, defined as:

$$\eta_{incr sol-th,annual} = \frac{E_{sol}}{Q_{sf,annual}} \quad (45)$$

The annual solar field efficiency is defined as:

$$\eta_{SF,annual} = \frac{Q_{sf,annual}}{A_A DNI} \quad (46)$$

The annual solar share is defined as:

$$x_{sf,annual} = \frac{Q_{sf,annual}}{\dot{m}_{fuel,annual} \cdot LHV + Q_{sf,annual}} \quad (47)$$

5.2 Power boosting

An operation at full load for 8760 hours has been firstly assumed. Thus, annual solar contributions discussed below represent lower limits on the range of possible values. In reality, plants will follow the demand profiles for the local utility. They may be shut down at night, and will likely undergo scheduled maintenance during the winter. Consequently, the local dispatch requirements will increase the calculated solar contribution.

The full operational scenario is interesting to evaluate plants performances when a power boosting integration is considered; solar production results as an addition to the reference combined cycle power output. It is to be noticed that GTs in the ISCC can not always operate at 100% load because of the overloading limit on the steam turbine. Thus, this load reduction is not related to an external load profile but to the integration strategy adopted.

Simulations have been carried out for a defined number of cases, where ambient temperature has been varied in a range from -5°C to 45°C and the effective DNI in a range from 0 to 1000 W/m^2 . In this case, the GTs load has not been reduced to vary the power output; a control has been activated during computations in order to maintain the load at the maximum value that guarantees that the overloading limit on the steam turbine is respected. In this way, it is univocally defined as the ambient temperature and the effective DNI are known.

The off-design behaviour of the solar field is evaluated through the thermal model available in Thermoflex® [65]. Inputs for off-design simulations carried out in Thermoflex® have been evaluated through the thermal model for thermal losses described in paragraph 2.7.1.

The obtained outputs have then been interpolated as a function of the ambient temperature and the effective DNI to obtain the values of the desired parameters for every hour of the year. Interpolation have been carried out with the free Excel library XonGrid 4 [100].

5.2.1 Representative days simulations

In this section, trends for some significant parameters are reported; they all are referred to the EVA HP layout. These parameters are useful to understand how the integration affects the combined cycle at varying ambient temperatures and DNI conditions and they explain the overall yearly behaviour of integrated cycles. Trends for the other configurations are not reported in this section since, even if with different quantitative results, the same conclusions can be deduced.

Chosen days for simulations are January 13th for winter, August 11th for summer and October 4th for autumn; they are representative of seasonal ambient variation. In this way, plant performances over the whole year are qualitatively described.

5.2.1.1 Solar Field analysis

In Figure 65, Figure 66, Figure 67 and Figure 68 the DNI, the effective DNI and ambient temperature for these days are shown. The ambient temperature effect on the solar field is limited, since it only affects the receiver heat losses, which slightly decrease with the growth of T_{amb} . The impact on the combined cycle is greater, since the increase of the ambient temperatures affects the GTs, lowering their efficiencies, and the air condenser, increasing the condensation pressure.

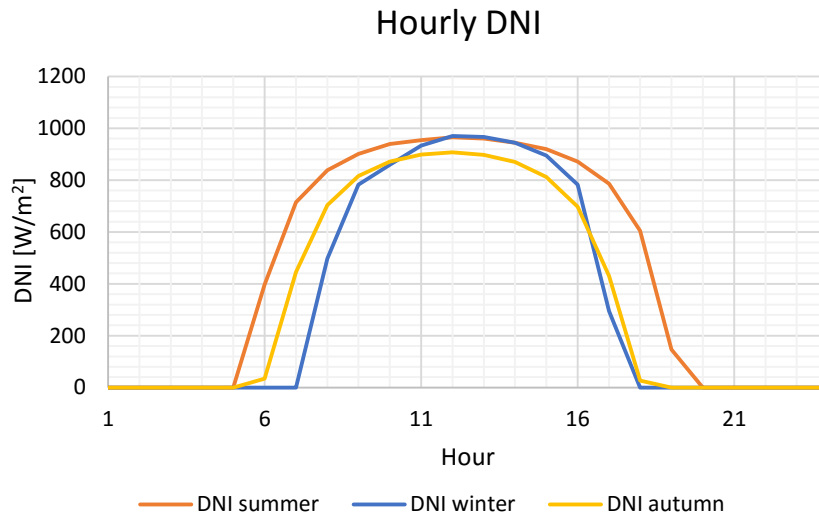


Figure 65: Daily trends of DNI.

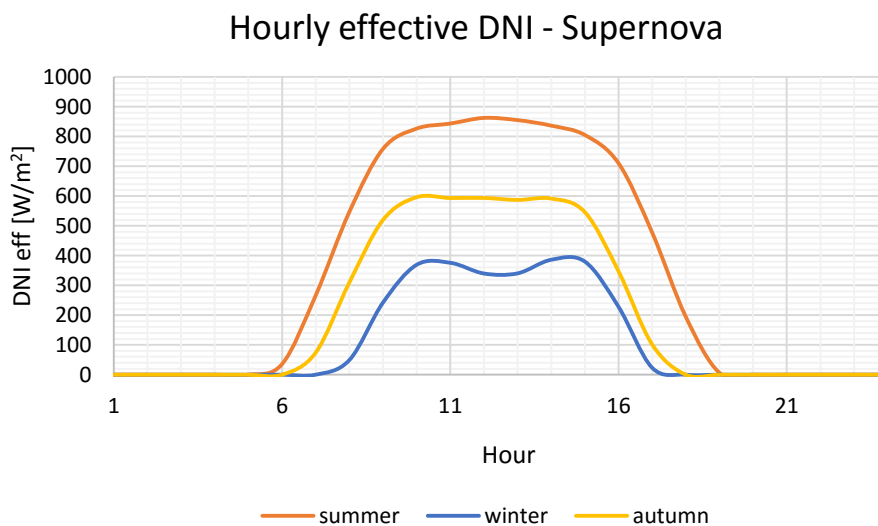


Figure 66: Daily trends of effective DNI for LFC.

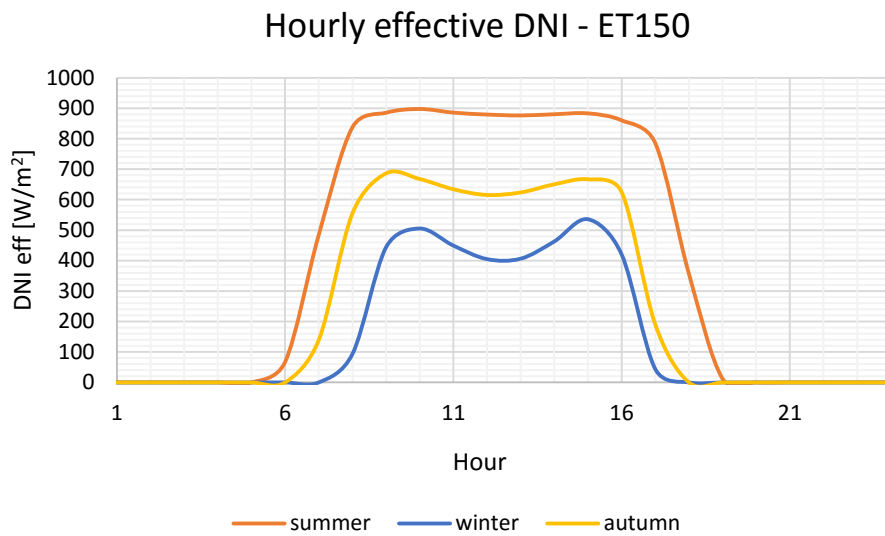


Figure 67: Daily trends of effective DNI for PTC.

In Figure 66 and Figure 67, trends for the effective DNI for PTC and LFC are shown. It can be seen that the effective DNI for parabolic trough is higher, more than about 43% during the winter day. In fact, Fresnel collectors have lower peak optical efficiencies (64,7% for Supernova and 75% for ET150). Moreover, in off-design conditions LFCs also suffer for the effect of transversal and longitudinal angles (see paragraph 2.6), while PTCs have only the penalisation of the incidence angle.

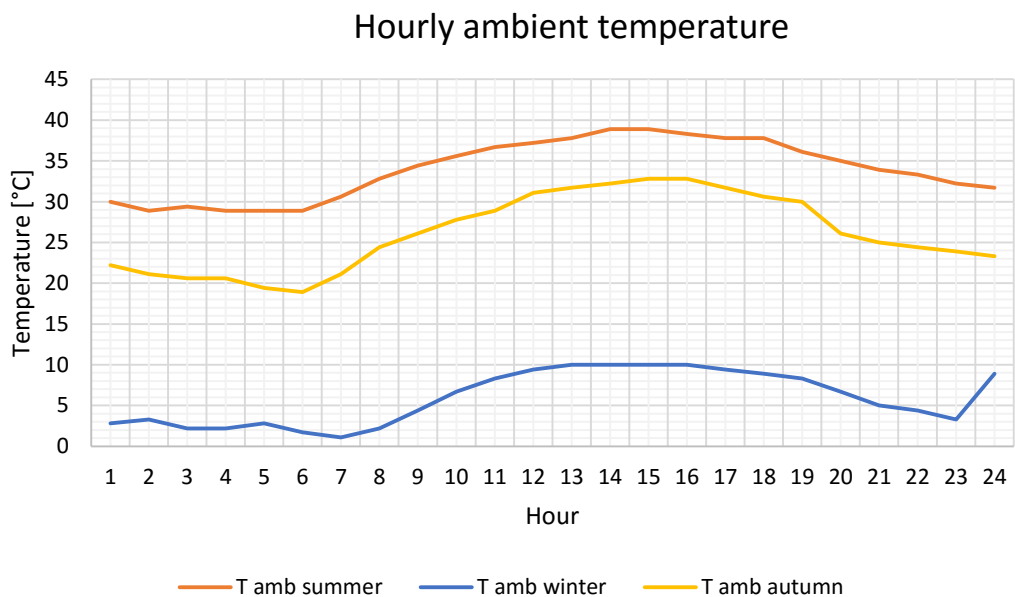


Figure 68: Trend of ambient temperature during representative days.

In Figure 69, Figure 70 and Figure 71, variations of DNI and thermal energy transferred to the working fluid (Q_{sf}) are shown. Trends are referred to EVA HP layouts for both PT and LFR technology, compared on equal collector aperture area. Since solar fields have the same total aperture area, they can be compared on equal basis for technologies employed in the different layouts.

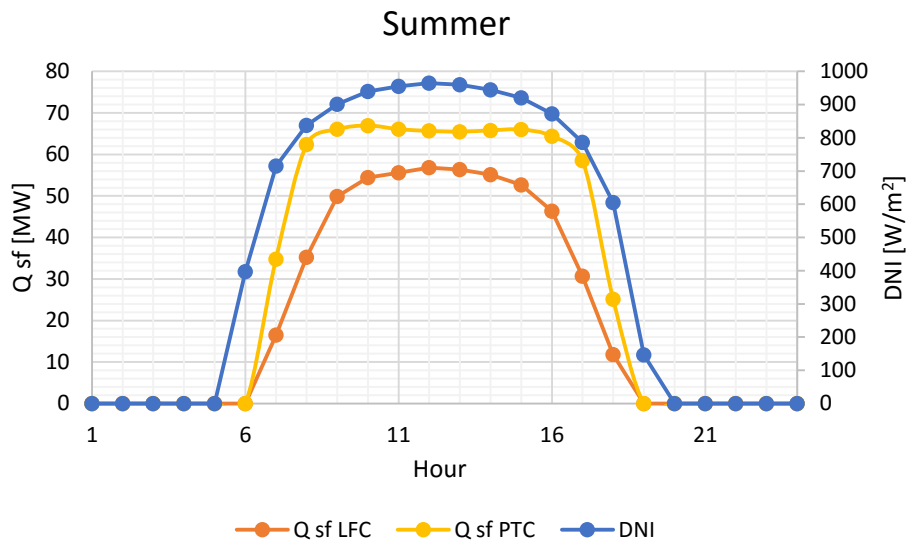


Figure 69: Trends of DNI and net heat absorbed by fluid in the solar field in the reference summer day for PTC and LFC.

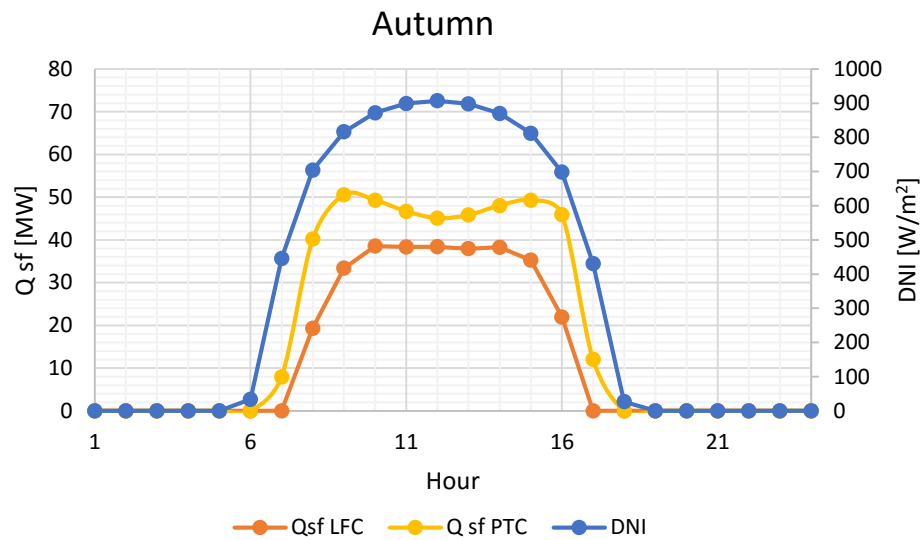


Figure 70: Trends of DNI and net heat absorbed by fluid in the solar field in the reference autumn day for PTC and LFC.

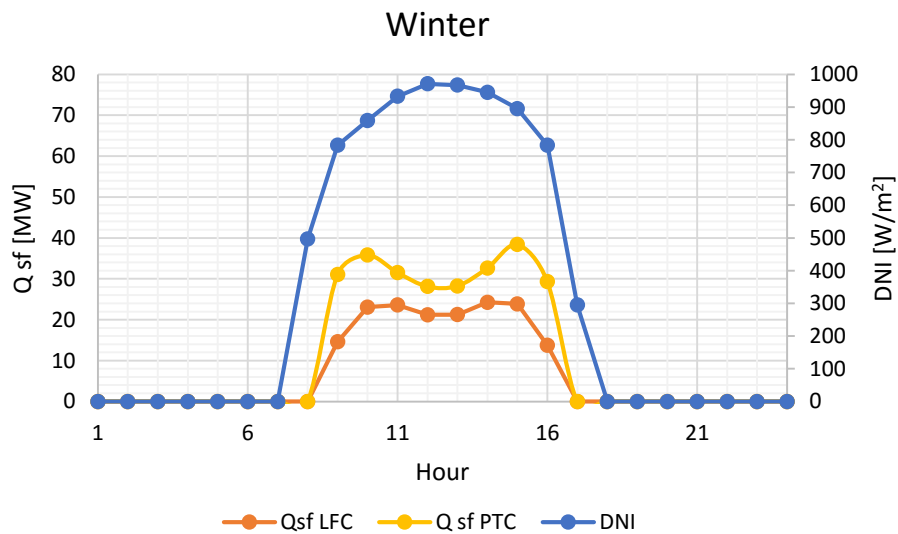


Figure 71: Trends of DNI and net heat absorbed by fluid in the solar field in the reference winter day for PT and LFC.

Even during winter, the DNI is very high, due to the geographical location of Las Vegas. However, the heat transferred in the solar field is rather lower than the summer one; this effect is caused by the higher values of the radiation incidence angle that penalises the overall solar field efficiency reducing the effective DNI on the solar receiver.

PTCs show better performance than the LFCs, which have a significant efficiency penalty for high incidence angle of radiation, particularly in the first and last hours of the day; in fact, the net power transferred to the working fluid for PTCs is about 25% higher than for Fresnel in summer days and up to 60% higher during winter days. The saddle trend in the central hours of the day, when the zenith angle is higher, is due to the cosine effect and it is more evident for PTC collectors, which, however, maintain the highest efficiency and thus the highest effective DNI. For the winter day, the shape is more evident because of the lower ambient temperature, which increases the thermal losses towards the ambient.

5.2.1.2 Cycle analysis

Figure 72 shows the hourly solar-to-electricity efficiency for EVA HP with SM1 integration.

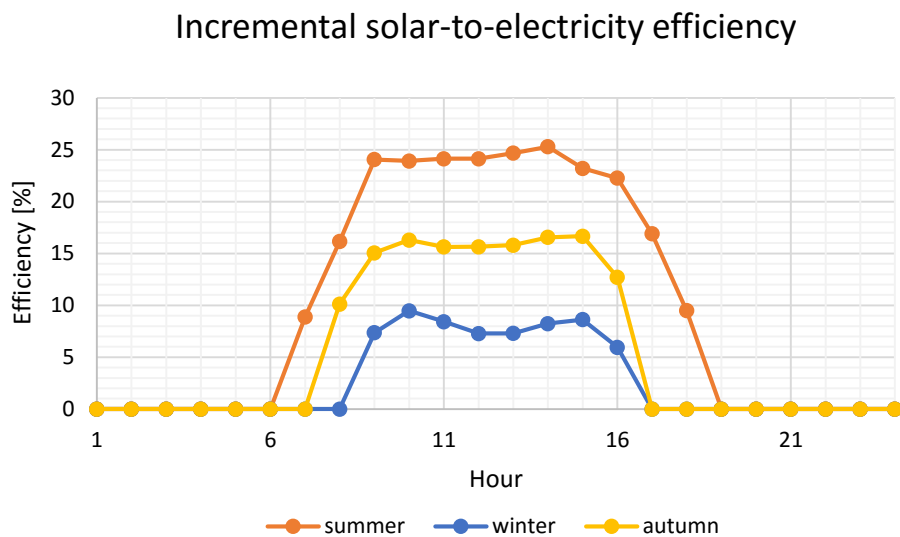


Figure 72: Daily trends of incremental solar-to-electricity efficiency for EVA HP SM1 configuration.

Reported curves refer to the integration with LFCs; for PTCs, they are similar qualitatively, though their $\eta_{incr\ sol-el}$ is higher for all the days analysed. In fact, PTCs are able to capture a higher amount of solar radiation, since they have a higher solar field efficiency than LFCs (about 65% for a LFC against about 55% for a PTC during summer). In summer days, the incremental efficiency reaches its higher values, since the DNI_{eff} is higher and thermal losses decrease (ΔT between ambient and collector decreases), increasing the electricity production attributed to the solar resource. During winter, $\eta_{incr\ sol-el}$ is sensibly lower. In fact, even if the DNI coming from the sun remains high, the DNI_{eff} significantly decreases because of the sun position. In addition, the temperature difference between the receiver and the ambient increases, worsening receiver thermal losses.

For Fresnel layouts, as described in paragraph 4.1.1, solar multiples 1,5 and 2 have been evaluated too. In Figure 73, Figure 74 and Figure 75, trends for the hourly electricity production are shown for EVA HP configuration with Fresnel solar collector and different solar multiples. As the SM increases, the required load reduction on gas turbines, needed to keep the steam mass flow under the maximum limit of the steam turbine, is higher to introduce in the cycle the higher solar steam produced.

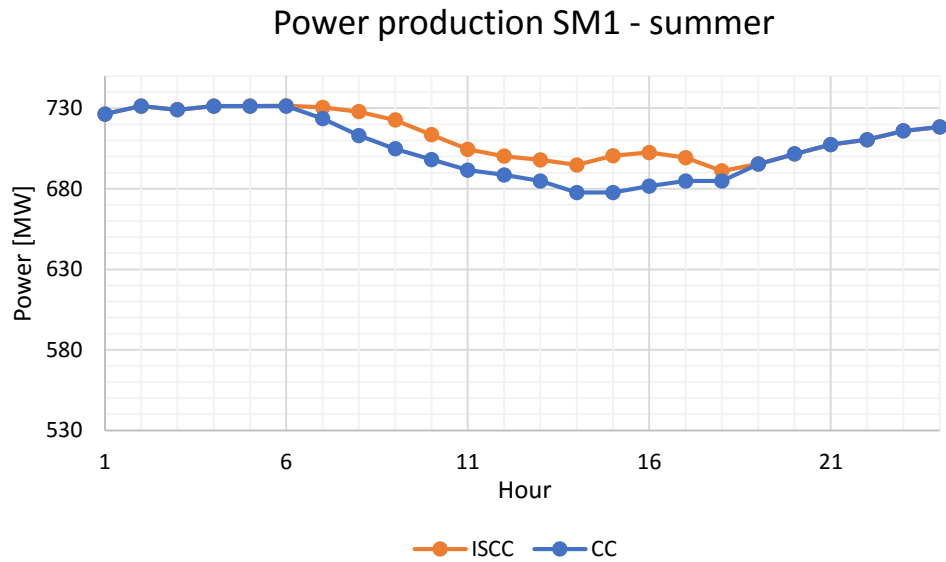


Figure 73: Daily summer trends of net power produced by reference CC with GTs at 100% load and ISCC SM1.

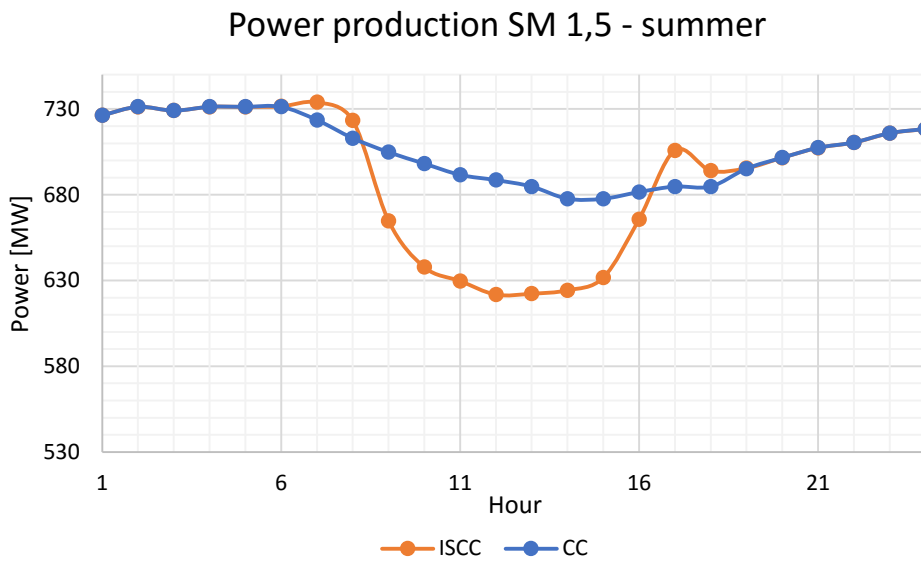


Figure 74: Daily summer trends of net power produced by reference CC with GTs at 100% load and ISCC SM1,5.

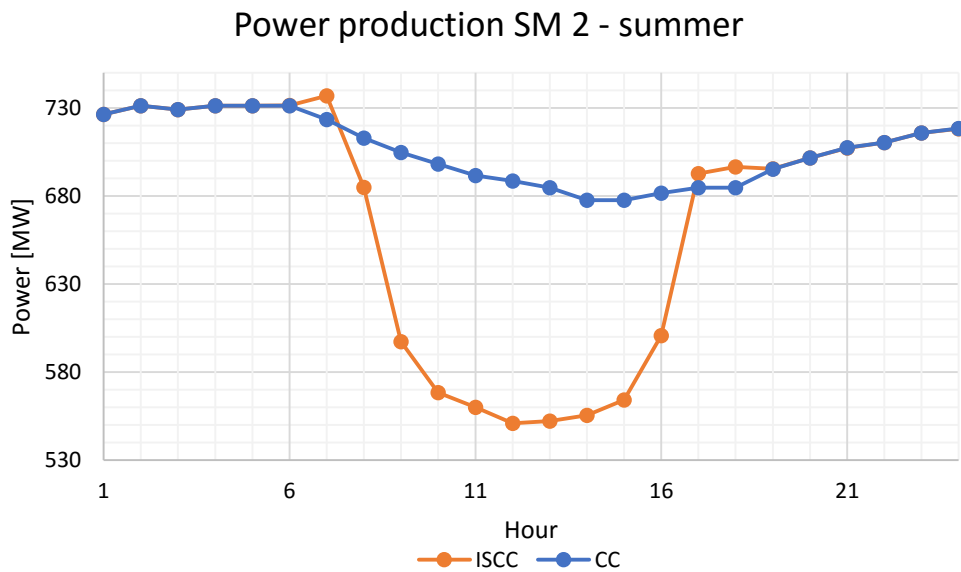


Figure 75: Daily summer trends of net power produced by reference CC with GTs at 100% load and ISCC SM2.

During night hours, behaviours of the different configurations are identical to the reference case since no changings have been made on the base combined cycle. During sunny hours, the three configurations show very different power production curves. Figure 73 shows that the solar integration with SM1 boosts the net power output in comparison with the reference

CC, since GTs are nearly at full load operating conditions in every hour of the day. In addition, in hours from 14 to 16, the ISCC shows an increase of the power augmentation with respect to reference CC. For the CC, the steam power output reduces during the day because of the increase of ambient temperature that worsens cycle performances, as discussed in paragraph 3.4, (lower gas turbines efficiency, lower condenser pressure). For the ISCC instead, the higher ambient temperature has a double influence: it reduces the power production because of the effect on gas turbines but it also has the benefit of reducing solar receiver heat losses, even if this effect is marginal with respect to the influence on GTs. At the increase of the ambient temperature correspond an increasing value of the DNI_{eff} with a consequent increasing solar power production. In this way, as the ambient temperature increases over the nominal one, the solar integration can be exploited with a higher efficiency. Moreover, the requested load reduction on gas turbines is lower; since the steam mass flow produced by exhaust gases cooling decreases (as for the CC), there is more margin before reaching the maximum limit imposed, so the solar steam introduction does not affect gas turbines performances.

SM 1,5 and SM 2 configurations (Figure 74 and Figure 75) show different trends, since the total GTs load is markedly reduced to let the steam turbine accept all the available steam produced by the solar field. It must be underlined that this integration does not allow the power boosting of the cycle, since GTs are often at load lower than 100%, and the total power producible in hours with high effective DNI is limited, if the solar contribution is always at the maximum level. However, the reduction of the net power is accompanied with the reduction of the natural gas requested by GTs, as shown in Figure 76.

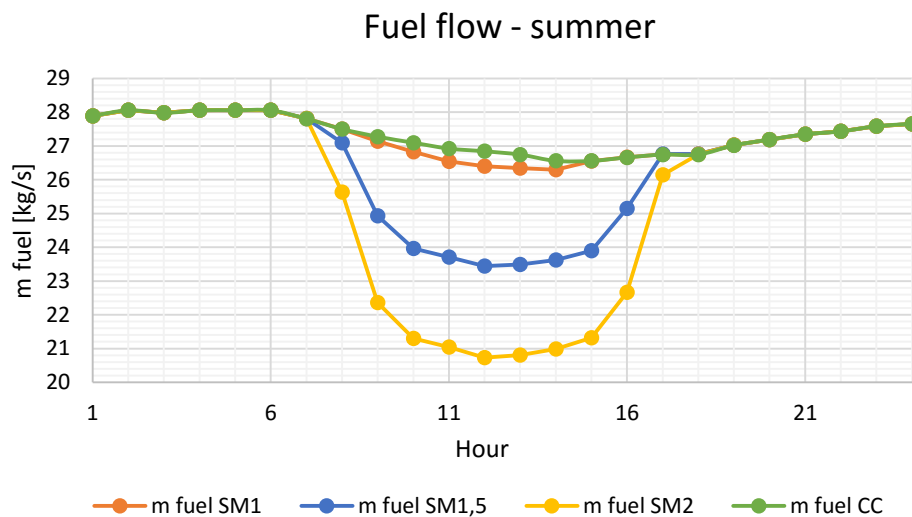


Figure 76: Trends of fuel consumption of reference CC with GTs at 100% GT load and SM1, SM 1.5 and SM2 ISCCs during the reference summer day.

The overall combined cycle efficiency (defined as the ratio of net power output with respect to the net fuel input) is higher for SM2 rather than SM1 configuration so the reduction of the fuel consumption prevails over the lower electricity output because of the high power production from solar steam.

This behaviour suggests that solar multiples higher than 1 may not be convenient when the generation strategy foresees the production of the maximum deliverable power. However, if a scheduled load is considered, results may change since the SM2 configuration allows a great part of the power output to be produced by the solar steam.

It is possible to keep at least the same power output of the reference CC by reducing the effective DNI, i.e. defocusing the solar field. In this way, it is possible to increase the GTs load, reaching, for hours from 7 to 17, the same net power output of the reference CC. For each sunny hour, the minimum defocused fraction of the solar field, required to keep the same energy output of the reference CC (without solar integration), has been found.

Figure 77 shows the fuel consumption of the EVA HP integration with SM2 as a function of the effective DNI and of the ration between produced power and nominal power (where the nominal power is the one of the same integration with SM1). It highlights that, when the DNI_{eff} is high (above 400 W/m^2), the power is limited by the maximum GTs power load so a high power production would require the reduction of the effective DNI. However, if the requested power is lower, the maximum solar production can be exploited with a higher fuel saving.

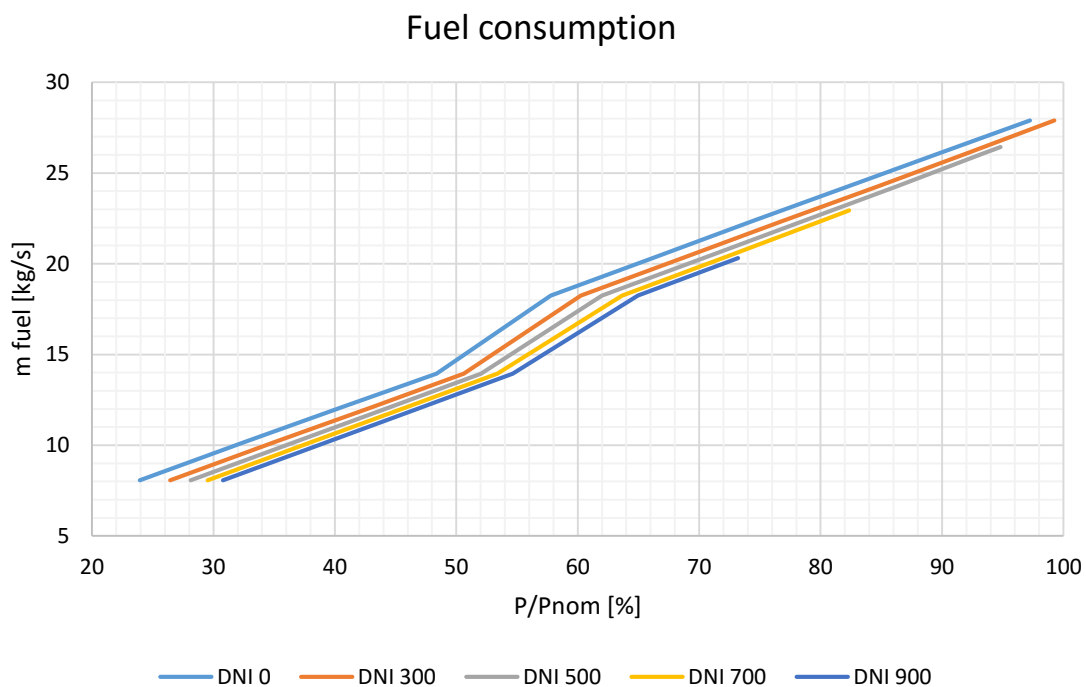


Figure 77: Fuel consumption as a function of the ratio between the produced power and the nominal power for the SM2 EVA HP integration at T_{amb} 30°C, DNI 800 W/m².

If combined cycle components (steam turbines and/or superheaters) are re-design to match the highest steam mass flow produced by the SF, the power output for high SMs increases. In Figure 78, power production for EVA HP SM2 with the revamping of the ST and all the high pressure superheater heat exchangers is shown.

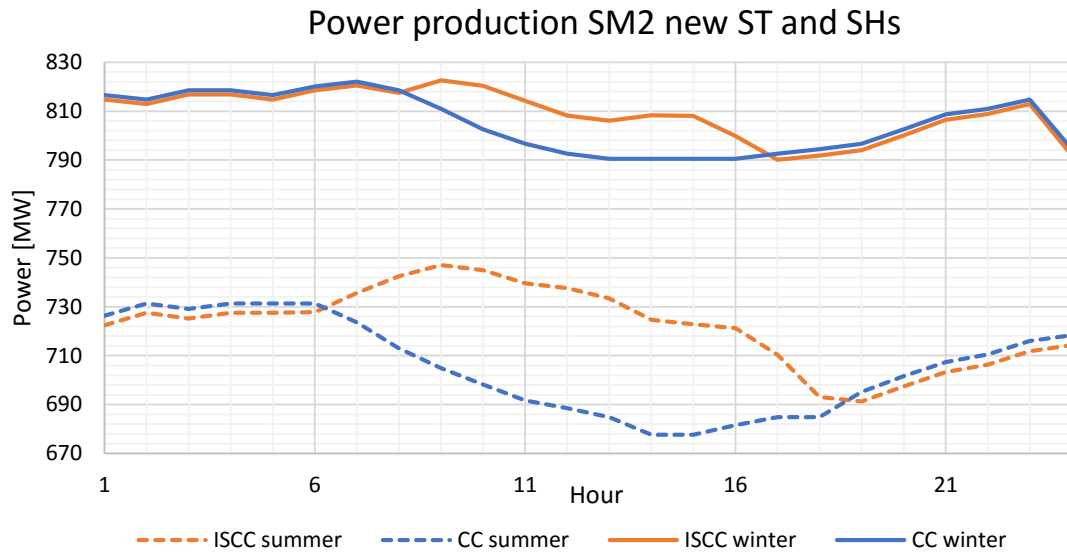


Figure 78: Trends of net power produced by reference CC with GTs at 100% GT load and ISCC SM2 with new ST and SHs during summer and winter days.

During sunny hours, a great increase of the net power produced by the ISCC is registered, boosting the power production of about 50 MW_e. It must be noticed that a penalisation (of about 4 MW) occurs during night hours because, since the new steam turbine nozzle areas are higher than old ones, when the solar steam is not available, the steam turbine inlet pressure decreases. The condenser pressure is the same of the reference CC at the same temperature and thus the new turbine expansion line and, consequently, the power output are smaller. The overnight penalisation is less evident during winter days because, since the ambient temperature is low, the steam produced in the HRSG is higher than in the nominal case, thus the superheater higher size is an advantage. In summer it is evident the higher solar production during daytime, but at night the power output is further reduced because higher superheaters areas require a higher desuperheating flow when the steam production is low.

In Figure 79 and Figure 80, trends for the temperature at the inlet of the new HP steam turbine for the EVA HP integration are shown. First, for the case with SM1 (old SHs), then also for the other analysed configurations with CC revamping.

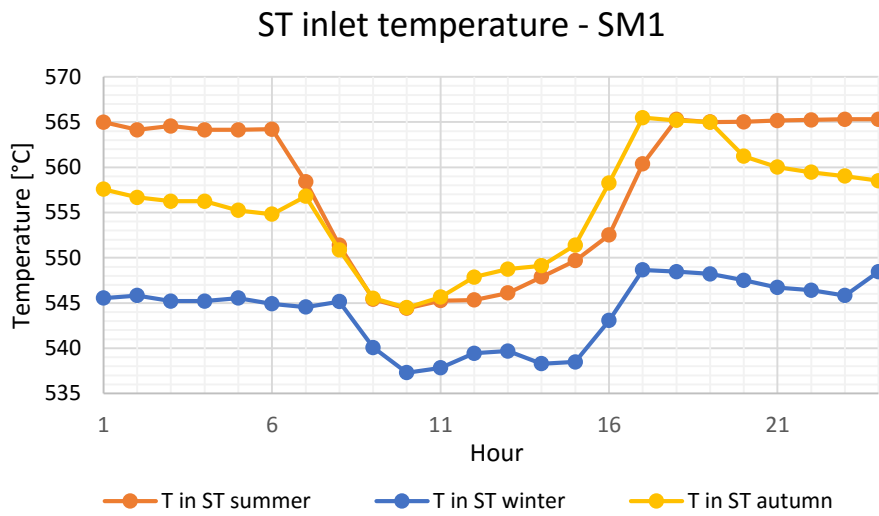


Figure 79: Trends of HP turbine inlet temperature for EVA HP SM1 configuration during representative days.

Figure 79 highlights that the temperature is almost constant during nights and it is lower for autumn and winter. This effect is due to the increased steam mass flow circulating in SHs, which is higher when the ambient temperature is lower and/or when the solar field is working. When the steam mass flow significantly increases above the nominal value, superheaters areas are too small to keep the nominal exit steam temperature (565 °C).

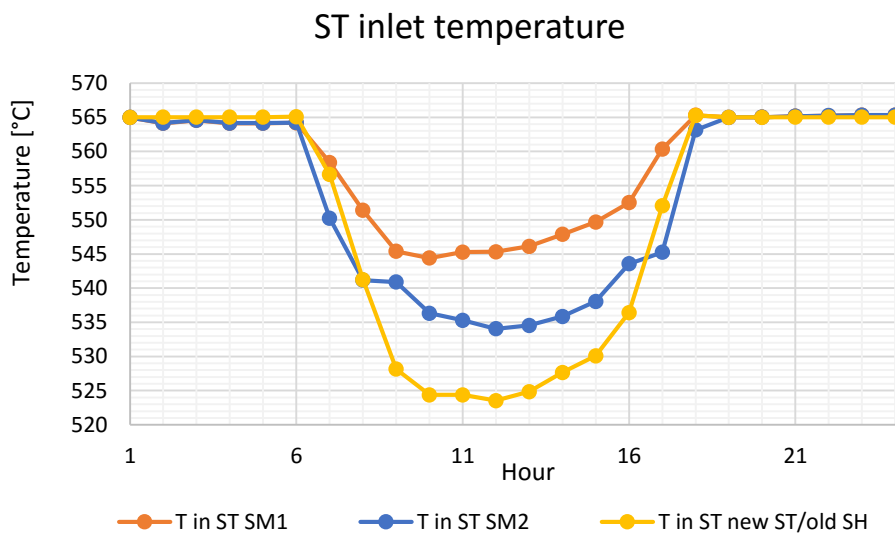


Figure 80: Trends of HP turbine inlet temperature for three different configurations during summer representative day.

In Figure 80, trends for EVA HP configuration with solar multiple 1 and 2 and with SM2 and the new ST (with old SHs) are shown for the summer day. The inlet ST temperature reaches 40°C below the nominal value for the configuration with the revamping of the steam turbine.

The SHs resizing allows reaching the nominal ST inlet temperature even when the solar steam production reaches its highest values. However, when the DNI is low or absent, SHs result oversized for the circulating steam, with a consequent excessive increase of SH tubes temperature. To avoid heat exchangers damages, a desuperheating mass flow is withdrawn from the high pressure line to keep the outlet steam temperature at its nominal value and this, as previously stated, affects the combined cycle performances.

In Figure 81, values of the ST inlet pressure for EVA HP with LFR configuration are shown.

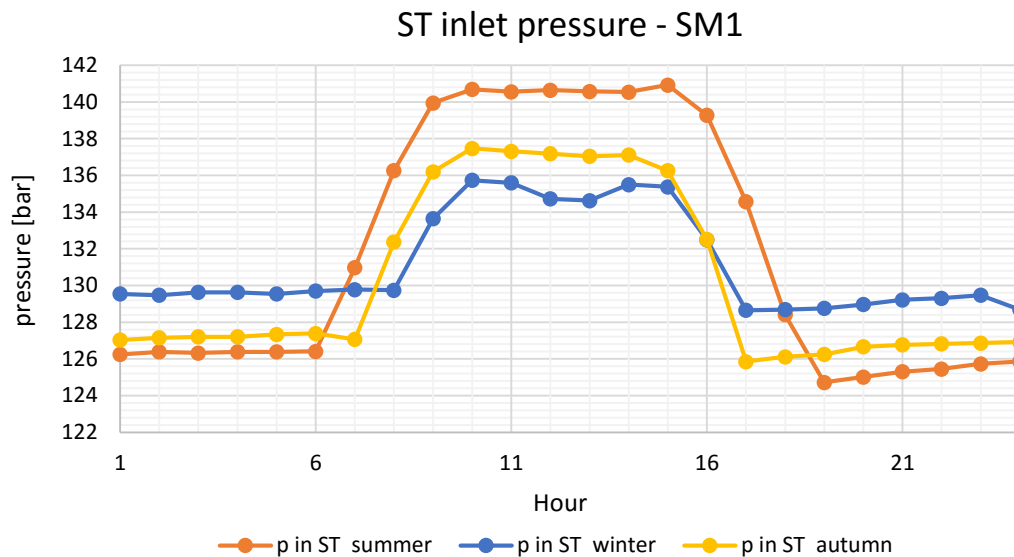


Figure 81: Trends of HP turbine inlet pressure for EVA HP SM1 configuration during representative days.

The pressure level varies seasonally, depending on the mass flow circulating in the heat recovery steam generator. During sunny hours, the steam mass flow rate in the ST increases thanks to the additional input of the solar field and the pressure significantly increases. In particular, for summer days, the increase of pressure can be very high; starting from 126 bar when no solar steam is produced, it reaches values of about 140 bar. During the central hours of the day, the pressure value is almost constant because of the plant regulation, which keeps the steam mass flow at HP ST inlet at 115% of the nominal value when there is abundance of solar irradiance. Pressure variations in the HRSG are tied to the steam turbine inlet pressure.

5.2.2 Yearly simulations results

In the following section, results for annual simulation are presented, in terms of overall electricity production and solar production.

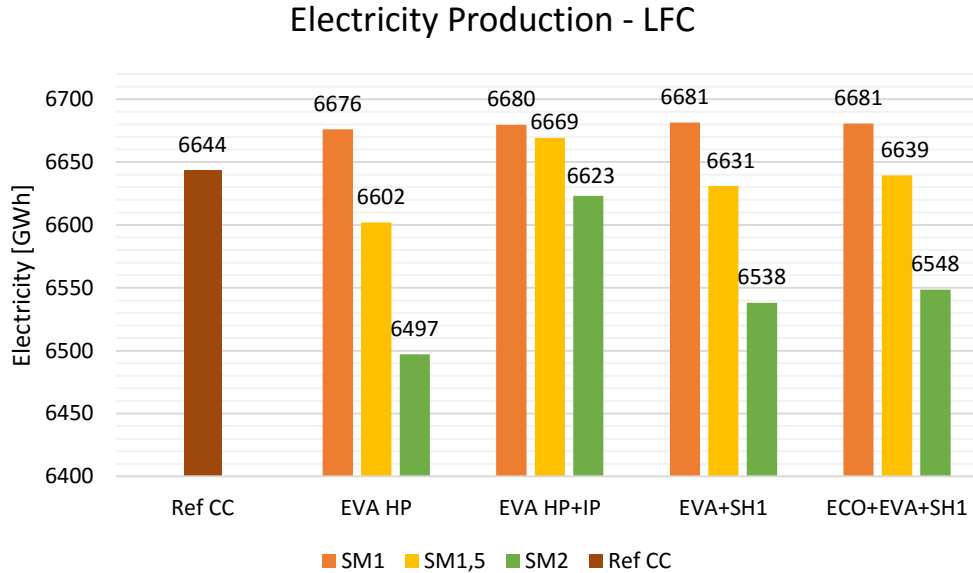


Figure 82: Annual electricity production for the reference CC and ISCC different layouts with LFC and different solar multiples.

In Figure 82, the annual electricity production for different solar multiple and different integration layout is represented. Configurations with solar multiple 1 always show an increase in the total electricity produced, which results in a power boosting effect with respect to the reference CC. Generally, the total electricity production decreases for configurations with higher solar multiple; the solar steam production increases significantly thanks to the bigger sizing of the solar field but the GTs load must be reduced in order to avoid overloading on the steam turbine. Overall, the gas turbines power reduction prevails over the solar production.

The EVA HP+IP integration, during the year, is characterised by the highest electricity production among the configurations with high solar multiples; in particular, with SM1,5, the annual electricity is still higher than the one of the reference case. This is because, at the same solar multiple, GTs load needs less reduction in the EVA HP+IP configuration than in the others. Since the total aperture areas (i.e. the sum of aperture areas of all ISCC solar fields) are almost equal, the HP solar field area results smaller in the EVA HP+IP layout than in the EVA HP one. The solar high pressure steam produced is lower and the high pressure stage of the ST does not reach its maximum capacity limit. Because of that, the control for GTs load is set on the IP ST, whose limit is set to the 115% of its nominal capacity, as for the HP ST. Since the nominal capacity of the IP ST is higher than the HP one, there is more margin for solar steam produced before the GTs load reduction is required.

(about 26,2 kg/s of total additional steam accepted in the EVA HP+IP configuration against 22,8 kg/s for EVA HP). The required load reductions for EVA HP and EVA HP+IP configurations are shown in Figure 83 and Figure 84.

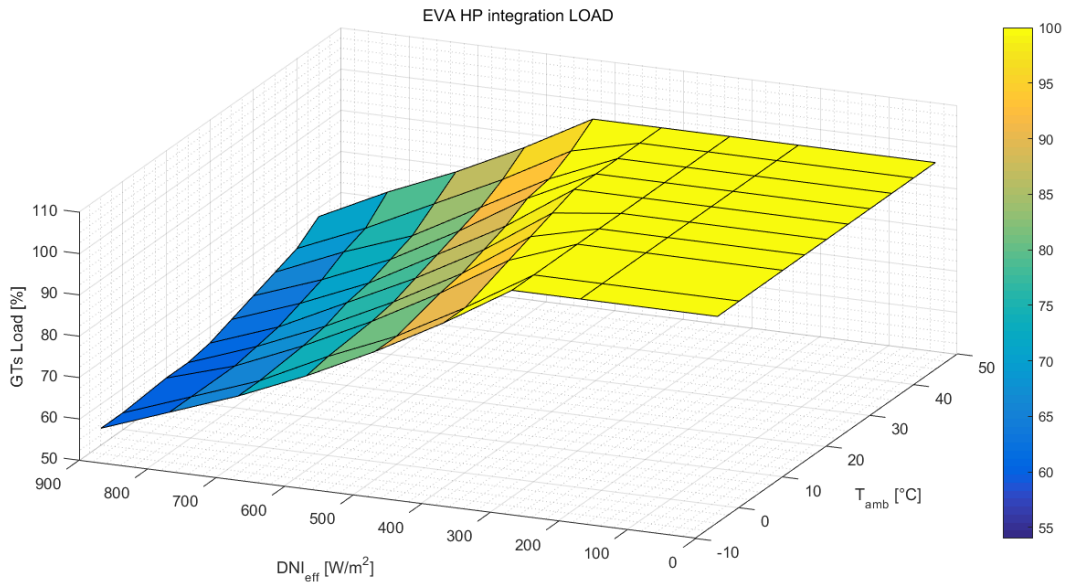


Figure 83: GTs load regulation as a function of the effective DNI and ambient temperature for EVA HP layout.

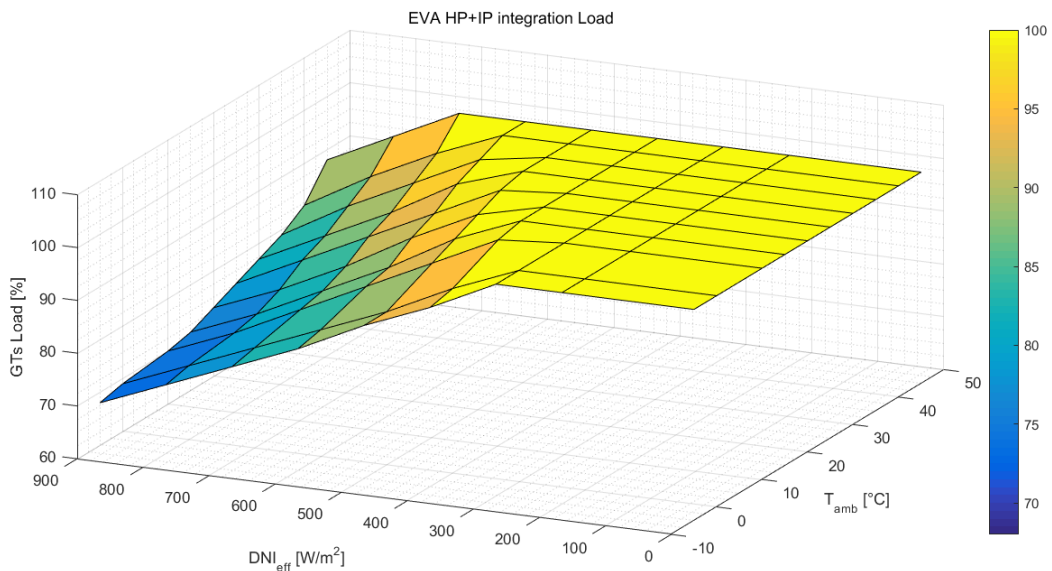


Figure 84: GTs load regulation as a function of the effective DNI and ambient temperature for EVA HP+IP layout.

The EVA HP+IP configuration produces more electricity than EVA+SH and ECO+EVA+SH ones because it is able to produce more solar steam without GTs load reductions thanks to the intermediate pressure solar evaporator.

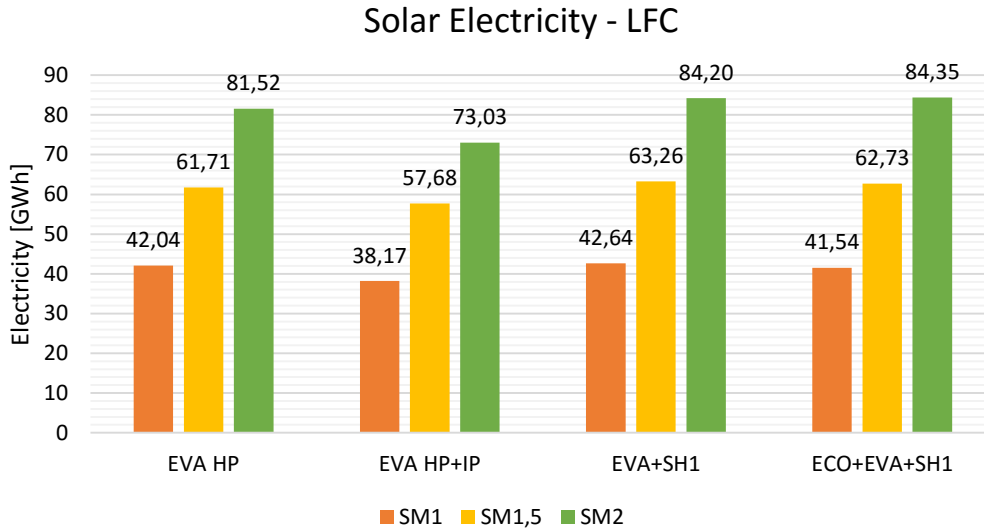


Figure 85: Annual electricity production attributed to the solar resource for different layouts with LFC and different solar multiple.

Figure 85 shows the solar electricity production for the previously analysed configurations. For SM1, EVA HP and EVA+SH show the highest solar production, since the temperatures of introduction of the heat in the cycle is higher. Instead, EVA HP+IP has a part of its solar field (i.e. IP evaporator) that gains heat at lower temperatures, and thus the total contribution of the solar field to electricity production is lower.

Because of GTs load reduction, annual electricity production can decrease markedly when a great amount of solar steam is available. With the aim of keeping the electricity production at least equal to the reference CC, the solar field can be partially defocused to raise the GTs load and consequently the cycle efficiency. Results for EVA HP defocused configurations are shown in Figure 86 and in Figure 87.

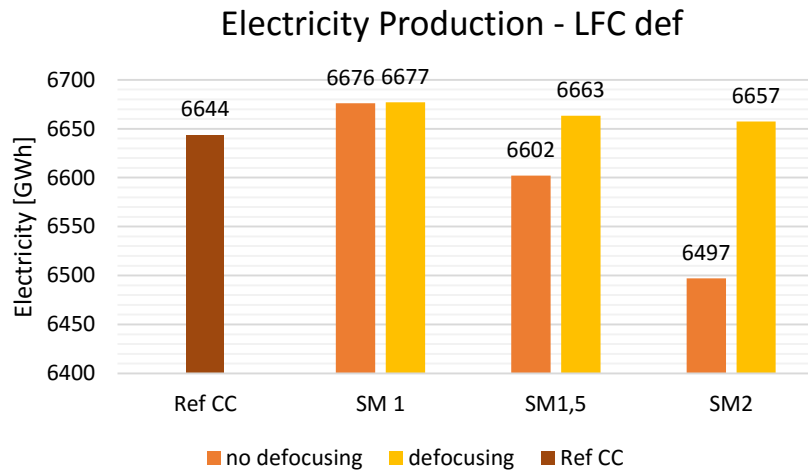


Figure 86: Annual electricity production with and without defocusing for the EVA HP layout with LFC and different solar multiples.

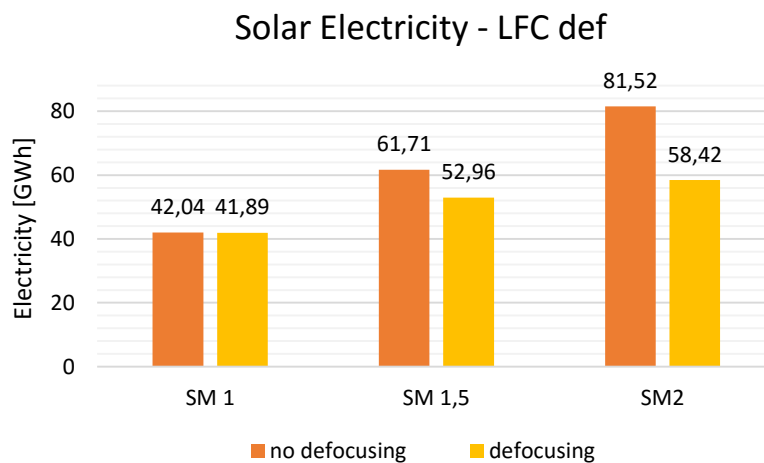


Figure 87: Annual solar electricity production with and without defocusing for the EVA HP layout with LFC and different solar multiples.

For SM1 configuration, there are not significant changes between the simulations, in fact GTs load decreases slightly without defocusing. The difference is more evident for higher solar multiples. The total electricity production is still higher for the SM1 configuration; in fact, since the load reduction is limited, the solar integration is reflected in the cycle power boosting. The defocusing is introduced to guarantee that the integrated cycle does not produce less energy than the reference combined cycle; in this way, for the hours which need defocusing, the power output is equal to the reference CC one and so, however, the solar power cannot be fully exploited. Moreover, even if with the defocusing of the solar field is

possible to achieve a higher overall electricity production, the solar production decreases proportionally to the defocused fraction of the solar field.

Another way to avoid the decrease of the net power output is to resize the ST. Annual results, in terms of Electricity production and solar electricity for these cases are shown in Figure 88 and in Figure 89.

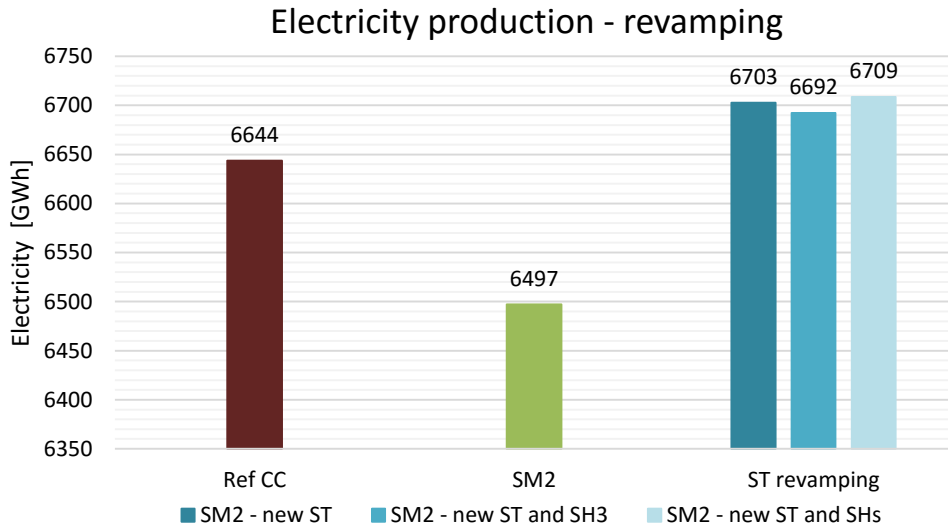


Figure 88: Annual electricity production for the reference CC and EVA HP LFC with and without revamping.

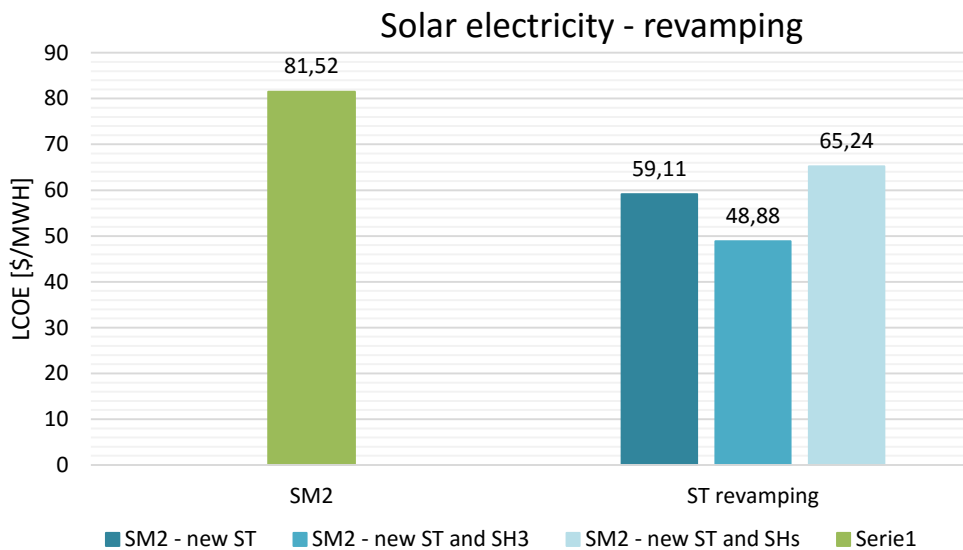


Figure 89: Annual solar production for the EVA HP LFC layout with and without revamping.

The boosting effect of the new ST is evident in comparison to the EVA HP SM2 configuration; in particular, the layout where all SHs have also been replaced shows the best results. However, the solar electricity production is lower for revamping CC configurations; in fact the solar electricity, defined as in Equation (42), accounts also for the power decrease with respect to the reference CC during night hours. This is due to the fact that, when the solar field is not operating, the ST is oversized in comparison with the steam mass flow produced by the HRSGs. In this way, when the solar steam is not available, the same steam flow of the reference cycle (at the same ambient conditions) is expanded in a larger turbine; inlet pressure is thus lower and the enthalpy variation exploited is lower too. Consequently, power output of the new turbine is reduced, as showed in Figure 78. Moreover, desuperheating is needed to control the heat exchanger temperature. Power decrease is higher for the new ST and SH3 because of the higher size of the heat exchanger and the higher request desuperheating.

In Figure 90 and Figure 91, integrations with different solar collectors, with solar multiple equal to 1, are compared.

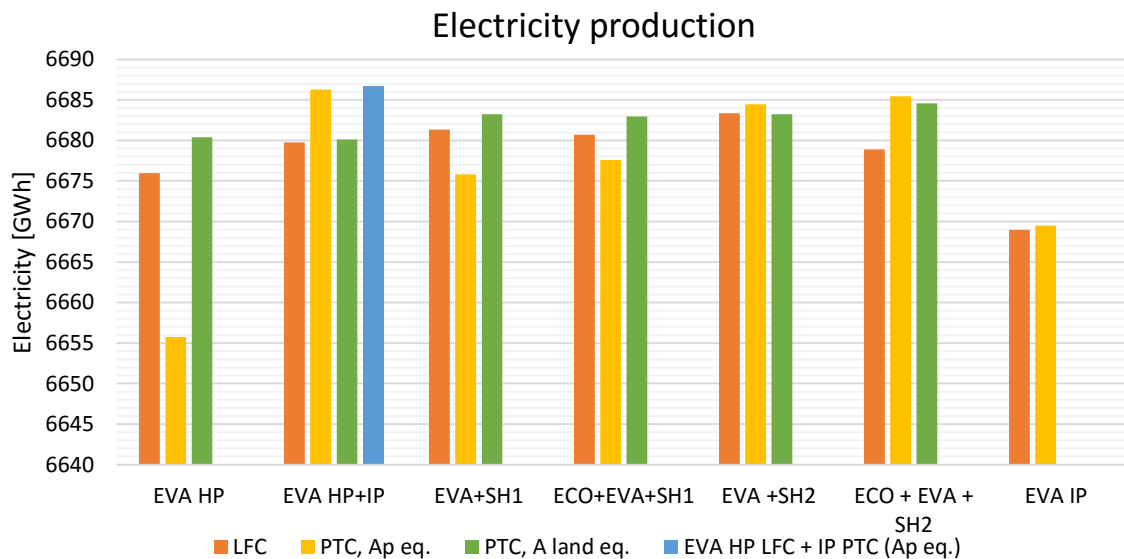


Figure 90: Annual electricity production for different layouts with SM1 and different solar technologies.

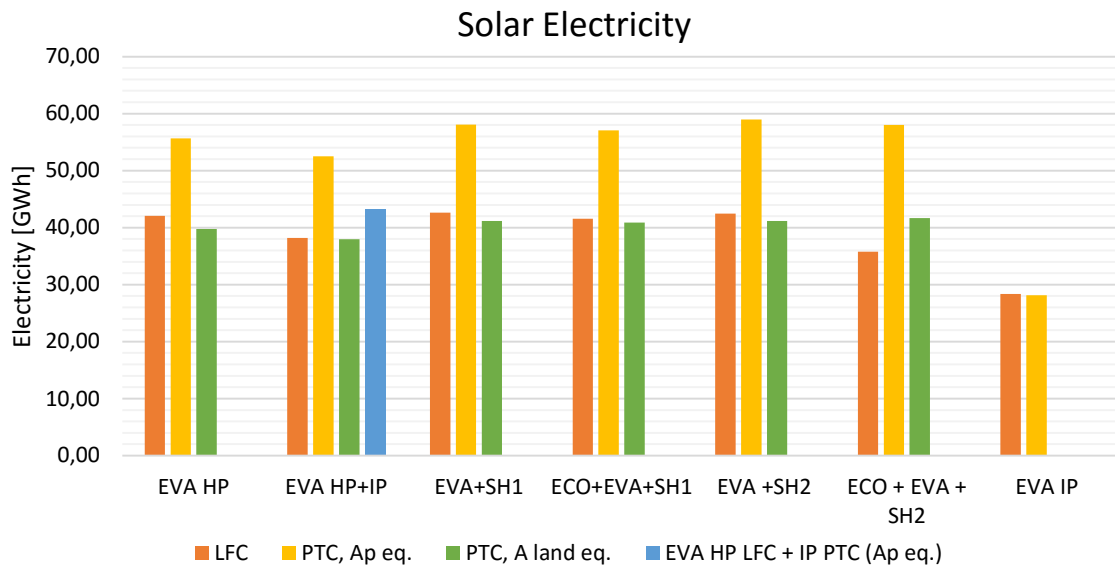


Figure 91: Annual solar electricity production for different layouts with SM1 and different solar technologies.

PTC configurations are compared on equal aperture area or on equal land area basis with respect to LFC layout all with SM1. PTC configurations with equal land area produce almost the same electricity output with respect to LFC, but the solar electricity production is slightly lower for PTC. In fact, one of the advantages of LFC is that their required land area is smaller than PTC because the latter requires a higher distance between each row to limit shading, while for LFC this requirement is minimised. For this reason, LFC can be more easily handled when only a limited land area is available, as can happen when the integration in existing plant is considered. Because of the higher overall efficiency, PTCs can produce, with the same aperture area, a higher quantity of electricity from the solar resource. However, since the steam production in the solar field is sensibly higher, the GTs load must be decreased more often and, therefore, the annual electricity production results lower. The only exception is the EVA HP+IP configuration because, in this case, the GTs load decreases only slightly and the boosting effect of the solar steam prevails on the load reduction. For configurations that include SH2, being equal the aperture area, a higher fraction of the solar field is dedicated to the superheating with a consequent decrease of the steam produced and so of the required GTs load reduction. In this way, the highest parabolic production is more evident, and the electricity production is higher for PTCs than for LFCs.

From the annual simulation, it can be seen that the increase of the solar multiple allows the production of more energy from the solar source and a fuel saving, at the expenses of a limitation on the maximum energy production. Instead, with solar multiple equal to 1 the power boosting effect is maximised. The analysis of $\eta_{incr,sol-el,annual}$ (Figure 92) confirms the same trend of the nominal conditions; annually, configurations with higher average temperature on solar field are characterised by highest values. x_{sf} , as for nominal conditions, is higher for parabolic troughs integration with equivalent aperture area since it doesn't

account for the GTs load reduction. It increases as the Q_{sf} increases and it is higher for equivalent area PTCs.

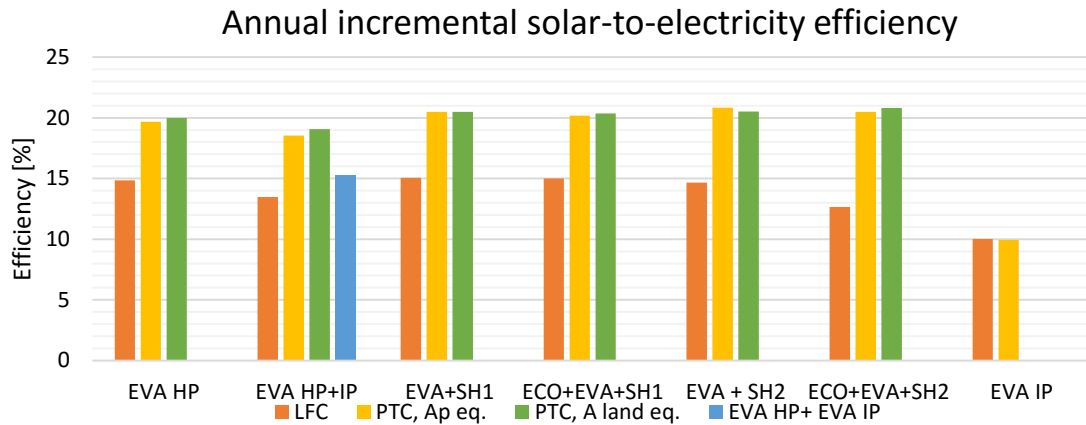


Figure 92: $\eta_{incr,sol-el,annual}$ for different layouts, SM1 and different solar technologies.

Among all the SM1 configurations, the highest electricity production is achieved with configurations with part of the superheating made in the solar field. In particular, the highest values are reached with PTCs at equivalent land area even if their solar production is slightly lower than Fresels one. EVA HP+IP also has a high electricity production, in particular when the two solar fields are designed using different collectors. Finally, EVA HP has one of the lower total electricity productions but it achieves the highest solar energy produced with LFCs. The economic analysis must be carried out to understand which solution represents the best compromises between costs and electricity production (solar and overall).

Results so far exposed are related to the power boosting mode, the solar field is used to produce additional energy during the year. For SMs higher than 1, the overall production is lower than the one of the reference case so there is no convenience in a larger solar field. The solar share is very low because the fossil production is always at its maximum value. For some cases, there is a slight reduction of the fuel consumption but this is due only to the requirement of keeping the steam turbine inlet steam mass flow within the maximum value so the reduction in CO₂ emissions is not properly considerable. The correct way to estimate the potential of CO₂ emissions reduction of ISCCs is by considering the fuel saving modality.

5.3 Fuel saving

This scenario considers a load curve during the year; an example of scheduled load for a combined cycle load has been adapted from data from the Italian GME (Gestore del Mercato Elettrico)[101]. Figure 93 shows the one week profile that has been extended on the whole year. It is characterised by several hours in which the plant is shut down, even during sunny

hours, so this may not be a perfect condition for the ISCC. However, this curve is not representative for every combined cycle.

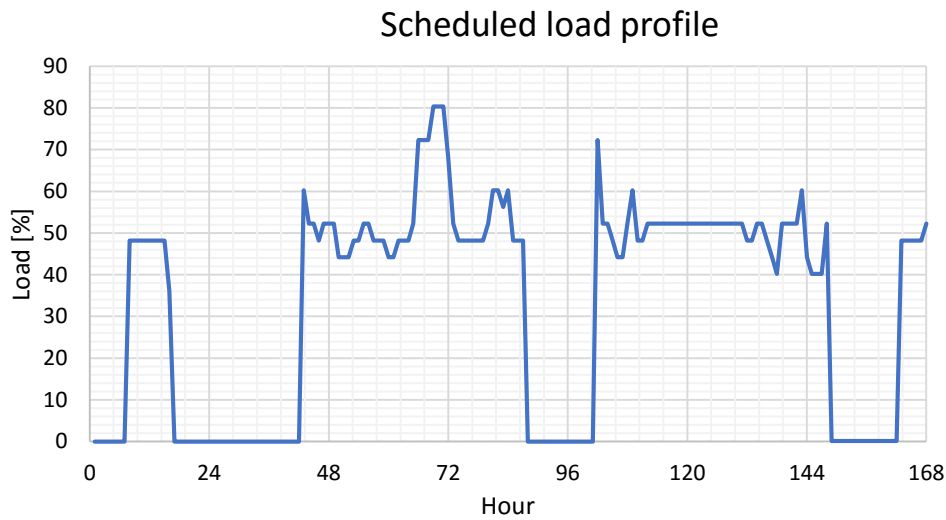


Figure 93: Scheduled load profile for the fuel saving scenario.

ISCC and reference CC have to be compared when producing the same power output. In this way, it is possible to estimate how much the solar integration can reduce fuel consumption, and thus CO₂ emissions, and how the different regulations can change electricity costs.

For this case, Thermoflex® simulation has been set up differently from the power boosting case. In particular, for every combination of temperature (from -5°C to 45°C, with 5°C steps) and DNI (from 0 to 1000 W/m²), several load conditions (from 100% to 20% of the GTs load) have been simulated.

Only the EVA HP configuration has been evaluated in this scenario, because from the previous analysis (and from the economic analysis presented in Chapter 6) it results the most convenient configuration. Solar multiples 1 and 2 have been simulated; in fact, it is interesting to verify if, with respect to the results of the power boosting strategy, there is an effective convenience in having a bigger size field when the electricity production is fixed. In this case, SM2 configuration allows producing a higher fraction of the requested electricity from the solar resource, further minimising fuel consumption with respect to the solar multiple 1 and thus reducing fuel costs. Cost analysis will then define if fuel cost reduction is enough to make integrations convenient.

Ambient conditions are the same of the power boosting analysis (representative year in Las Vegas) and the load profile requires often the plant to operate at GTs load lower than 50%. In some cases, solar field production allows shutting down one of the two gas turbines in the ISCC, while the reference CC needs to operate with both the turbines at low loads. In this way, in the integrated cycle, the GT efficiency is higher.

Over the representative year, both the SM1 and the SM2 allow producing the requested electricity with a fuel consumption reduction, which is more evident for the SM2 configurations; Figure 94 shows the fuel consumption over 48 hours (August 16th and 17th). When there is not enough DNI_{eff} to switch on the solar field, the fuel consumption is the same for the two plants while, during sunny hours, it is lower for the ISCC. The difference between the two lines reaches about 22% for the hours with high DNI_{eff} .

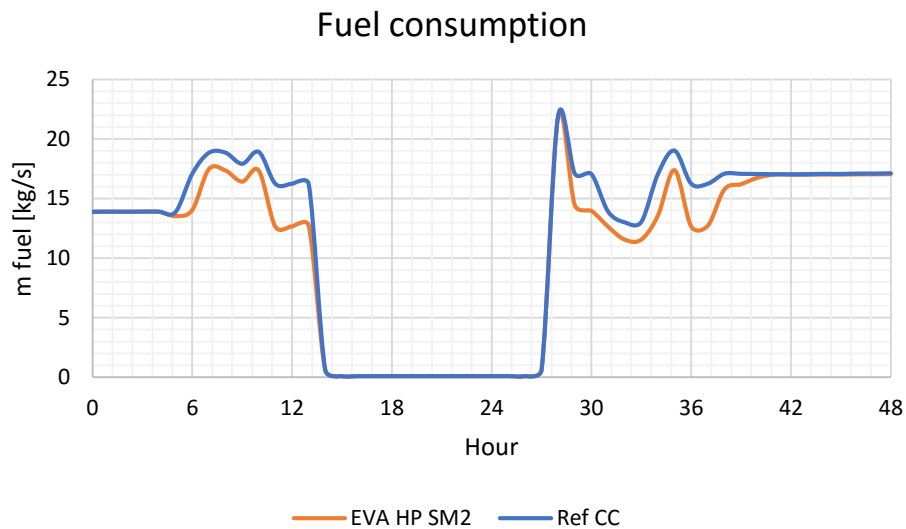


Figure 94: Fuel consumption over 48 hours (August 16th and 17th) for the reference combined cycle and EVA HP SM2 in the scheduled load scenario.

Consequently, the integrated plant allows reducing CO₂ emissions, from 346276 ton/yr of the reference CC to 306829 ton/yr and 301861 ton/yr respectively for SM1 and SM2 configurations. That is an emission reduction of 11,4% for SM1 and 12,8% for SM2.

Annual solar shares for these configurations with the fuel saving strategy increase with respect to power boosting one, in fact, when the plant is working and there is enough solar energy, only the fossil power is reduced by reducing GTs load.

Given load profiles are characterized by some days in which the plant does not operate or is shut down during hours of high radiation. Since ISCC has an integrated renewable fraction, in a scenario in which a subsidies program for renewable energy is foreseen, the plant would likely be working when the effective DNI is high enough to guarantee the solar production. To estimate what would result with this different scenario (Modified scheduled load), it has been decided to evaluate the electricity production with the integrated plant working at the 25% of the GTs total load (i.e. a single turbine operating at 50% load) when the solar field can work, to allow the solar production. In Figure 95 the new fuel consumption for the ISCC is represented for the same 48 hours of the previous case (August, 16th and 17th). Hours from

14 to 18, the higher fuel consumption of the ISCC, which is turned on to allow the solar production.

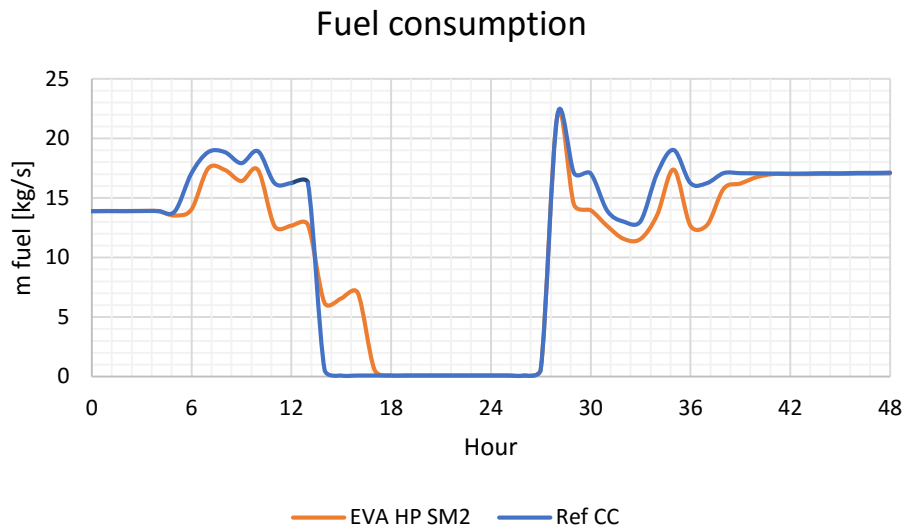


Figure 95: Fuel consumption over 48 hours (August 16th and 17th) for the reference combined cycle and EVA HP SM2 in the modified scheduled load scenario.

In this case, the solar share and the solar power increase but the fuel consumption increases too (and it is higher than the reference CC consumption) because the plant operates for a higher number of hours.

Table 43 summarises the main annual parameters for SM1 and SM2 configurations with the three load regulations analysed: full load (i.e. power boosting), scheduled load (i.e. fuel saving) and modified scheduled load.

Table 43: electricity production, solar share and CO₂ emissions for SM1 and SM2 EVA HP with three different load regulations.

	Electricity Production	Solar Electricity	x_{sf}	CO ₂ emissions
	[GWh/yr]	[GWh/yr]	[%]	[ton/yr]
Full load SM1	6675,97	42,04	0,84	2493905
Scheduled load SM1	2152,83	34,36	1,77	828439
Modified scheduled load SM1	3839,80	47,27	1,43	1461098
Full load SM2	6497,13	81,52	1,71	2422887
Scheduled load SM2	2152,83	63,25	3,53	815027
Modified scheduled load SM2	2303,88	90,67	4,62	877836

5.4 Other integrations – Power boosting

Yearly simulations have been carried out for fuel preheating and solar cooling configurations too, for these layouts, the power boosting only is considered (i.e. full load operation for 8760h per year). They are not included in the previous analysis since the solar field has been sized with a different approach with respect to other configurations and, being different the integration effects on the cycle, results are difficult to compare.

5.4.1 Solar fuel preheat hybridisation

The fuel preheating layout allows the reduction of water withdrawal-from the HRSG with a slightly increase of the steam cycle annual efficiency (from 35,49% to 36,54%). The annual fuel efficiency is only slightly increased by the preheating integration since the fuel inlet temperature increase is not very high. The boosting effect is still very light, in comparison to the previously analysed configurations.

Table 44: Annual simulation results for solar fuel preheat hybridization

	Ref CC	ISCC – fuel preheating
Electricity production [GWh/yr]	6643,64	6646,35
Solar Production [GWh/yr]	-	2,88
Fuel consumption [ton/yr]	924748	924606
Q_{SF} [GWh/yr]	-	16,406
x_{sf} [%]	-	0,137

The solar electricity production is equal to the total power difference between the integrated plant and the reference CC. It is about 2,88 GWh/year: this value is bounded to the higher power output of GTs (which accounts for about the 18%) and to the higher steam turbine power output (about 82% of the total power increase). The advantages of this integration is the little invasiveness of the layout in the reference power plant, its simplicity and the limited impact on the investment cost. Larger effects may be obtained by substituting the heat exchanger, with the aim of reaching higher fuel temperatures (e.g. 200°C) and therefore increasing the solar field size.

5.4.2 Solar cooling hybridisation

Air cooling integration increases the power output and the gas turbine efficiency during high ambient temperature hours. An advantage of using solar energy is that it produces energy for the absorption chiller when most needed, that is during peak times of the day and year.

GTs annual efficiency increases from 37,13% to 37,31%, but at the cost of an increased overall fuel consumption of the 1,4% (from 924748 ton/year to 937668 ton/year). Even if

the total electricity output increases, the effect of the higher fuel consumption prevails and $\eta_{CC,annual}$ reduces from 55,61% to 55,56%.

It is not possible to calculate the electricity contribution from the solar resource for this layout coherently with the given definition for the bottoming solar integration, since the solar input has the effect of increasing the fuel input and thus the two shares can not be separated from the solar one.

Table 45: Annual simulation results for solar cooling hybridization.

	Ref CC	ISCC - chiller
Electricity production [GWh/yr]	6643,64	6730,13
Fuel consumption [ton/yr]	924748	937668
Q_{SF} [GWh/yr]	-	24,83
x_{sf} [%]	-	0,205

Chapter 6

Economic analysis

In this chapter the economic analysis of analysed power plants is presented. The analysis is carried out using the LCOE method. Then, a sensitivity analysis has been conducted in order to analyse the impact of the variation of fuel price and solar field costs.

6.1 Method and cost assumptions

LCOE methodology attempts to compare different methods of power generation on equal basis and it can be regarded as the price at which the electricity must be sold to break-even at the end of the power plant lifetime. Based on IEA (International Energy Agency) simplified methodology, the LCOE is defined as:

$$LCOE = \frac{FCR \cdot C_{inv} + C_{O\&M} + C_{fuel}}{E_{annual}} \quad (48)$$

Where C_{inv} is the total investment cost, $C_{O\&M}$ accounts for the yearly operation and maintenance costs, C_{fuel} is the annual fuel expenditure and E_{annual} is the total electric energy produced in a year. FCR is the Fixed Charge Rate and is calculated with the following expression:

$$FCR = P_1 + \frac{k_D(1 + k_D)^l}{(1 + k_D)^l - 1} \quad (49)$$

Where k_D is the real debt interest, P_1 is the annual insurance rate and l is the life expectancy of the power plant. The Fixed Charge rate represents the percentage of the total plant cost required per year, over the project life, to cover the minimal annual revenue requirements. It depends on the expected lifetime and on the financial variables values assumed (see Table 47).

Table 46: Economic assumptions for FCR evaluation [34].

Debt financing percentage	60	%
Equity financing percentage	40	%
Debt interest rate	13	%
Annual insurance rate	1	%
Useful life	25	years
Nominal discount rate	8,2	%
FCR	10,53	%

Since the hybridisation is small ($x_{sf,annual}$ from about 0,8% to about 2%) the effect on the LCOE calculated as above can be limited and LCOE values for different configurations can be very close to each other. For this reason, the solar marginal LCOE can be calculated as the ratio between levelised plants costs, and the solar electricity production (calculated as the difference between the ISCC electricity production of the ISCC with the one of the equivalent combined cycle, see paragraph 5.1). Coherently with the definition of the solar electricity as the difference between the electricity production of the two plants at the same GTs load, the fuel consumption is not taken into account in the solar marginal LCOE¹¹ ($LCOE_{sm}$) since it is the same. $LCOE_{sm}$ is calculated as:

$$LCOE_{sm} = \frac{\Delta C}{E_{sol}} \quad (50)$$

Where

$$\Delta C = (FCR \cdot C_{inv} + C_{O\&M})_{ISCC} - (FCR \cdot C_{inv} + C_{O\&M})_{Ref\ CC} \quad (51)$$

$LCOE_{sm}$ represents the marginal cost of the additional MWh produced thanks to the solar integration in the combined cycle. This value can be compared with solar only power plant (i.e. parabolic trough SEGS type).

Investment costs for the reference combined cycle have been taken from Thermoflex®; investment costs also assess for Owner's Soft & Miscellaneous Costs, which include land, development expenses, legal and permitting expenses, et cetera. The total investment cost estimated by Thermoflex® for the reference combined cycle is 352,183 M\$, i.e. a specific investment cost of 485\$/kW; this value is lower than the ones founded in references [80]. Probably, Thermoflex underestimates the investment costs, also because some components of the combined cycle are not in PEACE library (e.g. moisture separator).

¹¹ Additional costs usually account also for the different fuel costs and the solar energy is evaluated as the net electricity production difference between the ISCC and the reference CC. In this analysis some configurations produce less energy than the reference CC, so the solar marginal LCOE is evaluated with respect to the equivalent combined cycle.

The solar integration is considered as made in an already existing plant, so for ISCC layouts, the total investment cost is evaluated by adding to the reference CC costs the additional costs sustained for components needed for the integration (e.g. additional pumps, solar collectors and additional land required for the solar field).

Annual operational and maintenance costs include expenses for operating and maintenance labours, materials and consumable items beside the fuel costs. They are expressed as a percentage of the total investment costs (see Table 47) [34]. O&M costs are separated for the solar part and the combined cycle one; solar O&M are evaluated as a fraction of the solar field investment cost while CC ones as a fraction of the fossil-only power plant components.

For the fuel cost component of the LCOE, Nevada natural gas price is taken from U.S. Energy Information Administration (EIA) and it is in accordance with medium USA gas prices [102]. The natural gas price results markedly lower than the one of European markets (of about 35c€/kg [103]). All the consideration are made without taking into account any special tariff for the solar production. All the economic assumption are summarised in Table 47.

Table 47: Costs assumptions for ISCC and CC power plants.

Fuel price	24,932	c\$/kg
Specific land area cost	2	\$/m ²
Specific investment cost for Supernova evaporator section	250	\$/m ²
Specific investment cost for Supernova evaporator section	300	\$/m ²
Specific investment cost for Nova evaporation section	200	\$/m ²
Specific investment cost for Polytrough 1800	100	\$/m ²
Specific investment cost for ET-150 evaporation section	360	\$/m ²
Specific investment cost for ET-150 superheating section	432	\$/m ²
CC O&M equipment cost percentage of investment per year	5	%
SF O&M equipment cost percentage of investment per year	1	%

6.2 Cost evaluation

In the following section LCOE and solar marginal LCOE analysis is presented for the various configurations presented in Chapter 4, using the results from yearly simulations. Two approaches have been adopted: the power boosting mode, where the power plant runs always at its maximum load, and the load following mode, where the power plant has to produce a defined power output.

6.2.1 Bottoming cycle - Power boosting

Figure 96 shows LCOE for integrations with LFCs. The introduction of the solar field increases LCOE of the power plant; overall, costs are higher for integrated plants but the electricity production does not counterbalance them, both for plants with SM1 and higher SMs. However, since solar collector are in early stage of their development, there are good

margin for cost reduction. In fact cost for solar field are sensibly higher with respect to combined cycle ones. LCOE are lower for plants with solar multiple 1 but they are still higher than CC one because the additional electricity produced is not enough to prevail over increased investment costs. Among the integrations with SM2, the lowest LCOE is the one of EVA HP+IP configuration. As explained in paragraph 5.2, GT's load remains higher, with a consequent higher annual electricity production. In addition, because of the lower temperature, the IP solar collector is cheaper than the HP one, reducing the impact on the total investment cost. However, LCOE is not very significant when considering the integration with a power boosting purpose, it may be more meaningful to analyse the cost of the additional solar production, i.e. the solar marginal LCOE. Figure 97 summarises $LCOE_{sm}$ for Fresnel collector integrations.

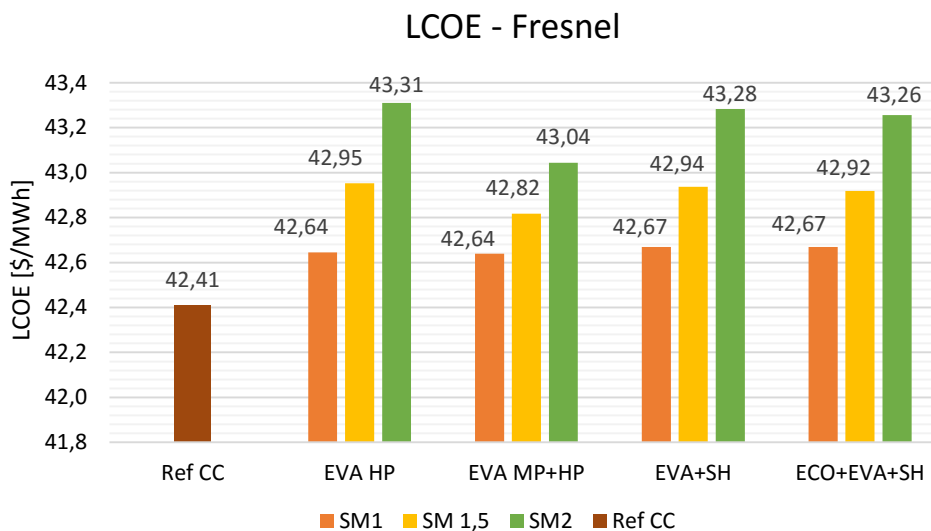


Figure 96: LCOE for the reference CC and ISCC layouts with LFC and different solar multiple.

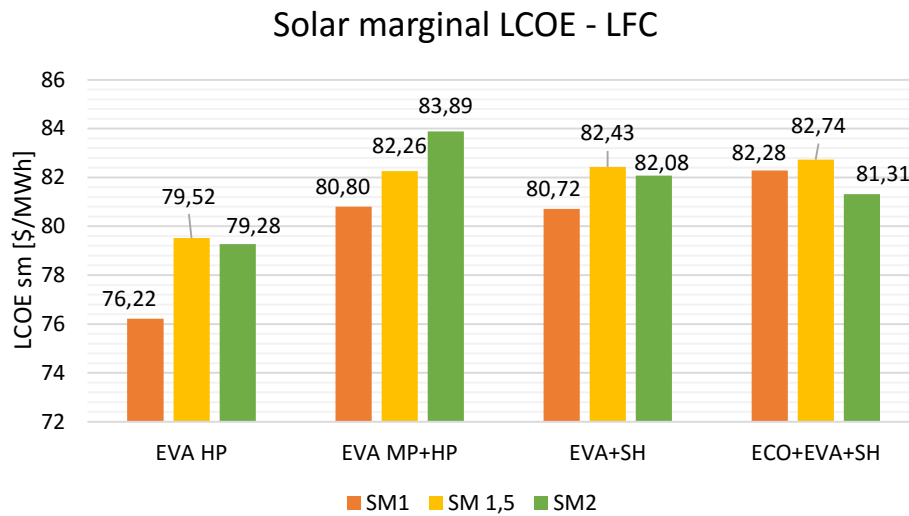


Figure 97: Solar marginal LCOE for the reference CC and layouts with LFC and different solar multiple.

EVA HP with solar multiple 1 shows the lowest solar marginal LCOE. This is due to the fact that this integration has the best compromise between the solar energy production and the additional costs related to the integration. SM 1,5 configurations have the highest $LCOE_{sm}$, because the costs increase is not counterbalanced by a significant increase in the solar electricity produced. Layouts with equal solar multiple have almost the same aperture area, so investment costs for configurations where a part of the superheating is made in the solar field are the highest. In fact, being equal the aperture area, the introduction of a part of SH increases overall solar field costs, which are not counterbalanced by the increase of solar energy production. EVA HP+IP SM1 layout has a higher $LCOE_{sm}$ because, even with lowest additional costs, the solar energy production is too small to be competitive with other integrations.

To obtain at least the same power output of the reference combined cycle in the same ambient condition, a fraction of the solar field can be defocused to increase GT load (see paragraph 5.2). Figure 98 and Figure 99 show results of the costs analysis for the EVA HP layout with and without defocusing for different solar multiples.

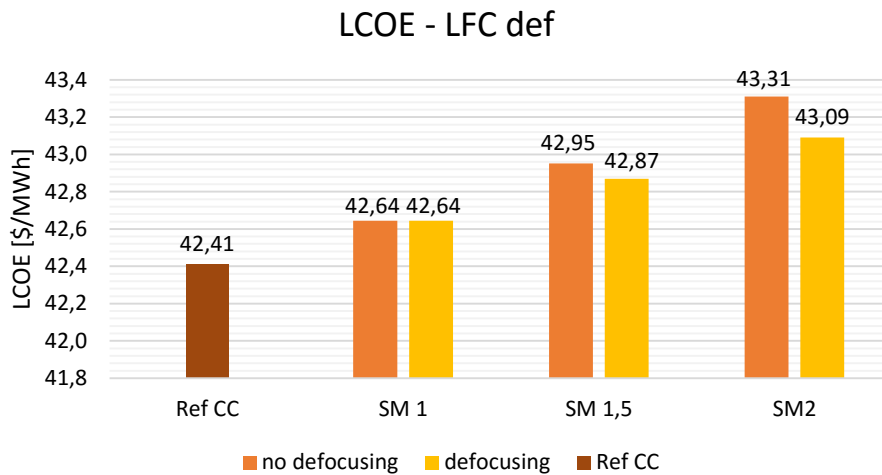


Figure 98: LCOE for EVA HP configuration with and without defocusing.

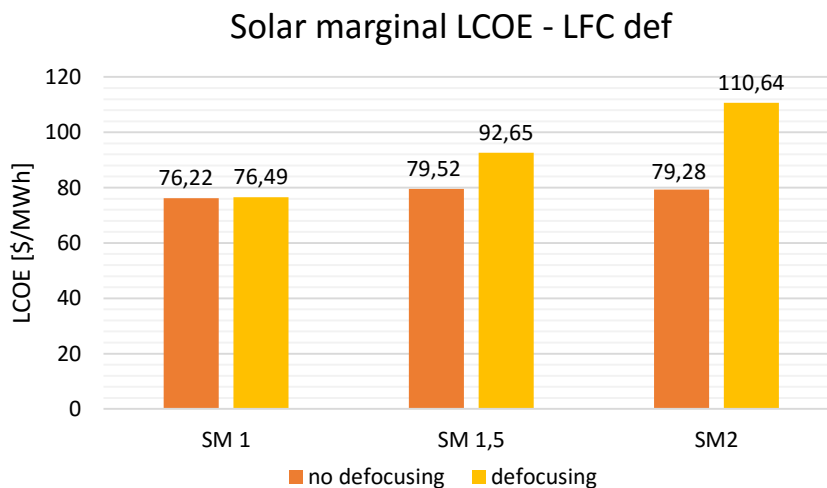


Figure 99: Solar marginal LCOE for EVA HP configuration with and without defocusing.

As shown in paragraph 5.2, there is no substantial differences in SM1 configuration with and without defocusing since it is necessary for just few hours per year. The defocusing reduces the power plant LCOE since it allows the plant to produce more electricity. However, the $LCOE_{sm}$ increases since the solar field investment is less exploited with this kind of regulation.

In Figure 100, the LCOE for the various configurations with the replacement of the ST is shown. It can be seen that the configuration with the redesign of the ST and all SHs is the one with the lower LCOE. In fact, it allows the inlet ST temperature to reach its nominal value, balancing the additional the cost increase due to the revamping of the steam turbine.

However, the solar marginal LCOE (Figure 101) increases significantly with respect to SM2 configuration without modifications. This is due to the fact that all the costs are charged on the solar part.

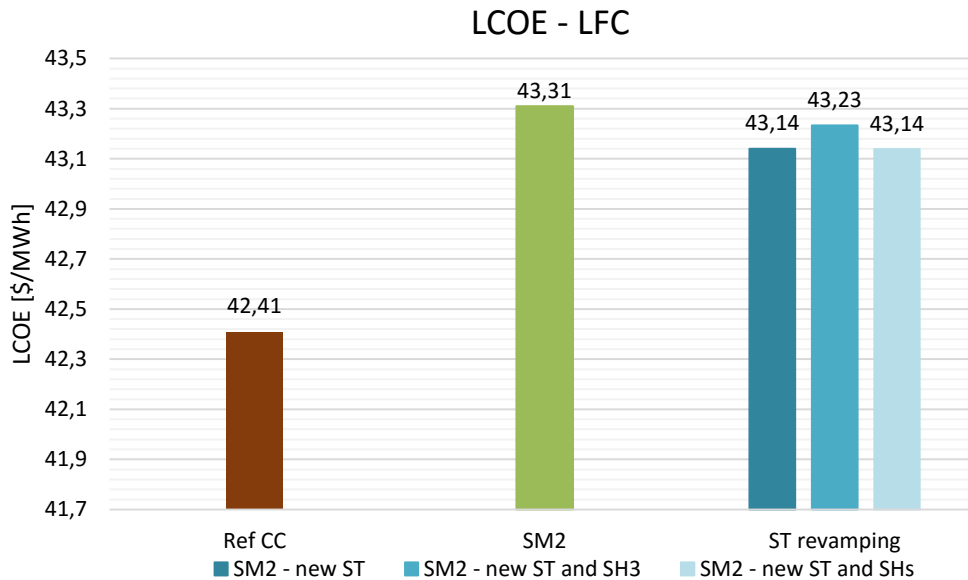


Figure 100: LCOE for EVA HP SM2 configurations with the replacement of the ST.

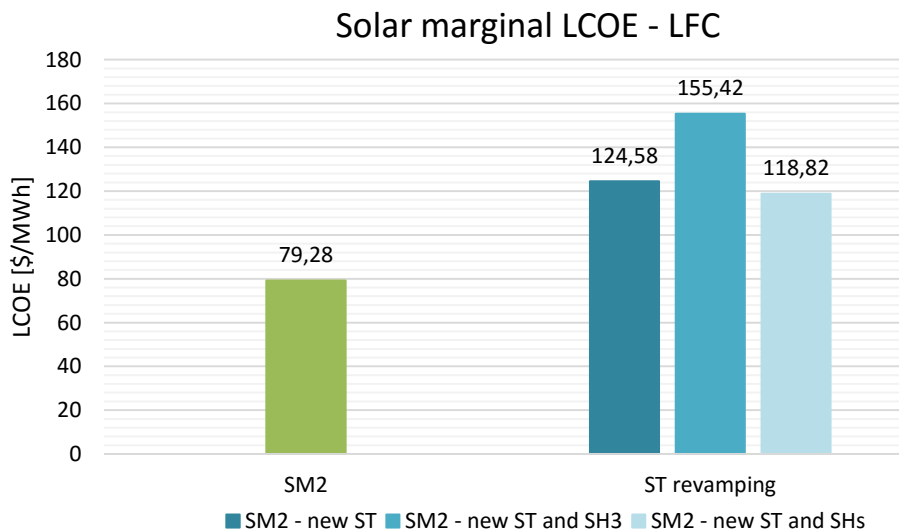


Figure 101: Solar marginal LCOE for EVA HP SM2 configurations with the replacement of the ST.

Probably, the resizing of steam turbine and heat exchangers may be more convenient with a bigger solar field, thus the solar electricity produced during the year would be higher and it would justify the higher cost for the components modifications.

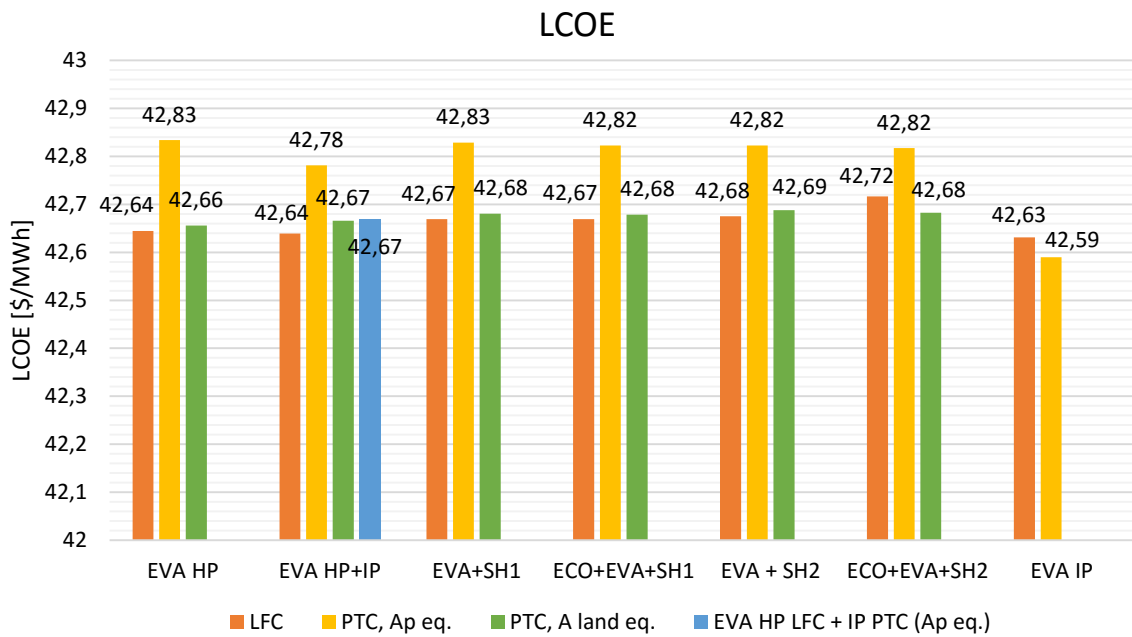


Figure 102: LCOE for different ISCC layouts with solar multiple equal to 1.

Figure 102 shows LCOE results for different configurations and solar technologies; LCOE are sensibly higher for integrations with PTCs with constant aperture area. In fact, PTCs have higher specific costs; moreover, the highest solar steam production causes a higher load reduction to maintain the correct ST inlet stream. In this way, the total electricity production does not counterbalance higher costs. Even for cases with constant land area, PTCs show slightly higher LCOE, since PTC costs can be about 45% higher than LFC ones. Moreover, the higher load reduction lowers the electricity production (see paragraph 5.2) so that the integration costs prevail. Configurations with EVA IP have a sensibly lower LCOE since the collector employed (Polytrough1800 for PTC configuration and Nova1 for LFC) are cheaper.

However, in this kind of economic analysis, the amount of solar steam produced is not considered individually; so, to consider the cost of the additional solar steam produced, $LCOE_{sm}$ is analysed. The only exception is the ECO+EVA+SH2 integration; in this case the electricity production balances PTCs costs (in fact, having a lower solar steam production, the load reduction is reduced even for the parabolic case).

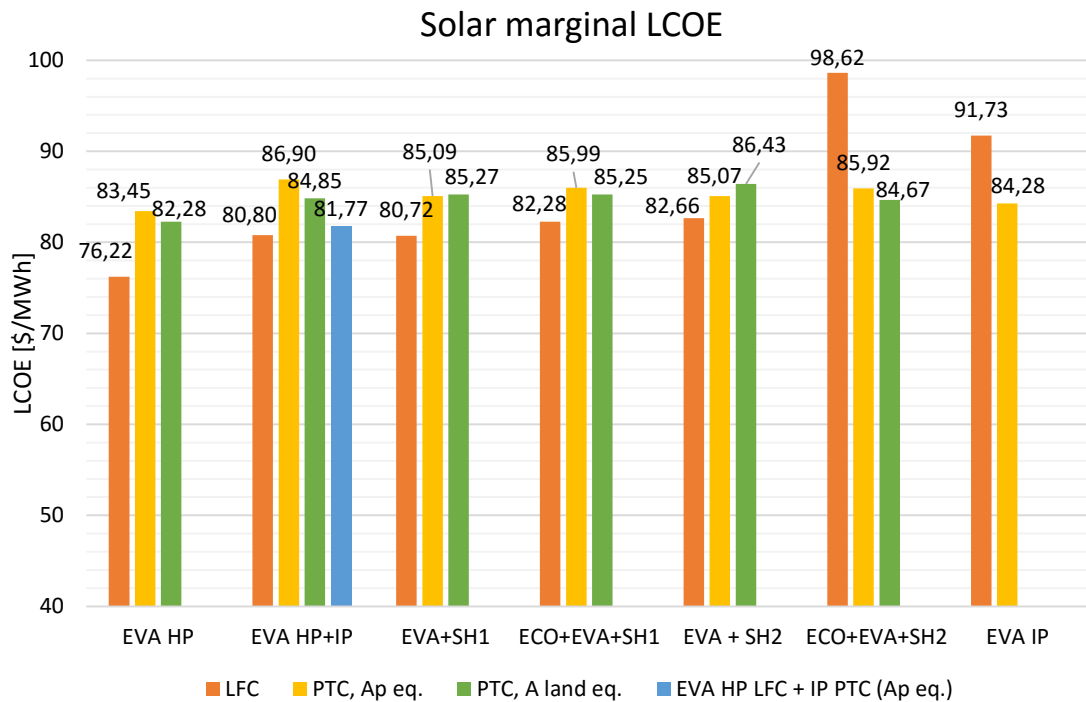


Figure 103: Solar marginal LCOE for different ISCC layouts with solar multiple equal to 1.

Figure 103 shows that the lower solar marginal LCOE is the one of EVA HP configuration. This layout is preferred for its simplicity and its lower additional costs. EVA+SH configuration also shows good performance; its costs are higher than the EVA HP layout, but, thanks to higher temperature of heat introduction, it is possible to produce more solar energy. EVA HP+IP with LFC and PTC shows low solar marginal costs and it is a good compromise between a good electricity output and solar production. EVA IP configuration, which has the lowest LCOE for both PTC and LFC, shows in comparison high solar marginal LCOE: even if the additional investment cost is relatively low, the solar energy produced is not sufficiently high.

Whichever configuration and solar multiple is employed, it is clear that the solar electricity produced with an ISCC is cheaper than the solar electricity produced in a solar only power plant (see Chapter 2). So the solar integration in a combined cycle, when the solar steam produced is employed as a power boosting for the base plant, has the benefit of reducing solar energy production costs with respect to the stand alone solar technology. With the maximum flow limit on the steam turbine, the total electricity produced is not enough to balance higher costs and so the overall LCOE is higher for integrated cycle. Anyway, if a schedule load is given, the solar integration can be employed with a fuel saving purpose and results may change significantly.

6.2.1.1 Sensitivity analysis

A sensitivity analysis has been carried out to evaluate the impact of fuel and solar field costs. The fuel cost is an important fraction of the power plants LCOE and the impact of the fossil fuel price on the reference CC is shown in Figure 104.

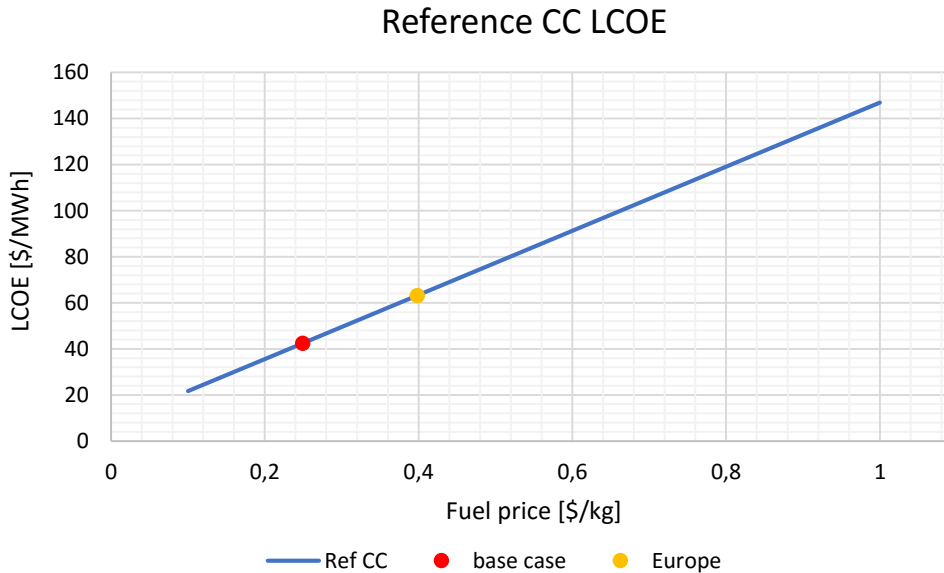


Figure 104: Reference combined cycle LCOE as a function of the fuel price.

The analysis showed that comparisons between the various configurations are not affected by the increase or reduction solar field costs of 25%. It has been observed that variations are symmetrical with respect to the base case. The variation is more evident for solar integration including at least one superheating section because of the higher cost of that section. It has been found that for cost lower than 120 \$/m², the LCOE of the EVA HP SM1 Fresnel configuration results lower than the reference CC (see Figure 105).

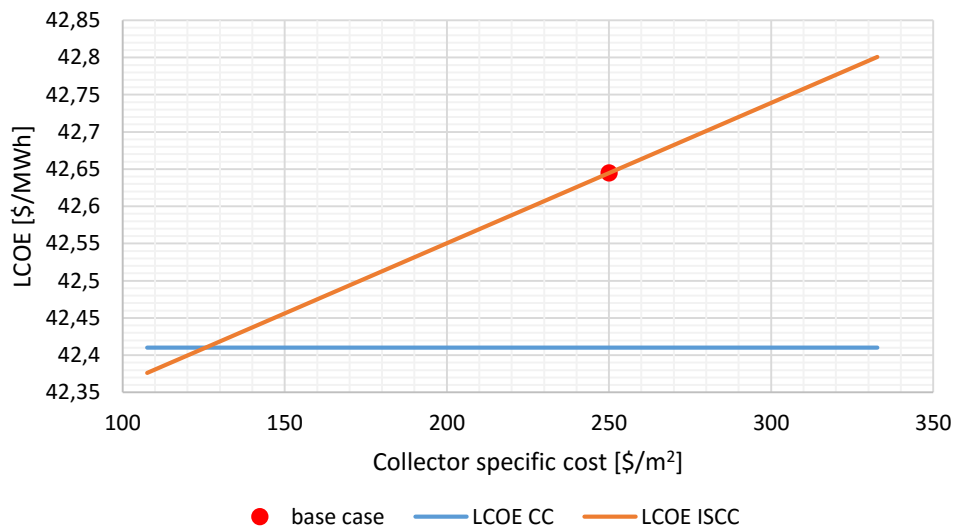


Figure 105: LCOE for the reference combined cycle and for ISCC as a function of the solar collectors cost specific to the aperture area.

The same approach has been followed for fuel price analysis; even in this case variations are symmetrical with respect to the base case and comparisons remain unchanged. It must be considered that the actual fuel price is quite low, due to trend of natural gas market in USA [104]. The increase of the fuel prices favours the ISCC over the reference combined cycle. The LCOE inversion point between the reference CC and the ISCC with EVA HP LFC configuration is for a fuel price of about 0,52 \$/kg, as shown in Figure 106.

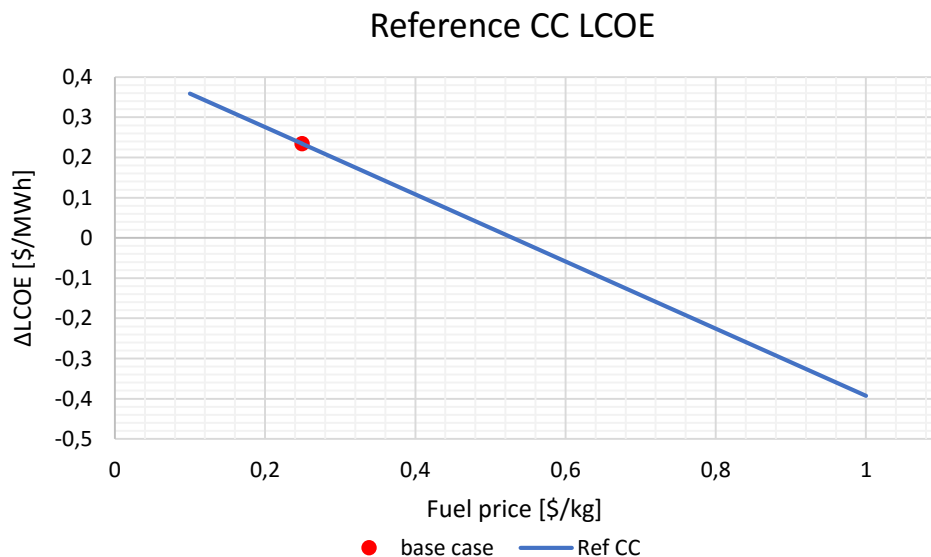


Figure 106: Δ LCOE, defined as the difference of the reference CC LCOE with the ISCC LCOE, as a function of the fuel price.

6.2.2 Bottoming cycle – Fuel saving

The main advantage of an ISCC that works under scheduled load condition is the reduction of fuel consumption and thus of fuel expenditure. In addition, fuel reduction allows reducing CO₂ emissions. When the scheduled load is imposed, the parameter of merit becomes the LCOE, since the solar marginal LCOE does not account for the fuel expenditure and it is more appropriate to compare different solar solutions. Two load profiles are defined for the ISCC (see paragraph 5.3): a scheduled load, which is the one used for the reference combined cycle, and the modified scheduled load, where ISCCs are always turned on when a sufficient radiation is available to produce the solar steam (representative scenario of a subsidized system). LCOE analysis in the fuel saving scenario has been performed for the EVA HP configuration with SM 1 and 2. In Figure 107 LCOE values are reported.

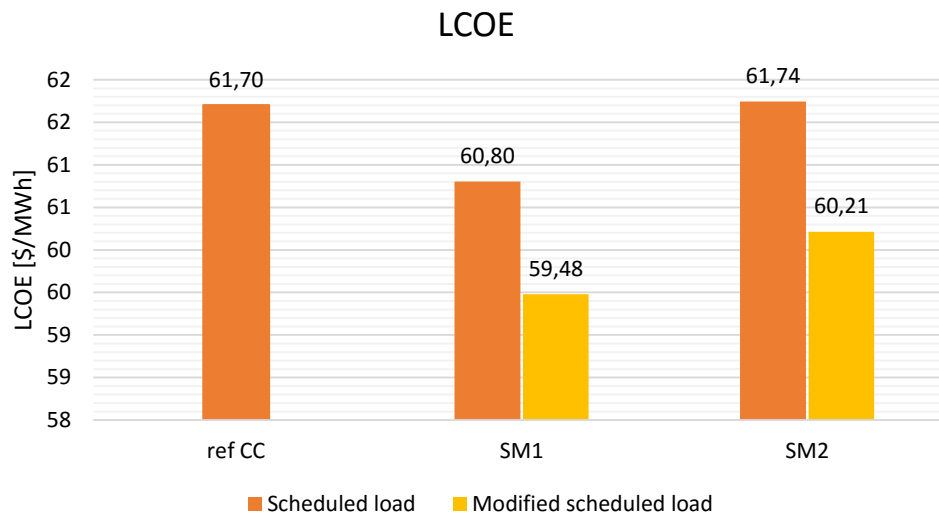


Figure 107: LCOE for the reference CC and EVA HP configuration with two different solar multiple in fuel saving scenario.

ISCC configuration with solar multiple equal to 1 has lower LCOE than the reference combined cycle. This result derives from the lower fuel consumption of the ISCC with respect to the reference combined cycle whereas their electricity production is the same; it means that the additional costs for the integration (i.e. solar field and additional pumps) are completely refunded by fuel savings. In addition, it must be considered that there is a reduction of the CO₂ emissions, without additional costs of removal systems. Therefore, is not possible to evaluate costs of the avoided CO₂, as long as the emission limitation is an additional benefit of a lower cost integration. On the other hand, SM2 configuration presents a LCOE slightly higher than the reference cycle. SM2 layout has higher investment costs that are not completely covered by fuel expenditure reduction. It must be highlighted that the modified scheduled load scenario further decreases the LCOE of solar configurations

with respect to the reference combined cycle; in this case also SM2 layout results more cost effective in comparison with the reference CC at scheduled load, even if the SM1 shows better performances.

6.2.3 Other configurations – Power boosting

In this paragraph the economic analysis for inlet air cooling and fuel preheating configuration, in the power boosting scenario, are presented. They are described separately from the bottoming cycle integrations, since the comparison is not made on equal aperture or land area basis, but the solar field is bounded to other network parameters (i.e. the inlet GT fuel temperature and desired temperature of GTs inlet air). For this reason, the solar share has lower values with respect to other configurations (i.e. 0,14% for fuel preheating and 0,2% for inlet air cooling). However, as said in the previous chapters, these configurations have a limited impact on the costs and complexity of the power plant. In fact, in solar cooling layout, the chiller does not directly modify the HRSG and, in the fuel preheating configuration, only the solar field and its pump are added (the heat exchanger of the reference combined cycle has not been substituted).

The introduction of the fuel preheating, increases the LCOE of the power plant from 42,410 \$/MWh to 42,418\$/MWh and its solar marginal LCOE is equal to 71,354 \$/MWh. The solar marginal cost results lower than the EVA HP and the impact on the LCOE is quite limited.

The solar air cooling allows the increase of the power output of the combined cycles, at the price of an increase of annual fuel consumption. This layout presents, indeed, an increase of the fuel expenditure and of investment costs for the introduction of the absorption chiller, the solar field, the evaporative tower, additional pumps and heat exchanger. For this layout, the LCOE increases from 42,410\$/MWh to 42,636\$/MWh; the solar air cooling is useful when an increase of the power output is needed, while the additional energy gain is not enough to achieve a LCOE reduction in comparison with the reference combined cycle. The use of solar energy together with the absorption chiller is particularly useful since, usually, solar steam production coincides with the summer peak request. As stated in previous chapters, it is not possible to separate the annual contribution of the solar resource from the yearly additional fuel needed when the chiller is active. Because of that, the marginal LCOE is defined as the cost of the additional MWh produced, including also the additional fuel costs, thus it is not comparable with the $LCOE_{sm}$ of the other configurations. Its value is 59,834\$/MWh.

Conclusions

The present thesis work presents the analysis of several layouts of Integrated Solar Combined Cycle (ISCCs) with line-focusing collectors in terms of nominal and annual performances and costs of the generated electricity.

In the first part of the work, an analysis of the existing plants and the state of the art of the ISCC technology have been presented. Advantages and disadvantages of the integration of solar collectors in different kind of power plants are pointed out; this work is focused on the integration in already existing combined cycles, changing as little as possible the base plant. From the literature review, it turns out that the most promising integrations are the ones where the solar field integrates a part of the thermal duty of the high pressure evaporator. The purpose of this thesis is to provide for a more consistent analysis of different ISCC layouts comparing several integration layouts in the same reference combined cycle.

A review of commercial solar collectors has been proposed together with a model to evaluate receivers thermal losses. This analysis has been made to select which solar collector is best suited for integrations. In particular, two Linear Fresnel collector (Supernova for high temperatures levels and Nova1 for lower ones) and two Parabolic Troughs (Eurotrough 150 for high temperatures and Polytrough1800 for lower ones) have been used in ISCCs.

As a first step, two models of reference combined cycle have been built in Thermoflex®: the first one reproduces the layout proposed in the European Benchmarking Task Force (EBTF) document and it is used to validate the results given by the software. Another plant layout has been designed using the HRSG arrangement of an existing combined cycle, with two HRSGs, each one equipped with a gas turbine (GE 9F.03), one shared steam turbine and an air cooled condenser. The net efficiency of the studied combined with the ambient temperature of 30°C cycle is equal to 55,985%. The behaviour of this reference plant has been analysed in off design conditions and its annual performances have been obtained. The annual efficiency, obtained with a full load simulation, is 55,61%.

The reference combined cycle is used as base to build the Integrated Solar Combined Cycle layouts. Several layouts of integration on the bottoming cycle have been studied:

- High pressure evaporator (EVA HP)
- High pressure evaporator and first high pressure superheater (EVA+ SH1)

- High pressure evaporator and first and second high pressure superheater (EVA+SH2)
- High pressure economiser, evaporator and first superheater (ECO+EVA+SH1)
- High pressure economiser, evaporator, first and second superheaters (ECO+EVA+SH2)
- Intermediate pressure evaporator (EVA IP)
- High and intermediate pressure evaporators (EVA HP+IP)

These layouts have been implemented with both linear Fresnel and parabolic trough technologies, with different solar multiples. For the EVA HP Fresnel configuration, the solar field has been sized to achieve an inlet steam turbine mass flow of about the 115% of its nominal value; this is considered as the overloading limit for the turbine. Whenever the solar inlet flow goes beyond this limit because of the solar steam production, GTs load is decreased. In order avoid GTs load reduction, EVA HP configuration with solar multiple equal to 1 and 2 have been simulated with the revamping of the steam turbine and the high pressure superheaters too. Parabolic trough layouts have been sized on equal aperture area and on equal land area of the Fresnel layouts.

In addition, two other configurations have been analysed: the fuel preheating hybridisation and the solar inlet air cooling.

It has been found that the solar integration increases the net power output of the power plant of about 20 MW_e for integrations with solar multiple equal to one. The solar-to-electricity efficiency is equal to 23,62% for linear Fresnel in the EVA HP configuration in nominal conditions. The solar steam is converted more efficiently in a ISCC rather than in a stand-alone solar power plant, whose solar-to-electrical efficiency is about 19% [67] for power plants with production of saturated steam from Fresnel collectors. The solar share (3-5%) is quite small for configurations without adaptation of the combined cycle, because of the limitation imposed by the steam turbine. It increases for configurations with revamping of the steam turbine (up to 8%).

The solar field area of the fuel preheating configuration (16510 m² for each HRSG against 109224 m² for Fresnel EVA HP) has a limited impact with respect to other configurations. The most evident effect is the steam turbine net power output increase (of about 1 MW, which is 0,41% of the total power output of turbine), thanks to the higher power produced of the steam turbine. A higher increment of gas turbine performances may be reached with a higher fuel inlet temperature: that would require a new heat exchanger and would increase solar share and solar fraction of the integrated cycle.

The inlet air cooling is an effective way of increasing the plant power output, that couldn't be possible in the reference combined cycle but, on the other hand, the lower gas turbine inlet air temperature requires higher fuel consumption. In addition, even if the GTs efficiency increases thanks to the air cooling, the steam cycle still works at the ambient temperature, worsening the performance of the bottoming cycle (e.g. the air condenser, that works with higher mass flow and the same ambient temperature).

Once the nominal conditions were defined, off-design annual simulations have been carried out. Variation of temperature, effective DNI and load have been simulated for a defined series of values to obtain a good interpolation of parameters. This is necessary in order to evaluate the response of the power plant to meteorological conditions variation. The chosen location for the ISCC is Las Vegas, with a typical desert climate, high annual DNI and high mean temperatures. Effective DNI has been evaluated for each collector for every hour, starting from the calculated sun position.

Annual values of overall electricity, solar electricity and other main parameters have been calculated for every configuration, at first assuming full load operation for 8760h per year (power boosting mode). In this case, the gas turbine works always at the maximum admissible load.

Results pointed out that integrations with high solar multiples don't allow the power boosting of the cycle, since GTs are often at lower loads than 100%. The total power producible in hours with high effective DNI is limited, if the solar contribution is always at the maximum level, because of the limitation imposed by the steam turbine. In this case, it is possible to produce the same power output only defocusing a fraction of the solar field, but the solar fraction reduces. However, the reduction of power production allows the reduction of the fuel flow requested by the gas turbines.

Configurations with solar multiple 1 are able to increase the net electricity output of 30÷40 GWh/year; the power boosting is associated with a slight fuel saving, due to gas turbine load reduction during high solar irradiance availability.

PTC configurations are compared on equal aperture area or on equal land area basis with respect to LFC layouts, all with SM1. Parabolic trough configurations, with equal aperture area, can produce a higher quantity of solar electricity because of their higher efficiency (PTC solar electricity is 30% higher than LFC). However, since the steam production in the solar field is sensibly higher, the GTs load must be decreased more often: as a result, PTCs produce higher solar energy but a lower total electricity production (6675 GWh/yr for LFC vs 6655 GWh/yr for PTC in EVA HP layout). The best annual performances are the ones of layouts which integrate superheating sections in the solar field; in particular, configurations with SH2. In fact, since a lower fraction of the solar field is dedicated to the evaporation section, the GTs load reduction is less important.

To choose the most convenient configuration, an economic analysis has been carried out, using the main results of annual simulations. The LCOE approach, based on the International Energy Agency (IEA) simplified methodology, has been followed. In addition, for each configuration, the solar marginal LCOE has been evaluated: it is the incremental cost of the additional power produced thanks to the introduction of solar integration.

In the power boosting mode, the discerning parameter used for the plants evaluation is the solar marginal LCOE. In fact, LCOE is always higher with respect to the reference combined

cycle and it varies only slightly among the various solar layouts. That is because ISCCs higher investment cost are not counterbalanced by the increase of electricity production.

Whichever configuration is employed, the solar electricity produced with an ISCC is cheaper than the solar electricity produced in a solar only power plant. In fact, the solar marginal LCOE is in a range of 75÷100\$/MWh, while solar stand-alone power plant LCOE ranges from 140\$/MWh to 330\$/MWh. It must be underlined that higher values of solar marginal LCOE (i.e. 118,82÷155,42 \$/MWh) are shown by configurations with steam turbine repowering, since all modifications costs are charged on the solar part of the power plant. The best results among repowered layouts are shown by the “SM2 – new ST and SHs” configuration (i.e. layout with revamping of steam turbine and all high pressure superheaters); this result is related to the fact that the redesign of all the HP superheaters allows better overall performances during the year. However, the solar electricity produced in layouts with revamping is more expensive in comparison with other layouts. Probably, the resizing of steam turbine and heat exchangers may be more convenient with a larger solar field, thus the solar electricity produced during the year would be higher and it would justify the higher cost for components modifications. Among all the ISCC layouts, EVA HP implemented with Linear Fresnel collectors has the lowest solar marginal LCOE (76,22\$/MWh).

A sensitivity analysis has been carried out for the best configuration and it has been found that the inversion point between the reference CC LCOE and the EVA HP ISCC with linear Fresnel is for a fuel price of 0,52\$/MWh, which is about the twice of the price assumed, or for a specific collector specific cost of 120\$/m².

Yearly simulations have been carried out for EVA HP configuration with linear Fresnel and solar multiple equal to 1 and 2 in a scheduled load scenario too (fuel saving mode); the results of the two ISCC configurations have been compared to the reference combined cycle that follows the same regulation strategy. Even if the solar production decreases, because in some days the plant is not operative, the annual solar share increases, since the fossil fuel input is lower and the solar field is never defocused when the power plant is operating.

The economic analysis showed that, with equal electricity production, ISCC layouts have lower fuel consumption, allowing the reduction of the fuel expenditure. In this case, the LCOE is used as parameter of merit, since it accounts for the ISCC fuel saving. In fact, for the ISCC layout with solar multiple 1, fuel saving compensates the additional investment costs for the solar field, so the LCOE is lower for the integrated plant (60,8 \$/MWh vs. 61,7 \$/MWh). For this reason, CO₂ emissions are avoided (about 11% for the SM1 with respect to the reference CC), thanks to use of solar energy. Otherwise, ISCC with solar multiple 2 has a higher LCOE with respect to the reference combined cycle, since the higher additional cost are not compensated by a sufficient fuel saving. For this reason, an additional load regulation has been introduced for both the ISCCs; in this power demand curve it is assumed that the ISCC is working during the hours with high irradiance at the minimum GT turbine

load, i.e. 25% of the total GT load. The LCOE estimated for SM2 configuration results lower than the one of the reference CC in this layout (60,21\$/MWh vs. 61,7 \$/MWh).

In this work, the economic evaluation of all presented ISCCs layouts is made without considering any subsidies schemes. The eventual presence of subsidies for the renewable fraction may affect the results significantly. This work analyses only a part of the possible integrations of thermodynamic solar collectors that can be analysed in further studies. Linear collectors can be well-implemented also in coal power plants, or in other Rankine cycle power plants (e.g. geothermal or biomass based power plant). Solar tower are not analysed in this work, but they can be used both in the bottoming cycle integration with DSG technology, and as air-preheater before the GT combustor (i.e. solarised gas turbines).

APPENDIX A:

Sun position

The standard time zone (STZ) meridian longitude [°] is defined as:

$$\phi_{LONG,STZ} = STZ \cdot 15 \quad (52)$$

Where STZ is the standard time zone of the chosen location.

The declination [°] is the angle between the connecting line of the sun with the earth centre and the earth's equatorial plane and it is defined as:

$$\delta = 23,45 \sin\left(360 \cdot \frac{284 + n}{365}\right) \quad (53)$$

Where n indicates the day of the year, whose value varies from 1 to 365.

The equation of time returns as output the difference in minutes between the mean solar time and the true solar time for any date of the year and it assumes values from -17 to 17 minutes. It is defined as:

$$E_n = 229,18 \cdot \left(0,000075 + 0,001868 \cos\left(360 \cdot \frac{n-1}{365}\right) - 0,03277 \sin\left(360 \cdot \frac{n-1}{365}\right) + \right. \quad (54) \\ \left. -0,014615 \cos\left(2 \cdot 360 \cdot \frac{n-1}{365}\right) - 0,04080 \sin\left(2 \cdot 360 \cdot \frac{n-1}{365}\right)\right)$$

Solar time [h] is based on 24 hour clock with 12:00 as the time when the Sun is exactly aligned with the south direction. The solar time equation, which bounds the solar time with the local time (related to a reference meridian), can be written as:

$$t_s = t - \frac{\phi_{LONG,STD} - \phi_{LONG,STZ}}{15} + \frac{E_n}{60} \quad (55)$$

Where t [h] is the local time of the day, whose value varies from 1 to 24, and $\phi_{LONG,STD}$ is the reference longitude of the timezone.

The solar angle [°] is defined as:

$$\omega = (t_s - 12) \cdot 15 \quad (56)$$

The zenith angle [$^{\circ}$] is defined as the angle between the connecting line of the sun with the observer position and the line perpendicular to the horizontal plane containing the observer. It can be calculated as:

$$\theta_z = \cos^{-1}(\cos \phi \cdot \cos \delta \cdot \cos \omega + \sin \phi \cdot \sin \delta) \quad (57)$$

Solar altitude [$^{\circ}$] is defined as the complementary angle of the zenith angle:

$$\alpha_s = 90 - \theta_z, \quad \text{if } \alpha_s < 0 \rightarrow \alpha_s = 0 \quad (58)$$

The azimuth angle [$^{\circ}$] is the angle measured between the north direction and the projection of the sun ray on the horizontal plane. It can be calculated as:

$$\begin{cases} \gamma = 180 - \sin^{-1}\left(-\frac{\cos \delta \sin \omega}{\cos \alpha_s}\right) & \text{if } \cos \omega > \frac{\tan \delta}{\tan \phi_{LAT}} \\ \gamma = 360 + \sin^{-1}\left(-\frac{\cos \delta \sin \omega}{\cos \alpha_s}\right) & \text{if } \cos \omega \leq \frac{\tan \delta}{\tan \phi_{LAT}} \end{cases} \quad (59)$$

Bibliography

- [1] International Energy Agency (IEA), “Key World Energy Statistics 2014,” p. 82, 2014.
- [2] International Energy Agency (IEA), “2012 CO2 emissions overview,” *CO2 Emiss. from fuel Combust.*, 2012.
- [3] H. Hellevang, “Carbon capture and storage (CCS),” in *Petroleum Geoscience: From Sedimentary Environments to Rock Physics, Second Edition*, 2015, pp. 1–662.
- [4] Iea, “25 Energy Efficiency Policy Recommendations,” pp. 1–12, 2011.
- [5] C. Della, C. Al, and P. Europeo, “Strategia europea di sicurezza energetica,” 2014.
- [6] F. Kreith and D. Y. Goswami, *Handbook of energy efficiency and renewable energy*. CRC Press, 2007.
- [7] “International Atomic Energy Agency.” [Online]. Available: <https://www.iaea.org/>.
- [8] International Energy Agency (IEA), “Energy Technology Perspectives (2008),” 2008.
- [9] R. Messenger and D. Y. et al. Goswami, “Photovoltaics Fundamentals, Technology and Application,” in *Handbook of Energy Efficiency and Renewable Energy*, 2007.
- [10] M. Romero-Alvarez and E. Zarza, “Concentrating solar thermal power,” in *Handbook of Energy Efficiency and Renewable Energy*, CRC Press, 2007.
- [11] G. Manzolini and P. Silva, “Solar energy conversion with thermal cycles,” .
- [12] G. Tzetzze, *Chillades (2, 118-128)*. .
- [13] C. Zamparelli, “Da archimede ad archimede,” 2006.
- [14] C. Silvi, “Uso dell’energia solare: storia, presente e futuro,” 2014.
- [15] G. Bonardi and C. Patrignani, *Energie alternative e rinnovabili*. 2010.
- [16] R. Pitz-Paal, “Concentrating solar power,” *Futur. energy Improv.*, no. January, 2013.
- [17] M. Waldron, “CSP deployment to 2018 over the medium term,” 2013.
- [18] CSP Toady, “CSP solar tower report: cost, performance and key trends.”
- [19] J. H. Peterseim, S. White, A. Tadros, and U. Hellwig, “Concentrating solar power hybrid plants - Enabling cost effective synergies,” *Renew. Energy*, vol. 67, pp. 178–185, 2014.
- [20] H. Hong, S. Peng, Y. Zhao, Q. Liu, and H. Jin, “A typical solar-coal hybrid power plant in China,” *Energy Procedia*, vol. 49, pp. 1777–1783, 2013.

- [21] BP, “Statistical review of world energy 2015.”
- [22] H. G. JIN and H. HONG, “Hybridization of concentrating solar power (CSP) with fossil fuel power plants,” in *Concentrating solar power technology*, 2012.
- [23] M. P. Petrov, M. S. Popa, and T. H. Fransson, “SOLAR AUGMENTATION OF CONVENTIONAL STEAM PLANTS: FROM SYSTEM STUDIES TO REALITY,” *World Renew. Energy Forum*, no. May, pp. 1–8, 2012.
- [24] S. D. Odeh, “Unified model of solar thermal electric generation systems,” *Renew. Energy*, vol. 28, no. 5, pp. 755–767, 2003.
- [25] M. S. Jamel, a. Abd Rahman, and a. H. Shamsuddin, “Advances in the integration of solar thermal energy with conventional and non-conventional power plants,” *Renew. Sustain. Energy Rev.*, vol. 20, pp. 71–81, 2013.
- [26] D. Popov, “An option for solar thermal repowering of fossil fuel fired power plants,” *Sol. Energy*, vol. 85, no. 2, pp. 344–349, 2011.
- [27] J. H. Peterseim, a. Tadros, S. White, U. Hellwig, J. Landler, and K. Galang, “Solar Tower-biomass Hybrid Plants – Maximizing Plant Performance,” *Energy Procedia*, vol. 49, no. 0, pp. 1197–1206, 2014.
- [28] E. Pihl and F. Johnsson, “Concentrating Solar Power Hybrids – Technologies and European Retrofit Potential,” no. June, 2012.
- [29] D. Popov, “Innovative solar augmentation of gas turbine combined cycle plants,” *Appl. Therm. Eng.*, vol. 64, no. 1–2, pp. 40–50, 2014.
- [30] SOLGATE Report, Ormat, Ciemat, Dlr, Solucar, and Tuma, *Solar hybrid gas turbine electric power system*. 2005.
- [31] G. Lozza, *Turbine a gas e cicli combinati*. Esculapio, 2006.
- [32] M. Horn, H. Führung, and J. Rheinländer, “Economic analysis of integrated solar combined cycle power plants,” *Energy*, vol. 29, no. 5–6, pp. 935–945, 2004.
- [33] J. Dersch, M. Geyer, U. Herrmann, S. a. Jones, B. Kelly, R. Kistner, W. Ortmanns, R. Pitz-Paal, and H. Price, “Trough integration into power plants—a study on the performance and economy of integrated solar combined cycle systems,” *Energy*, vol. 29, no. 5–6, pp. 947–959, 2004.
- [34] R. Hosseini, M. Soltani, and G. Valizadeh, “Technical and economic assessment of the integrated solar combined cycle power plants in Iran,” *Renew. Energy*, vol. 30, no. 10, pp. 1541–1555, 2005.
- [35] M. J. Montes, a. Rovira, M. Muñoz, and J. M. Martínez-Val, “Performance analysis of an Integrated Solar Combined Cycle using Direct Steam Generation in parabolic trough collectors,” *Appl. Energy*, vol. 88, no. 9, pp. 3228–3238, 2011.
- [36] G. Zhu, T. Neises, C. Turchi, and R. Bedilion, “Thermodynamic evaluation of solar integration into a natural gas combined cycle power plant,” *Renew. Energy*, vol. 74, pp. 815–824, 2015.
- [37] G. Manente, S. Rech, and A. Lazzaretto, “On the optimum integration of solar energy

- into natural gas combined cycles,” 2015.
- [38] B. Kelly, U. Herrmann, and M. J. Hale, “Optimization studies for integrated solar combined cycle systems,” *Sol. Forum 2001*, 2001.
- [39] C. O. Ojo, D. Pont, E. Conte, and R. Carroni, “Performance evaluation of an integrated solar combined cycle,” 2012, pp. 1–10.
- [40] A. Rovira, M. J. Montes, F. Varela, and M. Gil, “Comparison of Heat Transfer Fluid and Direct Steam Generation technologies for Integrated Solar Combined Cycles,” *Appl. Therm. Eng.*, vol. 52, no. 2, pp. 264–274, 2013.
- [41] G. Cau, D. Cocco, and V. Tola, “Performance and cost assessment of Integrated Solar Combined Cycle Systems (ISCCs) using CO₂ as heat transfer fluid,” *Sol. Energy*, vol. 86, no. 10, pp. 2975–2985, 2012.
- [42] Y. Li and Y. Yang, “Thermodynamic analysis of a novel integrated solar combined cycle,” *Appl. Energy*, vol. 122, pp. 133–142, 2014.
- [43] K. Petela, G. Manfrida, M. Liszka, and C. Carcasci, “INTEGRATING SOLAR POWER IN LARGE COMBINED-CYCLE POWER PLANTS 2 . Technology background – CSPP plants and possible,” 2015.
- [44] a. Perdichizzi, G. Barigozzi, G. Franchini, and S. Ravelli, “Peak shaving strategy through a solar combined cooling and power system in remote hot climate areas,” *Appl. Energy*, vol. 143, pp. 154–163, 2015.
- [45] G. Barigozzi, G. Franchini, A. Perdichizzi, and S. Ravelli, “Simulation of Solarized Combined Cycles: Comparison Between Hybrid Gas Turbine and ISCC Plants,” *J. Eng. Gas Turbines Power*, vol. 136, no. 3, p. 031701, 2013.
- [46] H. Nezammahalleh, F. Farhadi, and M. Tanhaemami, “Conceptual design and techno-economic assessment of integrated solar combined cycle system with DSG technology,” *Sol. Energy*, vol. 84, no. 9, pp. 1696–1705, 2010.
- [47] L. Rubini, G. Habib, and M. Lavra, “Tecnologie solari a concentrazione – Produzione di calore a media temperatura,” 2011.
- [48] “<https://www.sbc.slb.com/SBCInstitute/Publications/SolarPower.aspx>.” .
- [49] “<https://www.therminol.com/products/Therminol-VP1>.” .
- [50] “http://www.archimedesolareenergy.it/molten_salt.htm.” .
- [51] D. Braccio, F. Di Mario, D. Marano, and V. Sabatelli, “Solare termico a bassa e media temperatura,” 2011.
- [52] A. Giostri and C. Saccilotto, “Sviluppo di codici di calcolo per la simulazione economico-energetica di impianti solari termodinamici a concentrazione lineare,” 2009.
- [53] “<http://stg.anu.edu.au/facilities/concentrators.php>.” .
- [54] “<http://www.ripassoenergy.com/our-technology/>.” .
- [55] “<http://www.torresolenergy.com/TORRESOL/fototeca/es>.” .

- [56] “<http://www.amusingplanet.com/2013/08/the-solar-power-towers-of-seville-spain.html>.” .
- [57] “<http://www.alternative-energy-tutorials.com/solar-hot-water/parabolic-trough-reflector.html>.” .
- [58] “<http://www.flabeg-fe.com/en/solar-mirrors.html>.” .
- [59] SkyFuel, “ReflecTechSolar.” .
- [60] J. H. Lienhard, “Heat Transfer,” *J. Heat Transfer*, vol. 82, no. 1, p. 198, 2010.
- [61] B. Soediono, “Archimede solar energy brochure,” *Archimede*. .
- [62] “SCHOTT PTR® 70 Receiver Manual,” 2011.
- [63] Schott Solar, “SCHOTT PTR® 70 Receiver Manual.” 2011.
- [64] A. Giostri, “Transient effects in linear concentrating solar thermal power plant,” 2014.
- [65] ThermoFlow Inc., “Thermoflex v.25 User Guide.” .
- [66] P. Silva, “Concentrating solar power.” pp. 1–9.
- [67] A. Giostri, M. Binotti, P. Silva, E. Macchi, and G. Manzolini, “Comparison of Two Linear Collectors in Solar Thermal Plants: Parabolic Trough Versus Fresnel,” *J. Sol. Energy Eng.*, vol. 135, no. 1, p. 011001, 2012.
- [68] R. Forristall, “Heat Transfer Analysis and Modeling of a Parabolic Trough Solar Receiver Implemented in Engineering Equation Solver,” no. October, p. 164, 2003.
- [69] M. Geyer and E. Lüpfert, “EUROTROUGH - Parabolic Trough Collector Developed for Cost Efficient Solar Power Generation,” *Transportation (Amst)*., pp. 1–7, 2002.
- [70] INABENSA, “EUROTROUGH II - Extension, Test and Qualification of EUROTROUGH from 4 to 6 Segments at Plataforma Solar de Almería,” *Eur. Community*, no. April 2003, pp. 1–28, 2002.
- [71] “http://www.rioglass.com/?page_id=1899.” .
- [72] SkyFuel, “SkyTrough Next-Generation Solar Parabolic Trough Technology.” p. 4, 2009.
- [73] NEP Solar AG, “Technical Data for the PolyTrough 1800,” pp. 1–4, 1800.
- [74] Novatec, “Concentrated Solar Power by Novatec Solar.” .
- [75] Industrial Solar, “Technical Data Industrial Solar linear Fresnel collector LF-11,” 2014.
- [76] IRENA, “Concentrating Solar Power,” *Renew. Energy*, vol. 1, no. 2, pp. 331–339, 2012.
- [77] S. Benmarraze, “Linear Fresnel Reflectors Concentrated Solar Power : cost reduction and performance improvement trends,” 2015.
- [78] “<https://www.thermoflow.com/>.” .

- [79] D. Chase, “Combined-Cycle Development, Evolution and Future,” p. 14 p., 2000.
- [80] U. S. E. I. Administration, “Updated Capital Cost Estimates for Utility Scale Electricity Generating Plants,” *US Dep. Energy*, no. April, pp. 1–201, 2013.
- [81] R. Kehlhofer, F. Hannemann, B. Rukes, and F. Stirnimann, *Combined-Cycle Gas & Steam Turbine Power Plants*. 2009.
- [82] “<https://powergen.gepower.com/>.” .
- [83] GE, “POWER ing the World.” 2016.
- [84] “<http://www.ivanpahsolar.com/>.” .
- [85] EBTF, “European best practice guidelines for assessment of CO₂ capture technologies,” 2011.
- [86] Gecos, “Gas – Steam Cycle Simulation Code <http://www.gecos.polimi.it/software/gc.php>.” 2013.
- [87] “<http://www.energia.polimi.it/>.” .
- [88] <https://powergen.gepower.com/products/heavy-duty-gas-turbines/9f-03-gas-turbine.html>, “GE GT-9F03 fact sheet.” .
- [89] “Simeri Crichi power plant.” [Online]. Available: <http://www.edison.it/it/la-centrale-termoelettrica-di-simeri-crichi> <http://globalenergyobservatory.org/geoid/43979>.
- [90] T. P. Winterberger, “Performance Corrections for Steam Turbines With Multi-Pressure Condensers,” 2014.
- [91] “Puerto Errado 2 Thermosolar Power Plant.” [Online]. Available: http://www.nrel.gov/csp/solarpaces/project_detail.cfm/projectID=159 <http://www.novatecsolar.com/56-1-PE-2.html>.
- [92] J. F. Feldhoff, M. Eickhoff, L. Keller, J. L. Alonso, M. Meyer-Grünefeldt, L. Valenzuela, J. Pernpeintner, and T. Hirsch, “Status and first results of the DUKE project - Component qualification of new receivers and collectors,” *Energy Procedia*, vol. 49, pp. 1766–1776, 2013.
- [93] E. Zarza, M. E. Rojas, L. González, J. M. Caballero, and F. Rueda, “INDITEP: The first pre-commercial DSG solar power plant,” *Sol. Energy*, vol. 80, no. 10, pp. 1270–1276, 2006.
- [94] A. Robbiati, “Sviluppo di un codice di calcolo per l’ottimizzazione di un impianto solare termodinamico con fluido termovettore gassoso.”
- [95] General Electric, “Inlet air cooling.” 2008.
- [96] Schott, “SCHOTT PTR 70 Premium Receivers,” vol. 70.
- [97] “National Solar Radiation Data Base.” [Online]. Available: http://rredc.nrel.gov/solar/old_data/nsrdb/1991-2005/tmy3/.
- [98] W. B. Stine and M. Geyer, “Power From The Sun,” 2001. .
- [99] J. Blanco and S. Malato, “Medium temperature solar concentrators,” in *Solar Energy*

Conversion And Photoenergy System - Volume I, 2009.

- [100] “XonGrid Interpolation Add-in.” [Online]. Available: <http://xongrid.sourceforge.net/>.
- [101] “Gestore Mercati Energetici.” [Online]. Available: <http://www.mercatoelettrico.org/it/>.
- [102] “U.S. Energy Information Administration.” [Online]. Available: https://www.eia.gov/dnav/ng/ng_pri_sum_dcu_SNV_m.htm.
- [103] “Autorità per l’energia elettrica il gas e il sistema idrico.” [Online]. Available: <http://www.autorita.energia.it/it/dati/gpcfr2.htm>.
- [104] “CH4 2014: Gas Naturale il mercato che verrà.” [Online]. Available: <http://www.accadueo.com/interviste-ch4/ch4-2014-gas-naturale-il-mercato-che-verra/2886.html>.